

Dissertation zur Erlangung des Doktorgrades
der Fakultät für Chemie und Pharmazie
der Ludwig-Maximilians-Universität München

Time-Resolved Photoluminescence and Elastic White Light
Scattering Studies of Individual Carbon Nanotubes
and
Optical Characterization of Oxygen Plasma Treated Graphene



von
Tobias Dominik Gokus
aus
Kirchen (Sieg)

2011

Erklärung

Diese Dissertation wurde im Sinne von § 13 Abs. 3 bzw. 4 der Promotionsordnung vom 29. Januar 1998 (in der Fassung der sechsten Änderungssatzung vom 16. August 2010) von Herrn Prof. Dr. Achim Hartschuh betreut.

Ehrenwörtliche Versicherung

Diese Dissertation wurde selbstständig, ohne unerlaubte Hilfe erarbeitet.

München, den 29. Juli 2011

.....
(Unterschrift des Autors)

Dissertation eingereicht am: 29. Juli 2011
1. Gutachter: Prof. Dr. Achim Hartschuh
2. Gutachter: Prof. Dr. Alexander Högele
Mündliche Prüfung am: 27. Oktober 2011

Abstract

In the course of this work the excited state dynamics of individual single-walled carbon nanotubes (SWCNTs) were studied by a combination of confocal PL spectroscopy and time correlated single photon counting (TCSPC) measurements. Nonradiative decay channels dominate the excited state dynamics of SWCNTs leading to low photoluminescence (PL) quantum yields and PL decay times on the picosecond timescale. Knowledge about the microscopic nature of these decay channels is crucial to improve the material properties. The measurements on the single nanotube level revealed large tube-to-tube variations of PL decay times, which could be attributed to different defect densities for different tubes. For the present SWCNT material the PL decay times only depend weakly on the nanotube length. SWCNT material synthesized by using a cobalt-molybdenum catalyst (CoMoCAT) systematically display short monoexponential PL decays, while the PL decay dynamics of SWCNTs produced high pressure decomposition of carbon monoxide process (HiPco) is either mono or biexponential depending on the respective local environment of the nanotube. The transition from a bi- to monoexponential PL decay can be explained by synthesis-dependent differences in defect densities. This defect related nonradiative decay channels reduce the amplitude of one decay component below the experimental detection limit. It is further shown, that photo-induced defects and gold atoms adsorbed to the sidewalls of SWCNTs are shown to alter the PL properties of individual SWCNTs. Additional low-energy PL satellite bands arise in the spectra. Their origin can be attributed to emission from nominally dark excitons which are "brightened" due to defect facilitated mixing of intrinsic states with different parity/spin. The role of defects in the brightening process was investigated by time-resolved PL measurements and complementary Raman spectroscopy. Based on its energy separation and the unusually slow PL decay dynamics the lowest energy satellite band can be assigned to the radiative recombination of a triplet exciton.

In a second project a common-path interference scattering approach (iSCAT) utilizing a conventional inverted laser scanning confocal microscope combined with a photonic crystal fibre as a supercontinuum white light source is successfully tested for its capabilities for elastic scattering imaging and spectroscopy of individual SWCNTs.

Finally, it is shown that single layer graphene can selectively be turned luminescent upon exposure to a mild oxygen plasma. The treatment leads to a strong and spatially uniform PL which is characterized by a single, broad PL band extending from the visible to the near infrared spectral region. The analysis of the defect related Raman I_D/I_G intensity ratio indicates the formation of nanometer sized islands for which the sp^2 conjugated lattice of graphene is still preserved. Emission of quantum confined states within these islands is discussed as a possible origin of the PL.

Contents

Preface	ix
I. Theoretical Background and Experimental Details	1
1. Physical Properties of SWCNTs and Graphene	3
1.1. Structural Properties of SWCNTs and Graphene	5
1.2. Electronic Properties of Graphene and SWCNTs	10
1.2.1. Electronic Energy Dispersion Relation of Graphene	11
1.2.2. Brillouin Zone and Energy Dispersion Relation of SWCNTs	15
1.2.3. Optical Transition Energies: Kataura Plot	22
1.3. Optical Transitions in SWCNTs	23
1.3.1. Symmetries of SWCNTs	24
1.3.2. Selection Rules for Interband Transitions	26
1.3.3. Absorption and Photoluminescence	27
1.4. Excitons in Carbon Nanotubes	28
1.4.1. Excitonic Dispersion Relation	32
1.4.2. Exciton energies	36
1.4.3. Exciton Mobility in SWCNTs	37
1.5. Photoluminescence of SWCNTs	37
1.5.1. Excitonic description of the PL process in SWCNTs	38
1.5.2. Excited State Dynamics, PL Decay Times and Quantum Yield	38
1.6. Raman Scattering of SWCNTs and Graphene	41
1.6.1. Raman Scattering of Graphene and SWCNTs	43
1.6.2. Raman Spectra of graphene and SWCNTs	46
1.6.3. Disorder in Nanographitic Materials: The I_D/I_G ratio	48
2. Optical Microscopy Methods	51
2.1. Confocal Microscopy	52
2.1.1. Spatial Resolution of Optical Microscopes	54
2.1.2. Gaussian Laser Beam and Gouy Phase Shift	58
2.2. Interference Scattering Microscopy	60
3. Materials and Methods	71
3.1. The Confocal Microscope Setup	71

3.2.	Sample Preparation	75
3.2.1.	SWCNT Sample Material	75
3.2.2.	Sample Preparation for Confocal PL Measurements	77
3.2.3.	HiPCO SWCNTs Dispersed in Agarose Gel	78
3.2.4.	Sample Preparation for iSCAT Measurements	79
3.3.	Confocal PL Imaging and Spectroscopy of Individual SWCNTs	79
3.4.	Time Correlated Single Photon Counting	82
3.4.1.	Acquisition of PL Transients of Individual SWCNTs	84
3.4.2.	Transient Fitting: General Aspects	85
3.4.3.	Transient Fitting: Mono- and Biexponential PL Decays of SWCNTs .	86
3.4.4.	Transient Fitting: Wavelength Dependence of the IRF	89
3.5.	Interference Scattering Microscopy	91
3.5.1.	Characterization of the PCF White Light Output	93
3.5.2.	Acquisition of Elastic White Light Scattering Images and Spectra . .	94
II.	Time-resolved PL Studies of Individual SWCNTs	97
4.	Excited State Dynamics of Individual SWCNTs at Room Temperature	99
4.1.	Introduction	100
4.2.	PL Decay Time Distributions of Individual CoMoCAT SWCNTs	101
4.3.	PL Decay Time Distributions: Defect Mediated Nonradiative Relaxation .	105
4.4.	Length Dependence of PL Decay Times	108
4.5.	Conclusion	115
5.	Mono- and Biexponential PL Decays of Individual SWCNTs	117
5.1.	Introduction	117
5.2.	PL Decay Dynamics of Individual HiPco and CoMoCAT SWCNTs	118
5.2.1.	PL Decay Dynamics of HiPco and CoMoCAT (6,5) SWCNTs	119
5.2.2.	PL Decay Dynamics of HiPco (6,4) SWCNTs	120
5.3.	Kinetic Model for the Biexponential PL Decay in SWCNTs	122
5.3.1.	Contribution of the K-momentum Excitons	126
5.4.	Discussion	127
5.4.1.	Transition from Mono- to Biexponential PL Decays	127
5.4.2.	Biexponential Decays in HiPco (6,4) SWCNTs	128
5.5.	Conclusion	130
6.	Defect Induced PL of Dark Excitonic States in Individual SWCNTs	133
6.1.	Introduction	133
6.2.	Optical Characterization of Photoinduced Low-energy Emission Bands .	134
6.3.	PL Decay Dynamics of the Dark and Bright States	136

6.4.	Investigation of the Dark State "Brightening" Process	138
6.4.1.	Raman Spectroscopy of Photoinduced Defects	138
6.4.2.	The Role of Oxygen in the Photoinduced "Brightening" Process . . .	142
6.4.3.	Brightening by Treatment With a Colloidal Gold Solution	143
6.5.	Discussion	144
6.5.1.	Population Dynamics of the Bright and Dark States	146
6.5.2.	Assignment of the PL Satellite Bands	147
6.6.	Conclusion	149
III. Elastic White Light Scattering Spectroscopy of Individual SWCNTs		151
7.	Elastic White Light Scattering Microscopy of Individual SWCNTs	153
7.1.	Introduction	153
7.2.	Reference Measurements on Gold Nanoparticles	156
7.3.	Reference Measurements on Single Layer Graphene	161
7.4.	Elastic White Light Scattering Spectroscopy of Individual SWCNTs	162
7.4.1.	Discussion	164
7.5.	Determining the Resonant E_{22} Extinction Cross Section	166
7.6.	Manipulation of the iSCAT signal	168
7.7.	Combined PL and Elastic Scattering Measurements	171
7.8.	Conclusion	174
IV. Optical Characterization of Plasma Treated Graphene		177
8.	Optical Characterization of Oxygen Plasma Treated Graphene	179
8.1.	Introduction	179
8.2.	Preparation of PLG	180
8.3.	PL Spectroscopy and Time-resolved PL Measurements of PLG	180
8.4.	Raman Spectroscopy of PLG	183
8.5.	Elastic White Light Scattering of PLG	185
8.6.	Discussion	189
8.7.	Conclusion	194
V. Summary		195
9.	Summary	197

VI. Appendix	201
A. Scattered Field of a Carbon Nanotube	203
B. Elastic White Light Scattering of Single and Multi-layer Graphene	207
B.1. Introduction	207
B.2. Model for the Scattering Contrast of Graphene	208
B.3. Elastic White Light Scattering Measurements of Graphene	214
Bibliography	219
List of Figures	249
List of Tables	253
List of Publications	255
List of Conferences	257

Preface

Carbon is one of the most versatile chemical elements. Its ability to form strong covalent single, double and even triple inter carbon bonds, which allows the formation of one, two and three dimensional structures, such as chains, rings and cages, among those are also the building blocks of organic life, such as DNA, RNA, proteins. In addition to the rich variety of its chemical compounds, elemental carbon exhibits various stable modifications and allotropes with particular different physical and chemical properties. The most prominent modifications are graphite and diamond, which can be found in natural mineral deposits. Both materials have been studied since centuries and are still in the focus of active research efforts. The different physical properties of both materials, e.g. diamond is one of the hardest materials and electrical insulator opposed by the soft graphite with its near metallic conductivity, are the consequence of their different crystal structure.

The interplay of structure and material properties becomes even more apparent for nanostructures, whose physical dimensions approach the extension of the electronic wave functions and thus lead the confinement of electrons in one, two or even three dimensions. Nanostructures exhibit completely different, to some extend surprising physical properties, compared to their corresponding bulk counter parts.

The basic building block for low-dimensional carbon allotropes is the so called graphene, which is basically a single layer of sp^2 hybridized carbon atoms. Graphene and 1D carbon filaments served only as model structures for theoreticians [1–3]. While there existed reports on micrometer long one-dimensional carbon tubes since the early 50th and 70th [4–6] and also on the existence of 2D carbon monolayers by Boehm et al. in the 1960th [7], these discoveries remained essentially unnoticed. The synthesis methods for these materials required more refinement and new characterization methods had to be developed in order to allow for more systematical studies.

Within the last 25 years the research field of carbon and carbon based composites has evolved rapidly. The key event for this fast development was the discovery of the so called Buckminster fullerene C_{60} by Smalley et al. in 1985. Characteristic for the class of fullerene molecules is their either spherical or ellipsoid cage-like structures consisting of varying numbers of rings with five, six and seven carbon atoms. Their diameter varies between 0.4 nm for the smallest fullerene C_{20} up to several nanometers for fullerenes with several tens of carbon atoms. The smaller fullerenes represent the 0D conformation (allotrope) of elemental carbon. Along with the development of scanning tunneling and atomic force microscopes, which are able to image and manipulate objects on the nanoscale, the discovery

of C₆₀ marked the starting point of nano-science.

Six years after the discovery of the C₆₀ in 1991 Iijima et al. reported on the discovery of long one-dimensional carbon tubes with diameters of only a few nanometers. They presented the first high resolution transmission electron micrographs of so called multiwalled carbon nanotubes (MWCNT) , which are extended tube-like structures consisting of two or more concentrically arranged carbon tubes [8]. Only two years later, two different groups Ichihashi et al. and Bethune et al. reported independently on the synthesis and characterization of single walled carbon nanotubes (SWCNTs) which exhibit either metallic or semiconducting electronic properties [9,10].

The fast rise of the 2D allotrope of carbon, the graphene, begun in 2004 with a first report of on electronic transport measurements on this material by Novoselov et al. [11]. Almost at the same time, two different preparation methods for graphene were introduced, which made this material widely available to the scientific community. An elusive approach presented by Berger et al. is based on the epitaxial growth of graphene by thermally heating a silicon carbide substrates to high temperatures [12]. A more simple preparation method based on the mechanical exfoliation of high quality bulk graphite was introduced by Novoselov et al. For this graphite flakes are repeatedly peeled utilizing simple scotch tape and then transferred to a substrate [13]. The Even more fascinating were the ground-breaking follow-up experiments on graphene based electronic devices, which revealed the relativistic properties of the charge carriers close to the Fermi level resulting in a near ballistic sheet conductivity [11]. The observation of unusual physical phenomena, such as a room temperature anomalous quantum Hall effect [14] or the occurrence of the Berry's phase [15] added further to the attraction of this material.

Both, graphene and SWCNTs, exhibit remarkably high room temperature charge carrier mobilities of 30000 cm²/Vs for graphene [16,17], excellent thermal conductivity [18,19] and also mechanical properties [20, 21]. These outstanding material properties in combination with their nanometer dimensions in the case of SWCNTs and the scalability of the size and shape of a graphene sheet with lithographic techniques make these promising materials for novel electronic and optoelectronic devices, such as in field effect transistors [22,23], field emission displays [24], in carbon nanotube LEDs [25] or in fast graphene based photodetectors [26,27].

The performance of future SWCNT and graphene based electronic devices depends strongly on the interaction of the charge carriers with phonons, defects and local environment. Hence, detailed knowledge about the optical properties of SWCNTs and graphene are of special relevance as they provide insight into the electronic and vibronic structure and also the factors influencing them. Photoluminescence (PL), Raman and elastic white light scattering spectroscopy are fast and non-invasive methods to study these interactions. Complementary time-resolved PL measurements provide information about the excited state dynamics.

Experiments performed on the single molecule level avoid the averaging of observed values which causes the well known inhomogeneous broadening typically observed in corresponding ensemble measurements. With such experiments it is possible to identify specific subensembles and the underlying physical processes responsible for the ensemble broadening.

In this work various optical microscopy and spectroscopy techniques based on the detection of the PL, Raman and elastic (Rayleigh) scattered light, are employed to study the optical properties of individual SWCNTs and plasma treated graphene. Individual SWCNTs are weak PL and Raman emitters compared to typical organic dye molecules. Confocal laser scanning microscopy (CLSM) in combination with single photon counting detectors provides the high detection and collection efficiency as well as a good background rejection, which are crucial for the detection of those [28–31]. Although the maximum spatial resolution which can be achieved with standard confocal microscopy is limited by diffraction and is roughly on the order of the wavelength of the excitation light (250–400 nm), individual SWCNTs can be studied by preparing samples which contain spatially well dispersed SWCNTs.

Synopsis of the thesis

The experimental of this thesis are presented in **three** different parts, each devoted to a specific scientific question regarding the photo physics of SWCNTs or graphene. Each experimental chapter starts with an section which introduces the scientific problem to the reader and reviews the current state of knowledge. The thesis is structured as follows:

Chapter 1 establishes the theoretical background and is intended as a brief overview about the current state of knowledge. The structural and electronic properties of SWCNTs and graphene are reviewed in the framework of a free carrier approximation. On this basis the optical processes and the related optical transition rules are outlined. In 1D systems strong Coulomb interactions lead to the formation of excitons. SWCNTs exhibit a complex manifold of optically allowed and forbidden excitonic states within the free carrier band-gap. Their properties are discussed in Sec. 1.4. Following this, the PL process is presented in detail focusing here on the microscopic origin of the observed PL energies and the current models describing the PL decay dynamics. Furthermore, Raman scattering of SWCNTs is reviewed and it is elucidated how Raman spectroscopy can be used as a tool for determining the cluster size in sp² nanographitic materials.

Chapter 2 is devoted to the two optical microscopy techniques, which were employed throughout this work: Confocal microscopy and a common-path interference scattering method (iSCAT). The spatial resolution of optical microscopes is limited by diffraction. Confocal microscopes, however, offers an improved rejection of background light resulting in an enhanced signal-to-noise ratio and also a higher axial resolution compared to a wide-field

microscope. A general description of the confocal principle is given and the lateral and axial resolution limit of light microscopes is elucidated. In the second part of the section the common-path iSCAT method and its realization based on a confocal microscope in reflection mode is presented. The formation of the interferometric signal and its dependence on various phase contributions is elucidated based on a simple model for the mode-overlap between the reflected and scattered light fields.

In *Chapter 3* the experimental realizations of the confocal and iSCAT microscopy techniques are addressed. The confocal microscope setup is described in detail as well as the different modifications to the setup required to perform time-resolved PL and elastic white light scattering measurements. The different SWCNT materials studied in this work are introduced and the sample preparation yielding spatially well separated isolated SWCNTs is presented. The standard procedure for the acquisition of PL images and spectra is presented together with some representative experimental PL data. The basic principle of the TCSPC technique which is employed for the acquisition of PL transients are briefly discussed, along with details on the transient fitting procedure. As a last, the characteristics of the photonic crystal fibre which is used as a white light source for elastic scattering measurements are specified and its implementation in the microscope setup is shown.

In *Chapter 4* the time-resolved PL decays of individual CoMoCAT SWCNTs at room temperature are studied with the TCSPC technique. Fast PL decay times in the low picosecond regime are observed with tube-to-tube variations in the range of 1–40 ps. For the majority of the observed SWCNTs the PL decay is monoexponential. The origin the decay time variations is investigated by combining PL spectroscopic data with corresponding PL decay times for the same SWCNT. A correlation between PL decay times and PL linewidth indicate the presence of two distinct defect related phonon-assisted nonradiative decay channels. Variations in the defect concentrations for different SWCNTs might then account for the observed PL decay time variations. The nanotube ends represent an intrinsic type of nonradiative decay channel. It is known that if the highly mobile excitons reach these sites the PL is efficiently quenched. In order to study the contribution of this decay channel to the fast nonradiative decay rates, the dependency of the PL decay times on the nanotube length is investigated. The discussion of the results is supported by a numerical model for the diffusional motion of excitons in SWCNTs.

In *Chapter 5* it is shown that also intrinsic nonradiative decay channels contribute to the PL dynamics of SWCNTs. Recently, biexponential PL decays for SWCNTs synthesized by the HiPco CVD process were reported which was attributed to a weak phonon-mediated coupling between the bright excitonic state to a lower-energy dark state. In this chapter the influence of different local environments and synthesis-related effects on the PL decay dynamics of two different kinds of SWCNT materials, produced by the HiPco and CoMoCAT CVD processes, is investigated. It is found that the PL decay of HiPCO SWCNTs is mostly

biexponential with a characteristic, additional long decay component with a time constant on the order of several hundreds of picoseconds. CoMoCAT SWCNTs on the other hand exhibit a strictly monoexponential decay behavior irrespective of the local environment. Based on the more narrow PL linewidth and the systematically longer PL decay times of HiPco SWCNTs compared to the CoMoCAT material it can be concluded that this material is less affected by synthesis related defects. An established three level kinetic model, which was introduced to explain the biexponential PL decays in SWCNTs, is modified to account for additional defect-related nonradiative decay channels which affect the bright and dark excitonic states. By employing this modified model the observed transition from a bi- to monoexponential decay behavior for the different SWCNT materials can be reproduced.

The importance of defect-related external nonradiative decay channels on the decay dynamics of SWCNTs became evident in the previous chapters. It is predicted that symmetry breaking defects in SWCNTs can relax the optical selection rules which would allow the mixing of excitonic states with different parity and/or multiplicity. In *chapter 6* it is shown for the first time that by intentionally introducing defects using high power laser pulses the PL spectrum of individual SWCNTs can be considerably modified. The introduction of defects leads to the emergence of additional groups of low-energy PL satellite bands. These new PL bands and the changes to the main emission band, which are caused by the brightening process, are studied by (time-resolved) PL and Raman spectroscopy. Furthermore it is shown that low-energy PL bands with similar characteristics can be created when treating SWCNTs with a colloidal gold solution. The results of the studies suggest that the PL of the lowest energy satellite band can be assigned to the radiative recombination of a triplet exciton.

In *Chapter 7* the first results of white light scattering measurements on individual SWCNTs deposited on a transparent substrate are presented. Here, the general applicability of the interference scattering method (iSCAT) for the imaging and spectroscopy of the elastic scattering response of individual SWCNTs is investigated. In a first step the performance of the iSCAT setup is tested for materials with known optical properties, such as gold nanoparticles and single layer graphene. Exemplarily, the formation of the interferometric contrast of spherical gold nanoparticles is elucidated. The influence of different parameters on the scattering signal, such as the particle size, the axial displacement and the excitation wavelength on the signal is discussed. It is found that the scattering signal of individual (6,5) and (8,3) SWCNTs is mainly governed by the excitonic E_{22} optical transition. The presence of an individual SWCNT in the laser excitation focus reduces the amount of back reflected laser light off the glass substrate by approximately 4–8 %, which is of comparable magnitude as the scattering contrast of 20 nm gold nanoparticles. By comparing the scattering amplitudes of gold particles with well known optical constants and the one of SWCNTs, the resonant absorption/extinction cross section of the E_{22} excitonic transition of (6,5) SWCNTs can be estimated. An outlook on future experiments is given, where PL and elastic white light scattering measurements are combined to study the E_{11} and E_{22} optical transitions of the

same SWCNT.

The following *Chapter 8* is dedicated to the optical characterization of a luminescent graphene derivative, which was produced by a mild oxygen plasma treatment. The strong and spectrally broad emission of this novel material is studied with PL spectroscopy and the TCSPC method. Raman spectroscopy is utilized to study the structural changes and the degree of disorder introduced to the graphene lattice upon plasma exposure. The evolution of the defect related Raman I_D/I_G -ratio for increasing plasma exposure times indicates the formation of nanocrystallite sp^2 clusters with an average diameter of about 1 nm for the longest treatment times. The wavelength dependent elastic scattering contrast of the oxygen plasma treated graphene is distinct different to the one of pristine graphene. The elastic scattering contrast can be reproduced by employing a numerical model for the reflectance of a multi-layer system. The modeling yields optical constants which are comparable to the ones of graphene oxide. The formation of nanocrystallite islands which was indicated by the Raman analysis suggests that the microscopic origin of the broad PL might be due to quantum confinement, where the PL band is just a superposition of a multitude of narrow PL bands centered at different size-controlled emission energies. Based on the spectrally uniform reduction of the PL intensity in PL bleaching experiments and the absence of any spectral dependence of the PL decay dynamics PL from such a heterogenous ensemble of emitters can be excluded.

Finally, in *Chapter 9* the most important findings achieved in this work are summarized.

Part I.

Theoretical Background and Experimental Details

1. Physical Properties of SWCNTs and Graphene

SWCNTs and graphene cannot be found in natural deposits and need to be synthesized. Nowadays, there exist several synthesis methods to produce small quantities of SWCNTs and graphene. In the case of SWCNTs also large-scale production methods are well established with yields up to several kilograms per day, while large-scale synthesis routes for high quality single layer graphene flakes are currently in development.

There are basically two different routes for the preparation of graphene, following either top-down or bottom-up approaches. In the first case, graphite with high purity and crystallinity, like highly oriented pyrolytic graphite (HOPG) or Kish graphite, is used as a starting material. Separation and isolation of individual graphene layers is achieved either by chemical solution based exfoliation techniques relying on the incalation of chemical compounds between the individual layers [32] or by physical exfoliation. Indeed the first successful preparation of large single layer graphene flakes was reported for an experimental approach based on the micromechanical cleaving of highly crystalline graphite by repeatedly peeling with an adhesive tape [13]. Very early attempts to produce single graphene layers employed chemical approaches which yielded most of the times so called chemically modified graphenes, whose most prominent derivative is graphene oxide. These compounds can be used as graphene precursor materials. Appropriate chemical reactions, e.g. reduction of graphene oxide, remove the chemical functionalization and partially restore the carbon sp^2 graphene lattice. Nowadays, also wet chemistry approaches have been developed to produce aqueous dispersions of surfactant stabilized single layer graphene which relay on the exfoliation of graphite flakes in a ultrasonication bath and subsequent addition of a surfactant [33, 34].

Bottom-up approaches comprise e.g. the epitaxial growth of graphene on SiC [12, 35] or the chemical vapor deposition based growth of graphene on copper substrates [36, 37], which allows to produce high quality graphene flakes as large as one square centimeter and also heterogenous films of graphene flakes covering areas up to 75 cm^2 [38]. Another promising synthesis route is based on an organic chemistry approach, where self-assembly of conjugated macromolecule precursors leads to the formation of a two dimensional network conjugates carbon network. With this approach nanographenes and nanoribbons with defined morphology have been successfully synthesized [39, 40].

For the preparation of SWCNTs various synthesis methods have been established. The very first preparation methods for which the yield could be successfully upscaled to several grams per day were arc discharge and laser ablation methods [10, 41]. Both methods relay on the vaporization of a solid carbon target by heating using either an electrical discharge or intense pulsed laser irradiation. In the subsequent condensation step SWCNTs grow at catalyst particles. While both methods yield SWCNT material on the gram scale, the quality of the

material is low, containing large amounts of unwanted byproducts such as amorphous carbon and bundled SWCNTs. Chemical vapor deposition (CVD) methods on the other hand, such as the high pressure decomposition of carbon monoxide monoxide method (HiPco) and catalytic growth on cobalt molybdenum catalyst particles (CoMoCAT) processes, are nowadays used for the large scale production of SWCNTs. By adjusting the growth parameters high quality SWCNT material can be produced. The HiPco and CoMoCAT CVD methods and the different properties of the distributions of SWCNTs produced by them are outlined in more detail in Sec. 3.2.1.

Years before experimental evidence was found for the existence of free standing graphene, this planar conjugated carbon sheets attracted the interest of theoreticians. Graphene is the prototype of an extended sp^2 conjugated carbon network and served as a model system for understanding the electronic properties of graphite. For the very first calculations of its electronic dispersion relation simple tight-binding approximations were applied [1, 3]. This simple approximations reproduce the general properties of the electronic dispersion relation sufficiently well, which then can be further used to derive the 1D electronic band structure of SWCNTs by applying a zone-folding approach.

In this chapter the physical properties of graphene and SWCNTs are summarized. Beginning with the description of their structure, the electronic dispersion relation and the related optical transition energies are derived within a nearest neighbor tight-binding approximation, where the excited states are free electrons and holes. In Sec. 1.3 some general aspects of optical transitions in SWCNTs are introduced. Starting with a brief review of the symmetry elements in SWCNTs and the related point groups, the optical selection rules for interband transitions are derived. These are then discussed in more detail for the absorption and PL processes.

The simple tight-binding model fails to describe the excited state physics of carbon nanotubes quantitatively. Attractive and repulsive Coulomb interactions between the photogenerated charge carriers become increasingly important in one-dimensional structures and result in the formation of stable excitons, strongly bound electron-hole pairs, which are virtually dominating the photophysics of semiconducting and even metallic SWCNTs. The properties of these quasi-particles in SWCNTs are the topic of Sec. 1.4, where the theoretical approach is sketched, which is used to obtain the energies and wavefunctions of the excitons. Based on the previously introduced optical selection rules and the symmetry of the excitonic states the difference between optically bright and dark excitons is outlined. The last two sections of this chapter briefly review the PL properties Finally, in the last section of this chapter the different vibrational modes of graphene and SWCNTs which can be probed by Raman spectroscopy are presented. It is shown, how Raman spectroscopy can be used to determine the defect density and cluster size in graphene.

1.1. Structural Properties of SWCNTs and Graphene

In this section the geometry and related structural properties of graphene and SWCNTs are introduced. In particular SWCNTs exhibit a rich variety of different structures which in consequence lead to distinct physical properties, such as metallic or semiconducting behavior. However, it can be shown that all structures are well characterized by the so called chiral index (n,m) which is therefore commonly used to denote the various SWCNT species.

The basis for deriving the structural and electronic properties of SWCNTs is graphene, which is theoretically a planar mono-layer of carbon atoms. However, graphene deposited on substrates, such as silicon or siliconoxide, is not atomically flat, instead it exhibits ripples with height variations in the range of 0.32–0.16 nm, mainly following the substrate morphology [42, 43]. Similar structural corrugations are also observed for freely suspended graphene [44]. If deposited on atomically flat substrates such as mica these ripples are largely suppressed and one finds a graphene sheet thickness of 0.23 nm [43].

SWCNTs can be simply regarded as a rolled up rectangular stripe of graphene which form a hollow, seamless cylinder. Their diameters cover a range between 0.4 and several nanometers, strongly depending on the synthesis method. The length of SWCNTs is typically on the order of a few tens of nanometers up to several hundreds of micrometers, which is strongly influenced on the growth conditions and postprocessing steps. For example, acid treatment which is typically used to remove residual catalyst particles and also ultrasonication in order to facilitate micelle-encapsulation are known to efficiently cut the SWCNTs into smaller tube fragments. Ultra long SWCNTs with length up to 4 cm can be synthesized using special CVD growth conditions [45]. The ends of the tubes are either capped by fullerene-like end groups or un-capped with dangling or saturated carbon bonds. Because of their small aspect ratio between diameter and length, SWCNTs can be considered as one-dimensional crystals.

Real Space Unit Cell and Brillouin Zone of Graphene

The two dimensional carbon lattice of graphene provides also the basis for the structural properties of SWCNTs and is discussed in the following. Graphene is a monolayer of sp^2 hybridized carbon atoms, which are arranged in a hexagonal honeycomb lattice. In Fig. 1.1 (a) a small section of the hexagonal graphene honey comb lattice is depicted.

The real space unit cell of graphene contains two carbon atoms, which each belong to two different intersecting triangular sublattices, A (grey dots) and B (white dots). The unit cell (grey shaded) is spanned by the two graphite lattice vectors \mathbf{a}_1 and \mathbf{a}_2 , which enclose an angle of 60° [46]. In cartesian coordinates they are defined as follows:

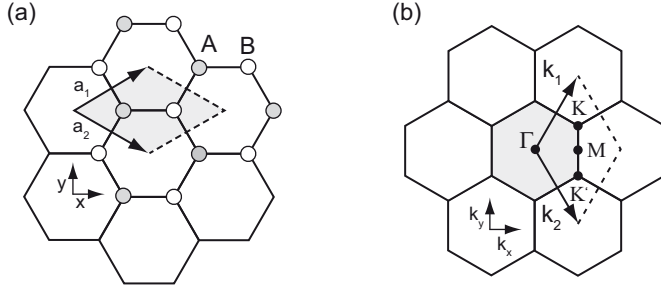


Fig. 1.1. (a) Real space unit cell of graphene. The real space lattice vectors \mathbf{a}_1 and \mathbf{a}_2 define the graphene unit cell (grey shaded rhombus), which contains two carbon atoms, each belonging to two intersecting sublattices, A (grey dots) and B (white dots). (b) The first Brillouin zone (BZ) of graphene (grey shaded) with the high-symmetry points Γ -M-K(K'). \mathbf{k}_1 and \mathbf{k}_2 are the reciprocal lattice vectors.

$$\begin{aligned} \mathbf{a}_1 &= \left(\frac{\sqrt{3}}{2}, \frac{1}{2} \right) a; & \mathbf{a}_2 &= \left(\frac{\sqrt{3}}{2}, -\frac{1}{2} \right) a \\ a &= |\mathbf{a}_1| = |\mathbf{a}_2| = \sqrt{3}a_{C-C} \approx 2.46\text{\AA} \end{aligned} \quad (1.1)$$

Here a is the graphene lattice constant and $a_{C-C} = 1.421 \text{ \AA}$ the nearest-neighbor carbon distance in graphite.

In the reciprocal k -space graphene exhibits a hexagonal Brillouin zone (BZ) as shown in Fig. 1.1 (b). The corresponding reciprocal lattice vectors \mathbf{k}_1 and \mathbf{k}_2 can be derived by exploiting the translation invariance of the lattice: $a_i \cdot k_j = 2\pi \delta_{ij}$ with $i, j=1,2$. In cartesian coordinates the k -vectors read:

$$\mathbf{k}_1 = \left(\frac{1}{\sqrt{3}}, 1 \right) \frac{2\pi}{a}; \quad \mathbf{k}_2 = \left(\frac{1}{\sqrt{3}}, -1 \right) \frac{2\pi}{a}. \quad (1.2)$$

The BZ contains three high symmetry points Γ , M and K (K'), which are located at the center, the corners and the middle of an edge, respectively.

The Unit Cell of SWCNTs

A SWCNT might be regarded as a rectangular stripe of graphene rolled up to a seamless cylinder. The size and orientation of such a rectangle and in consequence the structure of a SWCNT is therefore uniquely defined by the so called chiral vector. Fig. 1.2 illustrates the construction of the unit cell of a semiconducting (6,5) SWCNT. The chiral vector \mathbf{C}_h (red) and the 1D translation vector \mathbf{T} (black) form the edges of the rectangle with the corner points OBB'A. The lengths of both vectors correspond to the width and height of the unit cell, re-

spectively. The chiral vector interconnects the two crystallographic equivalent points O and A. Perpendicular to \mathbf{C}_h , the translation vector T extends from the origin O to the first lattice point B. By rolling up this stripe of graphene in direction of \mathbf{C}_h in such a way that point O superimposes onto A and point B onto B' one obtains the cylindrical unit cell of the SWCNT.

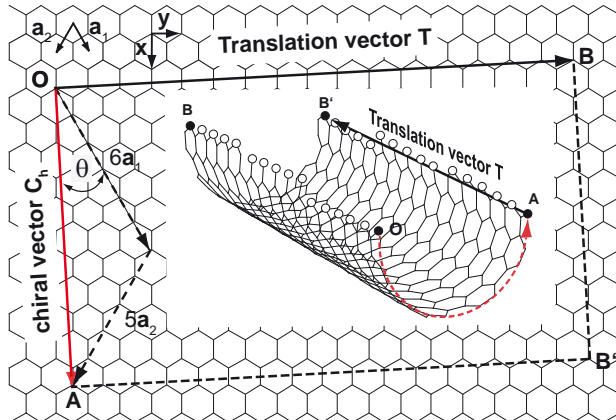


Fig. 1.2. Unit cell of a semiconducting (6,5) SWCNT. The unit cell can be constructed by rolling up a rectangular stripe of graphene. The edges of the sheet are defined by the chiral vector \mathbf{C}_h and the translation vector T normal to \mathbf{C}_h . The chiral vector is defined by the graphene lattice vectors \mathbf{a}_1 and \mathbf{a}_2 , e.g. in the case of the (6,5) SWCNT: $\mathbf{C}_h = 6 \cdot \mathbf{a}_1 + 5 \cdot \mathbf{a}_2$. Rolling up the rectangular sheet, so that point O superimposes on A and point B on B' the 1D cylindrical unit cell of the SWCNT is formed [47].

The chiral vector \mathbf{C}_h is defined as the sum of integer multiples of the graphene lattice vectors \mathbf{a}_1 and \mathbf{a}_2 :

$$\mathbf{C}_h = n \cdot \mathbf{a}_1 + m \cdot \mathbf{a}_2 \quad n, m \in \mathbb{N}. \quad (1.3)$$

The integer pair (n,m) is referred to as the so called *chiral index* and is commonly used for naming the various nanotube structures. The length of the chiral vector defines the circumference L or correspondingly the diameter d_t of a SWCNT:

$$L = |\mathbf{C}_h| \quad (1.4)$$

$$d_t = \frac{L}{\pi} = a \frac{\sqrt{n^2 + m^2 + nm}}{\pi}. \quad (1.5)$$

The orientation of the chiral vector \mathbf{C}_h with respect of the graphene lattice is characterized by the so called chiral angle θ , which is defined as the angle between \mathbf{C}_h and the graphene lattice vector \mathbf{a}_1 :

$$\theta = \arccos \frac{2n + m}{2\sqrt{n^2 + m^2 + nm}} . \quad (1.6)$$

Conveniently, the integers are chosen the way that $n \geq m$, which restricts the possible range of θ to angles between $0 \leq |\theta| \leq 30^\circ$. However, due to the hexagonal rotational symmetry of graphene, any tube (n,m) has an enantiomorphic (m,n) structural counterpart with a chiral angle in the interval $30^\circ \leq |\theta| \leq 60^\circ$. Such tubes differ by the direction of their helical screw axis, which is right-handed for (n,m) and left-handed for (m,n) SWCNTs. Two distinct directions of \mathbf{C}_h can be distinguished with $\theta=0^\circ$ or $\theta=30^\circ$. SWNTs with chiral vectors pointing in this directions called armchair and zigzag SWCNTs, respectively. The naming is based on the characteristic pattern which is formed by the carbon chain forming the edges of the respective graphene rectangle.

Based on the chiral index, SWCNTs can be classified into three major groups with distinct geometry: Armchair (n,n) , zigzag $(n,0)$ and chiral (n,m) tubes. The armchair SWCNTs exhibit a chiral angle $\theta = 30^\circ$, while for the zigzag SWCNTs θ equals 0° . Importantly, SWCNTs belonging to the group are achiral as their structures exhibit mirror and rotoreflectional planes [48]. All other SWCNTs belong to the group of chiral tubes with a helical screw axis along their axis. The physical properties might vary drastically for SWCNTs with similar chiral index, e.g. while the $(6,5)$ is semiconducting, the $(6,6)$ is a metallic SWCNT. Whether a SWCNT is metallic or semiconducting can be easily deduced from its chiral index. If the difference of n and m is an integer multiple of three, that is $(n - m) \bmod 3 = 0$, SWCNTs are metallic (semi-metallic), otherwise they are semiconductors. Consequently, all armchair (n,n) SWCNTs are metallic SWCNTs. The relation between chiral index and their metallic or semiconducting behavior is illustrated in Fig. 1.3. Here, each circle represents the end point of the chiral vector with chiral index (n,m) . Metallic SWCNTs are designated by the black solid circles.

Semiconducting nanotubes are further classified as S1 (solid grey circles) and S2 (open circles) type, depending whether $(2n+m) \bmod 3$ is equal to one or two, respectively. Characteristic for each type of semiconducting SWCNT is their systematic behavior of their optical transition energies which gives rise to characteristic family patterns in plots of transition energies against tube diameters [49–51]. An explanation for this systematic dependence of the optical transition energies on the SWCNT structure is provided in Sec. 1.2.

To complete the description of the unit cell one needs an expression for the translation vector \mathbf{T} , whose length defines the extensions of the graphene unit cell. Similar to \mathbf{C}_h , \mathbf{T} is defined as a linear combination of the graphene lattice vectors and the integers t_1 an t_2 :

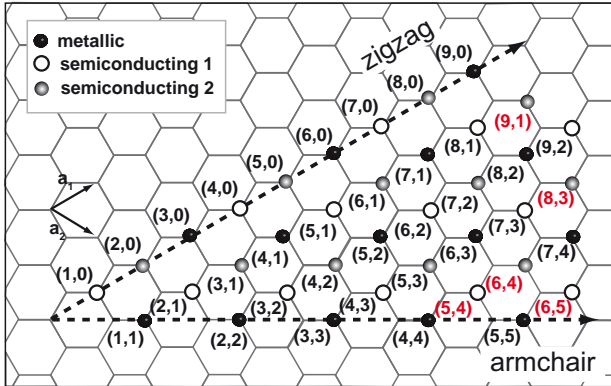


Fig. 1.3. The chiral index (n,m) determines whether SWCNTs are (quasi-) metallic (black dots) or semiconducting (green and blue dots). All tubes for which the relation $(n-m) \bmod 3 = 0$ holds exhibit metallic properties. This is fulfilled for all armchair SWCNTs with $n=m$. Semiconducting nanotubes belong to either of two families, S1 and S2, which systematically differ in their electronic energies. Red indices indicate small diameter tubes studied in this work.

$$\begin{aligned} \mathbf{T} &= t_1 \mathbf{a}_1 + t_2 \mathbf{a}_2 \quad t_1, t_2 \in \mathbb{N} \\ t_1 &= \frac{2m+n}{d_R}, \quad t_2 = -\frac{2n+m}{d_R}. \end{aligned} \quad (1.7)$$

Here d_R is the highest common divisor of $(2n+m)$ and $(2m+n)$. For the translation period T one obtains:

$$T = |\mathbf{T}| = \frac{\sqrt{3}L}{d_R}. \quad (1.8)$$

From Eqn. 1.5 and Eqn. 1.6 it becomes apparent that each chiral index (n,m) corresponds to an unambiguous combination of diameter d_t and chiral angle θ and thus fully defines the structure of a particular SWCNT. It is therefore commonly established to use the chiral index to specify the different SWCNT chiralities [52].

Having equations for the diameter and the length of the unit cell at hand, it is possible to calculate the number of graphene hexagons per unit cell N_h , which is just the ratio of the cylindrical surface area of the nanotube S_t and the area of a graphene unit cell S_g :

$$N_h = \frac{S_t}{S_g} = \frac{2(n^2 + m^2 + nm)}{d_R}. \quad (1.9)$$

Because each graphene unit cell holds two carbon atoms, the number of carbon atoms N_c is just twice the number of hexagons N:

$$N_c = 2N_h = \frac{S_t}{S_g} = \frac{4(n^2 + m^2 + nm)}{d_R}. \quad (1.10)$$

An ideal (6,5) SWCNT with $d_t=0.747$ nm has 90 carbon atoms per nanometer, whereas the (6,4) SWCNT with $d_t=0.683$ nm has 82 carbon atoms per nanometer. Armchair and zigzag SWCNTs with comparable diameters as the (6,5) or (6,4) chiralities exhibit far less carbon atoms per unit cell and therefore are frequently used as model systems for quantum mechanical calculations.

1.2. Electronic Properties of Graphene and SWCNTs

Graphene and one third of the SWCNTs are metallic or quasi-metallic [53]. This is a consequence of their special electronic band structure. In this section the electronic band structure of graphene and SWCNTs will be derived in the framework of a nearest neighbor tight-binding approach. The tight-binding approach is well established for calculating the electronic band structure of graphitic materials and yields qualitatively and quantitatively reasonable results for the band energies in graphene [1, 54, 55].

In a first step an the electronic energy dispersion relation of graphene is derived and its properties are discussed. In order to obtain the energy dispersion relation of SWCNTs new reciprocal lattice vectors need to be defined, which take into account the periodic boundary conditions imposed by the cylindrical structure of SWCNTs. The electronic energy dispersion relation of graphene then serves as starting point for a zone-folding approach, which is applied to derive the one dimensional BZ and corresponding energy bands of SWCNTs. The origin for the metallic and semiconducting behavior of SWCNTs can be illustrated using the "cutting line concept", which also provides an explanation for the systematical trends of optical transition energies of semiconducting SWCNTs. Further the energy bands of metallic and semiconducting SWCNTs and their related density of states are discussed.

It is to note that the band structure of SWCNTs obtained by the simple tight-binding approach does not include important additional effects which affect the shape and energetically position of the bands. For example curvature effects become increasingly important for small diameter SWCNTs. The bond angles between the atoms of the curved SWCNT sidewalls deviate from the ideal angles of a planar structure which allows a partial overlap between σ and π bands [46].

1.2.1. Electronic Energy Dispersion Relation of Graphene

Graphene has a planar structure, where each carbon atom is covalently bound with three neighboring carbon atoms. Carbon posses four valence electrons, two 2s and two 2p electrons. The energies of the 2s and 2p orbitals are of comparable magnitude, which allows them to mix and form hybrid orbitals. The carbon atoms in graphene are sp^2 hybridized, where one 2s and two 2p orbitals ($2p_x, 2p_y$) form three sp^2 hybridized orbitals, while one $2p_z$ orbital remains, which is oriented perpendicular to the plane defined by the hybrid orbitals. As there are two carbon atoms per unit cell with four valence electrons each, there are eight electronic bands, $3\sigma, 3\sigma^*, 1\pi$ and $1\pi^*$. The three σ bonds are filled by six electrons and constitute to the strong in-plane bonds to the three carbon neighbors, while the π band is filled with the remaining two electrons. The π electrons are delocalized across the whole plane and owe to the excellent current and heat conductivity of graphene. For the optical processes in the visible spectral range only transitions between the π and π^* bands are of relevance, as the smallest energy separation of the σ and σ^* bands is about ≈ 6 eV at the Γ -point [56].

In the following only the p_z electrons are considered for the tight-binding description of graphene. They form the π valence and π^* conduction bands, which touch at the Fermi level at distinct points, the K and K'-points in the graphene BZ. The fundamental assumption for the tight- binding approximation is that the electrons are localized at the ionic cores and thus can be approximated by their atomic wavefunctions. Starting point for the calculation of the electronic dispersion relation is the Schrödinger equation:

$$\hat{H}\Psi(\mathbf{k}) = E(\mathbf{k})\Psi(\mathbf{k}) . \quad (1.11)$$

$E(\mathbf{k})$ are the energy eigenvalues of the electronic state with wavevector \mathbf{k} and $\Psi(\mathbf{k})$ is the corresponding eigenfunction. \hat{H} is the Hamiltonian of the atomic wavefunctions with the general form:

$$\begin{aligned} \hat{H} &= -\frac{\hbar}{2m} \sum_k \nabla_k + U(\mathbf{r}_k) \\ \text{with } U(\mathbf{r}_k) &= \sum_l U(\mathbf{r}_k - \mathbf{R}_l) . \end{aligned} \quad (1.12)$$

The Hamiltonian of the system is the sum of all single particle Hamiltonians. The first term in Eqn. 1.12 corresponds to the kinetic energy of a particle with mass m and the second term corresponds to the potential energy. In case of a periodic crystal lattice, the potential is also periodic. The latter is the sum of the Coulomb interaction between the electron k and the ion cores located at atomic lattice sites in their rest position \mathbf{R}_l .

The ansatz for the wavefunction $\Psi(\mathbf{k})$ is a linear combination of Bloch functions $\Phi(\mathbf{k}, \mathbf{R})$:

$$\Psi(\mathbf{k}) = C_A \cdot \Phi_A(\mathbf{k}, \mathbf{R}) + C_B \cdot \Phi_B(\mathbf{k}, \mathbf{R}) . \quad (1.13)$$

The Bloch functions can be represented as a Fourier-series in k-space, where the amplitude factors and one obtains a linear combination of

$$\Phi_{A,B}(\mathbf{k}, \mathbf{R}) = \frac{1}{\sqrt{N_h}} \sum_{\mathbf{R}} e^{i\mathbf{k}\cdot\mathbf{R}} \varphi(\mathbf{r} - \mathbf{R}) . \quad (1.14)$$

N_h refers to the number of unit cells and \mathbf{R}_A are the lattice vectors. φ in Eqn. 1.14 are the atomic wavefunctions, here the normalized p_z orbitals. Operating with \hat{H} on the expression for $\Psi(\mathbf{k})$ given in Eqn. 1.13, multiplying with the conjugate complex wavefunctions from the left $\Phi_A(\mathbf{k})^*$ and $\Phi_B(\mathbf{k})^*$ and integrating over all coordinates \mathbf{r} one obtains the linear equation system:

$$\begin{aligned} C_A[H_{AA}(\mathbf{k}) - E(\mathbf{k})S_{AA}(\mathbf{k})] + C_B[H_{AB}(\mathbf{k}) - E(\mathbf{k})S_{AB}(\mathbf{k})] &= 0 , \\ C_A[H_{BA}(\mathbf{k}) - E(\mathbf{k})S_{BA}(\mathbf{k})] + C_B[H_{BB}(\mathbf{k}) - E(\mathbf{k})S_{BB}(\mathbf{k})] &= 0 . \end{aligned} \quad (1.15)$$

$E(\mathbf{k})$ are the electronic eigenvalues and H_{ij} are matrix elements of the Hamiltonian and S_{ij} the overlap integrals between the Bloch functions:

$$H_{ij} = \langle \Phi_A | \hat{H} | \Phi_B \rangle \quad S_{ij} = \langle \Phi_A | \Phi_B \rangle . \quad (1.16)$$

A non-trivial solution for the eigenvalues $E(\mathbf{k})$ exists, if the 2x2 determinant of Eqn. 1.15 vanishes, $\det[H - ES] = 0$. The determinant can be simplified by exploiting the fact that atoms A and B are identical, which allows to formulate the identities: $H_{AA} = H_{BB}$, $H_{BA} = H_{AB}^*$ and $S_{BA} = S_{AB}^*$.

Assuming that in the first place only the three nearest neighbors of each atom, A and B, contribute to the interaction and using the normalized atomic wavefunctions as basis set (e.g. $\varphi = 2p_z$), which leads to: $S_{AA} = S_{BB} = 1$, one can evaluate explicit expressions for the integrals H_{AB} and S_{ABW} ¹.

$$\begin{aligned} H_{AA}(\mathbf{k}) &= \varepsilon_{2p} = \langle 2p_z(\mathbf{r} - \mathbf{R}_A) | \hat{H} | 2p_z(\mathbf{r} - \mathbf{R}_A) \rangle , \\ H_{AB}(\mathbf{k}) &= \gamma_0 (e^{-\frac{1}{3}i\mathbf{k}\cdot(\mathbf{a}_1+\mathbf{a}_2)} (e^{i\mathbf{k}\cdot\mathbf{a}_1} + e^{i\mathbf{k}\cdot\mathbf{a}_2}) + 1) , \\ S_{AB}(\mathbf{k}) &= s_0 (e^{-\frac{1}{3}i\mathbf{k}\cdot(\mathbf{a}_1+\mathbf{a}_2)} (e^{i\mathbf{k}\cdot\mathbf{a}_1} + e^{i\mathbf{k}\cdot\mathbf{a}_2}) + 1) . \end{aligned} \quad (1.17)$$

The parameter ε_{2p} in Eqn. 1.17 corresponds to the Fermi energy. Due to the incorporation of the periodic potential of the crystal lattice in the Hamiltonian (compare Eqn. 1.12), H_{AA} is not equal to the energy of an atomic $2p_z$ electron. γ_0 and s_0 are the transfer integral (hopping

¹For a detailed derivation of the integral expressions: H_{AA} , H_{AB} and S_{AB} please refer to e.g. [46, 55]

integral), corresponding to the energy required to move an integral from site A to B, while s_0 is the overlap integral between atoms A and B, respectively. In explicit form those are written:

$$\begin{aligned}\gamma_0 &= \langle 2p_z(\mathbf{r} - \mathbf{R}_A) | \hat{H} | 2p_z(\mathbf{r} - \mathbf{R}_B) \rangle, \\ s_0 &= \langle 2p_z(\mathbf{r} - \mathbf{R}_A) | 2p_z(\mathbf{r} - \mathbf{R}_B) \rangle.\end{aligned}\quad (1.18)$$

Finally, one obtains for the electronic energy dispersion relation E_g of graphene:

$$E_g(\mathbf{k}) = \frac{\varepsilon_{2p} \pm \gamma_0 \cdot w(\mathbf{k})}{1 \pm s_0 \cdot w(\mathbf{k})}, \quad (1.19)$$

with the phase function $w(\mathbf{k})$:

$$w(\mathbf{k}) = \sqrt{1 + 4 \cos\left(\frac{\sqrt{3}k_x a}{2}\right) \cos\left(\frac{k_y a}{2}\right) + 4 \cos^2\left(\frac{k_y a}{2}\right)}. \quad (1.20)$$

The solution with the + sign in the numerator and denominator corresponds to the bonding π energy band, while the - sign gives the anti-bonding π^* bands. Conveniently, the parameters ε_{2p} , γ_0 and s_0 are used as free adjustable parameters and are fitted to the experimental data. Often the overlap s_0 is neglected which reduces Eqn. 1.15 to:

$$E_g(\mathbf{k}) = \varepsilon_{2p} \pm \gamma_0 \cdot w(\mathbf{k}). \quad (1.21)$$

Fig. 1.4 (a) shows the electronic dispersion relation of graphene for the first BZ calculated with Eqn. 1.19. The tight-binding parameters were: $\gamma_0 = 3.033$, $s_0 = 0.120$ and $\varepsilon_{2p} = 0$, the same as were also used for the calculations in reference [52]. Due to the non-zero overlap-integral the energy dispersion of the π and π^* -bands are not symmetric with respect of the Fermi energy. The band splitting is largest at the Brillouin zone center at the Γ point, with ΔE of about 20 eV. The evolution of the energy dispersion relation along a cross-sectional path connecting the high symmetry points K- Γ -M-K is shown in Fig. 1.4 (b). The π valence and π^* conduction bands touch at the positions of the K points and also the K' points at the Fermi energy level and form the entire Fermi energy surface of graphene. The density of states at these points is zero, which makes graphene a zero-bandgap semiconductor or a semimetal. The K points are located by the vectors $\mathbf{K}_f = \pm \mathbf{k}_1 - \mathbf{k}_2/3, \pm 2\mathbf{k}_1 + \mathbf{k}_2/3$ and $\pm \mathbf{k}_1 + 2\mathbf{k}_2/3$.

In close vicinity to these points the electron dispersion relation has a linear slope and the energy surface formed in this area has a conical shape (compare Fig. 1.4 (c)). For larger distances from the K (K') points the dispersion relation starts to deviate from its linear behavior. Importantly, this change occurs Depending on the different directions from the K point the deviations from linearity are differently, as can be observed for the directions $\Gamma \rightarrow K$ and $M \rightarrow K$ in Fig. 1.4 (b). This phenomenon is called trigonal warping.

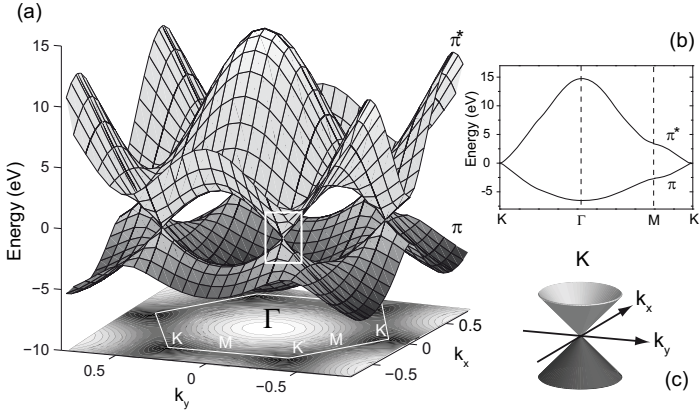


Fig. 1.4. (a) Electronic energy dispersion relation of graphene of the first Brillouin zone. The tight-binding parameters have been set to $y_0 = 3.033$, $s_0 = 0.120$ and $\varepsilon_{2p} = 0$ [52]. In the center of the hexagonal Brillouin zone (Γ point) the π valence and π^* conduction band separation is largest. Due to the finite overlap s_0 the bands are not symmetric with respect to the Fermi energy level. At the K points both bands are degenerate and in close vicinity to the K-point(s) the energy dispersion relation shows a linear behavior. (b) Cross section along a line connecting the high symmetry points: K → Γ → M → K' (c) Magnified area of the energy dispersion relation close to the K-point (white box in (a))

An expression for the linear energy regime of the dispersion relation can be derived from Eqn. 1.19 by setting $\varepsilon_{2p} = 0$ and $s_0 = 0$ and develop Eqn. 1.19 in a series for k , where only the lowest order terms are retained:

$$E_g(k) = \pm \frac{\sqrt{3}}{2} \gamma_0 k a . \quad (1.22)$$

In this regime the electrons mimic the behavior of massless particles, which move with a relativistic velocity: $v_f = \sqrt{3} \gamma_0 a \approx 10^6$ m/s. The same linear dispersion relation can be obtained using a theoretical description of the electrons based on the relativistic dirac equation.

$$E_g(\mathbf{k}) = \pm \hbar v_f |\kappa| . \quad (1.23)$$

Here κ is given as $|\mathbf{k} - \mathbf{K}|$ and v_f is the Fermi velocity with $v_f = 10^6$ m s⁻¹ [57].

2D Electron Confinement: Band Gap Opening in Graphene

The results of the previously discussed tight-binding model showed that ideal graphene does not exhibit an intrinsic bandgap in the energy regime relevant for optical transitions. Doping

due to the exchange of charge carriers with the substrate or by applying electric fields, leads only to shifts in the Fermi level. One of the challenges in the ongoing graphene research is the development of strategies for modifying the electronic structure of graphene in order to open up a bandgap without sacrificing the high mobility of the charge carriers. One approach is guided by the idea to reduce the size of the 2D graphene sheet in one dimension until electron confinement leads to quantization of the allowed k vectors, similarly to the situation in carbon nanotubes. Indeed these flat rectangular stripes with their finite width in one dimension and quasi-infinite length represent unrolled SWCNTs and are usually referred to as graphene nanoribbons. Similarly to the situation for SWCNTs, the nanoribbons are characterized by a chiral index (n,m) or accordingly by the corresponding chiral angle. Based on this one can further distinguish between chiral and achiral nanoribbons. Ab-initio calculations of the bandstructure of chiral and achiral nanoribbons showed that all are semiconducting with a bandgap which scales inversely with the width of the graphene stripe [58]. For a bandgap in the visible region the stripes would require a width well below one nanometer.

1.2.2. Brillouin Zone and Energy Dispersion Relation of SWCNTs

In the following the Brillouin zones and the energy dispersion relations of semiconducting and metallic SWCNTs are introduced. In the previous section it was shown that the structural properties of SWCNTs can be readily derived from the honeycomb lattice of graphene. In an analogous manner it is possible to derive the energy dispersion relation of SWCNTs by using the 2D graphene dispersion relation as a starting point. However, the one-dimensional nature of SWCNTs leads to quantization of the electron wave vector in circumferential direction of the tube, which constrains the values of the k vector in this direction. A new set of reciprocal lattice vectors considering the quantization conditions is derived from the ones of graphene. A zone folding approach is then applied to derive the one dimensional electronic dispersion relation of SWCNTs.

Reciprocal Lattice Vectors of SWCNTs

The reciprocal lattice vectors, which span the SWCNT BZ, can be constructed using the SWCNT real space lattice vectors, the chiral vector \mathbf{C}_h and the translation vector \mathbf{T} by exploiting the orthonormality condition:

$$\begin{aligned} \mathbf{k}_\perp \cdot \mathbf{C}_h &= 2\pi & \mathbf{k}_\perp \cdot \mathbf{T} &= 0 , \\ \mathbf{k}_\parallel \cdot \mathbf{C}_h &= 0 & \mathbf{k}_\parallel \cdot \mathbf{T} &= 2\pi . \end{aligned} \quad (1.24)$$

One obtains the following expressions for the SWCNT lattice vectors:

$$\begin{aligned}\mathbf{k}_\perp &= \frac{1}{N_h} \left(\frac{2n+m}{d_R} \mathbf{k}_1 + \frac{2m+n}{d_R} \mathbf{k}_2 \right), \\ \mathbf{k}_\parallel &= \frac{1}{N_h} (-m \cdot \mathbf{k}_1 + n \cdot \mathbf{k}_2).\end{aligned}\quad (1.25)$$

For the sake of convenience \mathbf{k}_\perp and \mathbf{k}_\parallel are represented in terms of the reciprocal lattice vectors of graphene, \mathbf{k}_1 and \mathbf{k}_2 . The SWCNT lattice vector pointing in direction of the nanotube axis, denoted as k_\parallel , is allowed to take continuous values within the interval $[-\pi/T, \pi/T]$, where T is the translation period. On the contrary, the lattice vector in circumferential direction, \mathbf{k}_\perp has to fulfill periodic boundary conditions, which constrains the number of allowed \mathbf{k} values. The reason for this is that any electron or phonon wave function must have a phase shift equal to an integer multiple $\mu 2\pi$ around the circumference of the SWCNT otherwise the wave function vanishes as consequence of destructive interference [46].

The periodic boundary conditions in real space are:

$$\mu \cdot \lambda = |\mathbf{c}_h| = \pi \cdot d_t, \quad (1.26)$$

which translates to the boundary condition for \mathbf{k}_\perp in reciprocal space:

$$k_{\perp,\mu} = \frac{2\pi}{\lambda} = \frac{2\pi}{|\mathbf{c}|} \cdot \mu = \frac{2}{d_t} \cdot \mu. \quad (1.27)$$

Here, the integer μ takes values from $-N_h/2 + 1, \dots, 0, \dots, N_h/2$, where N_h is the number of hexagons per unit cells, as defined in Eqn. 1.9.

Brillouin Zone of SWCNTs

The first BZ of armchair and zigzag SWCNTs are shown in Fig. 1.5 (a) and (b), respectively. For comparison the contour plot of the 2D band structure of graphene is depicted in the background. In general, the BZ of SWCNTs consist of multiple equidistant lines (black) equal to the number of graphene hexagons per unit cell N_h . They are oriented parallel to the axial lattice vector \mathbf{k}_\parallel . The lines are indexed by the cutting line numbers μ , starting with $\mu = 0$ for the line passing through the graphene Γ point.

The relative orientation of the BZ with respect to the graphene BZ is defined by \mathbf{k}_\perp . The BZ of armchair and zigzag tubes are symmetric in the sense that cutting lines with the same positive and negative μ value sample identical parts of the graphene BZ.

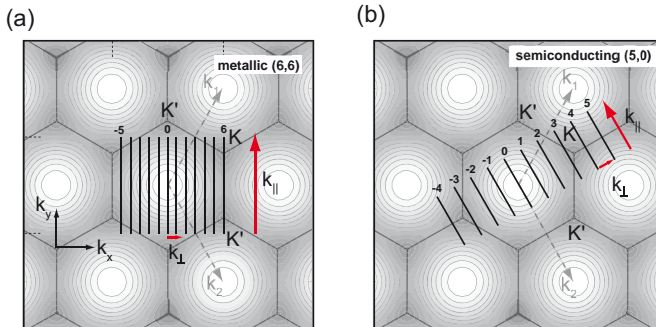


Fig. 1.5. Brillouin zone (BZ) of a metallic and semiconducting SWCNT with a contour plot of the graphene energy dispersion relation in the background. (a) The BZ of an armchair (6,6) metallic SWCNTs consists of $N_h = 12$ equidistant lines (black) parallel to the axial lattice vector \mathbf{k}_{\parallel} . The reciprocal lattice vectors \mathbf{k}_{\perp} and \mathbf{k}_{\parallel} are marked in red. (b) BZ of a zigzag semiconducting (5,0) SWCNT with $N_h = 12$ cutting lines. The indexing of the lines starts with $\mu=0$ at the line which passes through the graphene Γ point. The orientation of the lines defining the BZ of armchair and zigzag SWCNTs is the same for any chiral index (n,n) or $(n,0)$ and corresponds to the orientations of vectors along $\Gamma \rightarrow M$ or $\Gamma \rightarrow K$ respectively.

The distance between two adjacent lines and their length is given by the magnitude of the lattice vectors $|\mathbf{k}_{\perp}|$ and $|\mathbf{k}_{\parallel}|$:

$$|\mathbf{k}_{\perp}| = \frac{2}{d_t} \quad |\mathbf{k}_{\parallel}| = \frac{2\pi}{T} = \frac{2d_r}{\sqrt{3}d_t} . \quad (1.28)$$

Energy Dispersion Relation of SWCNTs: Zone Folding Approach

The 1D energy dispersion relations of SWCNTs, or equivalently their energy band, can now be derived from the graphene energy dispersion relation by applying a zone folding approach (also: confinement approach). The approach is based on the idea to constrain the allowed k values of the \mathbf{k} vector for the calculation of the graphene energy dispersion relation Eqn. 1.19 to take only k values which are also allowed for the SWCNT lattice vectors:

$$E_{\mu}^{\pm}(k) = E_g \left(k \frac{\mathbf{k}_{\parallel}}{|\mathbf{k}_{\parallel}|} + \mu \mathbf{k}_{\perp} \right) \quad \left(-\frac{\pi}{T} < k < \frac{\pi}{T} \quad \text{and} \quad \mu = 1, \dots, N \right) \quad (1.29)$$

Using the definitions of the vectors \mathbf{k}_{\parallel} and \mathbf{k}_{\perp} given in Eqn. 1.25 and substituting the graphene k vectors in the simplified expression for the graphene energy dispersion relation Eqn. 1.20 by those, one obtains:

$$\begin{aligned}
 E_\mu^\pm(k) = & \varepsilon_{2p} \pm \gamma_0 \left[1 + 4 \cos \left(\frac{\pi(2n+m)\mu}{2(n^2+nm+m^2)} + \frac{mkT}{N_c} \right) \times \right. \\
 & \cos \left(\frac{3\pi m \mu}{2(n^2+nm+m^2)} - \frac{(2n+m)kT}{N_c} \right) + \\
 & \left. 4 \cos^2 \left(\frac{\pi(2n+m)\mu}{2(n^2+nm+m^2)} + \frac{mkT}{N_c} \right) \right]^{1/2}.
 \end{aligned} \quad (1.30)$$

In Fig. 1.6 the zone folding process is illustrated for a metallic (6,6) armchair SWCNT. Here a plot of the graphene energy dispersion relation of the π valence and π^* conduction band is shown. Each line of the 1D SWCNT BZ (red), whose number N_h , length and orientation in respect to the graphene BZ is defined by the SWCNT reciprocal lattice vectors, acts as a cutting line giving rise to a pair of SWCNT conduction and valence subbands with the same index μ .

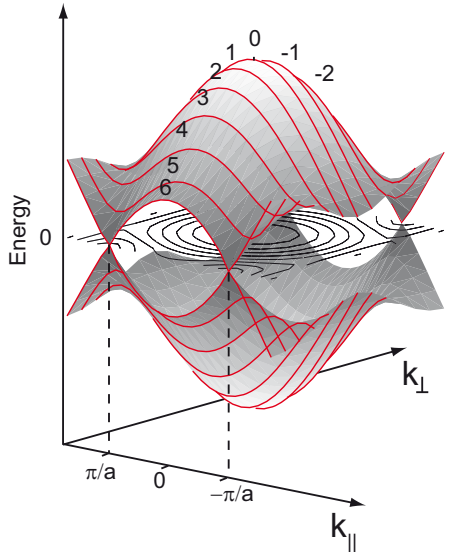


Fig. 1.6 Illustration of the zone folding approach for a (6,6) metallic armchair SWCNT. An contour plot of the energy dispersion relation of graphene is shown. The red lines correspond to the SWCNT BZ. Each of these lines intersects the graphene BZ (grey) and gives rise to a pair of conduction and valence bands with equal band indices beginning with $\mu=5$ to 6 (for clarity, not all are shown). The subbands with $\mu=6$ touch at the K point, which is characteristic for metallic SWCNTs.

The band structure, calculated according to the tight-binding model, of an armchair (6,6) and a zigzag (5,0) SWCNT are shown in Fig. 1.7 (a) and (b), respectively. Here the Fermi energy ε was set to zero and the overlap s_0 was set to zero. Due to the mirror symmetry of the BZ of armchair and zigzag SWCNTs, the energy bands are doubly degenerate. For the metallic (6,6) SWCNT in Fig. 1.7 (a), the valence and conduction subbands with the cutting line index

$\mu = \pm 6$ touch at the Fermi level. On the other hand, a finite band gap of 1 eV arises for the semiconducting (5,0) SWCNT in Fig. 1.7 (b).

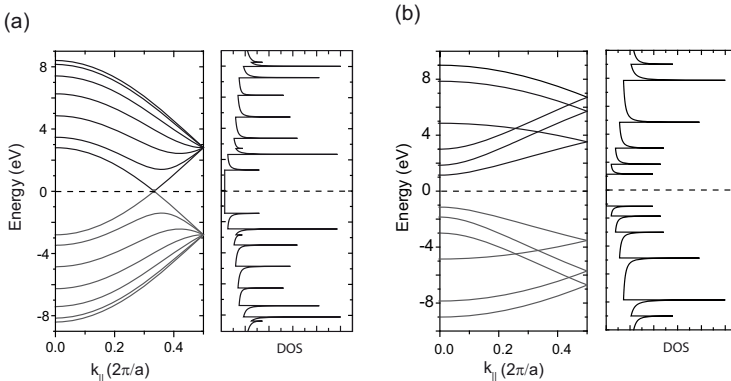


Fig. 1.7. Energy bands and corresponding density of states (DOS) of (a) a metallic armchair (6,6) SWCNT and (b) a semiconducting zigzag (5,0) SWCNT calculate according to the nearest neighbor tight-binding model (parameters: $\varepsilon_{2p} = 0$; $s_0 = 0$ and $y_0 = 3.0$). In case of the metallic SWCNT one pair of conduction and valence bands touches at the Fermi level, while for the semiconducting (5,0) SWCNT a large bandgap exist. The corresponding DOS exhibits narrow peaks, so called van-Hove singularities (vHs), located at energies, which correspond to extrema in the band structure. Importantly, in metallic SWCNTs the valence and conduction bands touch at the Fermi energy. In consequence, the DOS between the first pair of vHs has a finite value.

Another important electronic property with relevance for the optical transitions in SWCNTs is the electronic density of states (DOS). The DOS is linked to the curvature of the dispersion relation and is defined as the number of electronic states of either the conduction or valence band within an energy interval E and $E + \Delta E$. Accordingly, the joint density of states (JDOS) is defined, which is just the combined number of valence and conduction states in the energy interval. The DOS of structures with different dimensionality exhibit characteristic energy dependencies. In 3D bulk materials the DOS scales with \sqrt{E} , the one of 2D systems exhibits a step like scaling, while for one dimensional systems a $1/\sqrt{E}$ dependency is expected. In case of OD structures, such as fullerenes or quantum dots, even a δ -function like dependence is found, which is similar to the electronic states in molecules.

The DOS $n(E)$ for an one dimensional system is given by [59]:

$$n(E) = \frac{2}{q|k_z|} \sum_{\mu=1}^N \int_{-\infty}^{\infty} dk_z \delta(k_z - k_i) \left| \frac{dE_{\mu}}{dk_z} \right|^{-1}. \quad (1.31)$$

$q|k|_z$ is the total area of the Brillouin zone, where q is the number of carbon hexagons and $|k_z|$ is the reciprocal lattice vector in axial direction. k_i are the roots of the equation: $E - E(k_{\perp}, k_z) = 0$. From Eqn. 1.31 it becomes apparent that at any position of a local minimum or maximum in the electronic dispersion relation dE_{μ}/dk_z , the DOS becomes singular and gives rise to sharp features in the DOS, which are known as van Hove singularities (vHs).

For the energy range where the energy dispersion relation is linear, Mintmire et al. derived an expression for the DOS, which is valid for any type of SWCNT:

$$n(E) = \frac{4a_0}{\pi^2 d \gamma_0} \sum_{\mu=-N_h/2}^{+N_h/2} \begin{cases} |E|/\sqrt{E^2 - E_m^2} & |E| > |E_m| \\ 0 & |E| < |E_m| \end{cases}. \quad (1.32)$$

In the limit of this approximation, the DOS scales with the inverse of the diameter of the tube and the functional relation between the DOS and energy of $n(E) \propto (E^2 - E_{\mu}^2)^{-1/2}$ was found. Here, E_m are the energies, where the slope of the corresponding G-band vanishes and thus corresponds to the position of the vHs. For metallic SWCNTs E_m is given as: $E_m = i a_0 \gamma_0 / \sqrt{3} d$ with $i = 1, 3, 6, \dots$, while for semiconducting SWCNTs the index i takes the values $i = 1, 2, 4, 5, 7, \dots$ [46, 59]. The calculated DOS of a metallic (6,6) and a semiconducting (5,0) are shown in Fig. 1.7. For the present examples, the energetic positions of the vHs in the valence and conduction band are symmetric with respect to the Fermi level. Only for metallic SWCNTs the DOS retains a finite value within the energy range between the first pair of vHs of the valence and conduction band, which is the consequence of the bands touching at the K point.

The occurrence of the vHs in the DOS of SWCNTs was experimentally evidenced by scanning tunneling microscopy (STM) [60] and Resonance Raman measurements [61]. The high DOS of valence and conduction states associated with such vHs has important implications for e.g. optical transitions or charge carrier transport. If the excitation energy matches the energy of a transition between valence and conduction states which contribute to the vHs, the corresponding optical signals of such transitions are significantly enhanced and usually dominate e.g. the absorption spectra. In consequence, this is one of the reasons why excitation-resonance profiles of individual SWCNTs resemble a molecule-like behavior with quite narrow linewidth instead of that of an extended crystal.

The lines of the SWCNT BZ "cutting" through the BZ of graphene is an important concept ("cutting line concept"), which provides an explanation for the observation that SWCNTs are either semiconducting or metallic and furthermore can be used to explain systematic trends in the optical transition energies of them [62, 63]. Whether a SWCNT is semiconducting or metallic depends, whether a cutting line intersects an K or K' point of the graphene BZ. Enlarged sections of the energy dispersion relation of graphene around the K point are schematically depicted in Fig. 1.8. In the case of metallic nanotubes in Fig. 1.5 (a) the cutting line

intersects a K point of the graphene BZ. The situation is different for semiconducting SWCNTs. Here the K (K') point is always located between two adjacent cutting lines (Fig. 1.5 (b) and (c)) with the shortest distance of $2/3d_t$ to the closest cutting line.

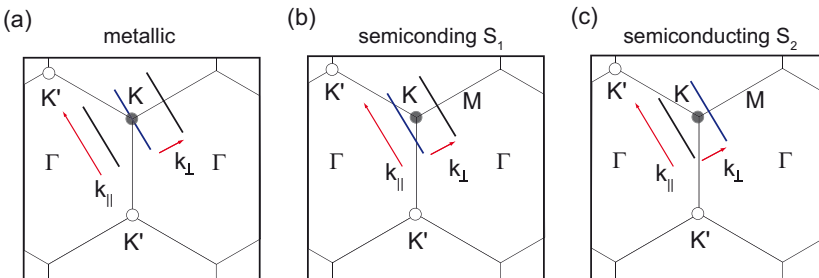


Fig. 1.8. Cutting line concept: The electronic properties of SWCNTs depend on the relative position of the SWCNT BZ (cutting lines) with band index μ in respect to the graphene K (K') points. (a) For metallic SWCNTs a cutting line is intersecting at least one K or K' point. (b) S1 type and (c) S2 type semiconducting SWCNTs. The smallest distance of a cutting line closest to a K (K') point (blue) is in both cases $1/3|k_{\perp}|=2/3d_t$. However, depending on the relative location of this cutting line in respect to the K point, either left (S1) or right (S2), the lines sample different sections of the dispersion relation of graphene. For increasing distance from the K points the equi-energy contours resemble a more triangular shape. For S1 and S2 SWCNTs with similar diameters, this results in sub bands with systematically different energy separations or correspondingly optical transition energies.

It was mentioned in the previous section that semiconducting SWCNTs can be divided into two "families", called S1 and S2 type SWCNTs. Both families show systematic differences in their optical transition energies giving rise to characteristic patterns in so called Kataura plots, where the optical transition energies are plotted against the diameter of the SWCNTs. The different behavior of the families originates from the deviation from circular symmetry of equi-energy contours for increasing distance from the K (K') points in the BZ of graphene. The equi-energy contours resemble a triangular shape with the corner of the triangle pointing in the three $\Gamma \rightarrow M$ directions [62, 64]. While for the S₁ SWCNT the closest cutting line to the K point is on the left side of the K point, the closest cutting line of the S₂ SWCNT is on the right side of the K point in direction of a line $M \rightarrow \Gamma$. In consequence, the cutting lines closest to the K points, which give rise to the valence and conduction bands with the smallest energy separation, sample different energy contours of the graphene energy dispersion relation. This in turn which affects the energy separation of the sub band or equivalently the optical transition energies. For example and thus the optical transition energies. This effect becomes especially obvious for SWCNTs with similar diameters, which are affected by the trigonal warping effect also affects the optical transition energies of metallic SWCNTs, which could be shown experimentally on the single nanotube level with elastic white-light scattering spectroscopy [65].

1.2.3. Optical Transition Energies: Kataura Plot

The energy separation between mirror imaged pairs of subbands depends on the cutting line index μ and the value of k_z . The first pair of vHs with the smallest energy separation with respect to the Fermi energy originates from cutting lines closest to the K or K' points (see Fig. 1.8). The spacing between these cutting lines and the K points are $|\mathbf{k}_l|$ for metallic SWCNTs and $|\mathbf{k}_l/3|$ and $|2\mathbf{k}_l/3|$ for semiconducting SWCNTs. The energy separation between the first pair of vHs can be derived in the small k approximation [59], by substituting k in Eqn. 1.22 for the values of $|\mathbf{k}_l|$:

$$E_{11}^M \approx 6ac_{C-C}\gamma_0/d_t \quad E_{11}^S \approx 2ac_{C-C}\gamma_0/d_t. \quad (1.33)$$

One of the important findings here, is that the energy separations for the different E_{11}^M/S transitions depends in the first place inversely on the diameter of the SWCNTs. In general, the term $E_{ii}^{M/S}$ is used to denote the energy separation and correspondingly the optical transitions (see Sec. 1.3) between the valence and the conduction subbands with indices i . The numbering starts with one for the bands closest to the Fermi level. The superscripts M and S indicate metallic and semiconducting SWCNTs, respectively.

Kataura et al. presented the first time a detailed theoretical analysis of the diameter dependence of E_{ii} for a wide range of SWCNT chiralities [66]. They used the tight-binding approximation for calculating the transition energies and summarized the results in the so called Kataura plot, where the E_{ii} transition energies are plotted as a function of the diameter, similar to the one shown in Fig. 1.9.

The E_{ii} in Fig. 1.9, are calculated based on an analytical expression derived by fitting the transition energies measured in resonant Raman scattering experiments [67]. The expression grasps the chiral angle dependence of the transition energies and furthermore considers curvature effects as well as corrections for excitonic effects.

Here the energies of the first three semiconducting and first metallic optical transitions are plotted. The general $1/d_t$ dependency of the transition energies can be observed. Moreover, branch like patterns in the transition energies can be observed. These are the so called family patterns. All tubes with $2n+m=\text{const.}$ belong to a specific family. All SWCNTs of a family have similar diameters and thus also similar transition energies ($E \sim 1/d_t$). The small differences in energy are caused by the trigonal warping effect. As was illustrated in Fig. 1.8, the trigonal warping effect is chirality dependent and leads to the systematic behavior of the transition energies of the S1 (filled circles) and S2 type (open circles) semiconducting SWCNTs.

Finally, it is to note that the energies of the conduction and valence bands of SWCNTs obtained by the zone-folding approach using the energy dispersion relation of graphene calculated according to the nearest neighbor tight-binding model yields only a qualitative picture. Especially for small diameter tubes, so called curvature effects, become relevant. The curvature of the SWCNT sidewall, leads to a reduced bond length between neighbored carbon-atoms

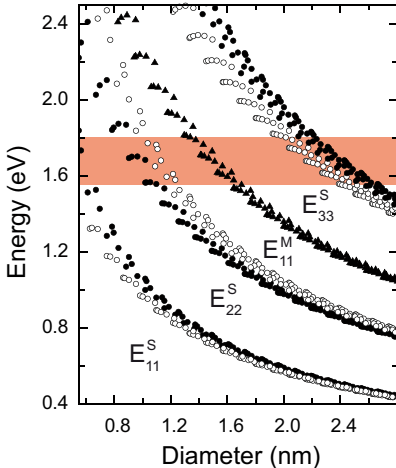


Fig. 1.9 Kataura plot: Energy separation E_{ii} as a function of tube diameter d_t for semiconducting (S) and metallic (M) SWCNTs. The E_{ii} values are calculated by an expression given in [67]. The filled and open circles correspond to S1 and S2 type semiconducting SWCNTs, respectively. The red shaded area indicates the energy range which is accessible for excitation with light in the visible spectral range.

in azimuthal direction. Furthermore, the bond angles deviate from the ideal 180° of sp^2 hybridized carbon atoms in the planar graphene, which changes the overlap of π -orbitals and further allows for the mixing of π and σ states corresponding to a rehybridization of the orbitals [46]. Including these effects in the theoretical calculations leads to corrections to the band energies. In consequence, the changes in the bond length for example lead to an opening of a small secondary bandgap on the order of 10 meV for $(n-m)/3$ -integer zigzag and chiral SWCNTs. Only armchair SWCNTs are intrinsic metallic SWCNTs. The tight-binding model can be further extended to include the interactions with second- and third-nearest neighbored carbon atoms.

1.3. Optical Transitions in SWCNTs

In the beginning of SWCNT research, optical transitions in SWCNTs, such as e.g. absorption or PL in carbon nanotubes, were understood in terms of intersubband transitions of free charge carriers. Although, it could be evidenced in recent experiments that the excited states in semiconducting and metallic SWCNTs are stable excitons, which dominate the optical processes, the general framework developed for the transitions in the one particle picture is still valid and can be easily transferred to the excitonic transitions.

In the previous section, basic expression for the energies and the DOS for the subbands close to the Fermi energy were derived. The optical transitions in carbon nanotubes can be described by interband transitions between valence and conduction subbands, which are governed by symmetry imposed selection rules. The experimentally measured intensity of an optical transition depends on the transition probability W or equivalently on the rate of the

transition. In the electric dipole approximation the probability of a transition W between an initial state $|\Psi_i\rangle$ and a final state $\langle\Psi_f|$ is given by Fermi's golden rule [68]:

$$W_{i \rightarrow f} = \frac{2\pi}{\hbar} |\langle\Psi_f|\hat{H}|\Psi_i\rangle|^2 g(E) , \quad (1.34)$$

where $\hat{H} = -\mathbf{p} \cdot \mathbf{E}_0$ is the electromagnetic interaction Hamiltonian defined as the product of the electric dipole moment $\mathbf{p} = e\mathbf{r}$ and the electric Field \mathbf{E}_0 . $g(E)$ denotes the joint density of states (JDOS) of the two states. With the assumption that the incident electric field is nearly constant along the particle, the integral term in Eqn. 1.34 can be approximated by:

$$e|\langle\Psi_f| - \mathbf{r} \cdot |\Psi_i\rangle| \mathbf{E}_0(r, t) \approx \mu_{if} \mathbf{E}_0(t) , \quad (1.35)$$

where μ_{if} is the transition dipole moment. In general, a transition is "allowed" if $W \neq 0$, thus if both the transition dipole moment μ_{if} and $g(E)$ are finite. In the case of SWCNTs, W becomes large for resonant excitation of transitions, where electronic states participate which contribute to the vHs in the DOS. Whether the transition dipole moment vanishes can be evaluated based on the symmetry of the participating initial and final electronic states and the symmetry of the interaction operator.

1.3.1. Symmetries of SWCNTs

The electronic states transform in the same way under a symmetry operation as the basis functions of the corresponding irreducible representation of the corresponding carbon nanotube [46]. Thus, if the symmetry group of a SWCNT is known, the irreducible representations of the electronic states can be evaluated. In the following, the most relevant symmetry elements found in SWCNTs are briefly summarized and the group of the wavevector notation of the irreducible representations is introduced, focusing mainly on the properties of chiral SWCNTs. The interested reader might find detailed review articles on the symmetry properties of carbon nanotubes in the references [46, 48, 69].

A carbon nanotube can be regarded as a 1D periodic crystal. Their full symmetry group is conveniently described in terms of one-dimensional crystallographic line groups [48]. These line groups \mathbf{L} can be represented as a weak direct product of a generalized translational group \mathbf{T} and an axial point group. For chiral and achiral SWCNTs the point groups of relevance are the dieder groups \mathbf{D}_{N_h} and \mathbf{D}_{2N_h} , respectively.

$$\begin{aligned} \mathbf{L}_{ac} &= \mathbf{T}_{N_h}^w \mathbf{D}_{q_h} && \text{armchair and zigzag SWCNTs} \\ \mathbf{L}_c &= \mathbf{T}_{N_h}^w \mathbf{D}_q && \text{chiral SWCNTs} . \end{aligned} \quad (1.36)$$

The translational group \mathbf{T} comprises pure translations $\mathbf{T} = \mathbf{T}_T^0$, e.g. screw axis $\mathbf{T} = \mathbf{T}_q^w$ and glide planes $\mathbf{T} = \mathbf{T}_C$ depending on whether the tube is chiral or achiral. The superscript w gives the number of screw axis and the subscript its order, where N_h is the number of graphene

hexagons per unit cell.

In order to determine the symmetry of the electronic states participating in the optical transitions not the complete line group symmetries need to be considered. Instead, it is sufficient to work with the dieder point groups, which are isogonal to the corresponding line groups in Eqn. 1.36 [46]. The relevant symmetry elements common to all dieder point groups are depicted in Fig. 1.10.

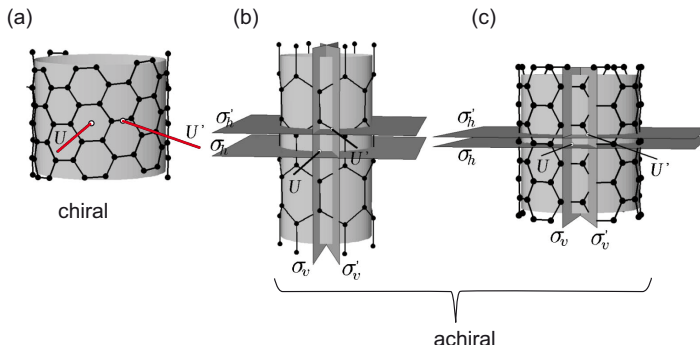


Fig. 1.10. Symmetry elements of carbon nanotubes: (a) The horizontal rotational axes U and U' are common to both chiral and achiral SWCNTs. (b-c) In addition to these rotational axes, achiral SWCNTs exhibit horizontal (σ_h ; σ_h') and vertical (σ_v ; σ_v') (glide) mirror planes, adapted from [48]

Common to all nanotube chiralities are two two-fold rotation axis, the U and U' axis, which are both normal to the cylinder surface. While the U axis passes through the center of a carbon hexagon, the position of the U' axis is located at the midpoint of a carbon-carbon bond (Fig. 1.10 (a)). Achiral tubes have additional vertical (σ_v ; σ_v') and horizontal (σ_h ; σ_h') mirror planes, which contain the midpoints of a hexagon. Each chiral carbon nanotube has its own line group symmetry, while armchair (n,n) and zigzag ($n,0$) tubes sharing the same chiral index parameter n belong to the same line group.

Throughout this work the line group notation for the irreducible representations of the electronic (and excitonic) states is used, which has the following general form²:

$$\text{wave vector} \rightarrow \quad k \mathbf{X}_\mu^\pi \quad \begin{matrix} \leftarrow \sigma_h/U \text{ parity} \\ \leftarrow \text{quantum number} \end{matrix}$$

↑ dimension(X= A,B,E,G)

²The character tables for the isogonal D groups are found in tables 2.4 and 2.5 in [46]. chiral SWCNTs: ${}_0A_0^+ \rightarrow A_1$; ${}_0A_{q/2}^+$ and ${}_0A_{q/2}^- \rightarrow B_1$; achiral SWCNTs: ${}_0A_0^- = A_{2u}$. An equivalent approach for obtaining the symmetries of carbon nanotubes is the group of wave vector approach (GWA). Conversion tables for the different notations are found in table 1 of reference [70]

X is the dimension of the representation, where A, B denote one-dimensional, while E and G are two- and four-dimensional representation, respectively. k and μ designate the quasi-translational, $k \in [0, \pi/a]$, and quasi-angular momentum quantum numbers, $[\mu \in [-q/2, q/2]$, respectively. For the Γ point states with $k=0$ of chiral SWCNTs the parity π is + (-) for even (odd) behavior upon U-axis rotation. Accordingly, the parity of the states in achiral tubes is defined based on their behavior upon σ_v reflection.

For the case of a chiral SWCNT the irreducible representations for the various electronic valence and conduction states are summarized in Tab. 1.1:

Table 1.1. Line group notation of electronic states of chiral SWCNTs [69]

	Valence Band		Conduction Band	
	$k=0, \pi/T$	$0 < k < \pi/T$	$k=0, \pi/T$	$0 < k < \pi/T$
$\mu=0$	${}_0A_0^+$	${}_0A_0$	${}_0A_0^-$	${}_0A_0$
$0 < \mu < q/2$	${}_kE_\mu$	${}_kE_{\pm\mu}$	${}_kE_\mu$	${}_kE_{\pm\mu}$
$\mu = q/2$	${}_0A_{q/2}^+$	${}_0B_0$	${}_0A_{q/2}^-$	${}_0B_0$

Optical transitions occur between valence and conduction band states located close to the K point for which the density of states is highest. In chiral SWCNTs these states are typically not directly located at high symmetry points of the BZ and their irreducible representation is ${}_kE_{\pm\mu}$. Due to the time-reversal symmetry of the K and K' these states are doubly degenerate and do not have a defined parity under rotation about the U-axis. In general, the parity upon rotation about the U-axis is only well defined for states with $k = 0$ or $k = 2\pi/T$.

1.3.2. Selection Rules for Interband Transitions

With the symmetries of the valence and conduction band it is now possible to assess the integral term of Eqn. 1.34. The integral does not vanish, if the direct product between the irreducible representations of the dipole operator \mathbf{p} and the electronic states has a common component [71]:

$$\mathbf{R}^{[f]} \otimes \mathbf{R}^{[p]} \otimes \mathbf{R}^{[f]} \supseteq {}_0A_0^+ . \quad (1.37)$$

For light polarized parallel to the nanotubes axis (z-axis) the dipole operator transforms like a vector along the z-axis. It has odd parity upon rotation about the U-axis and transforms as the ${}_0A_0^-$ representation. Thus, in order to fulfill angular momentum conservation, transitions induced by light polarized parallel to the SWCNT axis can not change the quantum number m : $\Delta m = 0$, but they change the U-parity.

Light polarized in x or y direction, perpendicular to the tube axis, transforms as the ${}_0E_{\pm 1}^+$ representation. In this case, the angular-momentum quantum number: $\Delta m = \pm 1$ can be

changed by the optical transition, while the parity is preserved

Furthermore, only "vertical" transitions are allowed. This statement embodies the linear momentum conservation, which requires that the electron momentum matches the photon momentum: $\hbar(\mathbf{k}_f - \mathbf{k}_i) = \hbar\mathbf{k}_{ph}$. However, light in the visible spectral range has a negligible small photon wave vector on the order of $k_{ph} \sim 10^7 \text{ m}^{-1}$ compared to the wave vector of an electron. The latter is on the order of the lattice constant and about four orders of magnitude larger: $\pi/a \approx 10^{11} \text{ m}^{-1}$. Thus, momentum conservation is fulfilled for transitions for which the electron wavevector does not change, corresponding to: $\hbar\mathbf{k}_f = \hbar\mathbf{k}_i$.

Summarizing the optical selection rules for interband transitions in SWCNTs:

- $\Delta k \approx 0$: only vertical transitions allowed
- $\Delta\mu = 0$: for light polarization parallel to tube axis: \mathbf{E}^{\parallel}
- $\Delta\mu = \pm 1$: for light polarization perpendicular to tube axis: \mathbf{E}^{\perp}

1.3.3. Absorption and Photoluminescence

A simplified energy diagram for the absorption processes in a semiconducting SWCNT is shown in Fig. 1.11(a). The first two pairs of mirror-symmetric valence and conduction subbands closest to the Fermi level (grey dotted line) are denoted as $v_{1,2}$ and $c_{1,2}$, respectively. Each of the three vertical arrows represents an allowed optical transition in agreement with the optical selection rules introduced in the previous section. In general, absorption of a photon leads to the excitation of an electron into the conduction band and simultaneously to the formation of a hole with opposite momentum in the valence band. The two transitions E_{11} and E_{22} are optically allowed transitions for light polarized parallel to the nanotube axis, while E_{12}^{\perp} is a transition only allowed for perpendicular polarization.

The PL process is schematically illustrated in Fig. 1.11(b). Upon absorption of a photon, corresponding to a E_{22} transition, $v_2 \rightarrow c_2$, an electron (hole) is generated in the second E_{22} conduction (valence) band. The electron (hole) undergoes a fast nonradiative intrasubband transition, $c_2 \rightarrow c_1$, to the bottom (top) of the first E_{11} conduction (valence) subband. Similarly to Kasha's rule in organic dye molecules [72], the radiative recombination of the electron and hole, E_{11} : $c_1 \rightarrow v_1$, starts from the bottom of the E_{11} band. PL due to radiative recombination of charge carriers associated with higher subbands, e.g. $c_2 \rightarrow v_2$, has not been observed.

In general, the optical transitions show a strong polarization anisotropy. Although the aforementioned transverse transitions are in general optically allowed, it is found that they are strongly suppressed and thus are experimentally difficult to assess. The reason for this is a strong depolarization effect also called antenna effect, which can be attributed to the large

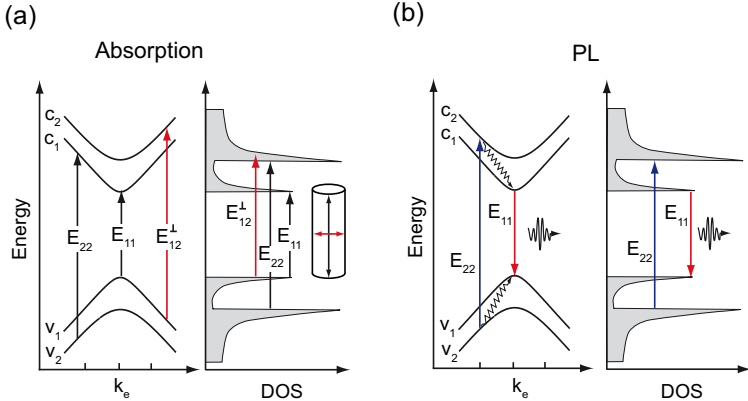


Fig. 1.11. Optical transitions in SWCNTs in the free-particle picture: (a) Absorption and (b) PL of a semiconducting carbon nanotube. In (a) the three arrows represent optically allowed vertical transitions between valence and conduction band as governed by the optical selection rules (see text). The PL process in (b) is initiated by E_{22} absorption, where an electron and hole are generated in the second conduction and valence subbands, respectively. Subsequent fast nonradiative transition of the electron (hole) to the bottom (top) of the first conduction (valence) subband (wiggly arrow) is followed by a radiative E_{11} transition, where the charge carriers recombine under emission of a photon.

geometrical anisotropy of SWCNTs [73–75]. Here the incident electrical field with its polarized normal to the tube axis induces a polarization inside the tube. The orientation of the corresponding polarization vector is antiparallel to the external field and thus the effective field strength of the excitation field is reduced. The effect is also responsible for the pronounced polarization dependence of the optical transition and this depolarization effect can be observed for example in polarized absorption or PL excitation spectroscopy [76,77].

1.4. Excitons in Carbon Nanotubes

In the previous sections the electronic and optical properties of SWCNTs within the picture of free, non-interacting electrons and holes were presented. Already in the early stages of the experimental studies of SWCNTs it became evident that electronic many body effects might be relevant for the photophysics of SWCNTs. Upon studying the E_{22}^S/E_{11}^S ratio by absorption measurements of SWCNT solutions [78] it was found that the E_{22}^S/E_{11}^S ratio when extrapolated to large SWCNT diameters ($d \rightarrow \infty$) does not approach the value of two which is predicted by the tight-binding model. This problem has been studied more systematically after it was discovered that surfactant individualized SWCNTs dispersed in aqueous solutions exhibit PL. Here a refined E_{22}^S/E_{11}^S ratio of 1.75 [50] was found. The controversy was puzzling theoreticians and experimentalists for quite a long time and became known as the "ratio

problem” [50, 79]. Extending the tight-binding model by incorporating of curvature effects and band rehybridization only result in minor improvements. In fact, early theoretical works considering many particle interactions/effects predicted the stability of excitons in carbon nanotubes and indicated their contributions to optical processes. [80–83], but a clear experimental distinction between excitonic recombination and bandgap PL at this stage of the research was missing. Only recently, two groups independently were able to provide evidence for the excitonic nature of the excited states in SWCNTs by performing two-photon PL excitation experiments [84–86], where states can be populated which are usually not observable in single-photon processes.

In general, absorption of a photon with appropriate energy by a semiconducting material might lead to the creation of an electron and hole, which are both localized in the same spatial area. If the attractive Coulomb force between electron and hole is sufficiently large they can form a bound electron-hole pair, known as exciton. Excitons are classified into two limiting cases, depending on the separation of the electron and hole, the so called Bohr radius. Wannier-Mott excitons, also called free excitons, are characterized by electron-hole separations exceeding the lattice constants of the unit cell. These excitons can be treated as hydrogen-atom like entities and correspondingly they exhibit different series of energy levels E_n and exciton-binding energies E_{bind} . Here n is an integer, where the state with $n = 1$ represents the excitonic ground state and $n = \infty$ the limit of the free unbound electron and hole. The exciton binding energy E_{bind} is defined as the energy difference between the free charge carrier band edge E_∞ and the specific energy of an excitonic level E_n :

$$E_{bind} = E_\infty - E_n . \quad (1.38)$$

The energy levels E_n are given by a modified Rhydberg-formula according to:

$$E_n = \frac{13.6 \text{ eV}}{n^2} \frac{\mu^*}{m_e} \frac{1}{\epsilon^2} . \quad (1.39)$$

Here μ^* is the reduced effective mass of the electron and hole, corresponding to $\mu^* = 1/m_e^* + 1/m_h^*$ and ϵ is the dielectric constant of the medium. The dielectric constant is a measure for the polarizability of the medium, i.e. how easily charges respond to an electric field. The polarized medium of the environment can compensate an external electric field, so that the effective internal field is smaller. This effect is called dielectric screening. In bulk semiconducting materials and especially in metals with $\epsilon > 10$ the attractive Coulomb interaction between photoexcited electron and holes is shielded by the field of the surrounding valence electrons. Therefore, the typical exciton binding energies of bulk semiconductor materials are on the order of 10–60 meV [87]. In consequence excitonic effects for these materials can only be observed at cryogenic temperatures.

A second type of excitons, the so called Frenkel excitons, can be found in ionic crystals or in materials with small dielectric constants ϵ . Characteristic for this type of excitons are electron-hole separations smaller than the lattice constant. They are strongly localized and have large exciton binding energies of 0.1–1 eV.

Regarding excitonic effects in SWCNTs, their one-dimensional structure leads to enhanced Coulomb interaction for both the electron-electron repulsion and the electron-hole attraction. This results in the formation of strongly bound Wannier-type excitons with exceptionally large binding energies on the order of 0.4–1 eV [84]. Excitons exist also in metallic SWCNTs, however with significantly smaller binding energies of only \sim 50 meV compared to the large energies of excitons in semiconducting SWCNTs [88]. The properties of excitons in semiconducting SWCNTs and their impact on the optical properties are the topics of the following sections.

From the Single Particle Picture to Excitons

The exciton energies and the symmetry of their wavefunctions determine the optical properties of carbon nanotubes. The theoretical description needs now to consider also Coulomb interactions, such as electron-electron repulsion and electron-hole attraction. The solutions for such a problem of two interacting particles can be found by using a solid state physics approach involving the solution of a Bethe-Salpeter equation [83, 89, 90].

In order to form an exciton the electron and hole wave functions must be localized at the same spatial region along the tube. The relative distance of both and the shielding of the surrounding electrons determine the exciton binding energies. While, in the single particle picture, both electrons and hole wavefunctions can be represented by single Bloch states, with the wave vectors k_c are k_v , this is not possible anymore for the exciton wavefunction. Because of the repulsive and attractive Coulomb interaction between electrons and holes, k_c are k_v are no valid quantum numbers anymore. However, in reciprocal space k_c are k_v can still be used to define the central positions of the corresponding wavefunctions and define the exciton center of mass wavevector \mathbf{K} and the vector for the relative motion of the electron and hole \mathbf{k} [91].

$$\mathbf{K} = (\mathbf{k}_e - \mathbf{k}_h)/2 \quad \mathbf{k} = \mathbf{k}_e + \mathbf{k}_h . \quad (1.40)$$

Instead of using a single Bloch functions, the Ansatz for the exciton wave function Ψ is a linear combination of products of electron and hole Bloch functions over all valence v and conduction c bands:

$$\Psi(\mathbf{k}_e, \mathbf{k}_h) = \sum_{v,c} A_{v,c} \phi_c(\mathbf{k}_e) \phi_v^*(\mathbf{k}_h) . \quad (1.41)$$

The resulting wavefunction Ψ is also localized in reciprocal space at the positions of

The coefficients $A_{v,c}$ for the exciton wavefunctions Ψ^n and energies Ω_n for the n -th excitation can be found by solving the Bethe-Salpeter equation:

$$\sum_{\mathbf{k}_c, \mathbf{k}_v} ([E(\mathbf{k}_c) - E(\mathbf{k}_v)]) \delta_{\mathbf{k}'_c \mathbf{k}_c} \delta_{\mathbf{k}'_v \mathbf{k}_v} + K(\mathbf{k}'_c \mathbf{k}'_v, \mathbf{k}_c \mathbf{k}_v) \Psi^n(\mathbf{k}_c \mathbf{k}_v) = \Omega_n \Psi^n(\mathbf{k}'_c \mathbf{k}'_v) . \quad (1.42)$$

The Hamiltonian for the many-particle problem needs now to consider electron-electron and electron-hole pair interactions for all electron and hole pair combinations. The first term of the expression correspond to the energies of the electron $E(\mathbf{k}_c)$ and hole states $E(\mathbf{k}_v)$. These energies are given as sum of the single particle energy and a self energy correction, which originates e.g. from electron-electron repulsion [69]. The second term is the electron-hole interaction Kernel K , comprising the interactions between all possible electron and hole pairs. The kernel itself is composed of two terms: 1. K^d the direct and 2. K^x the exchange (singlet-triplet) interaction.

The electron-hole kernel mixes states with all wavevectors and of all subbands. However, for small diameter tubes the energy separation between the vHs of different 1D subbands is fairly large. Thus it is a valid assumption that only electronic states, which contribute to a given vHs do mix to form an excitonic state [70]. In this case, the effective mass approximation (EMA) can be applied and furthermore the excitonic wave function can be approximated by an envelope function approach [92].

Using a variational Ansatz for the exciton wavefunction, it can be represented as a linear combination of products of single particle valence $\phi_c(\mathbf{r}_e)$ and conduction band states $\phi_h^*(\mathbf{r}_h)$:

$$\Psi^{EMA}(\mathbf{r}_e, \mathbf{r}_h) = \sum'_{v,c} B_{vc} \phi_c(\mathbf{r}_e) \phi_h^*(\mathbf{r}_h) F_v(z_e - z_h) . \quad (1.43)$$

The indices $v, c = \pm m$ denote the quasi-angular momentum quantum numbers, which are coefficient B_{vc} is dictated by symmetry. F_v are "hydrogen-like" envelope wavefunctions of the relative coordinates of the electron z_e and hole z_h . The index v resembles the principle quantum number in the 1D hydrogen like series and determines the number of nodes. The envelope functions is even or odd upon inversion: $z \rightarrow (-z)$ depending on the index v : even for $v = 0, 2, 4, \dots$ or odd for $v = 1, 3, 5, \dots$. For $v=0$ F_v is a simple Gaussian of the form: $F_0 = \exp(-(z_e - z_h)^2/2\sigma^2)$. The width of the Gaussian σ is the variational parameter in the calculations and its physical meaning is the separation of electron and hole corresponding to the exciton Bohr radius. The envelope function localizes the exciton along the SWCNT axis and has the same symmetry as the real excitonic wavefunction. For the excitonic ground state, it was found that the exciton Bohr radius in the range of 2–5 nm, significantly exceeding the graphene lattice constant a .

1.4.1. Excitonic Dispersion Relation

Since the majority of luminescent semiconducting SWCNTs are chiral SWCNTs, the following presentation of the topic focuses on the excitonic properties of those. The excitonic states of zigzag and armchair tubes can be treated in a similar way, which is described in detail in [70]. First considering only the excitonic states which exist within the first E_{11} bandgap. In this case optical transitions occur between subbands with index $\pm m$ in the vicinity of the K or K' points. The electronic states of the valence and conduction band close participating in the optical transitions are schematically depicted in the band diagram of Fig. 1.12 (a). Because K and K' are related by time-reversal symmetry, chiral tubes comprise a set of two doubly degenerate valence and conduction bands. The states at the band extrema have $\pm k_0 E_{\pm \mu}$ and $\mp k_0 E_{\mp \mu}$ symmetries for the valence and conduction band, respectively.

In the absence of Coulomb interaction the mixing of the electron and hole states, as indicated by the vertical and diagonal arrows, would result in four fourfold degenerate states. However, in fact the strong Coulomb interactions partially lift the degeneracy between the states, leading to the formation of a set of four excitonic states.

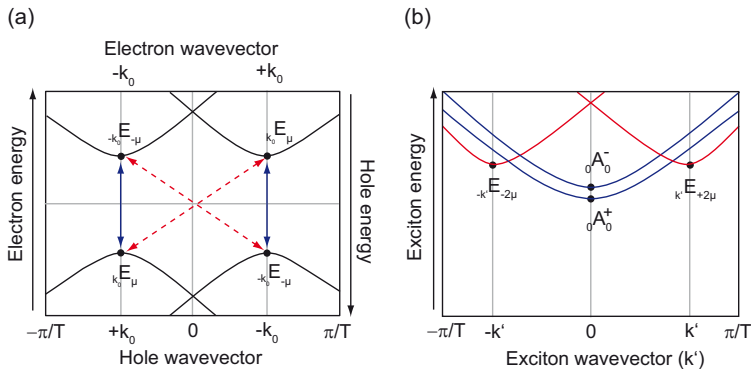


Fig. 1.12. Diagrams of the electronic and excitonic bands and their symmetries of a chiral (n,m) nanotube. (a) The two inequivalent valence and conduction bands. States involved in the mixing (solid circles) are labeled according to their irreducible representation. The arrows indicate mixing of the states, which gives rise to four excitonic bands with different symmetries. Vertical arrows indicate mixing of states within which gives rise to Γ point excitons with A symmetry, while the diagonal arrows result in two degenerate excitonic bands with E symmetry (b) Excitonic band structure. According to the optical selection rules only the $0A_0^+$, can be populated, adapted from [70].

In general, the irreducible representation of an excitonic state $D(\Psi^{EMA})$, can be determined by the direct product of the respective irreducible representations of the conduction state $D(\Psi_c)$, the valence state $D(\Psi_v)$ and the envelope function $D(F_v)$ [70]:

$$D(\Psi^{EMA}) = D(\Psi_c) \otimes D(\Psi_v) \otimes D(F_v). \quad (1.44)$$

In the case of chiral SWCNTs, $D(\Psi_c)$ and $D(\Psi_v)$ of the doubly degenerate electron and hole states are $\pm_{k_0} E_{\pm\mu}$ (see Fig. 1.12 (a)). The lowest-energy excitonic states with index $v=0$ envelope function transforms as ${}_0A_0^+$. With the direct product Eqn. 1.44 the symmetries of the excitonic states can be derived:

$$(k_0 E_\mu + -k_0 E_{-\mu}) \otimes (-k_0 E_{-\mu} + k_0 E_\mu) \otimes {}_0A_0^+ = \\ {}_0A_0^+ + {}_0A_0^- + {}_{k'}E_{2\mu'} + {}_{-k'}E_{-2\mu'}. \quad (1.45)$$

The mixing of states with opposite quantum numbers (vertical blue arrows in Fig. 1.12 (a)), such as $k_e=\pm k_0$ and $k_h=\mp k_0$, results in the formation of two excitonic states, which transform as the ${}_0A_0^-$ (A_2) and ${}_0A_0^+$ (A_1) representation. On the other hand mixing of states with same quantum numbers $k_e=k_h\pm k_0$ (diagonal red arrows) leads to two degenerate excitonic states with finite exciton momentum. These states have ${}_{k'}E_{\mu'}$ and ${}_{-k'}E_{-\mu'}$ symmetries, respectively. Here $k' \approx 2k_0$ and $\mu' = 2\mu$ correspond to the linear and angular momenta of the exciton, respectively.

The excitons can also be classified according to their center-of-mass momentum \mathbf{K} cor-

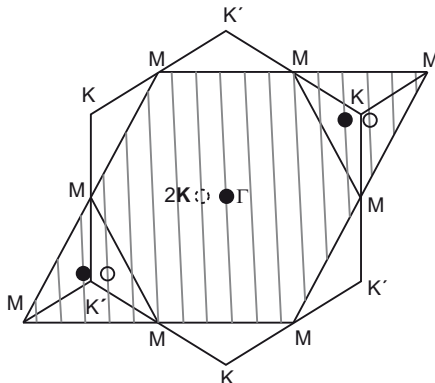


Fig. 1.13 The three inequivalent regions in the two-dimensional Brillouin zone of graphene. The cutting lines corresponding to a small excerpt of the BZ of a (6,5) SWCNT are shown. The electron-hole pairs (at a solid circle near K (or K')) and the corresponding center-of-mass momentum $2K$ (solid circle at Γ) of an $A_{1,2}$ exciton of the (6,5) SWCNT are indicated. The electron-hole pair with the electron (solid black) and hole lying on the second and first cutting lines to the K point and the electron-hole pair with the electron and hole lying on the first and second cutting lines to the K' point correspond to an E_{12} exciton with the center-of-mass momentum $2K$ (dotted circle near the Γ point) on the first cutting line next to the Γ point [91].

ponding to different characteristic positions in the graphene BZ. In Fig. 1.12 the situation is depicted for the case of a (6,5) SWCNT. Here, the graphene BZ is shown together with the cutting lines corresponding to the (6,5) SWCNT. Three different inequivalent regions can be distinguished, which are located at the zone-center around the Γ point and close to the K and K' zone borders. Upon optical excitation the electrons and holes are generated in subbands close to the K or equivalently K' points of the graphene BZ, which are both related by time-reversal symmetry. Therefore, four combinations of electron and holes need to be

considered. Excitons formed by the mixing of electronic (\mathbf{k}_e) and holes (\mathbf{k}_h) originating from different K (or K') regions have a center-of-mass-momentum $2\mathbf{K}$ close to the K or K' points, corresponding to the K-momentum exciton. For electron and holes created both in the same K (or K') region corresponding to ($k_e = \pm K$ and $k_h = \pm K'$) the exciton-momentum $2\mathbf{K}$ is close to the zone center Γ point of graphene (solid circle) giving rise to two excitons with ${}_0A_0^+$ and ${}_0A_0^-$ symmetry (Γ -point excitons).

On the other hand, if the electron originates from the K and the hole is from the K' region (or vice versa), $2\mathbf{K}$, the excitons lies in the K region (K' region) and are of E_μ symmetry. Due to their finite \mathbf{K} vector, these excitons are called K-momentum excitons. As in these excitons, the electrons and holes exist in different valleys they cannot recombine radiatively.

For the case of light polarized perpendicular to the tube axis optical transitions between bands with different subband indices m . For excitons formed by e.g. a E_{12} transitions, the electron and hole originate from the first and second cutting line to the K (K') point resulting in an exciton with its $2\mathbf{K}$ close to the Γ point (dotted circle in Fig. 1.13).

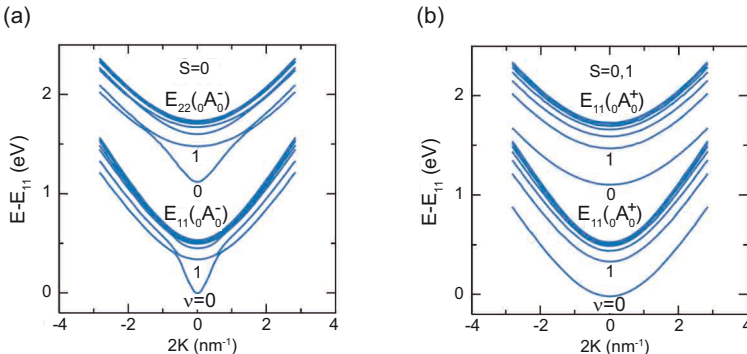


Fig. 1.14. Calculated excitonic energy dispersion relations of the ground and excited excitonic states of the first E_{11} and second E_{22} intersubband transitions in a (6,5) SWCNT. (a) ${}_0A_0^-$ singlet exciton state ($S=0$). The energy lowest E_{11} $v=0$ exciton exhibits a non-parabolic steep dispersion (b) The bands of the ${}_0A_0^+$ singlet and triplet excitons are degenerate. The $v=0$ excitonic ground state has a parabolic shape corresponding to the dispersion of a free particle, adapted from [70].

Up to now only the formation and properties of spin singlet excitons were discussed, basically neglecting the fact that electrons and holes carry a spin and the mixing of states considering the spin multiplicities, gives rise to a set of 12 triplet excitons, which are partially degenerate [91, 93]. For example in the case of the ${}_0A_0^-$ exciton the spin singlet and triplet states are degenerate due to the symmetry imposed vanishing of the exchange interaction vanishes.

The calculated excitonic energy dispersion relations for the ${}_0A_0^+$ and ${}_0A_0^-$ exciton manifolds of an (6,5) SWCNT are plotted as a function of the center-of-mass momentum $2K$ in Fig. 1.14 (a) and (b), respectively [91]. The dispersion relation of the optically allowed $E_{11} {}_0A_0^+$ singlet exciton in (b) exhibits parabolic shaped dispersion relation corresponding to the dispersion of a free particle.

Dark Excitons

Although the number of available excited states is significantly increased compared to the single-particle picture, most of the excitonic states in SWCNTs are forbidden by optical selection rules and are referred to as dark excitons. Dark excitons are excitonic states which do not decay radiatively to the ground state [57, 93] based on the selection rules for dipole-allowed optical transitions, which were presented already within the context of single particle optical transitions (Sec. 1.3.2).

According to the optical selection rules in Eqn. 1.37, an optical transition between the electronic ground state and an excitonic state is allowed when the direct product of the irreducible representations of the final exciton state, the electromagnetic interaction operator and the ground state have the total symmetric ${}_0A_0^+$ representation as a common element.

In SWCNTs the electronic ground state transforms as the totally symmetric ${}_0A_0^+$ representation and for light polarized along the SWCNT axis (z direction) at $k=0$ the operator transforms as a vector oriented in z-direction: ${}_0A_0^-$. With this it can be shown that out of the four energy lowest excitons ($v = 0$) of the first vHs, only transitions between the ground state and excitons with the ${}_0A_0^-$ are allowed. For excited excitons of the same with envelope functions F_v , $v > 0$ the decomposition presented in Eqn. 1.45 remains unchanged. Thus, only a *single* optically allowed exciton with ${}_0A_0^-$ -symmetry exists for each v . In summary, optical transitions for the following excitons are *forbidden*:

- The ${}_0A_0^+$ exciton, due to quasi-angular momentum conservation (parity forbidden)
- The doubly degenerate K-momentum excitons with $\pm k' {}_0E_{\pm\mu'}$ symmetry ($\mathbf{K} \neq 0$)
- Triplet excitons, due to spin selection rules

The selection rules are based on symmetry consideration, but whether a nominal bright state is experimentally observable depends also on the total oscillator strength for the particular transition. On the other hand, the optical selection rules apply only for the ideal case of an defect free SWCNT and it was predicted that symmetry breaking processes, like defects, impurities or exciton-phonon interactions, can relax the optical selection rules and allow the mixing of states with different parity and multiplicity depending on the nature of the defect [94].

In fact, Mortimer et al. could demonstrate in a pioneering experiment the controlled "brightening" of the ${}_0A_0^+$ dark exciton. The state turned luminescent, if the SWCNT is exposed to a high magnetic field parallel to the tube axis at cryogenic temperatures. The energy separation between the bright and by 1–5 meV [95]. The magnetic brightening [96, 97] Optical signatures of dark excitonic states have been observed also in PLE and linear absorption measurements

where the SWCNT samples were not exposed to additional external perturbations. The brightening of the dark state was there attributed to inherent synthesis introduced defects and impurities [98].

The K-momentum excitons can also participates in optical processes and their signatures can be observed as broad sidebands to the main PL or absorption bands [99–101]. While it is not optically active per se, strong exciton-phonon coupling in SWCNTs gives rise to exciton-phonon complexes with energies $E_{K-ex} \pm \hbar\omega_{ph}$. In PLE measurements this phonon sidebands of the $E\hbar\omega_{ph}$ appear 130 meV below the and the for the $E_{K-ex} + \hbar\omega_{ph}$ 160 meV above the PL and absorption bands of the ${}_0A_0^+$ exciton respectively [99].

Dark excitons are predicted to influence the optically processes further, as they might be involved in nonradiative decay process, where they trap large fractions of the excited state population [81, 84, 90, 102, 103].

1.4.2. Exciton energies

The multiple-particle interactions result also to significant changes of the exciton energies compared to the single-particle energies band gap energies. In Fig. 1.15 the effect of the attractive and repulsive Coulomb interactions on the an absorption spectra of an (8,4) SWCNT is demonstrated. The self energy term arising from the electron-electron repulsion, causes a significant blue shift of the bandgap energy (bandgap renormalization) of about 1.1 eV, which is nearly compensated by a red shift caused by the attractive electron-hole interaction responsible for the formation of the excitons 0.7 eV. The net effect is a blue shift of the excitonic transition energies compared to the free electron ones [79, 91, 104]. Furthermore, the lineshape of the absorption band changes to a Lorentzian.

For semiconducting SWCNTs, the self energy term, the energy correction due to the tight-binding energies due to electron-electron repulsion, is experimentally difficult to assess, as it requires the unscreened band gap energy and the exciton energy at the same time. The excitonic nature of the excited states in SWCNTs was evidenced by two independent work groups utilizing two-photon excitation-emission spectroscopy [85, 86]. Two-photon absorption allowed for determining the exciton binding energies. Actually, these represent a large fraction of the optical bandgap and for small diameter SWCNTs exciton binding energies in the range of 0.3–0.4 eV were measured [84–86].

Theoretical predicted and experimentally determined exciton binding energies for the bright ${}_0A_0^-$ are on the order of 0.3–1.0 eV, which is a significant fraction of the band gap energy. The energies depend strongly on the diameter and in addition on the chiral angle [81, 106–108]. Further it is predicted that for semiconducting SWCNT there is at least one dark excitonic state below the single bright [92, 106].

The exciton energy of the optically bright ${}_0A_0^-$ exciton can be easily determined with PL or absorption spectroscopy. In order to determine its binding energies, two-photon excitation absorption measurements were performed, where both an excited exciton state (E_{2g}) and the continuum band gap can be observed. The binding energies determined with this

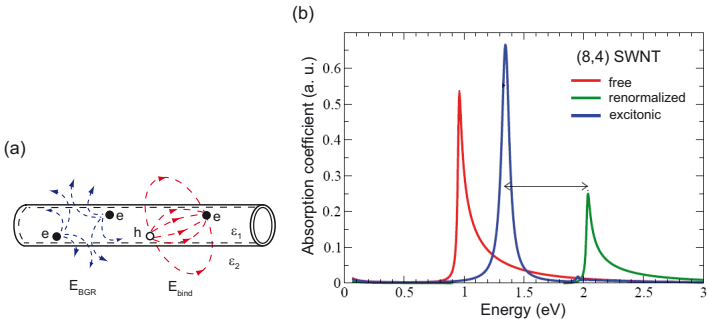


Fig. 1.15. (a) Schematic illustration of the two contributing Coulomb interactions governing the excitonic energies, adapted from [105]. (b) Calculated absorption spectra of the first optical transition E_{11} of a (8,4) semiconducting SWCNT. Coulomb interaction leads to (1) band gap renormalization due to the repulsive electron-electron (blue shift of the vHs) and (2) formation of excitons due to the electron-hole interaction (red-shift of the renormalized vHs and reshaping into a Lorentzian), modified from [104].

method are on the order of 0.2–0.4 eV, which is a significant fraction the single particle band gap [84–86, 109].

1.4.3. Exciton Mobility in SWCNTs

Fast pure dephasing times and small coherence length L_c of only 10 nm indicate that coherent excitations in SWCNTs do not play a significant role [110, 111] and justify the treatment of excitons as rigid particles with center of mass. Excitons are localized along the nanotube axis on a length scale of their exciton Bohr radius 1–2 nm [84, 90, 92, 112] and are delocalized along the nanotube circumference. Considering the large nanotube length up to several hundreds of nanometers, movement in axial direction can be well regarded as one-dimensional. The exciton transport in SWCNTs is diffusional with large diffusion coefficients D on the order of 0.1–10 cm²/s and corresponding diffusion lengths $L_D = \sqrt{2D\tau_{\text{eff}}}$ between 6–630 nm, strongly depending on the sample material and environmental conditions [112–115].

1.5. Photoluminescence of SWCNTs

It lasted more than ten years since the first reports of the discovery of SWCNTs until PL was observed experimentally. The crucial step which made the observation possible was the preparation to produce samples which contain isolated SWCNTs (see also Sec. 3.2.1). In pristine SWCNT materials strong intertube van-der-Waals forces of up to 500 eV/ μ m

tube-to-tube contact [41] lead to the formation of thin bundles with a hexagonal packing of SWCNTs and even larger aggregates in solutions. The exact mechanism which leads to the PL quenching in SWCNT bundles is still under debate. Presumably, charge carrier tunneling or Förster type energy transfer [116–118] from semiconducting tubes to metallic SWCNTs within these bundles and the subsequent nonradiative recombination of an electron hole pair is discussed as a possible radiationless deactivation pathway [49].

The following parts of this section review further aspects of the PL in SWCNTs. Starting with a summary of general PL properties. In PL studies of single SWCNTs it is observed that the PL energies exhibit tube-to-tube variations, which is attributed to the influence of a varying dielectric environment. Here, the model explaining the dependency of the PL energies on the dielectric environment is reviewed. As a last, the current results on the excited state dynamics of the PL process are presented and a model for the possible mechanism of the nonradiative decay is reviewed.

1.5.1. Excitonic description of the PL process in SWCNTs

The PL process in the single particle picture was introduced in Fig. 1.11. The general scheme presented there is also valid for the excitonic picture of the PL process. However now the origin of the PL is the radiative recombination of the bright $E_{11} \text{ } {}_0A_0^-$ exciton. Since there is virtually no Stokes shift between absorption and PL energies in SWCNTs [119], excitation energies exceeding the E_{11} energies are used. Off-resonant excitation, not matching an excitonic transition energy, leads to reasonable PL intensities, however in a typical PL experiment the bright $E_{22} \text{ } {}_0A_0^-$ exciton is excited. Alternatively, indirect PL excitation via an exciton-phonon complex such as the $E_{11} + \text{G-band}$ is also possible [82].

The contribution of free carrier transitions to the spectral properties of carbon nanotubes is very low. Nearly all of the oscillator strength after E_{22} excitation is transferred to excitonic states within the with a branching ratio of 10:1 between the decay into the ${}_0A_0^-$ and the free carrier bands [120]. The free carrier continuum can be only observed in PLE or absorption experiments [121].

1.5.2. Excited State Dynamics, PL Decay Times and Quantum Yield

The excited state dynamics of a system fundamentally depends on the interaction of the excited state with e.g. phonons, defects or other charge carriers. Thereby, knowledge about the excited state dynamics in combination with spectroscopic information is crucial.

The excited states in SWCNTs which are experimentally directly observable are the bright excitons of the different E_{ii} subbands, while only the E_{11} excitons recombines radiatively. In general the ground-state relaxation of an excited state can be either radiative k_r or nonradiative k_{nr} . The total decay rate of the system is then just the sum of both: $k = k_r + k_{nr}$. k_r is the spontaneous decay rate whose inverse $1/k_r$ corresponds to the intrinsic lifetime τ_0

of the excited state. There exist a broad range of (scattering) processes based on intrinsic and extrinsic interactions giving rise to various nonradiative decay pathways with the specific nonradiative decay rate k_{nr}^1 . The total nonradiative decay rate of the system is just the sum of all individual components: $k_{nr} = k_{nr}^1 + k_{nr}^2 + \dots$. Examples for such intrinsic processes are e.g. electron/exciton-phonon coupling or scattering by charge carriers or other excited states (Auger-recombination). Extrinsic processes might involve scattering with trap states caused by defects or impurities or nonradiative depopulation due to energy transfer processes.

The time dependent PL decay, described by the time constant τ_{PL} , reflects this complex interplay and is characterized by the PL decay time τ_{PL} , which is defined as:

$$\tau_{PL} = \frac{1}{k_r + k_{nr}}. \quad (1.46)$$

The QY is defined as the ratio of emitted photons to absorbed photons and can be expressed in terms of decay rates following:

$$QY = \frac{n_{emitted}}{n_{absorbed}} = \frac{k_r}{k_r + k_{nr}}. \quad (1.47)$$

A lot of effort has been put into the research of more suitable surfactants and preparation methods to increase the QY [122]. So far, the highest QYs for SWCNT samples of up to 20 % were reported for suspensions of SWCNTs encapsulated by various oxygen-excluding surfactants dispersed in organic solvents. Furthermore, high QYs of 7 % were also reported for individual SWCNTs, freely suspended between silicon pillars [123], while the QY for individual micelle encapsulated SWCNTs with ionic surfactants on substrates is rather low in the range of 0.1–1 % [124]. This broad range of behavior reflects the influence of the heterogeneous environment on the PL of SWCNTs.

Two different phonon assisted nonradiative decay mechanisms have been proposed by Perebeinos et al. for explaining the nonradiative PL decays in SWCNTs. In the case of hole-doped SWCNTs a phonon-assisted indirect exciton ionization process (PAIEI) [125] might occur. The process is schematically depicted in Fig. 1.16 (a).

Here, the photo-generated excitons relax starting from the first subband by simultaneous emission of a phonon and the generation of an intraband electron-hole pair within the valence band (for a p-doped SWCNT), satisfying both energy and momentum conservation [125]. The rate of the PAIEI process increases with increasing doping levels.

In fact, p-type self-doping of SWCNTs occurs for SWCNTs deposited on substrates and exposed to ambient conditions, which was attributed to the photoinduced chemisorption of preabsorbed oxygen [126]. Another prominent example which lead to p-type doping are chemical sidewall modifications, such as protonation [49, 127, 128] or oxidation reac-

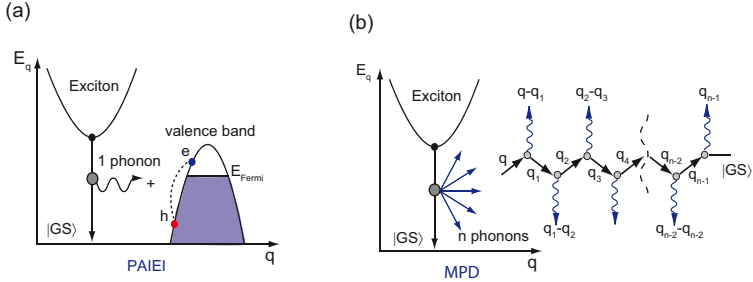


Fig. 1.16. Schematic illustration of the phonon-assisted nonradiative decay process in SWCNTs. (a) Phonon-assisted indirect exciton ionization process (PAIEI). (b) Multi-phonon decay (MPD), adapted from [125]

tions [129]. The doping is caused due to the formation of covalent bonds between the π system of the SWCNT and a electrophilic species, which results in the injection of a hole close to the reactions site. In the first case, charge transfer due to trapped charges located on the surface of the substrate or from the ionic surfactant are discussed.

The second nonradiative decay mechanism, which was proposed by Perebeions et al. is a multi-phonon decay (MPD) process. However, in the case of free mobile excitons this mechanism is less efficient than PAIEI. The predicted decay rates for small diameter SWCNTs $d < 0.8$ nm are around 0.01 ns^{-1} , thus by far too slow to explain the fast decays observed in our experiments. However, MPD decay rates are significantly larger for localized excitons, where the rate increase to $1-10\text{ ns}^{-1}$. Exciton localization or trapping can occur at sites along the SWCNT which exhibit local potential energy minima caused by changes in the local dielectric function or in the presence of charges. This was used to explain confined PL emission from short SWCNT segments of 20 nm observed in near-field PL experiments [130]. The interplay of both mechanisms, PAIEI and MPD of localized excitons might indeed lead to the observed PL quenching behavior and both are assumed to contribute to the rate: k_{nr}^{quench} .

Förster resonance energy transfer (FRET) between SWCNTs separated by only small distances of 2–4 nm or within SWCNTs in small bundles, where the SWCNTs are basically in direct contact and are oriented parallel to each other, is discussed as an efficient non-radiative decay channel [117, 118]. Exciton energy transfer starts in semiconducting SWCNTs from the higher energy E_{11} bright excitonic state of the donor SWCNT into a finite momentum state ($K \neq 0$) of the bright E_{11} exciton dispersion of the acceptor SWCNT. The higher momentum exciton eventually loses energy and reaches the minimum of the excitonic dispersion ($K=0$) from where it can recombine radiatively [117]. Even more efficient is a similar exciton energy transfer process from semiconducting to metallic SWCNTs. In fact PL quenching due to the

presence of metallic SWCNTs in small bundles of SWCNTs is discussed as one of the major reasons for the strongly reduced or even complete absence of PL from SWCNT bundles [131].

1.6. Raman Scattering of SWCNTs and Graphene

Raman scattering is the coherent, inelastic scattering process of photons by matter. In solids, the most frequently occurring scattering process involves the interaction of photo-excited electrons or excitons with one or more optical phonons. These electron-phonon scattering processes determine many transport properties, such as the mobility of the charge carriers, the thermal conductivity as well as the elastic properties. Furthermore, these electron phonon interactions critically determined the radiative and non-radiative excited state lifetime. Especially in 1D structures such as carbon nanotubes the exciton-phonon coupling is enhanced, which leads to observable phonon-sidebands in their absorption spectra. Furthermore, phonon-assisted charge carrier relaxation processes are very efficient in SWCNTs and represent nonradiative decay channels (vide infra).

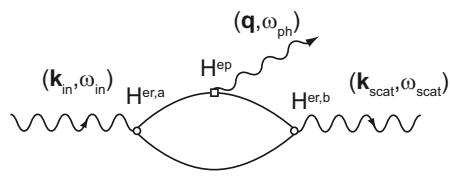


Fig. 1.17 Feynman diagram of a first-order Raman scattering process. The incident photon with energy $\hbar\omega_{in}$ and wavevector \mathbf{k}_{in} excites an electron-hole pair. In the following the electron is inelastically scattered by creating or destroying a phonon with energy $\hbar\omega_{ph}$ and wavevector \mathbf{q} . In the subsequent electron-hole pair recombination process, a photon with energy $\hbar\omega_{scat}$ and wavevector \mathbf{k}_{scat} is emitted.

For the simplest Raman process, a so called first-order scattering process, the inelastic interaction is governed by the scattering of the excited state with a single phonon. As illustrated in the Feynman-diagram in Fig. 1.17, the first-order Raman scattering process is comprised of three virtual interactions. The first step is the absorption of the ground state $|i\rangle$ of a photon, governed by the electromagnetic interaction Hamiltonian ($H^{er,a}$), with frequency ω_{in} leads to the formation of an electron hole pair. The electron is then inelastically scattered by either absorption or emission of a phonon with energy ω_{ph} and phonon wavevector \mathbf{q} (electron-phonon interaction Hamiltonian H^{ep}). Finally, the electron hole pair recombines forming the final state $|f\rangle$ by emission of a scattered photon with the energy ω_s and wavevector \mathbf{k} ($H^{er,b}$). The Raman scattering process is virtually instantaneous occurring on the femtosecond timescale [46] and fulfills the energy and momentum conservation laws:

$$\begin{aligned} \hbar\omega_{in} &= \hbar\omega_{scat} \pm \hbar\omega_{ph}, \\ \mathbf{k}_{in} &= \mathbf{k}_{scat} \pm \mathbf{q}_{ph}. \end{aligned} \quad (1.48)$$

Raman processes can be categorized depending on whether the excitation energy $E_{in} = \hbar\omega_{in}$ or the energy of the scattered photon $E_{scat} = \hbar\omega_{scat}$ matches the energy of an electronic transition. This is illustrated for four Raman processes in Fig. 1.18. If both, the excitation energy of the laser and the energy of the scattered photon, do not match the energy separation between two electronic levels (solid lines), $E_{in} \neq E_b - E_a$, the Raman process is a so called non-resonant process. In this case the optical transitions occur between virtual states (dotted lines) short-lived intermediate states, so called virtual states (dotted lines in Fig. 1.18).

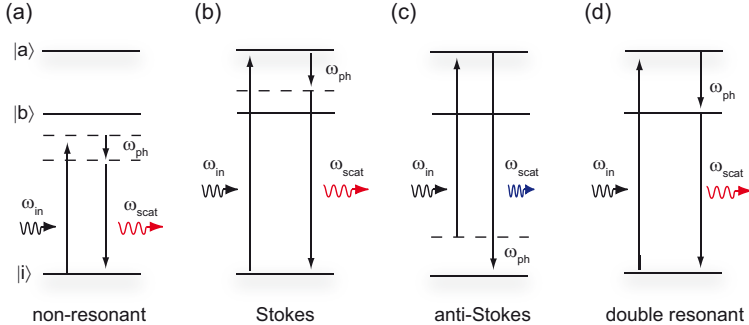


Fig. 1.18. Energy level diagrams of Raman scattering processes: (a) non-resonant Stokes Raman scattering (b) Stokes Raman Scattering: Creation of a phonon (c) Anti-Stokes Raman scattering: A phonon is destroyed during the process. The Raman scattering processes in (b) and (c) are resonant Raman processes with respect to the incoming and scattered light, respectively. (d) Double Resonant Raman scattering, where both incoming and scattered light are in resonance with electronic transitions. Dashed lines indicate virtual states, while solid lines correspond to electronic states.

The Raman processes illustrated in Fig. 1.18 (b), (c) and (d), on the other hand, are resonant Raman scattering processes (RRS), where the energy of the incident (incident resonance) or the scattered light (scattered resonance) matches an electronic transition, as it is shown in Fig. 1.18 (b) and (c), respectively. The process in Fig. 1.18 (d) is a double resonance Raman scattering process, where two resonant electronic transitions are involved.

The non-resonant Raman scattering cross sections of individual SWCNTs is extremely small, on the order of 10^{-17} cm^2 , which in consequence only leads to weak Raman signals at moderate excitation powers.

For a first-order Raman process as the one illustrated in the Feynman-diagram Fig. 1.17 the expression for the Raman scattering intensity can be derived from third-order perturbation theory and is given by [46]:

$$I(\omega_{ph}, \omega_{in}) = \propto \sum_{a,b} \left| \frac{M^{er}(\omega_{scat}, fb) M^{ep}(\omega_{ph}, ba) M^{er}(\omega_{in}, ai)}{(E_{in} - E_{ai} - i\gamma_r)(E_{in} - (E_{bi} \pm \hbar\omega_{ph}) - i\gamma_r)} \right|^2 . \quad (1.49)$$

Increased Raman intensities are expected if the denominator becomes small. The dominator is comprised out of two resonance terms. The first term is the incoming resonance, where the energy of the incident light E_{in} is equal to the energy difference $E_{ai} = E_a - E_i$ between the electronic states a and initial electronic state i . The second term corresponds to the outgoing resonance, where $\hbar\omega$ is the phonon energy and E_{bi} is the energy difference between electronic state b and the initial (final) electronic state i . Incoming and outgoing resonant Raman scattering conditions significantly enhance the Raman cross section by up to three orders of magnitude [132].

The processes related to the destruction or creation of a phonon are called Stokes (S)- and anti-Stokes (aS) Raman scattering, respectively. Correspondingly, the energy of the scattered photon E_{scat} is either reduced or increased by the amount of the phonon energy: $\hbar\omega_s = \hbar\omega_{in} \pm \hbar\omega_{ph}$. The probability for Stokes or Anti-Stokes scattering events depends on the initial phonon population of the state n , which follows for phonons with energy E_{ph} at a given temperature T the Bose-Einstein-distribution:

$$n = \frac{1}{\exp E_{ph}/k_B T - 1}, \quad (1.50)$$

where k_B is the Boltzmann constant. In the course of a first order Raman process the Stokes process leads to an increase of the phonon population, according to $n \rightarrow n+1$, correspondingly the phonon-population is reduced according to $n+1 \rightarrow n$ in the course of the anti-Stokes process. The intensity ratio between the Stokes and anti-Stokes scattered light $I(S)/I(aS)$ follows to a first approximation:

$$\frac{I_S}{I_{aS}} \propto \frac{n+1}{n} = e^{(E_{ph}/k_B T)}. \quad (1.51)$$

At room-temperature the intensity of the Stokes scattering process is considerably larger than the anti-Stokes intensity and therefore the Stokes scattered light is conveniently detected in standard Raman experiments.

1.6.1. Raman Scattering of Graphene and SWCNTs

The close relation of the graphene and SWCNT phonon dispersion relations on the one hand results in several Raman bands which both materials have in common. On the other hand the one-dimensional structure of SWCNTs leads to unique and characteristic phonon modes. Changes in the frequencies of the Raman modes are signature for doping (field and chemical) or can be used to monitor the effects of strain and stress (elastic and mechanical properties. Other modes require structural defects for their activation.

The unit cell of graphene contains two inequivalent carbon atoms, with three degrees of freedom each, giving rise to six phonon branches, three optical and three acoustical, which are (listed in order of decreasing energy): longitudinal optical (LO) ; in-plane transverse optical (iTO); out-of plane transverse optical (oTO); longitudinal acoustic (LA) ; in-plane-transverse acoustic (iTA) and the out-of-plane transverse acoustic (oTA) . The phonon modes associated with the iTO and LO branches give rise to four characteristic Raman bands of graphene. At the Γ -point the iTO- and LO-dispersions are degenerated, giving rise to a single Raman band: The G-band (green). The D- and G'-bands are associated with large momentum K-point phonon modes (blue), while the D^* -band is associated with phonons whose wavevector can interconnect both sides of the dispersion cone. The corresponding phonon dispersion relations along a path Γ -M-K- Γ interconnecting the high symmetry points of the graphene BZ are depicted in Fig.1.19. In ideal graphene, the iTO- and LO-dispersions are degenerate at the Γ -point giving rise to the G-band.

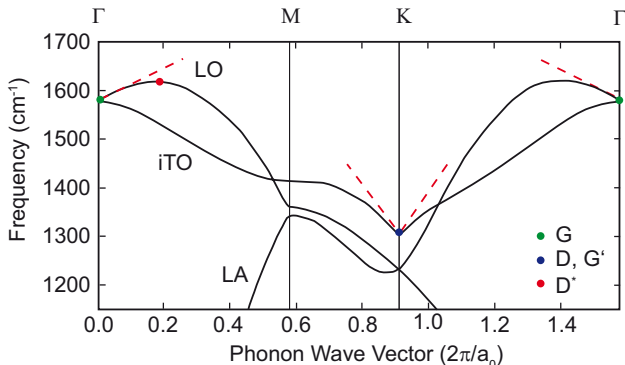


Fig. 1.19. High energy part of the phonon dispersion relation of graphene along the high symmetry lines of Γ -M-K- Γ of the graphene BZ showing the iTO (in-plane transverse optical), LO (out-of-plane transverse optical) and LA (longitudinal acoustic) branches. The phonon modes associated with the iTO and LO branches give rise to four characteristic Raman bands of graphene. At the Γ -point the iTO- and LO-dispersions are degenerated, giving rise to a single Raman band: The G-band (green). The D- and G'-bands are associated with K-point phonon modes (blue), while the D^* -band is associated with phonons whose wavevector can interconnect both sides of the dispersion cone. Modified from [133].

Raman processes in graphene and SWCNTs can be classified based on the number of phonons emitted during the course of the whole process. There are one-, two and multi phonon processes. Further, the order of a scattering process is defined as the position of the scattering event in the sequence of total scattering events [46, 132]. Fig.1.20 illustrates the various Raman scattering processes which give rise to the characteristic Raman bands

of graphene and SWCNTs. Exemplarily, the scattering processes here are illustrated for the linear range close to the K points in graphene. The following description is also valid for metallic SWCNTs and might be also adapted for the Raman scattering of semiconducting SWCNTs considering their excitonic dispersion relations.

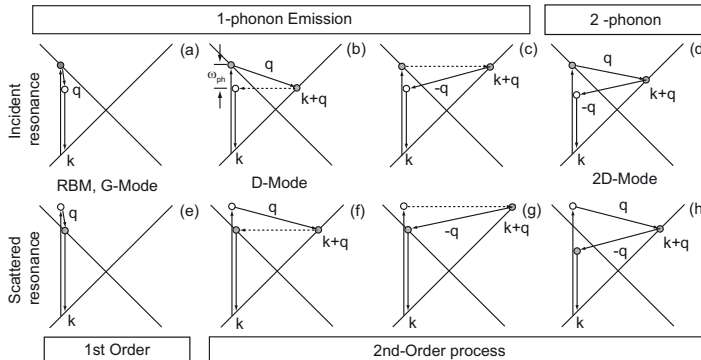


Fig. 1.20. Summary and classification of Raman scattering processes in graphene and SWCNTs. 1-phonon and 2-phonon-processes. First and second order processes. Further distinctions are possible regarding the incident (upper row) or scattered resonance process (lower row).

One-phonon processes and two-phonon processes are indicated by the upper name bar, while the order of these processes is given in the lower name bar. Two cases of resonance conditions can be distinguished. These are the incident (upper row) and scattered (lower row) resonances corresponding to the situation where either the excitation laser is resonant with an electronic transition or the scattered light. The end (starting) points of resonant transitions are marked as grey circle. Inelastic and elastic scattering events are indicated by solid and dashed arrows, respectively. The phonon modes of graphene and SWCNTs associated with these processes are given in the middle row. For the sake of convenience the processes in Fig. 1.20 are displayed as "intra-valley processes", where the elastic and inelastic scattering processes link two opposite sides of an equi-energy contour ring around the same K point. One Raman mode associated with this kind of scattering is the D'-mode. Due to momentum conservation, excitation with visible light allows only to probe Γ -point phonons with wave vectors $q \approx 0$. Defects in graphene and SWCNTs may relax this condition and give rise to phonon modes involving large q wave vectors. Second order Raman processes might also involve "inter-valley scattering", where the elastic and inelastic scattering occurs between states located at the K and K' points. The activation of these processes are allowed for phonons with large momentum, which follow a $q \approx 2k$ "selection rule". These double resonant inter-valley scattering processes follow basically the same schemes which are illustrated in Fig. 1.20, but in this case the scattering processes link electronic states close to

the inequivalent K and K' points. A prominent example for a Raman mode which is due to a double resonant "inter-valley" scattering process is the G' phonon mode.

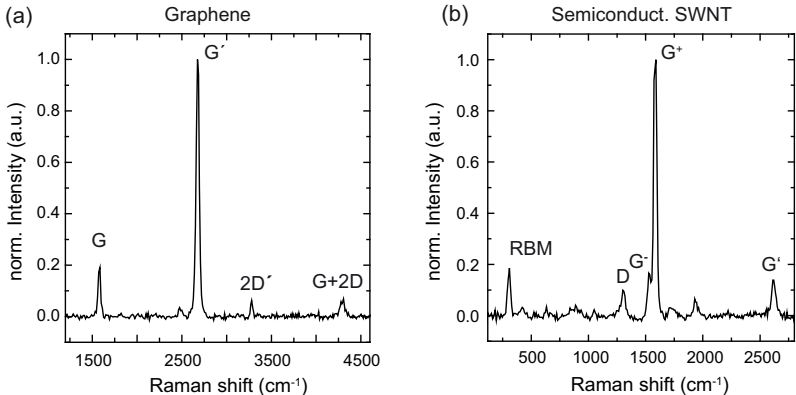


Fig. 1.21. Representative Raman spectra for single layer graphene (a) and a semiconducting (6,5) SWCNT (b). The most prominent Raman bands common to both materials are the G and G' (2D) bands at 1580 cm⁻¹ and 2600 cm⁻¹, respectively. The G' band in graphene is approximately 4–5 more intense than the G-band, opposed to the typical situation in carbon nanotubes. (b) The radial breathing mode (RBM) occurs in the spectral range of 250–400 cm⁻¹ and is a characteristic feature of SWCNTs. The spectral position scales inversely with the tube diameter. In semiconducting SWCNTs the G-band splits into a low and high frequency component, G⁻ and G⁺ respectively. Moreover, in (b) the defect induced D band at ~1300 cm⁻¹ can be observed which is a characteristic signature for defects in graphitic materials.

1.6.2. Raman Spectra of graphene and SWCNTs

The large number atoms in the unit cell of SWCNTs result in a considerably more complex phonon structure. Analog to the zone folding approach, which was used to obtain the electronic dispersion relation in Sec. 1.2.2 it is possible to derive the phonon dispersion relation of SWCNTs [52]. Raman scattering spectroscopy is extensively used for probing the vibrational and electronic properties of graphene and carbon nanotubes, providing detailed insight into the underlying phonon structure of these materials and the factors influencing them, such as stress, strain doping and defects [132].

Fig. 1.21 shows a representative Raman spectrum of graphene (a) and of a semiconducting (6,5) SWCNT (b). The most prominent phonon modes in graphene are the G- (E_{2g}) and the high frequency G' mode³ at 1580 cm⁻¹ and 2700 cm⁻¹. Two additional high frequency modes: the 2D' (3250 cm⁻¹), an overtone of the G-band, and a combination mode G+2D

³In other sources the 2D mode is referred to as G' mode. Here, the notation for the bands which is used in reference [134] is adapted

at 4300 cm^{-1} can be observed. In addition to these modes the Raman spectrum of the SWCNT exhibits two additional bands: The SWCNT specific RBM-band at $\sim 300\text{ cm}^{-1}$ and the defect-related D-band at 1350 cm^{-1} .

The G-Band

The G-band originates from a one phonon first order ($q = 0$) scattering process. It involves an optical phonon mode between the two carbon atoms in the graphene unit cell. The iTO mode is of E_{2g}^2 symmetry and corresponds to the stretching vibrations of carbon hexagons. In the case of graphene the corresponding G-band arises at $\sim 1580\text{ cm}^{-1}$ and has a single Lorentzian lineshape.

The G-band (A_1) is also observed in the Raman spectra of SWCNTs, whereas the phonon energy varies slightly. The degeneracy of the iTO- and LO-dispersions is lifted at the Γ -point, which leads to the splitting of the G-band into a high and low frequency component, denoted as G^+ and G^- in semiconducting SWCNTs, respectively. The reason for this is the confinement of the phonon vectors and curvature effects. The G^+ -band is associated with vibrations of carbon atoms in axial direction (LO mode), while the vibrational modes leading to G^- feature involve the motion of carbon atoms in circumferential direction of the SWCNTs (iTO mode). In contrast to the G^+ peak the frequency of the G^- is diameter dispersive according to $47.7\text{ cm}^{-1}/d_t^2$ [135].

The G'-band

The G' -band in graphene and SWCNTs, often also denoted as 2D band in literature, arises at $\sim 2600\text{--}2700\text{ cm}^{-1}$. The origin of the G' -band is a two-phonon, second order double resonant Raman process similar to the processes depicted in Fig. 1.20 (d) and (h). Two phonons with wave vectors \mathbf{q} and $-\mathbf{q}$ are involved in this process, therefore momentum conservation is fulfilled. The scattering process is an inter-valley process linking two inequivalent K-points. The double resonance links the phonon wave vectors to the electronic structure, which results into a strong dispersive behavior following different excitation energies. The shape and the width of the G' -band depends on the number of graphene layers. While for single layer graphene it resembles a single Lorentzian line shape, the G' -band of bilayer graphene is slightly broader. This is a consequence of a splitting of the band into four single components with slightly different frequencies. Also the Raman intensity-ratio of the G- and G' -band sensitively depends on the number of layers and is therefore used for analyzing the number of layers [134]. Characteristic for single layer graphene is the 4–5 times larger intensity of the 2D band compared to the G-band intensity.

The RBM-band

The most distinct difference of a SWCNT Raman spectrum to the one of graphene is the occurrence of the low-energy radial breathing mode (RBM) in the spectral region between 100 and 400 cm^{-1} . The RBM is a symmetric phonon mode originating from the simultaneous, radial displacement of all carbon atoms, which leads to a breathing-like vibrational motion. Its spectral position depends inversely on the diameter of the SWCNTs. This relation is commonly formulated as:

$$\omega_{RBM} = \frac{C_1}{d_t + C_2}. \quad (1.52)$$

For the parameters values $C_1=248\text{ cm}^{-1}\text{nm}$ and $C_2=0\text{ cm}^{-1}\text{nm}$ are suggested which were deduced for isolated single SWCNTs on a Si substrate [136].

This simple relation between the RBM frequency and the diameter is exploited for (n,m) chirality assignments of SWCNTs. For this resonance Raman experiments are performed, recording the RBM intensities for different laser excitation energies.

The D-band

The additional band, which arises in the mid frequency range between the RBM and G-Band at $\sim 1350\text{ cm}^{-1}$ is the so called D-band. The occurrence of the D-band is a distinct signature for disorder in graphitic materials. The corresponding phonon mode requires structural defects for its activation. The D-band peak arises from the breathing modes of sp^2 conjugated carbon rings. In highly crystalline graphene the number of defects is too small to observe the D-band. However, the graphene edges may act as sources for D-Band scattering [134, 137].

According to the classification in Fig. 1.20 (b), the D-band scattering process is a one phonon second order double resonance Raman process. The two resonance conditions correspond to the incoming (scattered) resonance and to the inelastic scattering process by a phonon. The latter can be described as *inter-valley* scattering of the excited electron into a $k+q$ momentum state, linking the two sides of the K-cone. The backscattering event of the excited electron into the initial k state, requires the presence of a defect. Any phonon with $q \approx 2k$ can give rise to the D-band. As the D-band scattering is a double resonance process it shows also a dispersive behavior for different energies of the incident Laser. Depending on the excitation wavelength the D-band frequency is shifted by $50\text{ cm}^{-1}/\text{eV}$ in graphene [138] and with a rate between $38\text{--}65\text{ cm}^{-1}/\text{eV}$ in SWCNTs [139].

In defective graphitic materials the defect activated D'- band at 1620 cm^{-1} can be observed. The origin here is a *intra-valley* double resonance process as it is depicted in Fig. 1.20 (a) and (f).

1.6.3. Disorder in Nanographitic Materials: The I_D/I_G ratio

The important fact that the intensity of the second order D and G^* Raman bands in graphitic materials is connected to the presence of defects is exploited to evaluate and discuss defect

densities in carbonaceous materials. The term defect in this context covers a broad range of different structural and electronic perturbations such as carbon vacancy sites, physisorbed ad-atoms on the surface as well as functional groups bound by covalent bond but also the edges of the material. Accordingly, mechanical deformation experienced by the structure, e.g. due to strain or twisting and also doping [140] any other sp^3 hybridized carbon sites due to e.g. chemical functionalization results in the emergence and/or increase of the Raman D-band. To date an overall comprehensive picture how the different types of defects affect the I_D/I_G ratio is just evolving. Most studies are related to the edges and finite size of nanographitic materials.

In most of the cases, the field discusses the data based on the results of an empirical study by Tuinstra and Koenig, where the D mode is related to the finite crystal size [141,142]. In this first comparative X-ray diffraction (XRD) and Raman studies on graphite and microcrystalline graphite the I_D/I_G Raman intensity ratio was found to scale inversely with the average cluster size L_a :

$$\frac{I(D)}{I(G)} = \frac{C(\lambda_{Ex})}{L_a} \quad (1.53)$$

In literature the relation in Eqn. 1.53 is commonly referred to as the Tuinstra-Koenig relation (TK1) [141]. The parameter $C(\lambda)$ is a wavelength dependent coefficient, which has been investigated systematically in reference [143]. For a typical Raman excitation wavelength of 514 nm $C=5.5 \cdot 10^{-3}$.

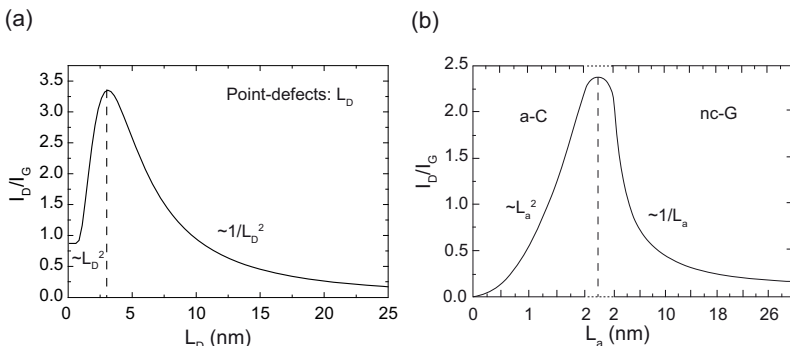


Fig. 1.22. Dependency of the Raman I_D/I_G ratio on the crystallite size L_a (a) For graphene treated with an argon-ion bombardment which preferentially produces point defects. Adapted from [144] (b) For various amorphous carbons, adapted from [145]. Two regimes can be identified in both graphs. Regime (1) for small cluster sizes, where the I_D/I_G increases with increasing with $L_a^{2/3}$ and regime(2) for cluster sizes larger than ~ 2 nm, where the I_D/I_G decreases with $1/L_a$.

Two different regimes can be distinguished for the dependency of the I_D/I_G -ratio on the crystallite size L_a . As the scattering process giving rise to the D-band requires defects, the intensity of the D-band is related to the number of defects. However, it requires intact carbon hexagons for its activation. If the number of defects increases the graphene carbon network starts loosing sp^2 connectivity and carbon clusters consisting of intact carbon hexagons are formed. Increasing the defect density leads to an increasing number of this clusters, while the average size of this clusters L_a decreases. For this regime of cluster sizes the D-band intensity I_D is steadily increasing.

Reaching a certain defect concentration the carbon network will start loosing intact hexagons and $I(D)$ starts to decrease. Ferrari et al. found that for this regime another relation holds $I_D/I_G = C(\lambda)/L_a^2$ with $C(514.5 \text{ nm}) \approx 0.55 \text{ nm}^{-2}$ [145]. The quadratic scaling law reflects the probability to find an intact carbon hexagon per unit area. While the previously mentioned work focused on various disordered and amorphous carbon materials, Lucchese et al. studied the effect of an argon-ion bombardment and induced amorphization for single layer graphene [144], where they observed a similar dependency of the I_D/I_G -ratio on the cluster size (compare Fig. 1.22 (a)).

2. Optical Microscopy Methods

The interaction of carbon nanotubes and graphene with light gives rise to a broad range of linear and also nonlinear optical effects, such as absorption, PL, elastic and inelastic light scattering, second harmonic generation or CARS. On the one hand the optical contrast generated by this emitted or absorbed light can be used for imaging of these materials on the other hand a spectroscopic analysis leads to valuable information about the electronic and phonon structure of these materials. Optical microscopy and related spectroscopy techniques provide experiments can be easily performed on ensembles as well as on the single nanotube level [31, 65, 136, 146, 147].

The first reports on the manufacturing and successful application of optical microscopes date back to the early 17th century and are connected to the names of the inventor, such as Zacharias Janssen, Galileo Galilei and Christiaan Hygens [68, 148]. An optical microscope generates a magnified real image of a small object using a lens system consisting of two convergent lenses, one close to the object under study, the so called objective, and an additional magnification lens(-system) at the user end, the ocular [148]. The general concept of the microscope remained basically unchanged until today. However, improvements in the fabrication of optical components and the illumination system lead to higher imaging quality, collection efficiency and in consequence the maximum spatial resolution. Due to the wave nature of light diffraction from lenses and apertures inside the microscope enforce a natural limit for the resolution of a microscope. close to the predicted theoretical limit of approximately half the wavelength of the excitation light (200–400 nm).

One approach to push the optical resolution limit closer to the theoretical limit is based on the optimization of the spatial intensity distribution within the focal area of the excitation and detected light. One of these concepts, which provides a slightly improved spatial resolution and a better rejection of background light compared to conventional wide-field microscopes is realized in laser scanning confocal microscopes.

In the first section of this chapter the fundamental parameters of an optical microscope, which are conveniently used to characterize e such as the point-spread function and optical resolution are introduced and the concept of the confocal microscope is briefly reviewed. Further literature giving an extensive overview about confocal microscopy and nano-optics in general might be found in refs. [68, 149]. The topic of the second section is the so called interference scattering microscopy (iSCAT). The signal formation relays on the interference between the elastically scattered light field of an object and a secondary reference field. Due to the interferometric enhancement of the scattering signal it is possible to detect even small nanoobject which are usually weak scatterers. In this work a common-path iSCAT approach is employed utilizing a standard inverted confocal microscope. A simple model for the formation of the

interferometric contrast is presented for the example of a small spherical object. The various phase contributions influencing the magnitude and sign of the signal are discussed.

2.1. Confocal Microscopy

Nowadays confocal microscopy is a widespread microscopy technique, which is successfully applied to study the optical properties of a broad range of different sample materials such as biological samples, inorganic semiconductor materials and even single molecules. The detected signal might originate from a variety of linear or non-linear light-matter interactions, such as fluorescence, Raman scattering, two-photon excitation or CARS.

The basic concept of the confocal microscope was first time proposed by Minsky in 1955, while an concept for a confocal microscope using an sample stage, which enabled the raster-scanning of the sample, was patented by him in 1957 [150]. The basic principle of the confocal microscope is based on the idea to use a point-like excitation source such as a tightly focused laser for illumination and simultaneously to detect only the light emanating from a single point of the sample, which can be realized by placing a pinhole in front of the detector. A schematic illustration of the confocal principle is shown in Fig. 2.1. The optical elements are arranged in the so called inverted or epi-geometry. Here, a single microscope objective is used for illumination of the sample as well as for the collection of the optical response. Excitation light is provided by a collimated laser beam (black line) and passes a beam splitter or equivalently a dichroic mirror. The laser beam is then focused by an infinity corrected objective onto the sample. The emitted light from the sample is collected by the same objective collected and is then guided via reflection from the beam splitter to a second lens, which focuses the light on a pinhole in front of the detector.

Both the objective and the second lens are aligned in a "confocal" arrangement, where each point of the object plane is directly mapped to a point of the conjugated image plane. However, the pinhole in front of the detector allows the detection of light from the sample which emanates from the small excitation volume confined to a in-focus sample position along the optical axis (blue lines). Light from emitters located either at off-axis sample positions (green line) or which are not located within the focal plane of the focusing objective (red lines) is efficiently blocked by the pinhole. A consequence of the point-like excitation and detection of the optical response is that for the acquisition of an image of a larger sample area, the optical response from many sample points needs to be collected. This can be achieved by raster-scanning of the sample area, either by lateral or horizontal stepwise movement of the sample with respect to the fixed position of the excitation laser by utilizing a piezo-driven sample stages or by varying the focus position across the sample. Such a lateral movement of the excitation beam can be realized by varying the position of the laser across the back aperture of the focusing objective by using galvanometric mirrors or acousto-optic deflectors.

The advantage of confocal microscopy compared to e.g. wide field microscopy is its improved axial and lateral resolution and more importantly it offers an improved background light re-

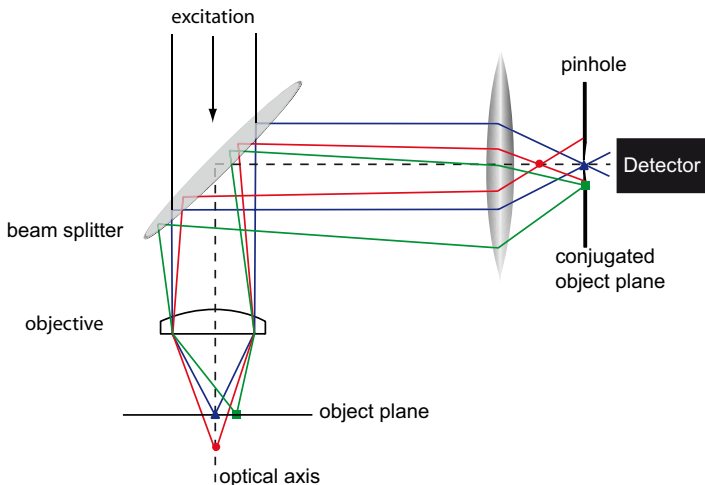


Fig. 2.1. Schematic illustration of the confocal principle for an epi-geometry. The lens system consists of two lenses arranged in a confocal geometry, where the focal point of one lens is in the focal point of the other one. The sample is illuminated by a point source. For this, the excitation beam passes a beam splitter and is focused on the sample. Only light emanating from an emitter positioned on the optical axis and in the focal plane of the first lens (blue triangle) can reach the detector. Light emanating from objects, either off-axis (green square) or out-of-focus (red circle), is efficiently blocked by the pinhole in front of the detector.

jection resulting in an improved optical contrast compared to the wide-field excitation. The size of the confocal pinhole is an important parameter as it determines the amount of light falling on the detector as well as axial resolution [151]. In general, the pinhole size should match approximately the (magnified) size of the diffraction limited excitation spot for optimum performance. The lateral optical resolution of confocal microscopes is only slightly improved compared to the white-field microscopes. Their advantage, especially regarding the imaging 3D objects is their considerably improved axial resolution. More details on the optical resolution and resolution limit of optical microscopes are found in the following section.

2.1.1. Spatial Resolution of Optical Microscopes

The resolution of an optical microscope is defined as the smallest distance between two objects in the image plane for which it is still possible to distinguish both. As it was mentioned in the introduction, diffraction of light at optical elements inside the microscope sets a natural limit to the spatial resolution. Or to put it in another way: The image of a point light source, such as a radiating point dipole, has a finite size and is spread in lateral and axial direction.

This broadening can be explained in the framework of the angular spectrum representation of optical fields in terms of spatial filtering by propagation and [68]. The point like response of a single radiating dipole can be described by a delta-function which is represented by an infinite spectrum of spatial frequencies k_x and k_y . By propagation of the light field from the point source into the farfield high frequency components ($k_x^2 + k_y^2 > k^2$) associated with the evanescent near-field are lost. Furthermore, the objective far away from the point source ($z \gg \lambda$) can only collect a limited fraction of the propagating field components. Both effects reduce the bandwidth of spatial frequencies and therefore inhibit the reconstruction of a point like image of the original source [68].

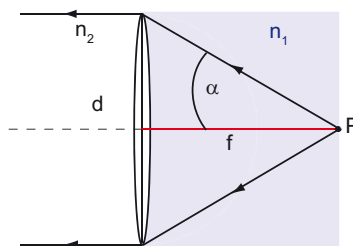


Fig. 2.2. The collection and focusing property of a lens depends on the maximum half-angle α of the cone of light, which can be accepted or focused by the lens. It is and the refractive index of the medium. The numerical aperture (NA) of lens is defined as: $NA = n_1 \cdot \sin \alpha$

Thereby, the resolution of a microscope depends on the maximum spatial frequencies $k_{x,max}$ and $k_{y,max}$ which can be accepted by the objective and is determined by the angular aperture 2α of the lens. The acceptance angle α is defined as the half-angle of the maximum cone of light, which can be collected or focused by the lens and is in consequence a function of the free aperture d and the focal length f : $\tan \alpha = d/2f$ (compare Fig. 2.2).

More conveniently, the so called numerical aperture (NA) is used to describe the collecting and focusing properties of the lens. The NA is related to α by:

$$NA = n \cdot \sin \alpha . \quad (2.1)$$

Here n is the refractive index of the medium between the lens and the focal point P. The maximum spatial frequencies e.g. in x-direction $k_{x,max}$ which can be collected by the lens is then related to the NA by:

$$k_{x,max} = k \cdot NA = \frac{2\pi}{\lambda} \cdot NA . \quad (2.2)$$

Considering now the image of a single dipole emitter which is oriented perpendicular to the optical axis (in x-direction). The spatial intensity distribution of the dipole in the image plane is given by the so called point-spread function (PSF) of the microscope. The PSF describes the spread of the electric field radiated by a point source when propagating from the object plane to the image plane and passing the optical components of the microscope. The PSF of the whole microscope is approximately the product of an excitation PSF and detection PSF $\simeq \text{PSF}_{det} \cdot \text{PSF}_{exc}$. The PSF_{exc} and PSF_{det} are equal to the spatial intensity distribution of the focused light in the object plane and the detected intensity distribution in the image plane, respectively.

In the paraxial approximation where $2\alpha \ll 90^\circ$ the PSF of a point source has the functional form of an Airy function [68]:

$$I(x, y, z = 0) = C \left[\frac{J_1(2\pi\tilde{\rho})}{2\pi\tilde{\rho}} \right]^2 \quad \tilde{\rho} = \frac{NA \cdot \rho}{M\lambda} . \quad (2.3)$$

J_1 denotes a Bessel function of the first kind, while ρ is the radial distance from the optical axis and M is the magnification of the optical system. A plot of the PSF defined in Eqn. 2.8 is depicted in Fig. 2.3.

The PSF is maximal at $\rho = 0$ and has additional substantially weaker side-maxima at larger radial distances. The width of the PSF, the so called Airy disc radius, is defined as the radial distance ρ at which the PSF becomes zero. Along the x-axis with $\rho = x$ the Airy disc radius Δx is:

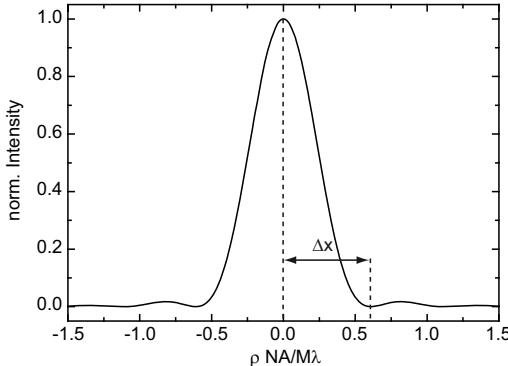


Fig. 2.3. PSF of a single dipole oriented perpendicular to the optical axis along the x-direction. The function was plotted based on the paraaxial expression of the PSF in Eqn. 2.8. The width of the PSF is the so called Airy disc radius and is equal to the radial distance ρ at which the PSF becomes zero.

$$\Delta x = 0.61 \frac{M\lambda}{NA} . \quad (2.4)$$

Δx depends only on the wavelength λ of the excitation light, the numerical aperture NA and the magnification M of the system. Although the PSF in Eqn. 2.8 was evaluated in the paraxial limit it is a good approximation for microscopes utilizing high NA objectives as there are only minor deviations in the width and height of side maxima compared to the results of exact calculations of the PSF [68].

With the knowledge about the lateral PSFs it is possible to evaluate the resolution limit of the microscope. Considering the situation depicted in Fig. 2.3, where the radiation of two point sources separated by the distance Δr in the object plane is detected in the image plane. The distance between the two emitters in the object plane Δr is mapped to the distance $M\Delta r$ in the object plane. Assuming that the two emitters radiate incoherently, their PSFs simply overlap giving rise to different image patterns strongly depending on the distance Δr between the emitters.

Based on this image patterns different definitions exist for the maximum resolution of a microscope. The widely used resolution criterion of Ernst Abbe states that two emitters can be well distinguished if the separation of their PSFs $\text{Min}[M\Delta r]$ in the image plane is equal or larger than the width Δx of a single PSF. In this case the maximum of one PSF coincides with the first minimum of the second PSF:

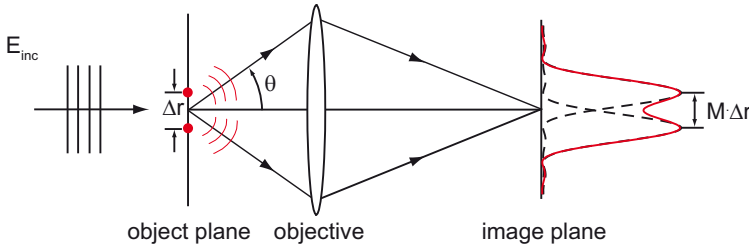


Fig. 2.4. Illustration of the optical resolution limit of a microscope. Two closely neighbored point sources separated by the distance Δr in the object plane are excited simultaneously.

$$\text{Min}[\Delta r] \geq 0.61 \frac{\lambda}{NA} . \quad (2.5)$$

An analogous criterion for the resolution limit where a two dimensional imaging geometry was considered was formulated by Rayleigh [148]. The resolution limit defined by Abbe appears to be somewhat arbitrary, as the overlapping PSFs of both emitters can be well distinguished even if their separation $\text{Min}[\Delta r]$ would be below the limit defined in Eqn. 2.5. Furthermore it is valid only for two parallel dipoles with fixed orientations perpendicular to the optical axis. The advantage of this formulation on the other hand is that it can be also applied to the case where two different dipoles exhibit different optical response upon excitation. The relative distance between the two emitters is not distorted.

An estimation for the theoretical limit for the spatial resolution of an imaging system can be derived using the expression in Eqn. 2.2. The minimum distance $\text{Min}[\Delta r]$ between two point sources separated by the distance $\Delta r = (\Delta x^2 + \Delta y^2)^{1/2}$ in the object plane is determined by the maximum bandwidth of spatial frequencies $\Delta k = (\Delta k_x^2 + \Delta k_y^2)^{1/2}$ which can be acquired by the system. It can be shown that, similar to Heisenberg's uncertainty relation, Δr and Δk are related by [68]:

$$\Delta k \Delta r \geq 1 . \quad (2.6)$$

Using Eqn. 2.2 as an upper limit for Δk constrained by the NA of the collecting lens, one obtains:

$$\text{Min}[\Delta r] = \frac{\lambda}{\rho_i \cdot NA} = 0.31 \frac{\lambda}{NA} . \quad (2.7)$$

Compared to the Rayleigh resolution limit the theoretically expected resolution limit is about two times smaller.

The key features of a confocal microscope are the small excitation volume due to a tightly focused beam, which allows selective excitation of spatially well isolated emitters and secondly the aperture in front of the detector. Compared to wide-field microscopes the lateral resolution of standard confocal microscopes is only slightly better. The resolution determining PSF of a microscope is in a first approximation proportional to the product of excitation PSF (PSF_{ill}) and detection pointspread function (PSF_{det}). In the case of the confocal microscope PSF_{ill} and PSF_{det} are identical, which leads to a square scaling of the total system PSF on the PSF_{ill} :

$$PSF(x, y, z)_{conf} \propto PSF(x, y, z)_{ill} \cdot PSF(x, y, z)_{det} \sim PSF_{ill}^2 , \quad (2.8)$$

and in consequence to the slight resolution improvement compared to wide-field illumination. The big advantage of confocal microscopy over wide-field microscopy is its enhanced axial resolution. The minimum axial resolution $Min[\Delta r_z]$ of two dipoles positioned along the optical axis is:

$$Min[\Delta r_z] = 2 \frac{n\lambda}{NA^2} , \quad (2.9)$$

where n denotes the refractive index in the object space.

In the last years confocal microscopy based "superresolution" techniques have been developed which provide subwavelength optical resolution. The most prominent ones are the stimulated emission depletion technique (STED) [152] or the stochastic optical reconstruction microscopy (STORM) [153]. Confocal microscopy is also the basis for e.g. tip-enhanced near-field microscopy and can be also combined with time-resolved optical techniques, such as pump-probe spectroscopy or TCSPC measurements.

2.1.2. Gaussian Laser Beam and Gouy Phase Shift

An important parameter for microscopy in general is the intensity distribution in the focal area, which is determined by the focusing optics and the properties of the excitation light. Nowadays lasers are established as standard light sources for confocal microscopy. They provide monochromatic, coherent light with a high degree of polarization. Typically the output is highly collimated with a negligible beam divergence even when propagating large distances. By using high NA microscope objectives this allows the tight focusing of the laser beams to diffraction limited focal volumes which is a fundamental requirement for single

molecule microscopy.

In most of the cases the fundamental output mode of a laser beam exhibits a Gaussian field distribution in its beam waist. In the paraxial approximation, the radial field distribution of a collimated Gaussian laser beam propagating in direction of the z-axis is given by [68,154]:

$$\mathbf{E}(\rho, z) = \mathbf{E}_0 \frac{w_0}{w(z)} e^{-\frac{\rho^2}{w^2(z)}} e^{i[kz - \phi_{Gouy}(z) + k\rho^2/2R(z)]}. \quad (2.10)$$

Here \mathbf{E}_0 denotes a constant field vector in a plane perpendicular to the propagation direction. $\rho = (x^2 + y^2)^{1/2}$ is the radial distance from the z-axis. The other parameters can be explained by examining the plot of the electric field \mathbf{E} of the Gaussian beam depicted in Fig. 2.5. w_0 is the beam radius at the position $z=0$.

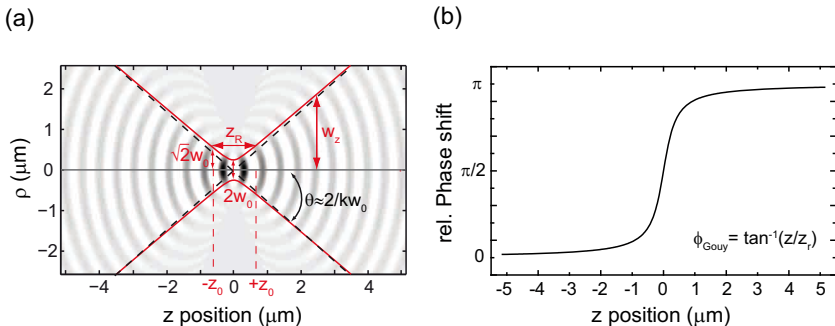


Fig. 2.5. (a) Characteristics of a paraxial Gaussian beam in the region of its beam waist. Plot of the radial electric field distribution along the z-axis. The surfaces of constant field strength form a hyperboloid along the z-axis (red curves). (b) Gouy phase shift: A Gaussian beam exhibits a phase shift of ϕ_{Gouy} when the beam propagates through its beam waist.

Furthermore following abbreviations are used in Eqn. 2.10:

$$\begin{aligned} w(z) &= w_0 + (1 + z^2/z_r^2)^{1/2} && \text{beam radius ,} \\ R(z) &= z(1 + z_0^2/z^2) && \text{wavefront radius ,} \\ \phi_{Gouy} &= \arctan z/z_r && \text{Gouy phase .} \end{aligned} \quad (2.11)$$

The parameter z_0 is defined as: $z_0 = kw_0^2/2$, where k is the wave vector of the light. The parameter z_r is the Rayleigh range and is defined as the axial distance between the focus and the position z_r where the beam radius increases to $\sqrt{2} w_0$. Related to this is the so called

bi- or confocal range b , which is defined as the distance twice the Rayleigh range: $b = 2 z_r$. Within this range the Gaussian beam is approximately collimated.

The beam radius $w(z)$ is defined as the radial distance ρ , for which the electric field amplitude $E(x, y, z)$ is reduced by a factor of $1/e$ compared to its corresponding value along the z-axis $E(0, 0, z)$. With increasing distance from the center the beam becomes more divergent and the beam radius $w(z)$ continuously increases. The points of constant $E(x, y, z)$ form hyperboloid surfaces along the z-axis. The asymptotes (black dashed lines) for $z \rightarrow \pm\infty$ enclose an angle $\theta = 2/k w_0$ with the z-axis. θ is called the divergence of the beam and can be directly related to the NA of a focusing lens by $NA = n \cdot \sin 2/k w_0$.

Besides the propagation term $k z$, the imaginary part of Eqn. 2.10 consists of two additional terms. The second term is the Gouy phase shift ϕ_{Gouy} . A Gaussian beam experiences an axial phase shift of π compared to a plane wave with the same optical frequency when traveling from $z=-\infty$ to $z=+\infty$ [155]. The evolution of the phase-shift is depicted in Fig. 2.5 (b)). The phase changes gradually as the beam is passing through its beam waist. The fastest phase change occurs on the distance corresponding to the Rayleigh range and thus the speed of the phase change can be controlled by focusing. The Gouy phase shift does not only occur for weakly convergent/divergent light beams such as the Gaussian beam but is a phenomena intrinsic to all propagating focused light fields [156]. The Gouy phase shift has important implications for optical experiments relying on the phase relations of the excitation light field such as interferometric light detection schemes, in nonlinear microscopy or for coherent control experiments [157].

The last term of the imaginary exponential expression of Eqn. 2.10 describes the curvature of the wavefronts. The change of curvature upon propagation along the z-axis is described by the wavefront radius parameter $R(z)$. Close to the beam waist at $z=0$ the radius approaches infinity, $R(z) \approx \infty$, and consequently the wavefronts in this region are simple planes. In the limit $z \rightarrow \pm\infty$ $R(z)$ depends nearly linear on z which is characteristic for a spherical wave. The wavefronts have their minimum curvature at the edges of the Rayleigh zone at $\pm z_0$, where $R(z_0) = 2z_0$.

2.2. Interference Scattering Microscopy

Interference scattering microscopy techniques (iSCAT) are microscopy techniques, where the detected signal is formed by interference of a scattered light field of an small particle and a reference field [158–160]. One prerequisite is that the scattered and reference fields are both coherent and that the spatial modes of both light fields overlap to some extent [160]. There are various approaches for the realization of the interference geometry, basically determined by the choice of the reference field. Despite classical Michelson and Mach-Zehnder designs [161], where the reference field is separated from the excitation beam and is traveling in a separate

arm of the setup, there are also common-path realizations where the incident and scattered beams propagate along the same geometrical path [162–164]. In the common-path schemes the reference field can be the incident excitation field [162, 165] or the beam reflected from an substrate interface back into the direction of the incidence [158, 163, 166]. The scattered field is either generated by the direct elastic interaction of the incident light with the particle or by scattering from refractive index inhomogeneities induced by the interaction of the particle with its local environment. The latter effect is for example exploited in the photothermal imaging method [147, 166, 167], which allows to determine the amount of heat deposited in a particle and in consequence their absorption.

One of the advantages of scattering methods is that it can be used to study non-fluorescent objects such as gold nanoparticles, non-luminescent semiconductor nanocrystals [167] but also biological samples such as viruses [168]. Due to the high sensitivity of the iSCAT method acquisition times can be very small for particles with moderate scattering cross sections which even allows the detection and distinguishing of particles in fluids [161, 169, 170]. The good SNR which can be achieved for the iSCAT signals allows also the application of the method for particle tracking experiments. Only recently the iSCAT method was successfully employed for the visualization of the translational and rotational motion of viruses deposited on lipid bi-layers [168].

For particles significantly smaller than the excitation wavelength the interferometric signal is not a pure "scattering" signal anymore, where the particles optical response is governed by the real part of its polarizability/susceptibility but rather due to the extinction or absorption properties of the particle. This property of the signal has been exploited in experiments in order to determine the extinction of a transmitted or reflected focused beam caused by a single molecule [171–173] and was also used to determine the extinction cross sections of semiconductor quantum dots [174] and GNPs [165, 175].

iSCAT based methods can achieve single particle detection sensitivity and were successfully employed to visualize individual gold nanoparticles (GNP) with sizes as small as 2.5–5 nm [158, 167, 176–178] and recently it was demonstrated that it is possible to image single organic molecules based on their absorption signals [172, 179]. By employing an common-path iSCAT scheme based on an inverted confocal microscope and a supercontinuum white light source, Lindfors et al. demonstrated for the first time that this iSCAT method is capable of distinguishing individual gold nanoparticles with diameters between 5–60 nm based on their plasmon spectra [158].

In the next two sections a realization of the iSCAT experiment based on a common-path approach which utilizes an inverted confocal microscope in reflection mode is presented. Following this, the formation of the interferometric scattering signal for the common-path iSCAT arrangement is elucidated for the simple case of a spherical particle with a diameters significantly smaller than the excitation wavelength.

Common-path iSCAT Geometry

In this work the common-path iSCAT approach is employed to study the scattering (extinction) properties of individual SWCNTs on a glass substrate. The approach can be easily realized on a conventional inverted confocal microscope in reflection mode [158, 163]. A schematic representation of the experimental scattering setup is depicted in Fig. 2.6.

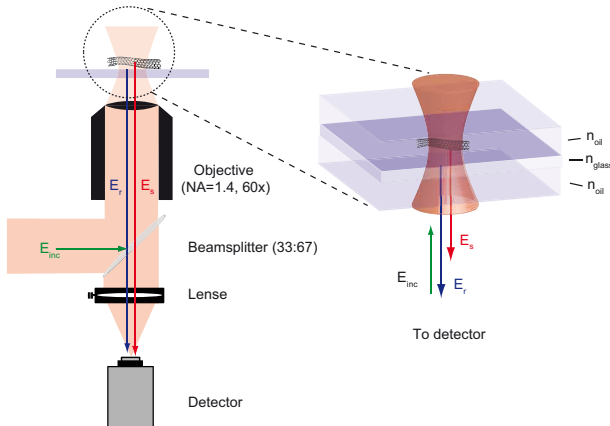


Fig. 2.6. Schematic representation of the common-path iSCAT geometry. Using an inverted confocal microscope setup, the incident laser field E_{inc} is focused by a high $NA=1.4$ objective on a particle deposited on glass coverslide. The sample is further covered by a thin layer of immersion oil to achieve refractive index matching conditions. Thereby, total internal reflection is avoided and the amount of back-reflected background light from the glass is reduced which enhances the scattering contrast. A small fraction of the incident light ($\sim 10^{-5}$) is reflected at the glass-oil interface E_r and serves as reference beam (black dashed line). The scattered field of the particle E_s (red dashed line) and the reflected field E_r (black line) are collected by the same objective and are focused on the detector.

The excitation light E_{inc} is reflected by a beam-splitter into a high NA immersion oil objective ($NA=1.4$, 60x), which focuses the light onto the sample. If an object is present in the focal volume two processes occur: First, elastic light scattering from the particle and second reflection of the incident light at the glass-oil interface. The scattered E_s and reflected light E_r are collected by the same objective, collimated and is then focused on a detector. Both the scattered and reflected fields add up coherently and thus give rise to the interferometric signal. In a similar way a transmission iSCAT geometry can be realized by collecting the light propagating into the upper half-space with a second objective.

A large fraction of the light focused on the sample by high NA objectives impinges on the sample under large angles of incidence. For instance, the maximum angle of incidence of light focused by an oil immersion objective with $NA=1.4$ on a glass-air is $\theta_{max} =$

$\arcsin NA/n_{oil} = 67^\circ$ which considerably exceeds the critical angle for total internal reflection for such a interface of $\theta_{crit} = 41^\circ$. In consequence, about $\sim 25\%$ of the incident excitation light undergoes totally internal reflection (assuming highest filling factor of the objective). This totally reflected light is collected by the objective and also reaches the detector. It represents a substantial contribution to the overall background signal. In addition to this, these high angle field components carry an additional incident angle dependent phase shift [68] which complicates the interpretation of the interferometric scattering signal. Total internal reflection can be efficiently suppressed by establishing refractive index matching conditions. This can be achieved by embedding samples with an immersion oil which matches the refractive index of the glass substrates. This reduces also the amount of backreflected light from the glass-oil interface by up to three orders of magnitude leading to an improved scattering contrast [180].

The Interferometric Scattering Signal

In the following an simple expression for the interferometric signal of iSCAT experiments using the back reflection geometry is derived. For the sake of simplicity the object under study is a spherical particle with a radius small compared to the excitation wavelength ($a \ll \lambda$). Furthermore, only on-axis phase relations between the reflected focused Gaussian laser beam and the scattered field of the particle. In this limit the scattering contrast and the parameters controlling the signal such as the particle size, the reflectivity of the substrate interface and different phase contributions inherent to the reflected and scattered fields can be discussed qualitatively. Moreover it is shown that the interference signal of small particles originates from the absorption of the particle. The presentation of this topic is based on refs. [158, 181, 182].

The scattered field \mathbf{E}_s and reflected fields \mathbf{E}_r are related to the incident excitation laser field \mathbf{E}_{inc} by:

$$\mathbf{E}_s = s \cdot \mathbf{E}_{inc} \quad \mathbf{E}_r = r \cdot \mathbf{E}_{inc} . \quad (2.12)$$

The scattered field propagates as a spherical wave, whose amplitude and phase are determined by the complex valued scattering coefficient s . Conveniently, the reflected field \mathbf{E}_r is expressed in terms of the fresnel reflection coefficients r , which is defined by the refractive indices of the different media and the angle of incidence [148].

The scattering coefficient s depends on the polarization of the incident light, the direction of the incident and detected light and the material properties of the particle and of the surrounding medium [182]. For spherical particles with diameters small compared to the excitation wavelength the scattering process can be treated as scattering of a dipole which results in simplified expressions for s . Assuming that the sphere is located directly in the center of the excitation focus and considering only the excitation and scattered light which is propagat-

ing in direction of the optical axis, the scattering coefficient s for light scattered back into the directions of the incident light is [182]:

$$s = -\frac{k^3}{4\pi} \cdot |\alpha| \exp i\phi_p \quad (2.13)$$

$k = 2\pi n_{med}/\lambda$ is the wavevector of the excitation light propagating in a medium with refractive index n_{med} . $\alpha=|\alpha| \exp i\phi_p$ is the complex polarizability of the sphere, where ϕ_p is the phase of the polarizability. The polarizability of a sphere can be defined in terms of the Clausius-Mosotti relation [182]:

$$\alpha = 4\pi \frac{\epsilon_{sphere} - \epsilon_{med}}{\epsilon_{sphere} + 2\epsilon_{med}} \cdot a^3, \quad (2.14)$$

ϵ_{sphere} and ϵ_{med} are the (complex) dielectric constants of the sphere (e.g. gold) and of the surrounding medium respectively and a denotes the radius of the particle.

Both fields, E_s and E_r , interfere in the detector plane and the measured intensity I_{scat} can be written:

$$I_{scat} \simeq |E_r + E_s|^2 = |E_r|^2 + |E_s|^2 + 2 E_r^* E_s \cos \Delta\phi. \quad (2.15)$$

The first and second terms of Eqn. 2.15 correspond to the reflected and pure scattered intensities respectively. The third term is the interference term, which depends critically on the relative phase difference $\Delta\phi$ between the reflected and scattered field. The phase shift $\Delta\phi$ is defined as the relative phase shift of the scattered field in respect to the reflected field and contains all phase contributions originating from both. Substituting the expressions of electric fields by their definitions given in Eqn. 2.12 the intensity reads:

$$I_{scat} \simeq |E_{inc}|^2 (r^2 + |s|^2 + 2 r |s| \cos \Delta\phi). \quad (2.16)$$

Basically three parameters, r , s and the phase $\Delta\phi$ determine the scattering intensity. Typically the scattering amplitude factor $|s|$ of nanoparticles is small compared to the reflectivity r . Thereby the strongest signal contribution arises from the back reflected light $\propto r^2$. This signal is than further modified by the pure scattering term $\propto |s|^2$ and the interference term. As $|s|$ is related to the radius of the particle a via the polarizability α this has implications for the contribution of both terms to the signal. In the following the different contributions to the detected intensity are discussed:

Particle size a: The scattering amplitude $|s|$ is related via the polarizability directly to the volume of the particle: $|s| \propto a^3$. Due to the different scaling of the pure scattering term $|s|^2$ and the interference term with the diameter of a^6 and a^3 respectively, the contribution of the interference term to I_{scat} becomes increasingly important for decreasing particle diameters. In consequence, for small diameter particles the interference term dominates the scattering signal completely and in this regime the detected signal scales with the third power of the diameter [165]. Thus, the scattering signals of small diameter nanoscale object originates from extinction (absorption) of the particle. This point will be elucidated in more detail in one of the following paragraphs.

Reflectivity r: Another factor determining the detected intensity is reflectivity r of the substrate/ immersion oil interface. According to Eqn. 2.16 a high reflectivity leads to an increase of the detected intensity and does also enhance the contribution of the interference term to the signal. It is to note that r has is a wavelength dependent function, depending on the refractive indices of the materials forming the interface and the polarization and angle of incidence of the incident light and thus can modify the line shape of the detected signal. By carefully adjusting r , e.g. by selecting different immersion media, one is able to enhance the scattering intensity or to invert the contrast [180].

Relative phase shift $\Delta\phi$: The third contribution to I_{scat} is the relative phase shift $\Delta\phi$ between the reflected field from the substrate interface and the scattered field of the particle. Both, the reflected beam and the scattered beam, experience a phase shift compared to a unperturbed plane wave propagating in the same direction: The reflected beam is affected by the Gouy phase shift ϕ_{Gouy} (compare Sec. 2.1.2) and the scattered beam by the phase delay due to the oscillator response of the sphere ϕ_p to the excitation light field.

First addressing the *Gouy phase shift* for the reflected laser beam. The basic phenomenon was explained in Sec. 2.1.2 and is extended in the following to the case of a reflected focused beam. Fig. 2.7 illustrates schematically the situation in the focal region. A Gaussian laser beam is focused on a sphere deposited on a substrate (black beam waist). The laser beam is propagating in positive z direction with the center of the beam waist located at $z = 0$. At the interface a fraction of the beam is reflected and propagates back into the direction of the detector in the farfield (black arrow). Measured from the position of the particle at $z = 0$ the reflected beam E_r accumulates a phase shift equal to $\phi_{Gouy} = -\pi/2$.

For a vertical displacement of the particle along the optical axis by a distance of $\pm z$ away from the focal plane or equivalently defocusing, the modified Gouy phase shift experienced by the reflected field E_r is [181]:

$$\phi_{Gouy} = -\pi/2 \pm \arctan(z/z_r). \quad (2.17)$$

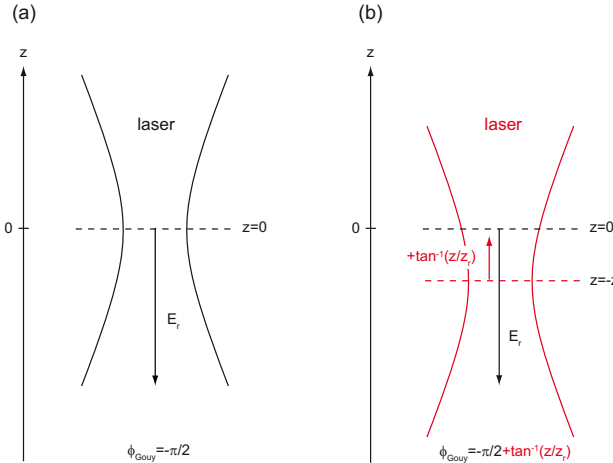


Fig. 2.7. Phase contribution to the relative phase shift ϕ_{total} between the incident and reflected fields. (a) The reflected field E_r experiences a Gouy phase shift of $-\pi/2$ when propagating from the substrate interface ($z=0$) to the detector in the far field. (b) A focus position below the substrate interface ($z = -z$) along the optical axis results in a modified Gouy phase shift of $-\pi/2 \pm \arctan(z/z_r)$ for the reflected field.

Here z is the focal position along the z axis with $z=0$ corresponding to the position of the particle and z_r is the Rayleigh range of the Gaussian beam (see also Sec. 2.1.2). Representatively, the situation is illustrated for focusing below the substrate interface at the position $z = -z$ (red beam waist). In this case the accumulated Gouy phase shift of the reflected beam increases, while for focusing above the interface $z > 0$ the field develops a smaller phase shift. This immanent effect on the scattering signal in iSCAT experiments is discussed by Hwang et al. in detail. It could be shown that the Gouy phase shift of the reflected field is basically the cause that in the case of small diameter particles absorption leads to the attenuation of the reflected (transmitted) laser beam [181].

Another factor which might give rise to an additional phase shift between the incident and reflected field is the reflectivity r itself. Depending on the refractive indices of the materials constituting the optical interface, the reflection coefficient r might change its sign corresponding to an additional phase shift of π . This might occur for a transition from an inner reflection ($n_{inc} > n_{trans}$) to outer reflection ($n_{inc} < n_{trans}$) and vice versa. If working with a single wavelength for excitation this should not be a problem, however as the refractive indices and thus r are wavelength dependent such a transition might occur when working with a broadband light source for excitation. Knowledge about the refractive indices of the substrate and immersion medium is therefore essential for interpreting the magnitude of the intensity signals.

The second phase contribution is associated with the scattered field \mathbf{E}_s and originates from the *oscillator phase* ϕ_p of the particle due to its response to the excitation field. The phase of the scattered field E_s is shifted by ϕ_p compared to the excitation field \mathbf{E}_{inc} . The phase shift arises from the wavelength dispersive optical response of the sphere and the propagation of the field as a spherical wave. The incident \mathbf{E}_{inc} and scattered field \mathbf{E}_s are related by the scattering amplitude s . In the electrostatic approximation for small particles s is proportional to the polarizability α [182].

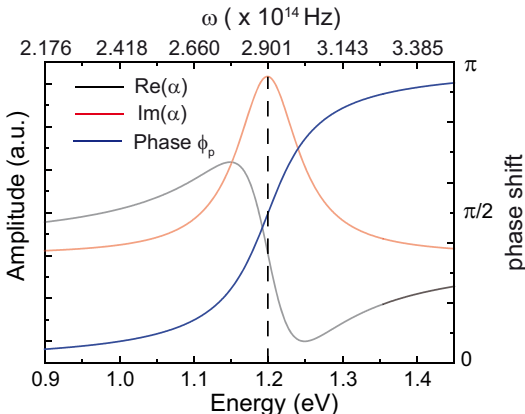


Fig. 2.8. Contributions to the relative phase shift ϕ_{total} between the incident and scattered fields: Phase shift due to the scattering response of the particle, here approximated by the polarizability of a dipole treated as damped harmonic oscillator. Blue curve: Phase shift plotted as function of the excitation energy (frequency). The phase shift is 0 for small excitation energies and increases to π for larger ones. At the resonance energy (1.2 eV) the phase shift equals $\pi/2$.

α in turn is a complex valued function of the excitation wavelength describing the optical response of the particle. Assuming that the small sphere can be treated as a dipole, the functional form of the polarizability can be approximated by the oscillatory part of the function of motion of a damped harmonic oscillator [182]. In Fig. 2.7 the real (black) and imaginary parts (red) of this idealized α are depicted. The phase shift ϕ_p (blue curve) between the oscillator and the incident driving field is defined by the imaginary and real part of the polarizability, according to $\phi_p = \arctan(Im(\alpha)/Re(\alpha))$. For excitation energies deviating from than the resonance energy the phase shift is small. The phaseshift steadily increases for increasing excitation energies. For energies exceeding the resonance energy the oscillator is not able to follow anymore the driving field, resulting in a phase delay of π . In the energy range close to the resonance energy the phase changes rapidly and the phase delay becomes $\pi/2$ when the excitation energy matches the resonance.

Accordingly, the phase shift ϕ_p due to the wavelength dependent response of the oscillator can be defined by using the expression of the scattering amplitude s in Eqn. 2.13:

$$\phi_p = \arctan \frac{\text{Im}(\alpha)}{\text{Re}(\alpha)} . \quad (2.18)$$

With Eqn. 2.17 and Eqn. 2.18 the relative phase shift $\Delta\phi$ between the reflected field and the scattered field is then given as:

$$\Delta\phi = \phi_{Gouy} - \phi_p . \quad (2.19)$$

Plugging in the explicit expression for $\Delta\phi$ into Eqn. 2.15 and neglecting the pure scattering term $|s|^2$ one obtains an expression for the scattering intensity valid for small particles:

$$I_{scat} \simeq |E_{inc}|^2 \left[r^2 + 2 r |s| \cos \left(-\frac{\pi}{2} + \arctan \frac{z}{z_r} - \arctan \frac{\text{Im}(\alpha)}{\text{Re}(\alpha)} \right) \right] . \quad (2.20)$$

Assuming that the particle is exactly in the focus at $z=0$, where the Gouy phase term becomes zero and using the relation $\cos(\pi/2 + \phi) = -\sin(\phi)$ Eqn. 2.20 becomes:

$$I_{scat} \sim |E_{inc}|^2 \left[r^2 - 2 r |s| \sin \left(\arctan \left(\frac{\text{Im}(\alpha)}{\text{Re}(\alpha)} \right) \right) \right] . \quad (2.21)$$

The light scattering of the particle in the focus effectively leads to attenuation of the intensity of the back reflected light. For the small particles under consideration, this is caused by absorption of light. This becomes more apparent when substituting $|s| = c |\alpha|$ in Eqn. 2.21 and using the relation $\text{Im}(\alpha) = |\alpha| \cdot \sin(\phi_p)$:

$$I_{scat} \sim |E_{inc}|^2 (r^2 - 2 r c \text{Im}(\alpha)) . \quad (2.22)$$

Eqn. 2.21 and Eqn. 2.22 are basically representations of the extinction theorem for the limit of small particles [182]. Usually, extinction is attributed to the real part of α : $\text{Re}(\alpha) = |\alpha| \cdot \cos(\phi_p)$ which causes a phase shift between the incident and scattered fields and thus leading to destructive interference [183]. In the case of resonant excitation and assuming a dipolar response of the particle, the phase ϕ_p becomes $\pi/2$. The scattering intensity is then approximately given as:

$$I_{scat} \sim |E_{inc}|^2 (r^2 - 2 r c |\alpha|) . \quad (2.23)$$

Thus, for resonant excitation and the particle placed in focus the contribution of the interference term is expected to be maximal. Indeed, the dependence of ϕ_{Gouy} on the axial displacement of the particle and its influences on the detected scattering/extinction intensity could be observed experimentally for a similar iSCAT arrangement as described here [174]. The ϕ_{Gouy} dependency on defocusing might also have practical implications for white light experiments. In the case that the microscope objective is not corrected perfectly for chromatic aberrations it focuses the various wavelength components differently. In consequence this results in different Gouy phases for different wavelength and thus might modify the shape and intensity of the iSCAT signal.

The simple model presented here could only show the basic ideas of the contrast formation. A more thoroughly modeling would profit from a detailed analysis of the spatial mode overlap between the reflected and scattered light field for all angles of incidence and collection angles which can be realized by the objective. In addition the calculation of the scattered fields of the GNP would require a more precise treatment e.g. in terms of the Mie-scattering theory. In the case of spherical, homogenous particles the Mie theory yields exact solutions and would represent certainly an improvement.

Scattering Contrast

The scattering signal of small particles I_{scat} is basically comprised of the intensity of the back-reflected light from the glass-oil interface which is modulated by the small contribution of the interference term (compare Eqn. 2.23). In order to emphasize directly the change in the back-reflected light caused by the presence of a scattering particle at a sample position it is convenient to define the contrast δ :

$$\delta(\lambda) = \frac{I_{scat} - I_{back}}{I_{back}} . \quad (2.24)$$

The contrast is just the difference between the scattering intensity emanating from the focal area I_{scat} containing the object and the back-reflected intensity I_{back} of the glass-oil interface from a background position. Further the differential signal is normalized to the background intensity in order to cancel out wavelength dependent transmission/reflection dependencies introduced by the optical elements, such as filters, beam splitters or grating, and also the wavelength dependency of the detection sensitivity of the detector.

Using the definitions for the intensities in Eqn. 2.15 and Eqn. 2.12, the optical contrast can be expressed in terms of the scattering and reflection amplitude coefficients:

$$\begin{aligned}\delta(\lambda) &= \frac{(r^2 + |s|^2 + 2r|s|\cos\Delta\phi) - r^2}{r^2} \\ &= \frac{|s|^2}{r^2} + 2\frac{|s|}{r}\cos\Delta\phi \quad \text{for : } s \ll r .\end{aligned}\quad (2.25)$$

From Eqn. 2.25 it becomes evident that the optical contrast δ should increase for a decreasing r . The reflectivity of an interface depends on the dielectric properties of the material and can be controlled by e.g. changing the embedding material in order to achieve refractive index matching conditions. This can be realized by embedding the scatterers deposited on a glass cover slide in microscope immersion oil. For such a glass-oil interface the elastic scattering contrast increases by up to two orders of magnitude compared to a glass-air interface [180]. Refractive indices are typically given for a specific wavelength and refractive index matching conditions can be easily realized for monochromatic excitation at this wavelength. For white light iSCAT, however, where ideal refractive index matching across a broad wavelength range is desired, it is favorable when the refractive indices of the substrate and immersion oil exhibit a similar dispersion. Otherwise the wavelength dependence of r might lead to modulations in the spectra, which might obscure the real lineshape of iSCAT signals.

3. Materials and Methods

The optical characterization of individual SWCNTs based on their PL and Raman response puts high demands on the collection and detection efficiency of the microscope components. Especially, PL studies of individual SWCNTs on substrates suffer from the overall low QY of the SWCNTs. The emitted PL wavelengths cover the NIR spectral range , a wavelength regime where silicon based detectors exhibit only small quantum efficiencies. For this purpose confocal microscopy is the method of choice, as it offers an improved signal to background ratio, compared to e.g. wide-field illumination and can be combined with high *NA* oil objectives and highly sensitive photodetector in order to improve the collection and detection efficiency of the setup.

In the following a detailed description of the confocal laser scanning microscope setup which is used for all experiments throughout this work is given. The sample preparation which yields spatially well separated individual SWCNTs is described. The general procedure of PL imaging and spectroscopy of individual SWCNTs is presented in Sec. 3.3. For the measurement of the time-resolved PL decays the TCSPC method is employed. The basic concept and its experimental realization are briefly introduced. An important aspect of this work is the evaluation of the decay constants such as decay times and amplitudes from the recorded PL transients. Therefore, the transient fitting procedure of mono- and biexponential decays is discussed in detail and possible sources of errors, which might occur especial for the transient fitting of SWCNT PL decays, are pointed out. Finally, the experimental aspects of the iSCAT spectroscopy method are elucidated, including the characterization of the white light output of the photonic crystal fibre (PCF) as well as a description of the elastic scattering imaging process and the acquisition of scattering spectra.

3.1. The Confocal Microscope Setup

The microscope used in this work is an inverted confocal microscope (Nikon TE-2000 S Eclipse). A schematic diagram of the microscope setup is depicted in Fig. 3.1. Depending on the outline of the experiment, different excitation lasers were used (compare Tab. 3.1). The standard excitation source for most of the experiments is a Ti:Sapphire oscillator (Coherent Mira 900-F), pumped by the output of a frequency doubled Nd:YAG laser at 532 nm (Coherent Verdi 10 W). The Ti:Sapphire laser can be operated either in continuous wave (CW) or in pulsed mode and its wavelength output can be tuned from 700 to 920 nm. When mode-locking it delivers pulses with a pulse duration of 150 fs at a repetition rate of 76 MHz. Alternatively, other lasers e.g. for Raman experiments, here represented by a CW HeNe laser (Thorlabs HYP020 594 nm, 2.0 mW) with an output wavelength of 594 nm can be coupled

into the microscope. An overview about all lasers used for different PL and Raman experiments throughout this work together with their main parameters is given in Tab. 3.1.

Table 3.1. Lasers used for the experiments

Laser	Company	λ_{out} (nm)	P_{out} (mW)
Ti:Sapphire	Coherent Mira 900	740–950	100–250
HeNe	Thorlabs HYP020	594	2
HeNe	Newport R-30995	633	17
DPSSL ^a	Cobolt Blues	473	350
DPSSL	Coherent Sapphire	568	50

^aDiode pumped solid state laser

Before the laser beam is guided into the microscope, it is first expanded and then collimated by a telescope (L1, L2), so that the beam diameter slightly exceeds the back aperture of the microscope objective. Neutral density filters (NLF, Thorlabs) are used to attenuate the beam to reasonable excitation power for the specific experiment. In addition a laser line filter (LLF) are placed in the excitation beam path in order to suppress wavelength components originating from the PL of the Ti:Sapph crystal. For this purpose narrow bandpass filters such as the Thorlabs FB760–10 or FB880–10 are utilized. Inside the microscope the excitation beam is reflected by a broadband 33/67 non-polarizing pellicle beamsplitter (BS1, Thorlabs BP133) into an infinity corrected high NA oil immersion objective. Two different types of oil immersion objectives were used in this work, either a Nikon Plan Fluor S 100x NA=1.3 or a Nikon CFI Plan Apo VC 60x NA=1.4 objective, depending on whether the experiments require a system that is highly corrected for chromatic abberations. The Nikon NA=1.4 objective is better corrected for chromatic abberations and is therefore used preferentially for the white light scattering experiments. The Nikon NA=1.3 objective is mainly used for the (time-resolved) PL microscopy of SWCNTs.

In order to acquire confocal scan images, the sample is raster scanned with respect to the diffraction-limited laser focus. This is achieved by using a closed-loop x,y-piezo sample stage (Physik Intstrumente P-517.2CL). The positioning of the sample stage and data acquisition is controlled by a PCI data acquisition device (National Instruments, NI PCI-6602) installed in a standard personal computer. For scan control and data visualization LabVIEW (LabVIEW, National Instruments) programs are used which were provided by Andreas Lieb and Miriam Böhmler.

The light emanating from the sample is collected by the same objective, passes the beamsplitter (BS2) and is then focused by a premounted tube lens ($l=200$ mm, Nikon, not shown) to a point outside of the microscope. In order to produce a collimated beam in the detection beam path which allows the use of interference filters a plano-concave lens (L5, $l=-50$ mm)

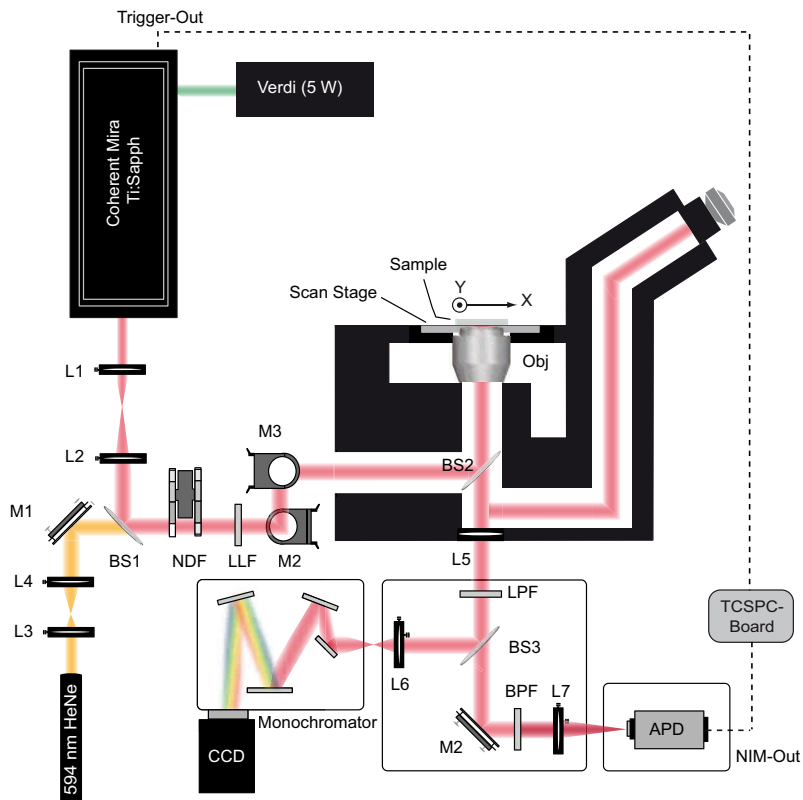


Fig. 3.1. Schematic diagram of the experimental setup, based on an inverted confocal microscope. Focusing onto the sample and light collection is done by the same objective. For the acquisition of images the sample is raster scanned with respect to position of the laser focus by a sample stage. Further, the light is guided to an avalanche photo diode (APD). Emission spectra are acquired by a combination of single grating spectrograph equipped with a thermoelectrically cooled CCD camera. In order to perform PL decay time measurements the APD is connected to a computer controlled TCSPC-board (details see Sec. 3.4).

is positioned directly outside of the exit port. Different long-pass etch filters (LPF) or notch filters are used to block the excitation wavelength. A 50:50 beamsplitter (BS2, Thorlabs EBS1) in the detection path allows for simultaneous use of an avalanche photo diode (APD) and a combination of a spectrograph and charged coupled-device camera (CCD) for the acquisition of PL scan images and spectra, respectively. Alternatively, the 50:50 beam-splitter can be replaced by a flip mirror for time-critical measurements which require higher photon counts. The light *transmitted* by BS3 is focused by the lens L7 on an APD (MPD, PDM 5CTC) with

an active sensing area diameter of $20\text{ }\mu\text{m}$. Because of the small size of the active area no additional pinhole is required to realize confocal detection. The APD is used for the acquisition of confocal scan images and to record PL transients. For this the fast NIM (Nuclear instrument module) output of the APD is connected to a TCSPC-card (Becker & Hickl SPC140) installed in a common personal computer (see also Sec. 3.4). Bandpass filters (BPF) are placed in front of the APD in order to select a spectral window of interest. Specifically for PL imaging and transient acquisition of certain SWCNT chiralities different narrow bandpass filters covering the spectral range between 830 and 1000 nm are used.

For the acquisition of spectra the light reflected by BS3 is focused by the lens L6 into a monograting spectrograph (Andor Shamrock SR-303i) equipped with an open electrode CCD camera (Andor IDUS OE DU420). The camera is Peltier-cooled to $-60\text{ }^{\circ}\text{C}$ for operating at a low dark noise level. The spectrograph features a triple grating turret with optical components arranged in the Czerny-Turner configuration. Three different gratings are available: 150 l/mm (Blaze: 800 nm), 600 l/mm (Blaze: 500 nm) and 1200 l/mm (Blaze: 1000 nm) which all provide a spectral resolution of less than one nanometer.

In order to perform e.g. PL decay time measurements of SWCNTs no additional modifications of the microscope setup are required. The key components of the TCSPC experiment are the high repetition rate (76 MHz) Ti:Sapphire oscillator, the fast single-photon APD and the TCSPC-electronics. The sync signal is provided by the internal photo-diode of the Ti:Sapphire laser which is connected via a BNC cable to the textitsync entrance of the TCSPC board, while the fast NIM output of the APD is connected to the signal entrance of the TCSPC card.

Detailed information on the specific experimental parameters, e.g. excitation power, spectra acquisition times and specific filter sets, are stated in a short paragraph at the beginning of each experimental chapter.

APD Specifications

The silicon based APD fabricate used in this work is characterized by a low dark count rate of only 200–300 Hz and a fast NIM timing output of 35 ps with a specified instrument dead time of 77 ns. The NIM timing output is a crucial component of the TCSPC experiments as it basically determines the instrument response function (IRF) for a single photon counting event and thus the maximum time resolution (see Sec. 3.4.2 for details).

The low dark noise and high NIM timing accuracy are a consequence of a relatively thin depletion region of the APD. The draw back of this small region is an overall lower quantum efficiency compared to other APD models. Fig. 3.2 plots the quantum efficiency against the detection wavelength as specified by the manufacturer. Small photon detection efficiencies of only 2–15 % are specified for the NIR spectral region between 800–1000 nm, which is just the spectral region of interest for the PL measurements of SWCNTs. In general, high detection efficiencies of the detectors are preferred as this reduces the acquisition times of e.g. PL transients and thus minimizes the probability of photo damaging the SWCNTs.

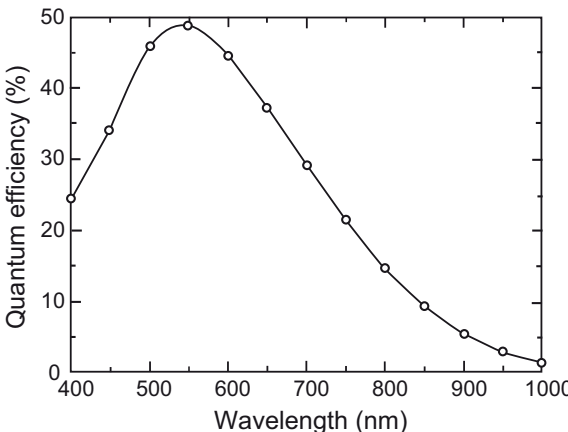


Fig. 3.2. Quantum efficiency of the silicon based APD (MPD, PDM 5CTC) for the spectral range between 400 and 1000 nm (manufacturer data). In the experimental relevant NIR spectral region between 800–1000 nm the quantum efficiency of the APD is exceptionally small with 15–2 %.

3.2. Sample Preparation

3.2.1. SWCNT Sample Material

A large fraction of the commercially available pristine SWCNT material is synthesized by chemical vapor deposition (CVD) methods. The most widely used CVD synthesis methods are the so called CoMoCAT [184] and the HiPco (high-pressure catalytic decomposition of carbon Monoxide) processes [185]. Both methods rely on carbon monoxide as a carbon feedstock gas, which is heated in a furnace to high temperatures and then decomposes under formation of SWCNTs at metallic catalyst particles.

In the HiPco process small amounts of iron pentacarbonyl are added as catalyst precursor. Iron clusters, which are the active catalysts, are formed *in situ* by decomposition of the iron pentacarbonyl. The carbon feedstock gas is here carbon monoxide. By controlling the pressure and temperature of the carbon monoxide, batches with different diameter distribution can be produced. Raman and AFM characterization of this material revealed that in general the SWNTs produced in the HiPco process are rather thin, which is reflected in broad diameter distributions centered in average at ~ 1.1 nm [185, 186]. In the CoMoCAT process bimetallic cobalt molybdenum catalyst particles are deposited on a solid silica support. The chirality selectivity is higher for the CoMoCAT process than for the HiPco process, resulting in quite narrow diameter distributions centered at diameters between $d=0.7\text{--}1.1$ nm, depending on the reaction conditions. In spectrofluorometric studies it was shown that the most prominent semiconducting chiralities in this materials are the (6,5) and (7,5) SWCNTs with

an abundance of more than 50 % of all luminescent semiconducting SWCNTs contained in the raw material [187]. The as-produced SWCNT material contains considerable amounts of residual catalyst particles (e.g. up to 35 wt% iron in the case of HiPco SWCNTs) and other carbonaceous materials. The SWCNT raw material can be "purified" by a treatment with strong inorganic acids such as e.g. nitric acid, which significantly reduces the fraction of these contaminants (~5 wt% iron for purified HiPco SWCNTs).

Aqueous Solutions of Individual Micelle Encapsulated SWCNTs

As-synthesized SWCNT material tends to form bundles due to strong intertube van-der-Walls forces. An effective way to break the bundles and to produce samples containing predominantly individual SWCNTs is to disperse the material in a solvent in the presence of a surfactant. The general procedure for this, is to disperse the raw SWCNT material in a solution of the surfactant under strong ultrasonication. In a subsequent centrifugation step residual bundles and other contaminants precipitate. The topmost volume of the supernatant solution contains mostly individual SWCNTs which then can be easily isolated with a pipet [49]. A vast variety of different nonionic, anionic and cationic surfactants as well as polymers, DNA and other biomolecules can be utilized for the preparation of such dispersions of individual SWCNTs either in aqueous or organic solvents [122, 188–193].

Table 3.2. SWCNT sample material used throughout this work

SWCNT Material	Surfactant	Comment	Literature	used in
CoMoCAT	SC and DOC	enriched in (6,5)	[194]	Chap. 4
CoMoCAT	DNA:(GT) ₁₀	enriched in (6,5)	[192]	Sec. 6.4.1
CoMoCAT	SC	length sorted	[195]	Sec. 4.4
HiPco	DOC	mild sonication	[113, 196]	Chap. 5

Typically, ionic tensides, such as sodium dodecyl sulfate (SDS) and the bile salts, sodium cholate (SC) or sodium deoxycholate (DOC), as well as biological polymers such as different kinds of single and double stranded DNA [192] are used to produce stable aqueous dispersions of SWCNTs. The aforementioned surfactants are ambiphil molecules with a one or more polar or charged functional groups and a large unpolar (less polar) molecular part. The unpolar part of the surfactant attaches to the unpolar sidewall of the SWCNT which results in the formation of stable micelles e.g. in the case of SDS or DOC. The polar endgroups of the surfactant which face away from the SWCNT surface facilitate the solubility of the SWCNTs and at the same time prevent the micelles to congregate.

In this work SC, DOC as well as short single-stranded DNA segments: GT₁₀ were used as surfactant materials. Two different SWCNT raw materials were used: CoMoCAT or HiPco SWCNTs. Aqueous solutions of individual surfactant encapsulated SWCNTs were provided by collaboration partners. A survey of the different SWCNT sample materials together with

the reference where the sample preparation is described in details is given in Tab. 3.2. Aqueous solutions of SC encapsulated CoMoCAT SWCNTs were provided by Prof. M. C. Hersam (Northwestern University, Illinois). A diameter discriminating density-gradient ultracentrifugation technique [194, 197] was used in order to prepare dispersions highly enriched with the (6,5) chirality. In addition to the main chirality the samples still contain considerable amounts of other small diameter semiconducting SWCNT chiralities, such as the (5,4), (6,4), (9,1) and (8,3).

3.2.2. Sample Preparation for Confocal PL Measurements

Samples were prepared on standard glass cover slides with a size of $24 \times 24 \text{ mm}^2$, a thickness of 0.13–0.16 mm and a refractive index of 1.52 (Marienfeld-Superior, Marienfeld GmbH). Prior to sample deposition the cover slides were cleaned by rinsing several times with tridistilled water and successively with methanol (Uvasol, VWR). A small volume (25–30 μl) of a diluted dispersion of micelle encapsulated SWCNTs (compare Tab. 3.2) is then dropped on a cleaned glass cover slide. After 2–5 minutes, the solution was removed by spin coating for 30 s with a rotation frequency of 2500 min^{-1} .

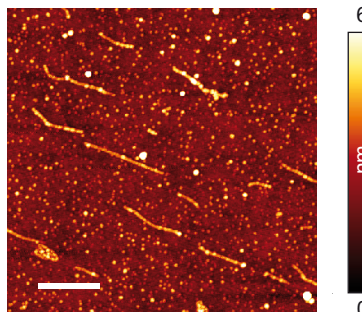


Fig. 3.3. AFM topography image of micelle encapsulated CoMoCAT SWCNTs enriched in (6,5) the chirality deposited on glass. The SWCNT coverage is less than one nanotube per square micrometer, which is a reasonable density for following confocal PL imaging. Due to the surfactant wrapping of the SWCNTs the average diameter of the SWNTs is about 2 nm, substantially larger as the average diameter of the CoMoCAT raw material of ~0.7–1.1 nm. Furthermore, the sample is covered by additional dot like features which are presumably small surfactant crystallites. The scalebar is $1 \mu\text{m}$.

The concentration of the SWCNT dispersions was adjusted such that the coverage of SWCNTs in the PL images was less than one nanotube per square micrometer. A tapping-mode AFM topography image of such a sample is shown in Fig. 3.3. The SWCNTs appear as elongated

topography features. They are spatially well separated so that individual SWCNTs can be distinguished also with optical microscopy. The average surface coverage with SWCNTs of this sample is about $0.6/\mu\text{m}^2$ which is also in good agreement with the SWCNT coverage determined in the corresponding PL images. This indicates that the (6,5) enriched SWCNT dispersion indeed contains mostly semiconducting SWNTs which emit in the detectable spectral range. The average diameter of the SWCNTs is about $\sim 2\text{ nm}$ and thus slightly larger than the average diameter of $\sim 0.7\text{--}1.1\text{ nm}$ of the raw CoMoCAT material. This increased diameter is due to the additional surfactant wrapping of the SWCNTs. The average length of the SWCNTs of this material is 545 nm. In the AFM image additional dot like features with similar heights as the SWCNTs can be observed. These are presumably residual small surfactant crystallites. Further, the spin coating procedure leads to the parallel alignment of the SWCNTs.

The photo-stability of SWCNTs can be significantly improved, if the samples is covered by a droplet of immersion oil and sandwiched between a second glass cover slide. This minimizes the probability of oxygen induced photo-reactions [126], which is a crucial factor for the PL decay time measurements, where the SWCNTs are exposed to pulsed laser irradiation for several minutes.

3.2.3. HiPCO SWCNTs Dispersed in Agarose Gel

The suspensions of DOC encapsulated HiPco SWCNTs were provided by Prof. B. Lounis (University of Bordeaux). Characteristic for these HiPco samples is the large fraction of long ($\gtrsim 2\mu\text{m}$) and brightly luminescent SWCNTs. This was achieved by carefully dispersing the SWCNTs using only very brief tip ultrasonication of $\sim 5\text{ s}$. Samples of individual HiPco SWCNTs on glass for standard confocal PL measurements were obtained as described in the previous section.

Samples of individual SWCNTs embedded in a matrix of agarose gel were prepared as follows: A 4 % solution of low melting agarose is prepared using a 1 % solution of DOC as solvent. The agarose solution is heated to 60°C until all gel was liquified, indicated by the transparent color of the liquid. The gel was then mixed vigorously with an even volume of the HiPco suspension. Then a small droplet ($10\ \mu\text{l}$) of this mixture is sandwiched between two cleaned glass cover slides. After the sample has cooled down to room temperature, the edges of the sandwich were sealed with vacuum grease in order to prevent the evaporation of water and thus prevent a structural rearrangements of the agarose gel. However, even with this precautions the sample quality significantly decreases within 1–2 days of storage. After this period of time large agglomerations of SWCNTs can be observed in the PL images and the fraction of individual SWCNTs is strongly reduced. Therefore, fresh samples were prepared at each measurement day.

3.2.4. Sample Preparation for iSCAT Measurements

In order to observe a decent iSCAT signal of individual SWCNTs it is crucial to reduce the amount backreflected light from the glass substrate. This can be achieved by establishing index matching conditions by covering the glass cover slide with immersion oil. First, a standard SWCNT sample was prepared according to the description in Sec. 3.2.2. The glass cover slide was then glued to the sample holder and an sample area with a suitable coverage of SWCNTs was searched by PL imaging. Following this, a small screw washer was carefully glued onto the glass cover slide enclosing the area. The washer was then filled with some droplets of immersion oil matching the refractive index n of the glass (e.g. Nikon Type A, $n=1.518$). Control reflectance spectra acquired for this kind of sample configuration do not exhibit fluctuations caused by multiple reflections and local changes of the oil film as it can be observed for samples simply covered by a thin film of immersion oil.

Gold Nanoparticles Deposited on Glass Substrates

Samples of individual gold nanoparticles (GNPs) on glass substrates were obtained by spin-coating (1 min at 1500 min^{-1}) $30\text{ }\mu\text{l}$ of a diluted solution of gold spheres with diameters of either $d=20\text{ nm}$ or $d=60\text{ nm}$ (British Biocell International, England) on a cleaned glass cover slide. The concentration of the solution was adjusted to yield a particle density of $\sim 1\text{ GNP}/\mu\text{m}$ in the white light scattering images. According to the procedure described in the previous section the sample was embedded in immersion oil.

3.3. Confocal PL Imaging and Spectroscopy of Individual SWCNTs

In the following, the general procedures for the acquisition of confocal PL scan images and spectra of individual SWCNTs is outlined and some representative PL data is presented. The measurement protocol introduced here is basically used for all confocal experiments conducted throughout this work.

In a first step individual SWCNTs are localized and identified by confocal PL imaging. Typically, the Ti:Sapphire oscillator is operated in pulsed mode is used as an excitation source tuned to an output wavelength of 760 nm , which matches a phonon-assisted transition of the (6,4) SWCNT. Low excitation densities of $\sim 35 \cdot 10^{12}\text{ photons pulse}^{-1}\text{ cm}^{-2}$ on the sample and small pixel integration times of $30\text{--}50\text{ ms}$ are used to prevent photo damaging and PL bleaching of the SWCNTs. In order to acquire PL images of a specific SWCNT chirality, narrow bandpass filters are placed in front of the APD, e.g. centered at $1000 \pm 10\text{ nm}$ (Thorlabs FB1000–10) or $880 \pm 20\text{ nm}$ (Thorlabs FB880–40), matching the center emission wavelengths of (6,5) and (6,4) SWCNTs, respectively. In Tab. 3.3 the different bandpass filters used for the PL detection of the various SWCNT chiralities are summarized.

In Fig. 3.4(a) a representative confocal PL scan image of a $20 \times 20\text{ }\mu\text{m}^2$ area of a sample containing well separated SC encapsulated CoMoCAT SWCNTs on glass is shown. The

Table 3.3. Band pass filters for PL imaging of specific SWCNT chiralities (n,m)

SWCNT (n,m)	Company	λ_{center} (nm)	FWHM (nm)
(5,4)	Chroma	834	6
(6,4)	Thorlabs	880	40
(9,1)	Thorlabs	930	10
(8,3)	Thorlabs	950	10
(6,5)	Thorlabs	1000	10
(6,5)	Chroma	980	20

image was acquired using a 800 nm and a 810 nm longpass edge filters in front of the APD. Therefore, each of the bright spots in the false-color image represents the integrated PL intensity over a spectral range of 800–1010 nm. The maximum detectable PL wavelength is determined by the low quantum efficiency of the silicon based APD for the NIR spectral region (compare Fig. 3.2).

Most of the SWCNTs are imaged as spot-like or slightly elongated features, which indicates that the SWCNT length is smaller or only slightly larger than the confocal excitation spot size. This observation is consistent with the average SWCNT length of 545 nm determined by AFM measurements of the same sample material. The optical resolution of the confocal microscope can be estimated by determining the cross sectional width of the intensity profiles of the smallest PL features. Such an intensity profile taken across the short axis of an elongated PL feature is shown in Fig. 3.4 (c). The FWHM of the intensity profile is close to the theoretically limit of $\Delta x \approx 0.61 \lambda / NA \approx 330$ nm. In several cases also large, bright clusters of SWCNTs are observed with diameters up to several micrometers. Because of the spin-coating procedure for material deposition, for such kinds of samples it is often observed that for a large fraction of the SWCNTs are aligned parallel. This can be observed for elongated features in the PL scan images as well as in corresponding AFM images. As for sample excitation a linear polarized laser is used, the PL response of the sample can be optimized by finding a good sample orientation with respect to the (linear) polarization of the incident light.

After a PL image is recorded, PL transients and/or spectra of the sample are acquired by selectively addressing the PL features of interest. For the acquisition of PL spectra a 150 lines/mm (Blaze: 800 nm) is used, as it offers the highest reflectivity of all gratings available and still provides sufficient spectral resolution. Representative PL spectra of the five semiconducting SWCNT chiralities which emit in the detectable spectral range of the APD are shown in Fig. 3.4 (b). The PL linewidth of individual micelle wrapped SWCNTs, such as SC or DOC, at room temperature on glass substrates are in the range of 17–40 nm, whereas the linewidths of individual DNA wrapped SWCNTs are systematically broader with 30–50 meV [198, 199].

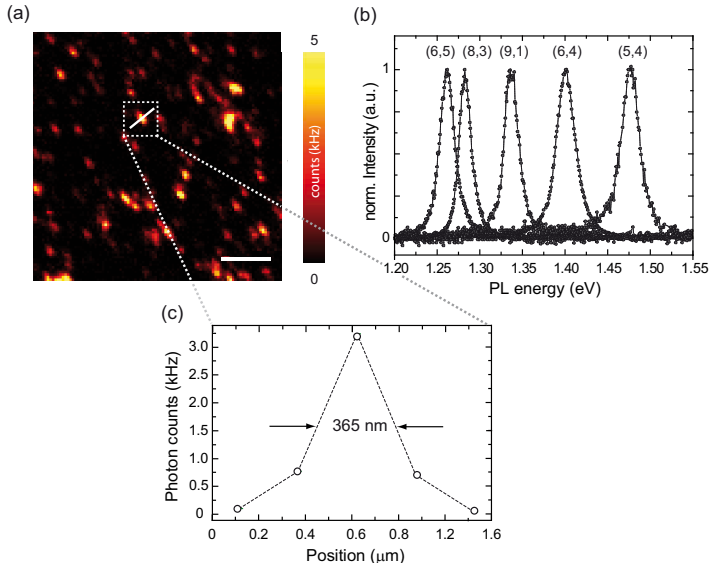


Fig. 3.4. (a) Representative confocal scan PL image of SC encapsulated CoMoCAT SWCNTs deposited on glass. Excitation light at 760 nm was provided by a high repetition rate tunable Ti:Sapphire oscillator operated in mode-locked mode. Typical photon fluences on the sample were $35 \cdot 10^{12}$ photons pulse $^{-1}$ cm $^{-2}$. By using a longpass edge filter at 800 nm, PL emission in the range of 800–1010 nm can be detected, where the maximum detectable wavelength is limited by the detection sensitivity of the silicon based detectors (APD or CCD camera). The SWCNTs appear as spot-like or slightly elongated PL features. (b) Representative PL spectra of all small diameter photoluminescent SWCNT chiralities, which emit in the detectable wavelength range. (c) Intensity profile across the narrow PL feature marked in (a). Based on the FWHM of this profile the optical resolution in the PL experiments is ~370–400 nm.

The chirality assignment is based on the comparison with the PL wavelengths (energies) determined in PLE experiments for SDS encapsulated SWCNT material in refs. [50, 200]. It is to note that due to the dependency of the PL energy on the local dielectric environment associated with a specific surfactant, the PL energies of the SDS wrapped SWCNT chiralities in the reference are systematically shifted to higher values (smaller wavelength) compared to the energies of the corresponding chiralities of DOC and SC encapsulated SWNTs. Furthermore, large tube-to-tube variations of the PL energies lead to broad distributions of PL energies for each chirality, which overlap to some extent. In general the observed PL energies of the different SWCNT chiralities are energetically well separated and in most cases an unambiguous chirality assignment is possible. However, if the observed PL energy falls in the energy range where the PL energy distributions of two chiralities overlap an unambiguous chirality assignment of PL bands cannot be accomplished by solely relying on one optical transition energy. Here, complementary information about the vibronic or electronic structure are required, such as e.g. the Raman RBM frequency the energy of the second E_{22} optical transition. For ensemble measurements, the E_{22} can be easily determined with PLE experiments, on the individual SWNT level, however, such measurements are difficult and require high photostability of the SWCNT.

3.4. Time Correlated Single Photon Counting

Time Correlated Single Photon Counting (TCSPC) is a time-domain based detection technique which can be used to measure the time-dependent intensity decay of a luminescent process. The method is based on the detection of single photons it is well suited for recording low-level light signals with picosecond resolution and extremely high precision.

The basic principle of the TCSPC method is to detect a fluorescence photon within a single excitation period and to measure precisely the time delay between the detection of the photon and a reference event. In practice the molecule is excited by a short laser pulse e.g. by a high repetition rate laser. Ideally each laser pulse leads the excitation of the molecule. As both the emission and the detection of a photon are statistical processes the detector signal is a train of pulses randomly distributed along the time axis.

The basic principle of the TCSPC method is schematically illustrated in Fig. 3.5. When a photon is detected the arrival time of the corresponding detector pulse is measured. Each detection event associated with a certain arrival time of the photon is collected and stored in a separate memory channel. After N signal periods a large number of photons are detected and a distribution of photon arrival times builds up. From the corresponding histogram of arrival times the original waveform of the PL decay can be determined [201].

One of the instrumental challenges of the TCSPC technique is to measure the arrival time of the emitted photon precisely and reproducible. The basic principle of the time measurement is schematically illustrated in Fig. 3.5 (b). Upon detection of a PL photon by the detector, e.g. an APD, a start pulse is generated and is send to the TCSPC electronics. If the start pulse exceeds

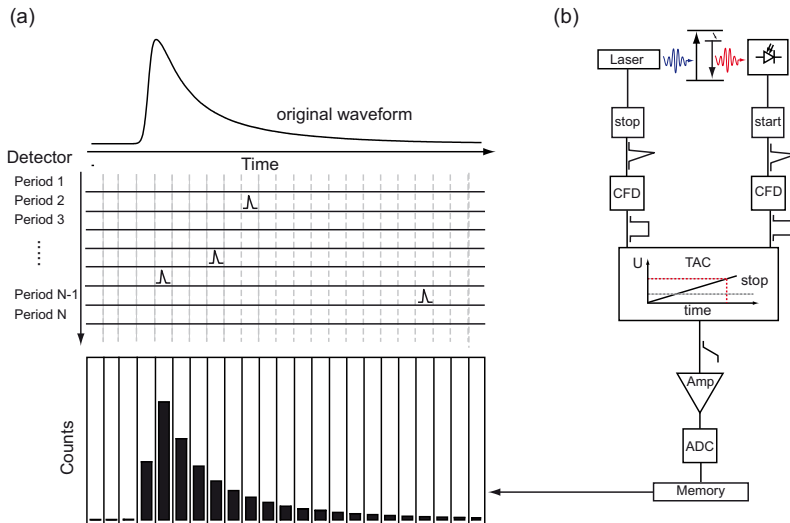


Fig. 3.5. (a) Schematic representation of the TCSPC method. The TCSPC method relies on the precise measurement of the time between the detection of a photon and a reference event. Typically the time reference are the electronic signals generated by laser pulses of the excitation source. For the detection of the emitted photons fast photo detector with single photon sensitivity are required. The arrival time of the photons are measured. The emission and detection of a photon are statistical processes and in consequence the measured times distribute along the time axis. Each measured time is allocated to a certain time channel, which in the end leads to a histogram of arrival times, which resembles the real waveform of the fluorescence intensity decay. (b) Schematic representation of the TCSPC reversed start-stop mode. The relevant electronic components required for the precise time measurement are depicted. Details are given in the main text, modified from [201].

the preset threshold level set for the CFD, the CFD triggers an Time to Amplitude Converter (TAC). This is basically a capacitor which builds up a ramp voltage until the stop pulse of the "sync" arrives. Thus the TAC generates an output voltage which depends linearly on the arrival time of the photon. The CFD eliminate the timing jitter which might be caused if the TAC is started/stopped when the amplitude of the start/stop pulse reaches a fixed threshold level and not a constant fraction of the pulse amplitude. In consequence such fluctuations of the pulse amplitudes would directly translate in erroneous photon arrival times.

The voltage output of the TAC is amplified, converted by an Analog to Digital (ADC) converter and then stored in a specific address of a memory. Each memory address corresponds to a time-channel (12 bit). The time bin per channel is defined by the time range of the TAC and the ADC sampling rate. Subsequent events are then stored in the memory by incrementing the data content of the memory location which corresponds to the memory address proportional to the detection time [201, 202].

The TCSPC electronics which uses the sync-pulses generated by high repetition laser systems typically operate in the so called reversed start-stop mode. In this mode, the time measurement is initialized by the detector upon detection of a photon and stopped by the sync-pulse of the following excitation period. The advantage of this operation mode compared to the normal start-stop mode is that the TAC of the TCSPC electronics has not to work with the high repetition rates of the excitation laser.

The basic requirement of the TCSPC method is that only one photon per excitation cycle is detected. This is easily fulfilled e.g. for the fluorescence of single dye molecules excited at low powers and of course also for the PL of SWCNTs. Experimental difficulties might arise, if more than one photon per excitation cycle is emitted. In this case the so called "pile-up" effect, might occur, which basically results in a deviation of the photon arrival histogram (transient) from the real intensity decay curve. The effect is due to the dead-time of the detector and the TCSPC electronics, which for APDs is on the order of several tens to hundreds of picoseconds. During this time after detection of a photon the electronics cannot process an additional detection event. The probability to detect the first photon of a photon train is the highest and in consequence photons at later arrival times would be underrepresented in the transients.

3.4.1. Acquisition of PL Transients of Individual SWCNTs

After localizing individual SWCNTs by PL imaging, the next step is to measure the time-resolved exciton decay of the SWCNTs. For the decay time measurements low excitation densities between $1.7\text{--}10 \cdot 10^{12} \text{ cm}^{-2} \text{ pulse}^{-1}$ are used to minimize sample heating effects and also PL bleaching. The TCSPC experiment is stopped when the number of detected photons in the $t = 0$ time channel reaches 1500–2000 counts. For a typical PL decay this corresponds to a total number of detected photons of $\sim 10^5$ and ensures a reasonable SNR. Even higher counts would be desirable as they improve the SNR of the transients, which in turn improves the quality of the transient fitting. However, increasing the collection time or excitation powers might cause irreversible photobleaching, hence a compromise between collection time and SNR has to be found. For typical APD count rates of 200–1500 Hz, the transient

acquisition times are in the range of 3–1 min. The 50/50 beamsplitter (BS3) in the detection path allows the simultaneous acquisition of PL transients and PL spectra. In this study only such transients were considered for data analysis, for which the corresponding PL spectra exhibits a single Lorentzian PL band.

3.4.2. Transient Fitting: General Aspects

For the transient fitting the program package "Fluofit" (Picoquant, Berlin) was used. It provides various fit options, such as tail-fitting and deconvolution, and is based on the maximum likelihood approach. The goodness of the fit can be controlled based on the weighted residuals and the corresponding χ^2 value, which both are displayed by the fitting program. In order to retrieve the decay constants from the recorded transients, a test function is constructed, which then is fitted to the experimental data. The test function I_{test} is a convolution of a model function F_{mod} and the IRF [203] according to:

$$I_{test}(t) = \int_{-\infty}^t IRF(t') F(t - t')_{mod} dt'. \quad (3.1)$$

The correct choice of the model function is dictated by the kinetics expected for the PL decay and consequently by the underlying kinetic model. In general, the model function F_{model} is a weighted sum of e.g. exponential or Gaussian functions. e.g for the case of exponential decays:

$$F_{mod}(t) = \sum_{i=1}^n C_i \exp(-t/\tau_i). \quad (3.2)$$

In order to obtain physical meaningful fit results, the number i of individual functions used to generate the model function should be kept as small as necessary to describe the PL decay. The transient fitting yields the decay constants such as the amplitude C_i and decay times τ_i . The decay constants obtained by the fitting for multi-exponential PL decays are displayed as fractional amplitudes A_i (intensity weighted amplitudes):

$$A_i = \frac{\tau_i C_i}{\sum_{j=1}^n \tau_j C_j}. \quad (3.3)$$

A_i basically corresponds to the number of photons which the i th decay component contributes to the steady state PL spectrum.

It can be shown that the smallest decay times which can be retrieved by deconvolution are approximately on the order of one tenth of the FWHM of the IRF [204]. In general, the IRF

of an TCSPC setup consists of several individual components. These components are related to the excitation, the propagation and therefore the optical path length and optical elements therein and finally the detector response. Assuming a delta-like excitation, which is justified for the femtosecond pulse excitation in the experiments, the timing characteristics of the APD is the most important aspect. The maximum time resolution in TCSPC experiments, which can be achieved by deconvolution of transients with the IRF, depends on the timing stability, the SNR of the data and the width of the IRF.

The IRFs which are required for the fitting procedure were recorded by detecting the reflected laser light from a bare cover slide. The laser power is attenuated by neutral density filters to APD count rates less than 10 kHz. All bandpass or longpass filters were removed from the detection beam path of the microscope and the same settings for the TCSPC electronics were used as for the acquisition of PL transients.

A typical IRF recorded for an excitation wavelength of 1000 nm is shown in Fig. 3.6 (a) (red curve) together with two PL transients. For the APD used in this work IRFs acquired for excitation wavelengths in the NIR spectral region exhibit a FWHM between 27–29 ps. Based on this width a time resolution for the TCSPC experiments of 3 ps can be estimated, which simultaneously corresponds to the experimental error of each fitted PL decay time. As can be seen in Fig. 3.6 (a), PL transients differing in their decay times by 2–3 ps can still be distinguished by visual comparison based on their shape.

The shape and width of the IRF depend critically on the excitation wavelength at which the IRF is acquired. This is illustrated in Fig. 3.6 (b). Here, four IRFs are plotted, which were acquired at different excitation wavelength: 530, 570, 800 and 1000 nm. For the APD fabricate used in this work, the IRF consists of a fast decaying component with a typical FWHM of 27–30 ps and a slow component persisting for several hundreds of picoseconds. The latter is the so called "diffusion tail" and originates from the detection of charge carriers generated in the neutral region of the APD and thus are not affected by the avalanche process. These charge carriers reach the cathode contact by diffusion. The amplitudes and slopes of the diffusion tails for different wavelength differ clearly. The diffusion tail becomes more pronounced for higher wavelength due to the higher penetration depth of NIR light into the silicon material. In addition minor differences in the width of the main peak can be observed [202]. Using an IRF for data fitting not recorded at a wavelength similar to the PL emission wavelength will lead to erroneous fit results for the decay times and also the decay dynamics (see Fig. 3.6).

3.4.3. Transient Fitting: Mono- and Biexponential PL Decays of SWCNTs

In this section the transient fitting procedures for the examples of mono- and biexponential PL decays of individual SWCNTs are illustrated. In the case of SWNTs it is difficult to distinguish between mono- and biexponential PL decays, especially if one of the contributing decay components exhibits a small amplitude and the SNR of the specific section of the

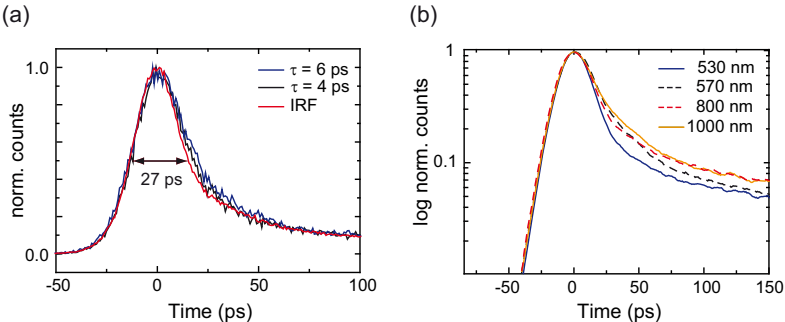


Fig. 3.6. (a) Time resolution of the TCSPC measurements. The time resolution which can be achieved by deconvolution is approximately equal to 1/10 of the FWHM of the IRF [204]. The typical IRFs used for all the transient fitting throughout this work have FWHM in the range of 27–29 ps, resulting in an uncertainty of the decay times of $\pm 3 \text{ ps}$. Differences of 2–3 ps in the decay times are already visible in the transients. (b) Wavelength dependence of the IRF. The four IRFs were recorded using femtosecond pulsed laser excitation at 530, 570, 800 and 1000 nm. The slow decaying tail at longer times (“diffusion tail”) originates from the different penetration depths of the light and in consequence the detection of charge carriers generated in the neutral region of the APD. This diffusion tail is distinct different for IRFs acquired with excitation light in the visible and NIR spectral region.

transient is small. Further complications might arise from uncertainties in determining the IRF or by spurious signal contributions in the IRF and transients caused by misaligned optical components, e.g. interference filters and lenses.

On the basis of the weighted residuals and the reduced chi-squared χ^2_{red} parameter it is possible to evaluate the goodness of a fit. The choice of the right physical model to describe the kinetics, e.g. a mono- or biexponential PL decay, is naturally important for the outcome of the fit. However, it is to note that using multi-exponential fits usually result in a decrease of the χ^2_{red} parameter. Simply validating the PL decay dynamics based on the argument of a decreasing χ^2_{red} when using a bi- or multiexponential model function might obscure the true nature of a PL decay. As a general guideline throughout this work, only such PL decays were counted as biexponential, if the corresponding χ^2_{red} value improves, by more than 0.4 % compared to the monoexponential one. For such a relative change of χ^2_{red} an improvement of the fit is still observable in the weighted residuals plot.

Fig. 3.7 (a) shows a representative PL transient (grey line) of a CoMoCAT SWCNT deposited on a glass cover slide. A single-exponential function (red curve) convoluted with the IRF (black curve) describes the transient over four orders of magnitude, clearly showing monoexponential decay dynamics with a PL decay time of $\tau = 15 \pm 3 \text{ ps}$. It is to note that for the PL decay time measurements of SWCNTs the IRF was acquired for laser light with a

wavelength of 1000 nm. and has a FWHM of 27 ps. To ensure optimum performance, the IRF is repeatedly recorded between TCSPC measurements. Due to the high SNR achieved in the experiments and the reproducibility of the IRF the time resolution of the setup is about 3 ps, close to 10 % of the FWHM of the IRF [204].

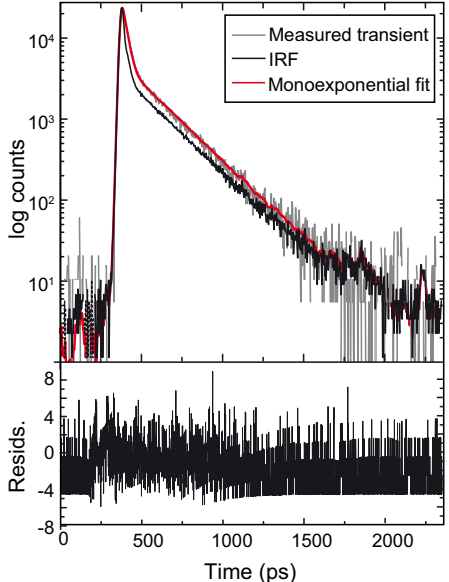


Fig. 3.7 Semilogarithmic plot of a representative transient of the PL decay of a (6,4) Co-MoCAT SWCNT (grey line) together with the independently recorded instrument response function (black line). A single exponential fit function (red line) convoluted with the IRF describes the transient over four orders of magnitude, clearly revealing the monoexponential decay dynamics with a lifetime $\tau=15\pm3$ ps. The goodness of the fit can be monitored from the weighted residuals (lower panel).

A representative example of a biexponential PL decay and the results of transient fitting such transients with mono- and biexponential model functions are shown in Fig. 3.8. The PL decay transient of a (6,5) HiPCO SWCNT is the grey curve, whereas the solid black and red curves are mono- and biexponential fits to the transient, respectively. Compared to the monoexponential PL decays, this transient exhibits a second slow decaying component at longer times (>0.75 ns). The presence of this component can be observed by visually comparing the different fit functions, which lead to the deviation of both fitting curves at longer times. The difference between both fits becomes even more apparent from their corresponding weighted residuals in Fig. 3.8 (b) and (c). In the case of the monoexponential fit (red) the weighted residuals clearly deviate from the zero line, while similar deviations are absent for the residuals of the biexponential fit (black). Correspondingly, the χ^2 decreases by about 13 % when using the biexponential model function, which allows to describe the PL decay dynamics of the SWCNT as biexponential.

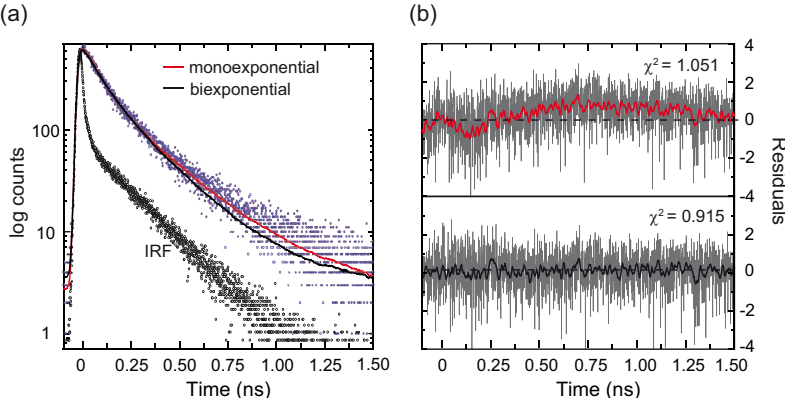


Fig. 3.8. (a) Representative PL transient (grey) of a (6,5) HiPco SWCNT embedded in agarose gel. The IRF is plotted for comparison (black). The solid black and red curves are mono and biexponential fits to the data. A monoexponential fit yields a decay time of 75 ps, while the bi-exponential fit results in $\tau_{\text{short}} = 68 \text{ ps}$, $\tau_{\text{long}} = 464 \text{ ps}$ and a fractional amplitude of $A_{\text{long}} = 7.4\%$. (b) and (c) display the corresponding weighted residuals. An improved χ^2 value is obtained for the biexponential fit.

3.4.4. Transient Fitting: Wavelength Dependence of the IRF

As indicated in Eqn. 3.1 the IRF is an incremental part of the TCSPC experiment. As the recorded transients are basically a convolution of the IRF and the real PL decay, the characteristics of the IRF critically influence the outcome of the fits, eventually leading to erroneous results for both the decay times and also for the decay dynamics. Thus, in order to obtain meaningful fit results, the reproducibility of the IRF in terms of absence of any time shifter or changes in its shape is required, especially when fitting transients of PL decays which are faster than the IRF.

The previously discussed wavelength dependence of the IRF (compare Sec. 3.4.2) might severely affect the results of the transient fitting. This needs to be especially considered for the data analysis of SWCNT PL decays. In typical PL experiments the SWCNTs are excited resonantly wavelength corresponding to the E_{22} optical transitions, e.g. at 500–600 nm for small diameter SWCNTs $d < 0.8 \text{ nm}$, while their NIR PL is detected at 800–1000 nm. Thus, there is a large wavelength difference between excitation and detection. Using now an IRF recorded at the excitation wavelength instead of the PL emission wavelength for fitting, the PL fitting yields erroneous results for both the decay times and decay dynamics.

In Fig. 3.9 (a) a representative PL transient of an individual CoMoCAT (6,5) SWCNT encapsulated in SC is shown. The transient (black) was recorded utilizing an APD and spectrally selecting the PL emission with a narrow bandpass filter centered at 980 nm. The corresponding IRF (red) was recorded by detecting the backreflected excitation light from

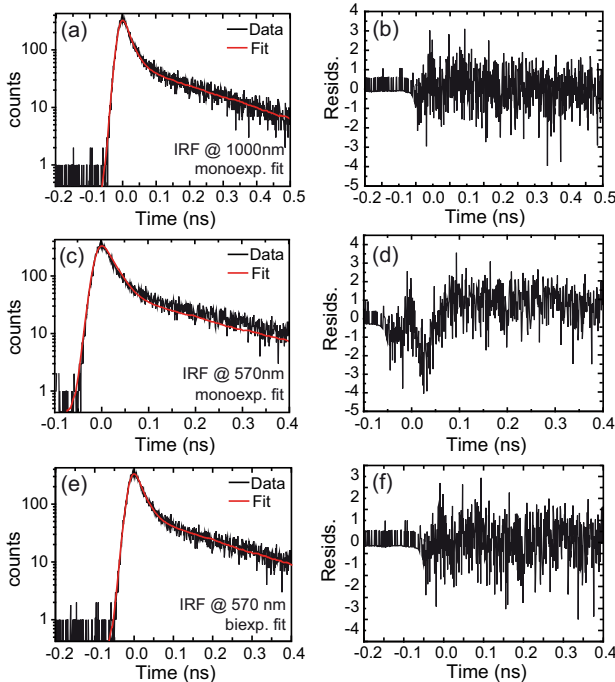


Fig. 3.9. Influence of IRFs acquired at different wavelengths on the outcome of the PL transient fitting. The PL transient was acquired for sodium cholate (SC) encapsulated (6,5) Co-MoCAT SWCNT, which emits at 980 nm. If the wavelength, which was used for recording the IRF and the PL emission wavelength differ by more than 150 nm, an additional decay component is required in order to obtain a good fit. (a-b) Monoexponential fit with an IRF recorded at 1000 nm with corresponding weighted residuals. (c-d) Monoexponential fit with an IRF recorded at 570 nm. In this case, a single exponential model function does not describe the PL decay. (e-f) Biexponential fit with an IRF recorded at 570 nm. A biexponential model function describes the PL decay well.

a bare glass cover slide. The excitation wavelength was 1000 nm selected with a bandpass filter from the white light output of a PCF. The PL decay dynamics can be well described by a single exponential, which is further confirmed by the plot of the weighted residuals in Fig. 3.9 (b). The fit yields a decay time $\tau = 10 \text{ ps}$.

The transient shown Fig. 3.9 (c) is identical as in (a), but in this case an IRF recorded at 570 nm is used for fitting (red curve). A single exponential function does not yield a good fit, as there are now significant deviations between IRF and data arise in the time range related to the diffusion tail of the IRF. This becomes obvious from the fit curve as well as for the corresponding residuals (d). The fit yields a decay time which is slightly larger ($\tau = 14 \text{ ps}$) compared to the fit with the IRF recorded at 1000 nm excitation. However, a decent fit can be obtained when changing the model function to a biexponential function (Fig. 3.9 (e),(f)), which yields the decay constants: $\tau_{short} = 9 \text{ ps}$ and $\tau_{long} = 125 \text{ ps}$ with the fractional amplitudes $A_{short} = 84\%$ and $A_{long} = 16\%$ respectively. It was found that the effect of a "wrong" IRF on the fit results becomes negligible small if the differences between the excitation and detection wavelength is smaller approximately 200 nm e.g. 800 nm (excitation) and 1000 nm (detection). The decay times obtained by fitting with such IRFs differ by only 2–3 ps, which is on the order of the experimental error.

Another factor which might influence the shape of the IRF are so called afterpulse events which leads to time-shifted copies of the IRF with smaller intensities. These afterpulse events are caused e.g. when light is reflected multiple times by the dielectric layers of interference filters, which are commonly used in the collimated beam path of the detection arm of the microscope. Also close stacking of interference filters should be avoided, as this might lead to pulse distortions. Detection of a signal with an APD, where more than one photon is detected per excitation cycle, which might happen at high count rates could lead to variations of the IRF shape, due to very high APD counts required to compensate too small CFD rates.

3.5. Interference Scattering Microscopy

The general arrangement of the common-path interference scattering method in back reflection mode was already introduced in Sec. 2.2. There the focus lied on the simple description of the contrast formation process. Experimentally, the iSCAT method can be easily realized with the inverted confocal laser scanning microscope setup, which is depicted in Fig. 3.1. Scattering experiments with a monochromatic excitation source using the tuneable Ti:Sapphire oscillator can be easily performed without changing the excitation or detection beam path of the setup.

In order to perform white light scattering experiments, an additional excitation beam path is necessary. The supercontinuum white light for the elastic scattering experiments is generated in a photonic crystal fiber (Femtowhite 800 NKT Photonics). The PCF and the additional optical elements are placed in the beam path between the Ti:Sapphire oscillator and the microscope. For the coupling of the pump laser and the optical components, which are placed into

the beam path, are schematically depicted in Fig. 3.10. The pulsed output of the Ti:Sapphire oscillator (Coherent Mira 900-F) is first expanded by a concave lens ($L_1, f=-50$ mm) in order to fill the back aperture of a low NA air objective (Leica Achromat $NA=0.66 \times 40$). The objective is used to couple the pump light into the fibre by focusing through the front facet of the PCF directly into the fibre core. While the objective is fixed in its position the PCF is mounted on a three axis translation stage which allows to optimize to move the fibre with respect of the focus and thus to realize different coupling conditions. The white light output of the PCF is strongly divergent and is therefore first collimated by the lens L_2 . Additionally, the diameter of the white light beam is expanded by a telescope (L_3 and L_4) and a pinhole in the focus of L_3/L_4 is used for spatial filtering in order to obtain a Gaussian beam profile. The white light is then guided to the microscope by an additional mirror and is focused by a high $NA=1.4$ oil immersion objective (Nikon CFI Plan Apo VC 60x) which is highly corrected for chromatic aberrations onto the sample. Moreover, all lenses in the excitation path (L_2, L_3 and L_4) and detection path of the microscope are achromatic doublets.

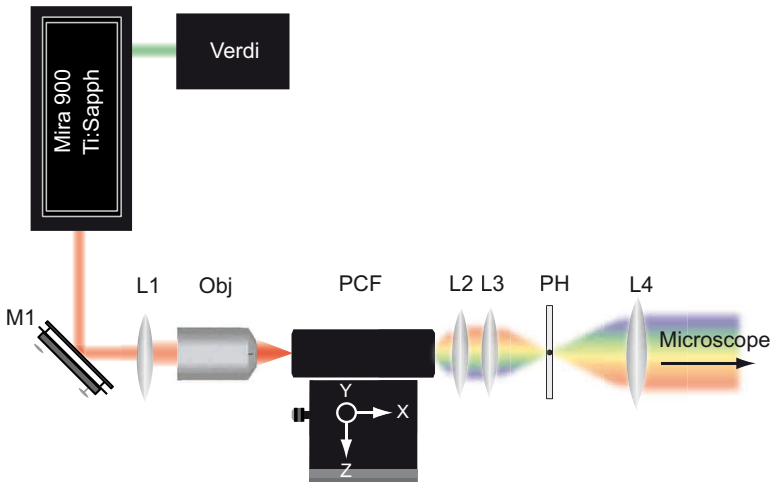


Fig. 3.10. Excitation beam path for white light scattering experiments. The output of a Ti:Sapphire oscillator is coupled into a photonic crystal fiber (PCF) by focusing with an low NA air objective (Obj). Before entering the objective the beam is expanded by a concave lens to fill the backaperture of the objective. The PCF is mounted on a three axis translation stage to move it with respect to the focus of the objective. The white light beam is strongly divergent and is therefore collimated by lens L_2 . In order to adjust the beam diameter, the collimated white light guided into a telescope (L_3, L_4). A pinhole in the foci of L_3 and L_4 is used for spatially filtering of the white light beam in order to generate an ideal Gaussian mode.

The general layout of the detection beam path for the iSCAT experiments corresponds to the one depicted in Fig. 3.1. The only difference here, is that all longpass or bandpass filters are removed. Accordingly, the APD is used for acquisition of elastic scattering images of the

sample, while spectral information on the scattering response are obtained by the combination of spectrograph and CCD camera (compare also Sec. 3.1). In order to prevent saturation or eventually damaging of the photo+detectors, additional neutral density filters are placed in front of those to attenuate the scattered light to reasonable power levels.

3.5.1. Characterization of the PCF White Light Output

The white light generation in the PCF is based on a variety of different non-linear optical effects such as self-phase modulation, stimulated Raman scattering, phase matching and soliton generation [205–207]. These processes require high power, femtosecond laser pulses for activation. The spectral composition of the white light depends critically on different parameters, such as the pump wavelength, the coupled power, pulsedwidth, the polarization of the pump light [208]. The PCF is polarization maintaining throughout the whole spectrum range and the zero dispersion wavelength is at 750 nm.

The ideal pump conditions for the white light generation which result in a broad white light spectrum which covers the desired spectral range of interest between 500–1000 nm are a pump-wavelength of 800 nm and a coupling power of 250 mW. It is to note, that the maximal usable wavelength range of the white light output is determined by the detection efficiency of the silicon based CCD camera. A representative white light spectrum for this standard pump settings after passing through the optical elements of the excitation and detection beam path and detection by the spectrograph/CCD camera combination is shown in Fig. 3.11 (a). In the excitation beam path the white light is first transmitted and then reflected by pellicle beam-splitters (BS1 and BS2) and is further reflected at an oil covered glass cover slide.

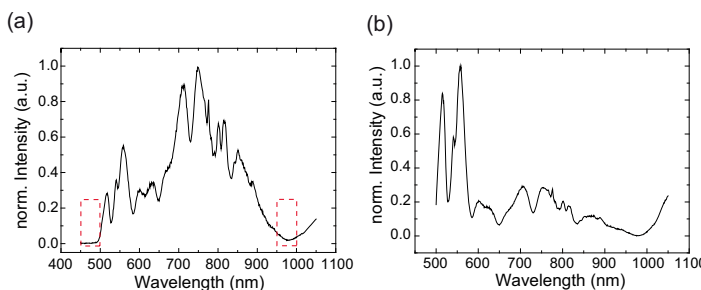


Fig. 3.11. (a) Representative spectrum of the supercontinuum white light after reflection at a glass-oil interface and detected with the CCD camera and grating (150 l/mm, Blaze: 800 nm). The pump wavelength is 800 nm and the coupling power is 250 μ W. (b) Same spectrum as in (a), but corrected for the combined detection efficiency of the spectrograph and CCD camera.

The spectrum is strongly modulated throughout the whole detection range. This can be attributed to the spectrally non-uniform output of the PCF which exhibits strong maxima at distinct wavelengths depending on the pump and coupling conditions (compare [208]). In

addition the transmission/reflection characteristics of the optical components of the whole optical setup as well as the detection efficiency of the CCD camera lead to further modulations of the white light. The components which affect the spectral shape of the white light strongest are the pellicle beam splitters and the combination of the grating (150 l/mm, Blaze: 800 nm) in the spectrograph and CCD camera (Fig. 3.12 (a) and (b), respectively).

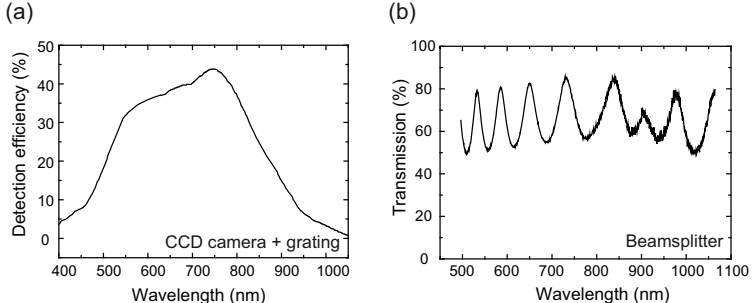


Fig. 3.12. (a) Detection efficiency of the combination of spectrograph (grating: 150 l/mm; blaze: 800 nm) and CCD camera (based on manufacturer data). (b) Transmission profile of the beam splitter (BS2), which is used inside the microscope.

The beam splitter introduces the periodic narrow modulations observed in Fig. 3.11 (a) with relative changes in transmission of about 30 %. The low detection efficiency of the spectrograph and CCD, resulting from the small quantum efficiency and reflectivity of the grating, for wavelength below 500 nm and above 900 nm (marked by the red boxes in Fig. 3.11 (a), leads to the fast decaying slopes of the white light intensity in those regions. The same white light spectrum corrected for the detection efficiency is shown in Fig. 3.11 (b). However, the white light spectrum extends further into the NIR region. The same measurements repeated with an NIR-IR optimized InGaAs-camera (Roper, OMA V) confirm significant white light contributions up to a wavelength of $1.5 \mu\text{m}$.

Another important aspect for white light experiments exploiting the temporal characteristics of the white light is the strong chirp of the white light pulses. The manufacturer specifies a time delay between the blue (500 nm) and red (1000 nm) spectral component of approximately one picosecond for a pump wavelength of 800 nm and a power of 150 mW [208].

3.5.2. Acquisition of Elastic White Light Scattering Images and Spectra

Elastic scattering imaging of the samples basically follows the PL imaging procedure described in Sec. 3.3, except that all longpass and bandpass filters are removed from the excitation beam path. For all white light measurements a high NA immersion oil objective (Nikon CFI Plan Apo VC 60x $NA=1.4$) is used, which is highly corrected for chromatic aberrations.

For the acquisition of confocal scattering scan images, the wavelength integrated white light scattering intensity at each scan pixel was detected by an APD. Excitation is provided by the supercontinuum white light output of a PCF, which is pumped by the 800 nm fundamental of a Ti:Sapphire oscillator. For imaging, the excitation power was reduced by neutral density filters, so that the light reflected from the substrates yields APD photon count rates between 0.5–1 MHz. For this, count level typical integration times per pixel are 5–10 ms. Scattering spectra are acquired by a combination of spectrograph (grating: 150 l/mm (800 BLZ)) and a thermoelectrically cooled CCD camera.

The spectroscopic quantity determined in the white light iSCAT experiments is the wavelength dependent optical contrast δ , according to the definition introduced in Eqn. 2.24. Therefore, in order to determine δ two spectra of different sample positions need to be acquired. One spectra at the position of a scattering particle and an additional background spectra acquired at a suitable position next to the particle. The normalization of the differential intensity by a background spectrum the signal does not depend anymore on the actual spectral composition of the white light given that the white light intensity is stable for the measurement.

In general, due to the interferometric nature of the scattering signal it is sensitive to any inhomogeneities of the substrate surface, such as the surface roughness but also residual surfactant when using surfactant encapsulated SWCNTs. In sum 3–5 background spectra at different locations in close vicinity of the GNP were recorded. An average I_{back} is then used for determining δ . Prior to the measurements it was ensured that the white light output is stable, by monitoring the temporal evolution of the reflectivity from a bare glass cover slide over a extended period of time (2 min). Long term drifts of the white light on a timescale of 0.5–1 hour occur, which result in relative changes of different spectral fractions of the white light. Most likely, the origin of these changes are mechanical drifts of the optical components caused by temperature fluctuations. However, these slow changes do not affect the actual measurements of δ , taking into account the much shorter acquisition times of the scattering spectra of 10–500 ms.

Assuming a shot-noise limited excitation source the SNR in the scattering experiments should be mainly determined by the intensity of the back reflected light $SNR \propto \sqrt{I}$, which in turn depends linearly on the incident intensity. Thus, in general the SNR can be enhanced by increasing either the excitation power or the acquisition times. In order to improve the SNR further and to eliminated possible short term intensity fluctuations in the spectra which might result from instabilities of the white light, the final contrast spectrum is averaged over many spectra. Experimentally the averaging is realized by jumping alternately between the position of a particle and an empty background while continuously acquiring spectra at this positions. A Labview script (National Instruments) synchronizes the movement of the scan-stage with acquisition of spectra at the two different positions. The contrast $\Delta I/I_{back}$

3. Materials and Methods

for each jumping cycle and the average spectrum is calculated on-the-fly. An adequate SNR can be obtained for averaging over 20–30 spectra.

Part II.

Time-resolved PL Studies of Individual SWCNTs

4. Excited State Dynamics of Individual SWCNTs at Room Temperature

The excited state dynamics of individual CoMoCAT SWCNTs deposited on glass substrates at room temperature was studied by a combination of TCSPC and PL spectroscopy. It is found that the PL is dominated by fast nonradiative processes resulting in PL decay times in the low picosecond regime. For small photon fluences the PL decay dynamics is predominantly monoexponential. At higher excitation densities Auger recombination leads to a considerable reduction of PL decay times and in some cases to an additional fast decay component. Tube-to-tube variations of PL decay times on the order of 3-40 ps are observed. The origin of this decay time variations and of the fast PL decay times can be attributed to two different phonon-assisted nonradiative decay channels, which both require different types of defects for their activation. A weak correlation of PL decay times and PL linewidth supports the idea, that one type of defect is responsible for nonradiative excited state decay and excited state dephasing. However, the experimental data further implies the presence of a second type of defect which causes nonradiative decay only. Variations in the defect concentrations of different SWCNTs might then account for the observed PL decay time distributions.

One type of structural defect which exists in every SWCNT are the nanotube ends. It is known that these efficiently facilitate PL quenching and thus represent an inherent nonradiative decay channel. As the excitons in SWCNTs are highly mobile, they can probe large segments of a SWCNT probe within their lifetimes and eventually can interact with local defect sites along the tube. Based on this, one would expect for an ideal SWCNT with the nanotube ends as only defect sites a dependence of the PL decay times on the SWCNT length. In order to study this effect PL decay time measurements on length fractionated SWCNTs were performed. It is found that samples with larger average length indeed exhibit longer decay times. However, the differences in average decay times are small compared to the large spread of decay times observed for individual tubes. For the present CoMoCAT material PL quenching at the nanotube ends is not the dominant decay channel responsible for the fast observed PL decay times. Furthermore, it can be shown that even individual SWCNTs show heterogeneous decay times along their length, stressing the importance of extrinsic parameters influencing the excited states dynamics of SWCNTs. The observed PL decay times are discussed on the basis of a simple numerical random walk model for the diffusional motion of excitons.

This chapter is based on the paper "Exciton decay dynamics in individual single wall carbon nanotubes at room temperature" which was published in *Appl. Phys. Lett.*, **92**, 153116 (2008)

4.1. Introduction

The PL of semiconducting SWCNTs is due to the radiative recombination of the optically allowed ${}_0A_0^-$ exciton [85]. However, the PL process in SWCNTs is not very efficient compared to e.g. the fluorescence of organic dye molecules. Small QYs of only 0.01–7% are reported, strongly depending on the sample material and experimental conditions [119, 123, 209–212]. A broad range of values between tens to hundreds of picoseconds has been reported also for the PL decay times [209, 213–218]. Controversial reports exist also for the PL decay dynamics for which mono-, bi- and even multi-exponential decays have been observed [209, 217–219]. All these observations lead to the question for the processes governing the excited state dynamics of SWCNTs.

The reported picosecond PL decay times are orders of magnitudes smaller than the theoretically predicted [94, 106] and experimentally deduced [119, 209, 210, 220] radiative life times of 10–100 ns. From this discrepancy it became obvious that efficient coupling of the bright exciton to nonradiative decay channels is the main reason for the fast excited state decay. However, the microscopic nature of these nonradiative channels and moreover whether those are of intrinsic or extrinsic origin is still under debate. In general, it was found that the processes leading to fast nonradiative relaxation are mainly scattering processes, such as exciton-phonon or exciton-exciton scattering (Auger recombination) at higher exciton densities. In SWCNTs phonon-assisted processes, for instance multi-phonon-decays and phonon-assisted indirect exciton ionization can become very efficient for localized excitons (compare Fig. 1.16).

The electronic states which are populated in the course of the nonradiative decay process are also widely unknown. On the one hand, it is indicated that mainly intrinsic states are involved and the fast decay is the result of transitions from the bright state to excitonic dark states with different parity or spin. Temperature dependent PL measurements revealed that the excited state relaxation reflects a complex interplay between the bright and dark states [95, 221], which is further supported by the findings of ultrafast spectroscopic measurements [102]. On the other hand also coupling to extrinsic defect and trap states is discussed which might be created in the presence of charges or due to heterogeneities of the local dielectric environment [217]. Alternative nonradiative decay channels might involve energy transfer which was observed for SWCNTs in small bundles or aggregates of SWCNTs [116, 117, 222] or between closely neighbored SWCNTs [118]. Especially in small bundles the presence of metallic SWCNTs leads to very efficient PL quenching [49, 212].

The majority of the time-resolved PL measurements so far are ensemble studies of films or suspensions of surfactant coated SWCNTs. In these studies different experimental approaches, i.e pump-probe [217], Kerr-gating techniques [209], TCSPC [223] or femtosecond correlation spectroscopy [219] have been used. The broad range of reported decay times and dynamics is not surprising, as for ensemble studies a more complex decay behavior is expected due to their heterogeneous composition. Defects and environmental coupling are spatially localized and a unique property of a given nanotube. As a result, ensemble

measurements will always represent an inhomogeneous averaging. Suspensions of SWCNTs consist of a multitude of different SWCNT chiralities often with overlapping PL contributions and chirality specific differences of the decay behaviors might be obscured or even misinterpreted. Intertube interactions and reabsorption and -emission of PL are possible (no Stokes-shift), which complicate the analysis of the PL decay dynamics further.

However, PL decay time measurements on the single nanotube level avoid these complications. Heterogeneous broadening effects are inhibited and allow to distinguish the PL decay dynamics of different sub ensembles. Confocal PL microscopy in combination with TCSPC provides the required high detection sensitivity and temporal resolution to study the PL decay times of individual, spatially isolated SWCNTs.

At the time of this work, only a single report on the PL decay times of individual SWCNTs has been published [223]. Here, TCSPC experiments were performed on (6,4) micelle encapsulated HiPco SWCNTs at cryogenic temperatures between 50–180 K. Fast picosecond PL decay times (20–180 ps) were observed in agreement with the reported ensemble data, while the PL decay dynamics was found to be monoexponential. The temperature dependence of the PL decay times is characterized by a gradual increase for decreasing temperatures down to ~60 K, where the decay times start to saturate. This behavior was explained by the temperature dependence of the nonradiative decay rate. For this, a model of a thermally activated phonon-mediated coupling of the bright exciton to extrinsic defect related trap states was assumed. In this picture, excited state mobility is required to reach the localized defect size within their life times. The monoexponential decays observed in these experiments, indicate that the transport to the defect sites is much faster than the nonradiative processes on the picosecond time scale.

However, due to the difficult nature of low-temperature measurements only a limited data set for PL decay times was acquired. The room-temperature experiments presented in the following sections extend this low temperature study and provide further insights into the PL decay dynamics of SWCNTs.

4.2. PL Decay Time Distributions of Individual CoMoCAT SWCNTs

For PL imaging and PL spectroscopy a laser scanning confocal microscope was employed (compare Sec. 3.1). A mode-locked Ti:Sapphire oscillator provided high repetition pulsed excitation light (76 Mhz) at a wavelength of ~760 nm, which is focused by a high numerical aperture oil immersion objective ($NA=1.3$) on the sample. For PL imaging low excitation powers (expressed as photon fluence) of $\sim 35 \cdot 10^{12}$ photons $\text{pulse}^{-1} \text{cm}^{-2}$ were used, while the fluence for the acquisition of PL transients was lowered to approximately $\sim 1.7 \cdot 10 \cdot 10^{12}$ photons $\text{pulse}^{-1} \text{cm}^{-2}$. The procedures for the acquisition of PL transients and for the transient fitting to retrieve the PL decay times are described in Sec. 3.4.1 and Sec. 3.4.2, respectively.

Individual CoMoCAT SWCNTs deposited on glass substrates exhibit fast PL decay times in

the low picosecond regime. Tube-to-tube variations of the PL decay times between 1–40 ps are observed. Three representative PL transients (black curves) of (6,4) SWCNTs are depicted in Fig. 4.1(a) together with their corresponding monoexponential fits (red curves). The transient fitting yields decay times of $\tau_1=4$, 18 and 36 ps.

For the present CoMoCAT material the PL decay dynamics is strictly monoexponential. Extremely long lifetimes in the range of nanoseconds as reported in the literature have not been observed in this single nanotube measurements. Only in very few cases, for less than 5 % of all measured transients, better fitting results could be achieved by using multiple decay components with time constants of similar magnitude. This is most likely due to spatial averaging along inhomogeneous nanotubes or the presence of a second nanotube with same chirality within the focal detection area. This is comparable to the situation in ensemble measurements, which are expected to result in multi-exponential decay profiles where the fitted lifetimes reflect the summation over decay times with different contributions [224].

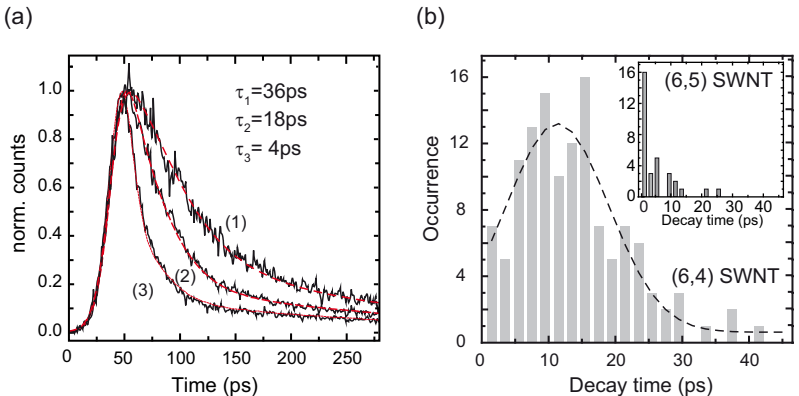


Fig. 4.1. (a) PL transients (black curves) and decay times of three different (6,4) SWCNTs. The red curves are monoexponential fits to the experimental data taking into account the measured instrument response function. The fits yield decay times in the range of a 1–40 ps revealing large tube to tube variations. (b) Histogram of exciton decay times observed for 126 different (6,4) SWCNTs. The distribution is fitted with a Gaussian function centered at 11 ps and a width of 16 ps. The average PL decay time is $\langle \tau \rangle = 14\text{ ps}$. Inset in (b) Histogram of CoMoCAT (6,5) SWCNTs. The distribution is shifted to smaller decay times with an average PL decay times of $\langle \tau \rangle = 5\text{ ps}$.

In order to investigate the tube-to-tube variations of the PL decay times in more detail, statistical numbers of PL decay times were acquired for two different SWCNT chiralities, the (6,4) and (6,5). The results are plotted as histograms in Fig. 4.1(b) which consists of 126 PL decay times in the case of the (6,4) and 32 in the case of the (6,5) SWCNT. The distribution of (6,4) decay times is fitted by a Gaussian function (red dashed line) to evaluate its width (FWHM) and the center decay time with 16 ps and 11 ps, respectively. The average PL decay

time $\langle \tau \rangle$ is 14 ps. To the best of our knowledge no literature data for PL decay times for CoMoCAT (6,4) SWCNTs at room temperature exist, however the observed $\langle \tau \rangle$ is in general agreement with the fast ensemble PL decay times 10 ps reported for nanotubes dispersed in suspensions [225]. The distribution of PL decay times of the (6,5) chirality in Fig. 4.1(c) is markedly different. It is shifted to smaller PL decay times with an average value of $\langle \tau \rangle=5$ ps. Remarkably, this value agrees well with the 6 ps determined by pump-probe measurements for the same micelle CoMoCAT nanotube material allowing for a direct comparison of the results achieved by both techniques [217].

Comparing the largest observed PL decay time of 40 ps with the long radiative lifetimes on the nanosecond scale [94, 110, 209] it becomes immediately apparent that fast nonradiative decay processes k_{nr} are dominating the excited state recombination. Consequently, the observed large tube-to-tube variations of the PL decay times can be attributed in the first place to corresponding changes of their nonradiative decay rates k_{nr} . One possible factor which might easily influence the nonradiative decay rate k_{nr} is investigated in more detail in the following.

In SWCNTs multiple-exciton interactions become increasingly important at higher exciton densities. While the formation of stable bi-excitons is predicted [226] but haven't been experimentally observed so far, fast exciton-exciton annihilation (Auger recombination) on the other hand is known to strongly affect the photophysical processes at such power levels [213, 227–229]. In consequence, this results in the reduction of PL decay times and correspondingly to saturation and decrease of PL intensities as well as to a more complex decay dynamics.

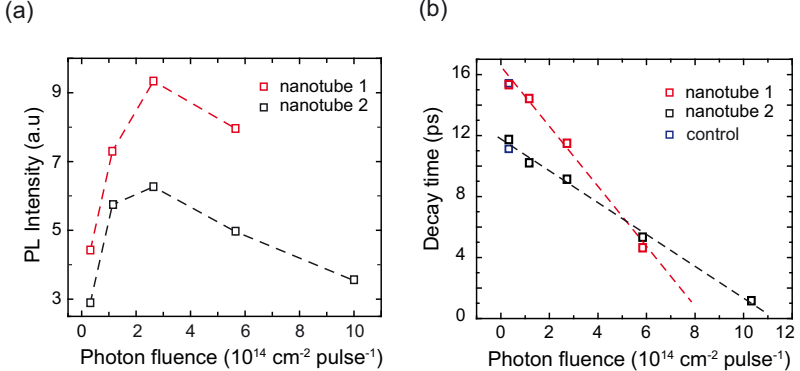


Fig. 4.2. Dependence of the integrated PL intensity and PL decay times on the photon fluence. Here, medium to high laser excitation powers are used exceeding typical powers for transient acquisition by one order of magnitude. (a) For excitation powers exceeding $10^{14} \text{ photons pulse}^{-1} \text{ cm}^{-2}$ Auger recombination becomes efficient, leading to a decrease of PL intensities and correspondingly to a decrease of (b) PL decay times. The examples presented here are reversible cases, not affected by PL bleaching (blue control data).

For photon fluences smaller than $10^{13} \text{ photons pulse}^{-1} \text{ cm}^{-2}$ which are typically used for the acquisition of PL transients, the probability for the creation of an exciton per pulse is expected to be significantly less than one (~ 0.06)⁴ and thus multi-exciton effects are not expected. However, in order to ensure that Auger recombination can be excluded as a possible origin for the observed PL decay time distributions and to estimate an upper limit for the excitation power where Auger recombination might become relevant in single SWCNT measurements, the dependence of the PL intensities and PL decay times on the photon fluence was investigated.

Exemplarily, these dependencies are plotted in Fig. 4.2 for two different SWCNTs, for which a reversible power dependence of these quantities was observed (blue control points). It is found that for the present sample material the effects of the Auger recombination becomes visible for photon fluences exceeding $10^{14} \text{ photons pulse}^{-1} \text{ cm}^{-2}$. For this excitation intensities it starts to dominate the decay dynamics [227], leading to a reduction of PL intensities and PL decay times. While the PL intensities first increase linearly, they start to decrease and then eventually saturate. The dependence of the PL decay times is characterized by a linear decrease even for lowest excitation powers. In some cases an additional fast decay component on the order of 1–7 ps is observed, often accompanied by spectral changes of the PL, such as small spectral shifts and PL linewidth broadening.

⁴The estimation of the numbers of excitons created per excitation pulse is based on following assumptions: The SWCNTs are excited with the incident light polarized parallel to their axis. Further an absorption cross section per unit length of $\sigma_{abs}=85 \text{ nm}^2 / \mu\text{m}$ [124] is assumed and an average length for the SWCNTs of $\langle L \rangle=545 \text{ nm}$ as determined by AFM measurements for the same sample material (compare Sec. 3.2.2). The pump fluence is $10^{12} \text{ photons cm}^{-2} \text{ pulse}^{-1}$.

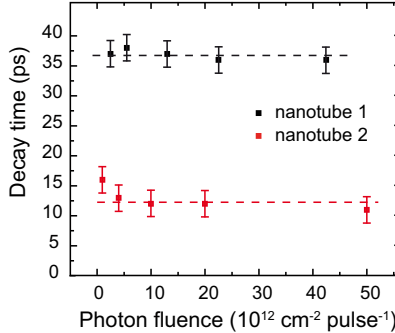


Fig. 4.3. (a) Dependence of the PL decay times on low laser excitation powers (as pump fluence). No changes in the decay times are observed for the average excitation powers $\sim 1.7\text{--}10\cdot 10^{12} \text{ photons pulse}^{-1} \text{ cm}^{-2}$ used in the experiments.

For the range of the low pump fluences of $2\text{--}10\cdot 10^{12} \text{ photons cm}^{-2} \text{ pulse}^{-1}$ used throughout this study, the measured transients result in constant decay times to within $\pm 2 \text{ ps}$ (Fig. 4.3). Based on this observation, exciton-exciton annihilation can be ruled out as the origin of the PL decay time variations.

4.3. PL Decay Time Distributions: Defect Mediated Nonradiative Relaxation

In order to obtain more insight into the nonradiative decay process, the PL decay times are plotted against their corresponding PL emission energies and PL linewidth. Both parameters are determined by fitting single Lorentzian functions to the PL bands. In the following treatment of this subject only the (6,4) chirality is considered.

A plot of the PL decay times against PL linewidth is shown in Fig. 4.4 (a). The first observation is that similar to the PL decay times, the observed PL linewidth also exhibit tube-to tube variations with values between 21 and 46 meV, in agreement with similar single SWCNT studies [31, 223] and where attributed to extrinsic factors, such as structural and chemical defects as well as to heterogeneities in the local environment. Although there is no direct one-to-one correlation between the PL decay times and PL linewidth, it is found that large PL decay times can be associated with a narrow PL linewidth vaguely following the trend indicated by the black dashed line in Fig. 4.4 (a).

The PL energies of the (6,4) SWCNTs are distributed about $\pm 25 \text{ meV}$ around the average value of 1.403 eV (see Fig. 4.4 (b)), consistent with the observation of similar energy variations reported for other single SWCNT studies [31, 118, 230–232]. This effect can be attributed to the heterogeneous local environment of the SWCNTs which causes fluctuations of the dielectric

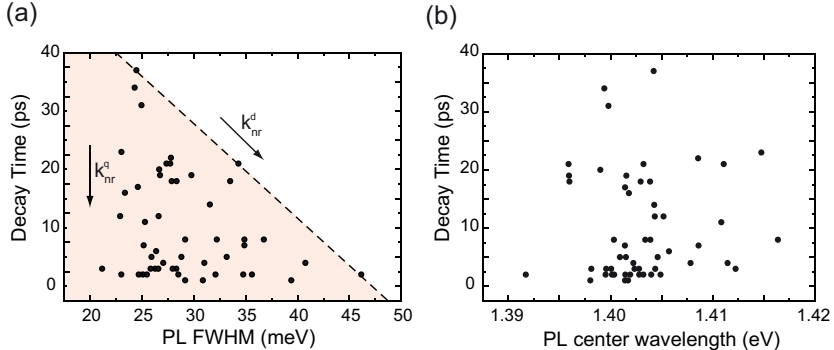


Fig. 4.4. (a) Plot of PL decay times of (6,4) CoMoCAT SWCNTs against the PL linewidth (FWHM). A weak correlation between PL line width and PL lifetimes is found: Large PL decay times are correlated with narrow PL linewidths (dashed line as guide for the eye). (b) Plot of PL decay times vs. PL emission wavelength. No obvious correlation between PL energy and PL decay times can be observed.

constant ϵ along the tube and thus leads to varying exciton energies (see also Sec. 1.5). No obvious correlation between the PL energies and PL decay times is observed, which would be expected for a thermally activated transition of the bright exciton to an energetically low lying dark or trap state [223], where the transition rate depends on the excitonic energy and For such a scenario, a correlation of long PL decay times with red shifted PL energies would be expected, reflecting the larger activation energy required for this process. The absence of such a trend might indicate that the activation energy or the depths of potential energy basin are larger than kT and thus the coupling rates between the bright and the dark/trap states are extremely fast. However, as the exciton trapping at such sites is spatially localized, confocal microscopy is limited in its resolution and the spectra represent the averaging over a large tube segment or even over the entire SWCNT.

Discussion

In the following the origin of the correlation between the PL linewidth and PL decay times in Fig. 4.4 is discussed in more detail. The formation of the triangular pattern of data points in Fig. 4.4 (a) might be attributed to two different relations between the PL decay times τ and corresponding PL linewidth Γ :

1. Decrease of τ **without** broadening Γ (vertical arrow) ,
2. Decrease of τ **with** broadening Γ (inclined arrow) .

Here it is suggested that these two effects are due to two different types of defects, which both facilitate fast nonradiative decay: First, defects which lead to pure *PL quenching* and simply

reduce the PL decay times and second, defects whose interaction with the excitons lead to both: *PL quenching* and *excited state dephasing*. The nonradiative decay rates associated with these defects are denoted as k_{nr}^q and k_{nr}^d , respectively. Variations in the defect concentration for different nanotubes might then account for the observed PL decay time distributions.

To elucidate this assumption further, the origin of the weak correlation between the PL decay times and the PL line is discussed.

In the dipole-approximation the homogenously broadened Lorentzian lineshape Γ of a transition is related to the finite lifetime of the excited state corresponding to: $\tau = \tau_{rad} + \tau_{nr}$, by the energy-time "uncertainty principle": $\Delta E \cdot \Delta \tau \gtrsim \hbar$. The lifetime, or its inverse, the transition rate, is associated with an energy dispersive process resulting in population decay.

A second broadening mechanism for the linewidth is the dephasing of the excited state. Here, quasi-elastic scattering processes lead to changes in the phase of the excited state wavefunction and thus to the loss of coherence. Scattering processes can have intrinsic origins such as e.g. exciton-exciton or electron-phonon scattering [233] or are associated with interactions of the emitter with its direct environment. The time T_2^* associated with these processes is the so called dephasing time. The experimentally observable linewidth is then given as the sum of the PL decay rate, $1/\tau$, and the dephasing rate $1/T_2^*$:

$$\Gamma = \frac{1}{2\tau} + \frac{1}{T_2^*} \quad (4.1)$$

Based on the measured PL decay times in the picoseconds range, one would expect a linewidth in the range of 0.02–0.05 meV, up to two orders of magnitude smaller than the experimentally determined linewidth. Hence, it is obvious that the measured linewidth are not lifetime broadened dephasing is the dominating process controlling the PL linewidth. Very small dephasing times on the order of 20–50 fs are required to explain the range of experimentally observed linewidths. This estimation is in good agreement with the values for T_2^* of ~50–200 fs reported in refs. [233, 234]. The broad range of observed PL linewidth can then be explained in the first place by changes of the dephasing rate.

It was found that the main contribution to the fast dephasing times in SWCNTs at low exciton densities is exciton-phonon scattering with low-energy phonon modes such as low-frequency acoustic phonon and twisting modes [235]. It is predicted that certain types of structural defects like the Stone-Wales or the "7–5–5–7" defect give rise to localized low-energy phonon modes between 100–500 cm⁻¹ which significantly decrease the T_2^* times and thus lead to linewidth broadening [236]. It might be further speculated that the defect related phonon modes facilitate also nonradiative relaxation. For localized excitons trapped at defects sites it is predicted that a multi-phonon-decays can become an efficient nonradiative relaxation pathway [125]. The availability of additional low-energy phonon modes might enhance these decay rates even further. However, regardless of the exact nature of the defect or the origin of the dephasing event, the weak correlation found in Fig. 4.4 (a), implies that the origin of the dephasing also serves as an additional non-radiative decay channel k_{nr} .

For a simple linear relation between the linewidth and the PL decay times it would be expected that the PL decay times are spread in a confined area along the dotted line in Fig. 4.4 (a). However, this could not explain the PL decay times in the lower left part of the shaded area, where narrow PL linewidth are correlated with fast PL decay times. To explain this, it is suggested that another type of defect which leads to PL quenching is responsible for this observation.

A process which is known to lead to efficient PL quenching is doping of SWCNTs. For the mechanism of the radiationless relaxation of the exciton Auger recombination process and a phonon-assisted indirect exciton ionization process are proposed [125, 227], as discussed in Sec. 1.5.2, which is predicted to become efficient even at moderate doping levels. Unintentional hole-doping of SWCNTs occurs spontaneously due to the adsorption of oxygen at the SWCNT sidewalls or the trapping of charges. Another possible source for hole-doping of SWCNTs are protonation reactions of the sidewalls [49] or of preadsorbed oxygen [127, 129]. Protonation occurs also during the purification steps of SWCNT raw materials, where strong acids are used to remove residual catalyst.

Summarizing the results so far, the total nonradiative decay rate k_{nr} of a SWCNT can be decomposed in three individual contributions:

$$k_{nr} = k_{nr}^0 + k_{nr}^d + k_{nr}^q + \dots \quad (4.2)$$

Here k_{nr}^0 is the "intrinsic" nonradiative decay rate of the unperturbed SWCNT, which originates from e.g. electron-phonon coupling. k_{nr}^d k_{nr}^q are the nonradiative decay rates related to the "quenching" type defect and the "dephasing" type of defect. The nonradiative rate of a SWCNT is mainly determined by extrinsic decay channels which can be related to defect induced local phonon phonon modes. Differences in the defect concentrations then account for the large variation of PL decay times.

4.4. Length Dependence of PL Decay Times

The results of the previous section indicated that extrinsic defects give rise to nonradiative decay channels which significantly influence the decay dynamics of the SWCNTs. One intrinsic defect inherent to all SWCNTs and not considered so far are the SWCNT ends.

The nanotubes ends are either capped by semispherical fullerene-like molecule fragments or can remain uncapped with dangling or saturated carbon bonds. Tight binding calculations [237] and STM measurements [60, 238, 239] indicate a critically modified electronic band structure confined to the region at the ends. Additional midgap states arise close to the Fermi level which exhibit a steadily increasing DOS for decreasing distance towards the tube ends. It is predicted that the presence of these states might lead to PL quenching of the excitons and thus would represent an additional nonradiative decay channel [240]. Indeed, PL quenching at the SWCNTs ends could be directly visualized with high resolution near-field optical microscopy where it is possible to record simultaneously the PL response as well as the

topography of the SWCNT. Considering the instrument response function it was found that the PL decays on a length scale of 50–90 nm towards the end [241], which is on the order of the exciton diffusion length for surfactant wrapped SWCNT material [126, 128].

Considering the high mobility of excitons in SWCNTs (compare Sec. 1.4.3), one would expect for an ideal SWCNT with the nanotube ends as only defect sites a dependence of the PL decay times on the nanotube length L , where long SWCNTs exhibit large PL decay times [240]. Based on this assumption, the decay time variations observed in the previous section could be solely explained by either varying nanotube length or by varying diffusion coefficient D . While a recent ensemble study on the length dependence of the QY could indeed confirm the aforementioned trend between PL decay times and nanotube length [240, 242] it remains to be clarified whether PL quenching at the nanotube ends is indeed a considerable nonradiative decay channel.

PL Decay Time Distributions of Length Fractionated CoMoCAT SWCNTs

In the following the effect of the SWCNT length on the PL decay times are studied. For this different seven different samples of micelle encapsulated CoMoCAT SWCNTs with different length distributions are studied (provided by Dr. F. Hennrich, FZK Karlsruhe). Analogues to the measurement procedure described in the previous sections, large numbers of PL decay times for each sample are acquired and plotted in histograms. Length fractionated samples were provided by size-exclusion chromatography following the description in ref. [195].

Two representative PL decay time histograms of (6,4) SWCNTs with average length of $\langle L \rangle = 435$ nm and 250 nm are shown in Fig. 4.5 (a) and (b), respectively. The corresponding histograms of the SWCNT measured by atomic force microscopy are given in the insets. According to the predicted trend, the PL decay time distributions of the sample containing longer tubes is slightly shifted to longer decay times compared to the one in Fig. 4.5 (b) which leads to the average decay time of $\langle \tau_{435\text{ nm}} \rangle = 5.8$ ps and $\langle \tau_{250\text{ nm}} \rangle = 3.8$ ps.

The general trend that batches with larger average SWCNT length exhibit longer average decay times is also found in the Fig. 4.6. Here the average decay times of all seven samples are plotted against their corresponding average length. It is to note that the sample materials used for this study were treated differently in terms of the sample preparation procedure, e.g. for the micelle encapsulation of one batch mild ultrasonication conditions, such as low powers and short bath times, were used (cross), while for another batch the micelle encapsulation of the SWCNTs was removed by heating of the sample (black solid circle). For comparison, the data-point of the (6,4) CoMoCAT SWCNTs (Hersam SWCNTs) studied in the previous Sec. 4.2 is added (facedown triangle). While batches with similar average length (e.g. for $\langle L \rangle = 230$ nm and 435 nm) exhibit decay times of comparable magnitudes, the average decay time of the batch treated by "mild" ultrasonication with $\langle L \rangle = 380$ nm appears to be systematically shifted to a substantially smaller decay time. This might be due to the fact that the "mild" treatment does not lead to efficient separation of the SWCNTs and the sample contains a significant amount of small bundles, where energy transfer or PL quenching with metallic SWCNTs leads to the reduced $\langle \tau \rangle$. In general, the averaged decay times of all batches are

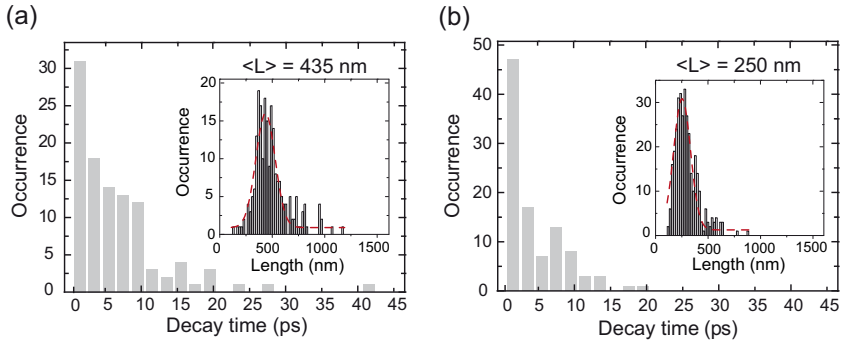


Fig. 4.5. Decay time distributions of (6,4) SWCNTs with average length (a) $\langle L \rangle = 435 \pm 90 \text{ nm}$ and (b) $\langle L \rangle = 250 \pm 80 \text{ nm}$. The average decay times of $\langle \tau_{435\text{nm}} \rangle = 5.2 \text{ ps}$ and $\langle \tau_{250\text{nm}} \rangle = 3.8 \text{ ps}$. The insets show the corresponding length distributions of the samples determined by AFM measurements.

significantly smaller than for the Hersam (6,4) SWCNT material, $\langle \tau \rangle = 14 \text{ ps}$, stressing the importance of the sample preparation on the excited state dynamics.

Neglecting the data for the Hersam SWCNTs, it is found that the average decay times of the various samples differ only by one to three picoseconds. These differences are small compared to the broad distribution of PL decay times, which suggests that for the present material PL quenching at the nanotube ends is neither the determining nor the only contribution to the fast nonradiative PL decay.

The data in Fig. 4.6 represents the ensemble averaged decay times critically affected by the underlying diameter distribution and thus represents ensemble data. A direct one-to-one correlation between SWCNT length and PL decay time can not be determined for the present material with confocal microscopy alone. As indicated by the length distributions in the insets of Fig. 4.5 most of the SWCNTs are shorter or only slightly larger than the diameter of the diffraction limited laser excitation focus ($\Delta x \approx 370 \text{ nm}$). In the PL scan images these appear as diffraction limited spots and thus information about their real size can not be retrieved. For the observation of a direct correlation one would need to perform combined AFM and PL decay time measurements on the same tube. For SWCNTs larger than the excitation focus on the other hand, it is possible to localize the tube ends based on the onset of the PL in the PL images. In this case it is possible to acquire PL transients from confocal areas close to the tube ends and neighbored sections, which allows to investigate the effect of the nanotube ends further.

For this experiments HiPco SWCNTs wrapped with the surfactant sodium deoxycholate (DOC) are used. Because of the mild preparation conditions used during the individualization step [128] the abundance of SWCNTs with a length $> 2 \mu\text{m}$ is larger than e.g. for the standard CoMoCAT SWCNT material. Furthermore, it was found that the optical properties

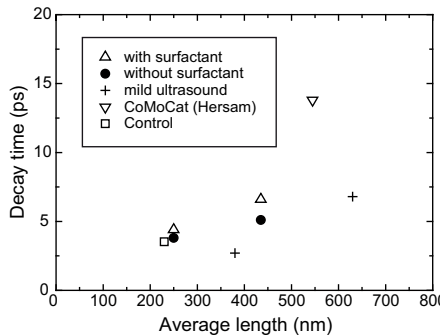


Fig. 4.6. Length dependence of the PL decay times for various length sorted CoMoCAT SWCNT materials. Batches with larger average SWCNT lengths exhibit slightly larger average PL decay times. Larger differences in average PL decay times are found for SWCNT materials with similar length but different individualization treatment (mild ultrasonication). Presumably, these batches exhibit a larger fraction of residual bundles, where intertube interactions lead to reduced PL decay times.

of the HiPco material is less affected by defects which manifests in higher PL intensities and larger PL decay times [243]. The PL properties of the HiPco material are presented in more detail in the next chapter. Here it is important to note that the PL decay times of this material are systematically larger and a large fraction of those tube deposited on glass display a biexponential decay dynamics. In order to compare the mono- and biexponential PL decay times of the different sample materials, the decay times in the following are represented as an effective decay times τ_{eff} ⁵.

Exemplarily, two confocal PL scan images of extended (6,5) HiPco SWCNTs are depicted in Fig. 4.7. The positions along the tube at which the transients were acquired are marked by the circles and the corresponding τ_{eff} are added. The diameter of the circles correspond to the diameter of the laser excitation focus of ~ 500 nm. Remarkably, the PL decay times along a single SWCNT vary by up to 30% between neighbored measurement points.

The SWCNT in Fig. 4.7 (a) exhibits PL decay times at the ends which are considerably smaller than the ones in the neighbored measured point on the tube. PL spectra measured at the same positions along the SWCNTs only show small variations in the PL energies of about $\pm 1\text{--}2$ meV and no variations of their PL linewidth. This indicates that no changes in chirality occur along the SWCNT and/or other tubes are present in the focal area. Hence, the reduced decay times might indeed originate from PL quenching at the ends. However, this behavior is not characteristic for every long SWCNT. On some occasions one observes also the contrary situation, where segments close to the tube ends have similar (± 3 ps) or even larger decay

⁵ $\tau_{eff} = \frac{A_s}{A_s+A_l} \cdot \tau_{short} + \frac{A_l}{A_s+A_l} \cdot \tau_{long}$. Here A_s and A_l are the decay amplitudes of the short and long decay component respectively.

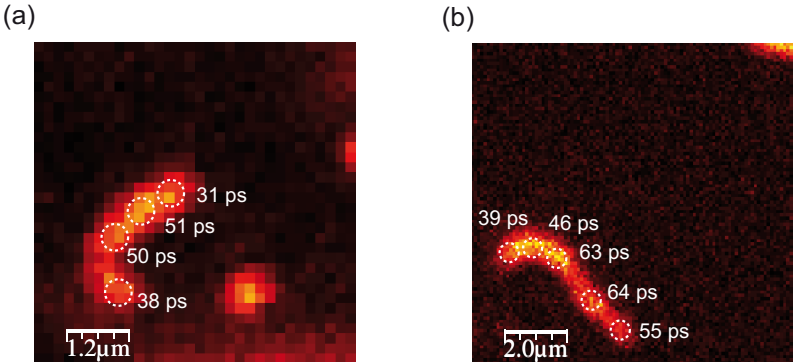


Fig. 4.7. Position dependent PL decay times of long (6,5) HiPco SWCNTs wrapped in sodium deoxycholate (DOC). The PL decay times were acquired at positions indicated by the white circles. The diameter of the circles is ~ 500 nm and resembles approximately the diameter of the excitation focus. Both tubes show considerably reduced decay times at positions close to the tube ends.

times.

Assuming a diffusion coefficient belonging to the upper end of reported literature values of $10 \text{ cm}^2/\text{s}$ and considering the longest observed PL decay time of ~ 50 ps for the SWCNT in Fig. 4.7 (a) this would result in a maximum diffusion length of $L_{Diff} = 320$ nm. Excitons generated within the two inner marked circles should be well separated from the influence of the SWCNT ends. With the assumption that the SWCNT ends are the only nonradiative decay channel it would be expected that the decay times at these positions are on the order of the radiative decay time.

The results so far showed that PL quenching at the nanotube ends is not the PL decay time determining nonradiative decay channel. For the present SWCNT material other decay channels such as defect are dominating the excited state decay. The observed length dependence of the PL decay times supports further the picture of highly mobile excitons in SWCNTs.

Discussion

In the following we want to analyze the length dependence of the decay with a recently introduced numerical model and further put the findings into context with the report on the length dependence of the PL decay times in ref. [240].

Starting with the latter and briefly summarizing the findings of this study. In agreement with the results presented here, in this PL ensemble study on length fractionated DNA-wrapped SWCNTs with average length between $\langle L \rangle = 100\text{--}500$ nm it was found that for increasing $\langle L \rangle$ also the decay becomes slower. With the assumption that PL quenching at the nanotube ends is the only contribution to the nonradiative decay, they employed an analytical model for the

diffusional motion of excitons to reproduce the observed length dependence. Based on this, the PL decay times is expected to saturate very slowly with increasing length and this would not account for a faster saturation of PL decay times as observed in Fig. 4.6 or for the length dependence of PL decay times in [244].

To illustrate this, the length dependence of the PL decay times is simulated with an numerical model for the exciton diffusion in SWCNTs based on Fick's 2nd law [115, 245]. The approach is based on finding solving Fick's 2nd law for the position and time dependent exciton population n along the SWCNT axis. The numerical model offers a high flexibility for the simulation of the effect of single localized defect sites on the mobility of the excitons [245]. The SWCNT is discretized into segments with size Δx . Considering a single pulse excitation, the temporal evolution of the exciton population $n(x,t)$ is described by:

$$\begin{aligned} n(x, t + \Delta t) = & \frac{1}{2}[n(x - \Delta x, t) + n(x + \Delta x, t)] \\ & - n(x, t)[k_{rad}(x) + k_{nrad}(x)]\Delta t \end{aligned} \quad (4.3)$$

At each time step Δt the exciton travels with equal probability (0.5) a distance of Δx to the left or right neighboring segment, corresponding to a 1D random walk. Furthermore, the exciton population decays at a rate given by the sum of the radiative $k_{rad}(x)$ and nonradiative $k_{nrad}(x)$ rates. The advantage of this approach, is that the site dependent rates $k_{rad}(x)$ and $k_{nrad}(x)$ can be freely set for each segment. For example, the effect of localized PL quenching sites can be modeled by assuming $k_{nrad}(x) \rightarrow \infty$ or equivalently setting the population at this position equal to zero. The initial population $n(x, 0)$ along the nanotube is given by a Gaussian intensity distribution, approximately resembling the focal intensity distribution provided by the tightly focused laser beam. Different exciton mobilities, represented by the diffusion constant $D = \Delta x^2 / 2\Delta t$, are fixed by adjusting the temporal and/or spatial step width accordingly. For typical D values of $1-10 \text{ cm}^2/\text{s}$, as found for micelle encapsulated SWCNTs on substrates, a good choice for a reasonable accuracy is $\Delta x = 2-4 \text{ nm}$ and correspondingly $\Delta t = 2 \cdot 10^{-2} - 2 \cdot 10^{-3} \text{ ps}$. Finally, the time dependent PL intensity I_{PL} can be expressed as sum over all SWCNT segments:

$$I_{PL}(t) = \sum_x k_{rad}(x)\Delta t n(x, t) \quad (4.4)$$

The PL decay times are then evaluated by fitting the PL decay by monoexponential functions.

The model is first employed to reproduce the length dependence of the PL decay times for the length fractionated CoMoCAT materials. Fig. 4.8 (a) shows the simulated length dependence of the PL decay times assuming two different scenarios: different scenarios were assumed: First, The nanotube ends are the only nonradiative decay channels, according to the description in [240] (red curve). Second, an additional defect related decay rate for each tube segment

k_{nr} is assumed. An alternative approach to consider defect related nonradiative decay can be realized by assuming that only PL quenching defects at positions $n(x', t)=0$ contribute while k_{nr} is set to zero. Then the nonradiative decay would be controlled purely by diffusion to these sites and would depend on the relative distance and number of defect sites along the tube. Using a decay rate close to the inverse of the average PL decay times of the samples of $k_{nr} = 1/8 \text{ ps}^{-1}$ the modeled curve describes the experimental length dependence sufficiently well (black curve). The curve converges more rapidly for increasing average SWCNT lengths and appears to be a better description of the data compared to the red curve. The modeling yields a diffusion coefficient of $D=6.3 \text{ cm}^2/\text{s}$ which corresponds for the observed range of $\langle\tau\rangle$ values between 4–6 ps to exciton diffusion lengths of 70–80 nm. These numbers are on the lower end of reported exciton diffusion length of micelle encapsulated SWCNTs [126].

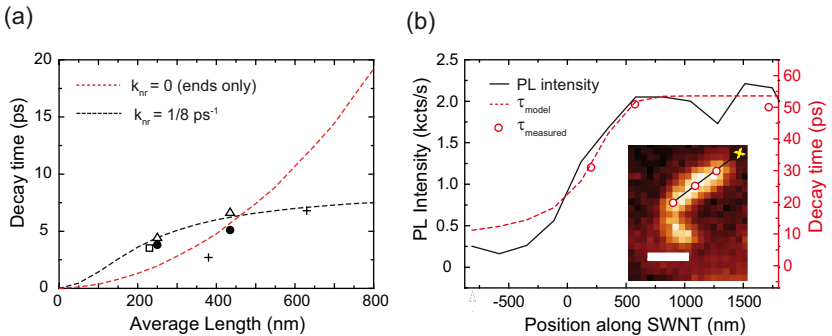


Fig. 4.8. Modeled length dependence of the PL decay times. (a) For the red curve PL quenching at nanotube ends is the only nonradiative decay channel. Using a radiative rate of $k_{rad} = 2\text{--}3 \text{ ns}$ the curve saturates for rather high SWCNT length and one would need to assume $D=36 \text{ cm}^2/\text{s}$. A more rapid saturation of PL decay times with increasing length is observed when taking into account an additional average nonradiative decay rate $k_{nr}=1/8 \text{ ps}^{-1}$ (black). The data points of Fig. 4.6 are shown for comparison. (b) Simulation of the position dependent PL decay times along the intensity profile SWCNT in Fig. 4.7 (a). The starting point of the cross-section is marked by the arrow. The scalebar is $1.2 \mu\text{m}$.

Fig. 4.8 plots the PL intensity (black) and the modeled PL decay times (red) in dependence of the x position along the tube of Fig. 4.6. The black line in the inset indicates the cross section along the tubes, while the red circles in the inset mark the points where the experimental data was recorded. In order to estimate the position of the nanotube ends ($x=0$), the fading end of the PL intensity profile was fitted by an exponential and it was assumed that the nanotube end is close to the position, where the PL intensity has decreased to a value of I_{PL}/e , taking into account the convolution of the real extension of the SWCNT with the gaussian excitation focus. The PL decays can be reproduced by setting $D=6.3 \text{ cm}^2/\text{s}$ and using an average nonradiative decay rate of $k_{nr}=1/55 \text{ ps}^{-1}$. The smaller nonradiative rate for HiPco nanotubes is also reflected in the generally longer total decay times as compared to

the previously discussed CoMoCAT nanotubes.

4.5. Conclusion

In summary, the first PL decay time measurements of individual SWCNTs at room-temperature were presented. For the SWCNT material under study, micelle encapsulated CoMoCAT SWCNTs deposited on glass substrates, fast PL decay times in the picosecond regime with tube-to-tube variations between 1–40 ps were found, while the excited state decay is monoexponential for the regime of low excitation fluences. At higher photon fluences nonradiative Auger recombination of excitons dominates the excited state dynamics leading to reduced PL decay times and PL intensities. It is found that the PL decay dynamics of the CoMoCAT SWCNT material is dominated by extrinsic defects, whose associated local phonon modes facilitate the fast nonradiative decay. The origin of the broad PL decay time distribution can be explained by two different defect related nonradiative decay channels. One type of defect can be associated with efficient PL quenching. A second type of defect leads to fast PL decay times and also affects the dephasing time T_2^* which is supported by a weak correlation between PL decay times and PL linewidth. Tube-to-tube variations in the PL decay times can be attributed to varying defect concentrations of the individual SWCNTs.

The dependence of the PL decay times on the SWCNT length was investigated for different length fractionated SWCNT samples with average length between 200–600 nm. The small differences between average decay times of only 1–3 ps indicate that for the rather defective CoMoCAT SWCNT material under study, the effect of PL quenching at the SWCNT ends is not the dominating nonradiative decay channel. For long HiPco SWCNTs the influence of PL quenching at the nanotube could be observed, which presumably owes to the fact that this material is less affected by defects. PL decay times acquired from diffraction limited segments close to the tube ends compared to the one taken at neighbored sections are decreased by up to ~30 %. Furthermore, the observed variations of PL decay times along single SWCNTs further support the idea that defects and the effect of an inhomogeneous local environment are crucial factors influencing the excited state dynamics of SWCNTs.

5. Mono- and Biexponential PL Decays of Individual SWCNTs

The following chapter is based on the paper "*Mono- and Biexponential Luminescence Decays of Individual Single-Walled Carbon Nanotubes*" that has been published in *J. Phys. Chem. C*, **114** (33), 14025.

5.1. Introduction

The knowledge about the PL decay dynamics, such as the time constants and their corresponding amplitude of different decay components allows to verify or exclude certain kinetic models, which consider the radiative or nonradiative coupling between participating states. The excited state relaxation of a simple molecular two level system follows a monoexponential PL decay. More complex decay dynamics deviating from a simple exponential decay are expected, e.g. when the decay rate becomes a function of time as it is predicted for a PL process where diffusion driven PL quenching at localized defect sites is the dominating nonradiative relaxation channel [246].

Biexponential PL decays in SWCNTs were observed in time-resolved PL measurement on ensembles as well as in single nanotube measurements for different types of sample materials and environments [124, 218, 224, 247]. The reported biexponential decays are characterized by a fast dominating decay component with decay times between 60–200 ps and a less contributing decay component with time constants between 0.6 and 4.8 ns (representative values from [218]).

The current model which explains the biexponential decays in SWCNTs is an "intrinsic model", which considers transitions between a dark and the bright excitonic state within the same SWCNT. The bright state has a slightly larger energy than the dark state and both states are weakly coupled by phonon-mediated processes. The states can decay radiatively and nonradiatively to the ground state, however, only the emission of the bright state is detected and the coupling to the dark state manifests as a long lived PL component corresponding to a delayed luminescence [124, 218, 224]. This kinetic model will be reviewed and discussed in more detail in Sec. 5.3.

In order to explain the biexponential PL decay dynamics of different SWCNTs chiralities observed in ensemble measurements also so called "extrinsic models" are employed. A recent model considers here the radiative and nonradiative transitions of the bright excitonic states of SWCNTs belonging to the same chirality, but being part of two different subensembles, which differ e.g. in their average length and/or average defect density. These factors affect the nonradiative decay rates and in consequence lead to differences in the average PL decay

times of both subensembles. Experimentally, these difference gives rise to a biexponential decay behavior, where the decay amplitudes are then governed by the relative occurrence of SWCNTs belonging to either of this subensembles [218].

Differences in the observed PL decay dynamics for ensembles of SWCNTs comes not surprising and can be attribute to the heterogeneous composition of the SWCNT materials and inhomogeneous environments. The heterogeneity of the sample composition can be avoided by performing experiments on the single SWCNT level focusing on only one SWCNT chirality. Nominally identical experimental conditions, such as the same SWCNT material, chirality, surfactant and environment, should then yield comparable and reproducible results for the PL decay times and dynamics. But also here a broad range of different PL behaviors are reported. For example PL decay measurements performed on individual CoMoCAT (6,4) and (6,5) nanotubes by different groups distinctly different PL decay behaviors were observed, ranging from very short monoexponential decays, like it was found in this work, to biexponential ones with a long PL decay time component [124,223,243].

Motivated by this disparity of the PL decay dynamics in single SWCNT studies, a collaboration with the research group of Prof. Lounis was established. In a cooperative effort the influence of different environments and synthesis method related effects on the PL decay dynamics of CoMoCAT and HiPco SWCNTs was investigated. While for the majority of single SWCNT studies most only the PL properties of the brightest SWCNTs are considered which are supposed to be less affected from defects thus resemble a more "intrinsic" PL behavior. In order to investigate the role of defects on the excited state dynamics also weakly luminescent nanotubes need to be considered in contrast to the study in ref. [243].

5.2. PL Decay Dynamics of Individual HiPco and CoMoCAT SWCNTs

PL decay time measurements employing the TCSPC technique were performed on individual (6,4) and (6,5) HiPco and CoMoCAT SWCNTs encapsulated by the surfactant DOC. In order to study the effect of different nanotube environments on the PL decay times and decay dynamics the SWCNTs were exposed to two different environments, agarose gel and deposited on a bare glass substrate. Three different kinds of samples were studied:

1. HiPco SWCNTs immobilized in aqueous agarose gel
2. HiPco SWCNTs deposited on glass substrates
3. CoMoCAT SWCNTs immobilized in aqueous agarose gel

The general protocol for the acquisition of PL transients and corresponding PL spectra is identical to one described in Sec. 3.3. The excitation wavelength for this experiments are 800 or 810 nm, resulting in off-resonance excitation of the studied SWCNT chiralities. Very low

excitation fluences $\lesssim 10^{12}$ photons pulse $^{-1}$ cm $^{-2}$ were used, ensuring that less than one photon is absorbed per excitation pulse. Mono- and biexponential PL decays were distinguished based on the goodness of the transient fit. A PL decay was regarded as biexponential, if the fit visually improves the weighted residuals and the corresponding reduced χ^2 parameter. The transient fitting and data evaluation is described in detail in 3.4.3. The amplitudes of the two decay components of the biexponential decays are represented as fractional amplitudes, where A_{long} denotes the long decay time component, using the definition in Eqn. 3.3.

5.2.1. PL Decay Dynamics of HiPco and CoMoCAT (6,5) SWCNTs

In the following the results of the PL decay time measurements for (6,5) HiPco and CoMoCAT SWCNTs are presented first. Similarly, to the procedure described in the previous chapter (Chap. 4), histograms of PL decay times were prepared for each of the three samples.

In agreement with ref. [243], the PL decays of the majority of (6,5) HiPco SWCNTs embedded in agarose gel and 50 % of the SWCNTs studied on glass display a biexponential decay behavior. However, in contrast to ref. [243], the PL decay of (6,5) CoMoCAT SWCNTs on glass substrates and in embedded in gel is strictly monoexponential.

All three samples exhibit broad distributions for the short decay time components τ_{short} , which are depicted in Fig. 5.1(a)-(c). The dotted curves are Gaussian fits to the distributions in order to estimate the center positions and width of the distributions. The distribution for the HiPco SWCNTs in gels are centered at $\langle \tau_{short} \rangle = 50$ ps (FWHM=14 ps) and on glass at $\langle \tau_{short} \rangle = 36$ ps (FWHM = 9 ps). The smallest average decay times are observed for CoMoCAT on glass with $\langle \tau_{short} \rangle = 18$ ps (FWHM = 7 ps). The average values for the decay times are in good agreement with the findings for SC encapsulated CoMoCAT SWCNTs in the previous chapter. The relative shift of the center positions of the distributions clearly reflects the influence of the different heterogeneous environments. Especially, the large shift of the center positions of the PL decay time distributions in Fig. 5.1(a) and (c) stresses the large influence of factors related to the synthesis method, such as defects or impurities, on the PL decay dynamics, which is consistent with the observations in ref. [243].

The short and long decay times of all observed biexponential decays in HiPco SWCNTs are plotted in Fig. 5.1(d). The long time component τ_{long} exhibit large tube-to-tube variations, ranging from 0.4 to 2 ns with an average value of $\langle \tau_{long} \rangle = 450$ ps. The corresponding short time component $\langle \tau_{short} \rangle$ varies between 30 to 60 ps. Interestingly, τ_{long} of HiPco SWCNTs in gels (red circles) are systematically shifted to larger times compared to the ones of HiPco SWCNTs on glass (black squares). The same behavior can be also observed for the corresponding distributions of τ_{short} of both HiPco materials in Fig. 5.1(a) and (b). Furthermore, both τ_{short} and τ_{long} are weakly correlated, where large τ_{short} can be associated with large τ_{long} . Furthermore, the fractional amplitudes of the long PL decay time component A_{long} increase with increasing τ_{long} as demonstrated in Fig. 5.1(e) (red line as guide to the eye). Remarkably, only in very few cases biexponential decays are observed for

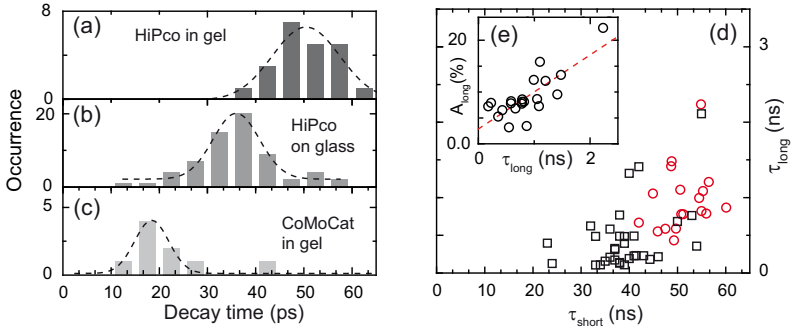


Fig. 5.1. PL Decay time histograms of (6,5) HiPco and CoMoCAT SWCNTs in different environments for the short decay time component (τ_{short}). The dashed curves are Gaussian fits to the distributions. The corresponding center position and the FWHM of the Gaussians are given in parenthesis. (a) HiPco SWCNTs embedded in gel with (τ_{short}) = 50 ps (FWHM= 14 ps). (b) HiPco SWCNTs deposited on glass substrates ((τ_{short}) = 36 ps, FWHM = 9 ps) (c) CoMoCAT SWCNTs on glass substrates ((τ_{short}) = 18 ps, FWHM = 7 ps). About 50% of all HiPco SWCNTs showed biexponential decays, where the fraction in gels was considerably higher than for SWCNTs on glass substrates. CoMoCAT SWCNTs displayed all monoexponential decays. (d) Plot of τ_{long} against τ_{short} for (6,5) HiPco SWCNTs deposited on glass (red squares) and in gels (solid circles) (e) Plot of the fractional amplitude of the long decay time component A_{long} against τ_{long} .

HiPco SWCNTs if the fast decay time component is smaller than ~ 35 ps.

The measurements so far reproduced most of the findings presented in ref. [243], such as the environment induced and synthesis method related shifts of the average PL decay times, with significant faster PL decay times of the CoMoCAT material. Moreover, the biexponential PL decays for HiPco SWCNT in gels and on glass substrates were confirmed. However, the most striking difference to the study mentioned is the strictly monoexponential PL decay of CoMoCAT SWCNTs irrespective of the chosen environment.

5.2.2. PL Decay Dynamics of HiPco (6,4) SWCNTs

Turning now to the PL decay dynamics of (6,4) HiPco SWCNTs. The decay time distributions of (τ_{short}) for (6,4) SWCNTs embedded in gels and deposited on glass follow the same trend, which was observed for the (6,5) SWCNTs. As shown in Fig. 5.2, SWCNTs embedded in agarose gel exhibit a broad PL decay time distribution centered at $\tau_{short}= 51$ ps (FWHM=29 ps) while the decay times of SWCNTs on glass substrates are significantly shifted to shorter average decay times with (τ_{short}) = 18 ps (FWHM = 11 ps).

The fraction of (6,4) SWCNTs in agarose gel which exhibit biexponential decays was less than ~ 10 %, whereas the biexponential decays could only be observed the brightest and longest

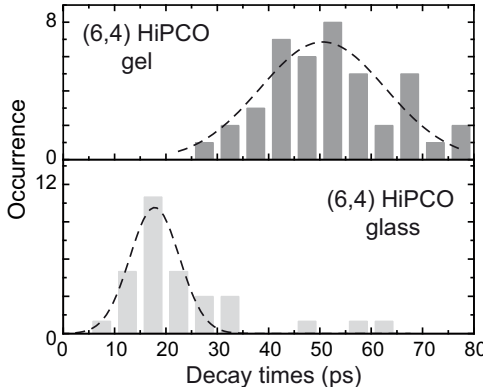


Fig. 5.2. Histogram of PL decay times of HiPco (6,4) SWCNTs in agarose gel and deposited on glass. The distribution of (6,4) SWCNTs on glass is significantly shifted to smaller decay times. Average decay times (width) of the distributions are $\tau_{short}=51$ ps (FWHM=29 ps) and $\langle\tau_{short}\rangle=18$ ps (FWHM=11 ps) for SWCNTs embedded in gel and deposited on glass, respectively.

tubes with decay constants, τ_{long} and A_{long} , of comparable magnitude as for the (6,5) HiPco SWCNTs. No biexponential decays of (6,4) deposited on glass cover slides could be observed.

In order to investigate the absence of biexponential decays in CoMoCAT SWCNTs in general and the low yield of biexponential decays of (6,4) SWCNTs, the PL decay times are plotted against the corresponding PL linewidth. The plot in Fig. 5.3 comprises the various (6,4) data sets of the various (6,4) HiPco and CoMoCAT samples, where the (6,4) CoMoCAT data set is taken from the TCSPC experiments of the previous. For comparison, the data of the (6,5) CoMoCAT SWCNTs deposited on glass (red square) is plotted.

Interestingly, similarly to the findings in the previous chapter Fig. 4.4 (a), a weak correlation between the PL decay times and PL linewidth can be observed for all data sets. Here, a small PL linewidth is correlated with large PL decay times. A narrow PL linewidth and large PL decay times were attributed to only a small number of PL quenching or "dephasing" defects. Based on this argument, one would expect the lowest defect concentration for the (6,4) HiPCO SWCNTs in gels, followed by the (6,4) HiPCO SWCNTs on glass, while the (6,4) CoMoCAT SWCNTs on glass are most influenced by defects or local perturbations due to the environment. Presumably, the longer decay times of HiPCo SWCNTs in gel owe to the fact that the SWCNTs are decoupled from the glass substrates. The substrate is known to strongly influences the excited state properties, leading to exciton localization, energy shifts, reduced QYs and even to the complete suppression of PL of bare SWCNTs deposited on SiO₂ substrates [123, 231]. The distribution of (6,5) HiPco SWCNTs on glass (red squares) is shifted to smaller PL linewidth and longer PL decay times compared to the (6,4) HiPco

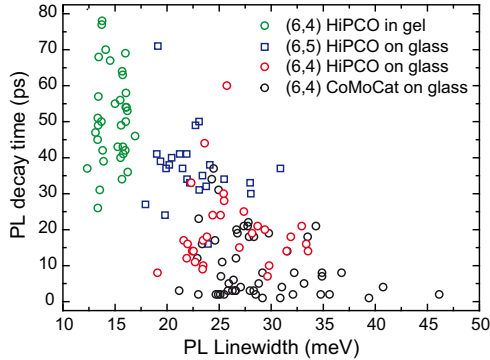


Fig. 5.3. Plot of PL decay times against PL linewidth (FWHM) of (6,4) SWCNTs in different environments: (6,4) HiPCo SWCNTs in gels (green), (6,4) HiPCo SWCNTs on glass (red) and (6,4) CoMoCAT SWCNTs on glass (black). A weak correlation between PL decay times and PL linewidth can be observed, where narrow PL linewidth are associated with long PL decay times. The different environments and SWCNT materials give rise to systematic shifts of the distributions. Especially, SWCNTs in gels exhibit a very narrow linewidth distribution but a broad decay time distribution, while it is very broad for CoMoCAT (6,4) SWCNTs on glass.

SWCNTs on glass. This would indicate that in general (6,5) SWCNTs are less affected by defects. However, the comparison of the properties of two different SWCNT chiralities is elusive, as also tube specific intrinsic properties might cause such a systematic shift of the PL decay times. For example, the electron phonon coupling is predicted to scale inversely with the tube diameter [234]. However, the difference of the diameters of both tube chiralities is rather small, $d_{(6,5)}=0.747$ nm vs. $d_{(6,4)}=0.683$ nm, and is expected not to be the dominant factor.

In summary, the comparison of the PL decay time/PL linewidth plots of the different (6,4) HiPCo and CoMoCat in various environments further validate the picture presented in the previous chapter, where tube-to-tube differences of the nonradiative decay rates, which were attributed to different defect concentration, could be identified as the origin of the observed PL decay time distributions.

5.3. Kinetic Model for the Biexponential PL Decay in SWCNTs

This section starts with an extended review of the model for the biexponential PL decay in SWCNTs which was proposed in refs. [124, 224]. The model is employed to reproduce the biexponential decays which were observed for the majority of the HiPCo SWCNTs. The parameter space is evaluated and furthermore the coupling of various excitonic dark states is discussed.

The kinetic model is an "intrinsic" model, which describes the population dynamics of three coupled intrinsic (excitonic) states. An energy level diagram of the model is depicted in Fig. 5.4 (a). The three states participating, are the two energetically lowest singled exciton states of the E_{11} manifold: the odd parity bright state $|B\rangle$ or accordingly the $(_0A^-)$ exciton and the even parity dark state $|D\rangle$ with the $(_0A^+)$ representation, and the electronic ground state $|F\rangle$. According to the experimentally determined values for the dark-bright splitting energy of similar small diameter SWCNTs between the two excitonic states in ref. [95], here a value of $E_{DB}=5$ meV is assumed.

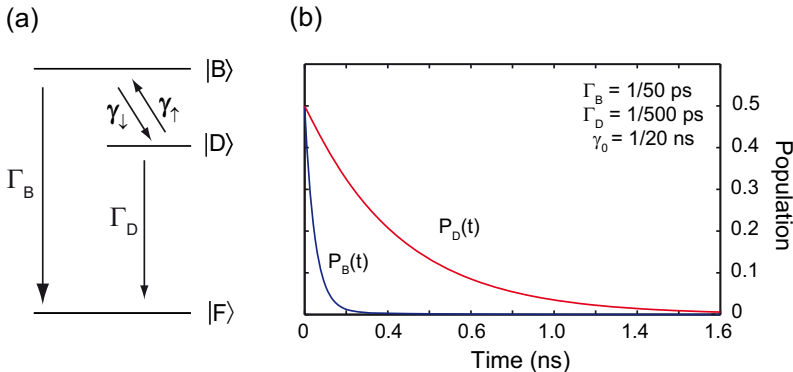


Fig. 5.4. (a) Energy level diagram of the three level model, which is employed for modeling of the biexponential PL decays (details see main text). Small phonon-mediated coupling rates (γ_\downarrow , γ_\uparrow) and a finite initial population of $|D\rangle$ are required in order to obtain significant population transfer from the dark excitonic state back to the bright state. (b) Time evolution of the bright and dark state population. Values for the transition rates are used, which yield the average decay times $\tau_{short} = 50$ ps, $\tau_{long} = 450$ ps and corresponding amplitudes A_{long} as observed in the experiment.

$|B\rangle$ and $|D\rangle$ relax into the ground state $|F\rangle$ with the decay rates Γ_D , which is a purely nonradiative decay rate and Γ_B , which is the sum of the intrinsic radiative rate and an fast dominating nonradiative rate. Further a weak phonon-mediated coupling between $|D\rangle$ and $|B\rangle$ is assumed, presumably activated by defect scattering or coupling to acoustic phonon modes, whose energies matches the dark-bright splitting energy [95, 96]. The transition rates for downhill and uphill scattering processes are denoted as $\gamma_\downarrow = \gamma_0(n + 1)$ and $\gamma_\uparrow = \gamma_0 n$, respectively. Here γ_0 is the zero temperature bright to dark transition rate [94] and n represents the Bose-Einstein occupation number of a phonon mode, which is given by:

$$n = 1 / [\exp(\Delta E_{DB} / k_b T) - 1] \quad (5.1)$$

The kinetic rate equations describing the temporal evolution of the bright $P_B(t)$ and dark state $P_D(t)$ populations write:

$$\begin{aligned}\dot{P}_B(t) &= -(\Gamma_B + \gamma_{\downarrow}) \cdot P_B(t) + \gamma_{\uparrow} \cdot P_D(t), \\ \dot{P}_D(t) &= \gamma_{\downarrow} \cdot P_B(t) - (\Gamma_D + \gamma_{\uparrow}) \cdot P_D(t).\end{aligned}\quad (5.2)$$

These coupled differential equations can be solved analytically using e.g. $P_B = \exp(\lambda \cdot t)$ as a test function and one obtains the general solutions for the time-dependent populations of the bright and dark state ⁶:

$$\begin{aligned}P_B(t) &= C_1 \cdot \exp(\lambda_1 \cdot t) + C_2 \cdot \exp(\lambda_2 \cdot t), \\ P_D(t) &= \frac{1}{\gamma_{\uparrow}} (C_1 \cdot (\lambda_1 - a_1) \cdot \exp(\lambda_1 \cdot t) \\ &\quad + C_2 \cdot (\lambda_2 - a_1) \cdot \exp(\lambda_2 \cdot t)).\end{aligned}\quad (5.3)$$

The decay constants λ_1 and λ_2 are equal to the inverse of the decay times $\lambda = 1/\tau$ and are given as:

$$\lambda_{1/2} = \frac{(a_1 + a_2)}{2} \pm \quad (5.4)$$

$$\sqrt{\left(\frac{(a_1 + a_2)}{2}\right)^2 + \gamma_{\uparrow} \cdot \gamma_{\downarrow} - a_1 \cdot a_2}. \quad (5.5)$$

For the sake of convenience, new rates a_1 and a_2 are introduced, which are defined as follows: $a_1 = -(\Gamma_B + \gamma_{\downarrow})$ and $a_2 = -(\Gamma_D + \gamma_{\uparrow})$. C_1 and C_2 are general amplitude factors, which can be determined by fixing specific initial conditions. For instance C_1 and C_2 can be determined by setting the initial population of the bright state to a value N : $P_B(0) = C_1 + C_2 = N$, where N varies between zero and one. Assuming that after excitation all of the exciton population is only distributed between either the dark or bright state, their initial populations are related by: $P_B(0) + P_D(0) = 1$. In order to compare the modeled decay constants with the experimental ones, the modeled amplitude factors and decay times were used to calculate the fractional amplitudes. From Eqn. 5.3 and Eqn. 5.5 it becomes clear that due to the coupling of the excitonic states there is no simple functional interdependency anymore between the population of the excitonic states and the decay constants. The number of free adjustable parameters in this model is quite high. While the radiative and nonradiative decay rates of the bright state are known from theory or from PL decay time measurements, obviously no numbers exist for the nonradiative decay rate of the dark exciton. Moreover, the branching ratio between the dark and bright state which governs the initial population of these states has not been investigated. Therefore, it is crucial to evaluate how these parameters affect the outcome of the

⁶A detailed derivation of the solution for this problem may be found in the supplementary material of ref. [248].

modeling and to determine the range of their values, for which the experimental results can be reproduced.

As it is the aim of the modeling to investigate the transition from a biexponential decay to a monoexponential decay (or vice versa), the parameter, which shall be reproduced by the model is the fractional amplitude of the long decay time component A_{long} . This is based on the idea that if A_{long} drops below a certain threshold, defined by the experimentally achievable sensitivity and the accuracy of the transient fitting, a biexponential decay can not distinguished anymore from a monoexponential decay. Exemplarily, the modeled population decays of the bright and dark exciton populations are plotted in Fig. 5.4 (b). The average experimentally observed biexponential PL decay constants of $\tau_{short}=50$ ps, $\tau_{long}=450$ ps and a long time component fractional yield $A_{long} = 11\%$, can be reproduced (compare Fig. 5.1 (d)), by assuming the transition rates: $\Gamma_B=20 \text{ ns}^{-1}$, $\Gamma_D=2 \text{ ns}^{-1}$, $\gamma_0=0.05 \text{ ns}^{-1}$ and an equal initial population of $P_B(0)=P_D(0)=0.5$.

A value of 0.5 for the initial dark and bright state population appears to be quite arbitrary. However it can be shown that indeed a constant value for $A_{long}=11\%$ can be reproduced for a broad range of initial populations. This is illustrated in Fig. 5.5 (a), where the range of γ_0 and P_B is plotted, which yields a constant value of A_{long} of 11 %. Here the same fast decay rates Γ_B and Γ_D are assumed as described in the previous paragraph. Importantly, the smaller the initial dark state population ($P_B \rightarrow 0$) gets the more the bright-dark coupling rate γ_1 needs to increase to reproduce the default amplitude value, until it is of comparable magnitude as Γ_B . The whole parameter space of γ_0 and the $P_B(0)$ covering the range of experimentally observed A_{long} values is indicated as the red shaded surface in Fig. 5.5.

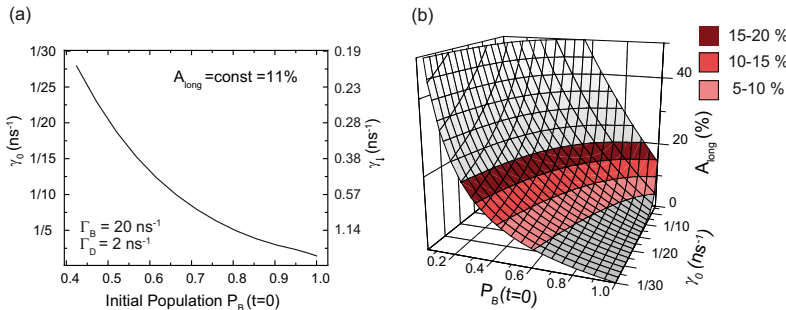


Fig. 5.5. Parameter space for which the three level model yields the experimental decay constants: (a) Range of γ_0 and initial population of the bright excitonic state (P_B) reproducing an average fractional amplitude $A_{long} = 11\%$. (b) A_{long} as function of the zero-temperature coupling rate γ_0 and the initial population P_B . The red shaded surfaces indicate the range of experimentally observed A_{long} values.

In general, for reproducing the biexponential decay constants, transition rates, γ_\uparrow and γ_\downarrow , orders of magnitude smaller than the nonradiative decay rates Γ_B and Γ_D need to be assumed. According to the model, the experimental decay times derived from the fits τ_{short} and τ_{long} are

dominated by the corresponding fast nonradiative decay rates. The situation is different for the fractional amplitude A_{long} . Its magnitude is mainly determined by the zero-temperature coupling rate γ_0 and to a lesser extent by the initial bright and dark state population. The small value of γ_0 corresponding to a bright-to-dark transition probability less than ~ 400 , clearly shows that branching to the lower dark states is not the main factor responsible for the general low PL QY (for the present material) in agreement with [125].

Large initial bright state populations close to 0.8 (vanishing initial dark state population) require slightly larger coupling rates on the order of 0.2 ns^{-1} . Further approaching a bright population of one the bright-dark coupling rate γ_\downarrow needs to get larger than γ_B in order to observe biexponential decays.

In summary it could be shown that for the set of nonradiative decay rates, $\Gamma_B=20 \text{ ns}^{-1}$ and $\Gamma_D=2 \text{ ns}^{-1}$, the three level model can reproduce the experimental range of A_{long} values and indicates that for this an finite initial population of the dark state is required as well as coupling rates, significantly smaller than the observed decay rates. The slow coupling constants found here indicate a non-equilibrium distribution between the bright and dark exciton states in agreement with the results of magnetic brightening PL measurements on these particular excitonic states [220].

5.3.1. Contribution of the K-momentum Excitons

In order to improve the results of the modeling, exact information on the branching ratio after non-resonant or resonant photoexcitation are required to assess the initial dark and bright state population. But more importantly the precise nature of the dark excitonic state needs to be experimentally determined as well as the corresponding dark-bright splitting energy.

To date, there exist no reports on the exact branching ratio of the excited state population after non-resonant photo-excitation and on the corresponding decay cascade into the bright exciton. However, it could been confirmed that upon resonant excitation of the E_{22} excitonic state, fast interband relaxation into the E_{11} manifold takes place within 40–200 fs [249]. Evidence on the population of other dark excitonic states of the E_{11} exciton manifold than the ${}^0A_0^+$ state after resonant E_{22} excitation was found in E_{22} lineshape analysis. Here it was found that the E_{22} exciton decays primarily into the doubly degenerate K-momentum excitons of the E_{11} excitonic manifold [120].

For the modeling of the biexponential decay so far, it was assumed that the dark exciton participating in the bright-dark coupling is the energetically lowest ${}^0A_0^+$ state. However, two additional degenerate finite momentum states, the K-and K'-momentum excitons, exist in chiral SWCNTs, which are energetically located ≈ 40 meV above the bright exciton in (6,5) SWCNTs [99, 100]. Direct optical excitation of this state is forbidden due to momentum conservation selection rules, but they can be indirectly populated via a phonon sideband located at $E_{11} + 170$ meV [99]. Although the energy separation E_{DB} is considerably larger than $k_b T$ its contribution to the biexponential PL dynamics cannot be excluded a priori

as phonon-assisted coupling between both states might be promoted by zone boundary D phonons.

Similarly to the modeling of the biexponential decays involving the $_0A_0^+$ state, the experimental biexponential decays can be also reproduced when considering the energetically situation of the K-momentum exciton. Assuming identical nonradiative decay rates and equal initial population of the bright and dark state, the model yields similar slow γ_0 rates as for the lower lying state.

According to the model, a large initial population of the dark state is a prerequisite for a detectable fractional amplitude A_{long} and thus for the observation of biexponential decays of HiPco SWCNTs. In order to test whether these higher lying dark states influence the PL dynamics significantly, PL decays of (6,5) SWCNTs at two different excitation wavelengths were recorded. In one case a wavelength of 834 nm was chosen to nearly match the energy of the K-exciton-phonon state, while in the other case an excitation wavelength of 920 nm was chosen which is quite close to the energy of the E_{11} transition of the bright state. Interestingly, switching between these two excitation wavelengths does not change the decay dynamics substantially. Only small changes in the fractional amplitudes and decay times have been observed (data not shown), which indicates that the K-momentum exciton is not involved the biexponential decay. However, in order to clarify the origin of the dark state participating in the coupling low-temperature PL decay time measurements are required.

5.4. Discussion

The main findings of the experimental sections regarding the PL decay dynamics CoMoCAT and HiPco SWCNTs exposed to different environments can be summarized as follows:

1. Biexponential decays for (6,5) HiPco SWCNTs in agarose gel and up to ~50 % on glass
2. Monoexponential decays for CoMoCAT SWCNTs
3. Biexponential decay only for (6,5) HiPco SWCNTs with $\langle \tau_{short} \rangle \gtrsim 35$ ps
4. No biexponential decay for HiPco (6,4) SWCNTs despite large PL decay times

In the following the aforementioned observations are discussed. It will be shown that the kinetic three-level model, which was introduced in Sec. 5.3 can be extended to explain also the transition from mono to biexponential PL decays.

5.4.1. Transition from Mono- to Biexponential PL Decays

The three level model in Sec. 5.3 represents the "ideal" SWCNT with only a minimum number of defects. However, weak PL QYs of the bright state are limited to a few percent

[123,124,211,212,250] and is attributed to nonradiative relaxation pathways, typically occurring in the tens of picoseconds. In fact, the systematical shifts of the PL decay time distributions and also PL linewidth distributions of (6,4) HiPco and CoMoCAT SWCNTs in different environments indicate that the average number of defects for the different materials should be different (compare Fig. 5.3). In order to account for such additional extrinsic defects, the three level model is modified by introducing an additional fast nonradiative decay rate Γ_{NR}^{ex} . Further it is assumed that Γ_{NR}^{ex} affect the dynamics of both states, $|D\rangle$ and $|B\rangle$. This additional defect related decay channel is indicated in Fig. 5.4 (a) by the red dotted lines.

The quality of the transient data might strongly influence whether a PL decay is identified as mono- or biexponential. A high SNR of the transients is necessary so that the least square fitting procedure yields reliable values for the decay constants, especially if one of the fractional amplitudes of a decay component is small. Mono- and biexponential decays might become experimentally indistinguishable, if both decay times τ_{short} and τ_{long} are of comparable magnitude and/or if the fractional amplitude A_{long} decreases below a certain threshold which is given by the overall detection sensitivity of the TCSPC experiment (including the fitting).

This transition from a biexponential to monoexponential decay dynamics can be reproduced by adding an additional defect related decay channel with the rate Γ_{NR}^{ex} . The effect of a steadily increasing Γ_{NR}^{ex} on the long decay time component on A_{long} is illustrated in Fig. 5.6 (a) and (b), where the evolution of τ_{long} as a function of τ_{short} and A_{long} as a function of τ_{long} are modeled for increasing values of Γ_{NR}^{ex} from 0 to 30 ns^{-1} .

The areas below the dotted lines indicate the regime where τ_{short} and τ_{long} are experimentally indistinguishable and correspondingly A_{long} is extremely small. In this case, the experimental PL decays are monoexponential. In this context, also the observation that biexponential decay are mostly measured for SWCNTs with a longer τ_{short} can be explained. For instance, adding a typical rate [125] of $\Gamma_{NR}^{ex} = 20\text{ ns}^{-1}$ to the previous values of Γ_B and Γ_D , the exciton recombination dynamics becomes fast and monoexponential with a decay time $\tau_{short}=25\text{ ps}$ in agreement with the experimental observation.

5.4.2. Biexponential Decays in HiPco (6,4) SWCNTs

Although the decay times of some (6,4) SWCNTs in gels were quite large decay times, in some cases exceeding $\tau_{short}>50\text{ ps}$, only a very small fraction of (6,4) SWCNTs showed a biexponential decay could. Regarding the PL decay dynamics of individual (6,4) HiPco SWCNTs deposited on substrates, there are at present only two publications [223, 247]. In both cases these are low temperature TCSPC experiments, however controversial decay dynamics were reported. While Hagen et al. reported on strictly monoexponential decay of HiPco SWCNTs [223], whereas the PL dynamics in the study of Högele et al. for low excitation power could be best described by a biexponential decay, with similar decay times as observed here [247].

Assuming the same three level model for the population dynamics of the (6,4) SWCNT, there might be various factors, which can reduce A_{long} below the detection limit. First a reduced

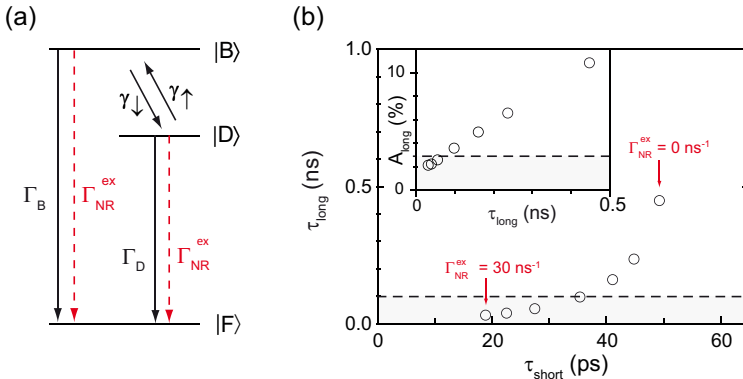


Fig. 5.6. (a) Modified three level model for the coupling between dark and bright excitonic states. An additional extrinsic defect related non-radiative decay channel which affects the population of both states is added (red arrow). (b) Theoretical long decay times τ_{long} as a function of the short component τ_{short} , deduced from modeled PL decays. Here an extrinsic fast defect related nonradiative decay rate Γ_{NR}^{ex} was assumed, which affects the population dynamics of both, the $|B\rangle$ and $|D\rangle$ states. Increasing Γ_{NR}^{ex} from 0 to 30 ns^{-1} results in an decrease of the τ_{short} and τ_{long} . Inset: The corresponding A_{long} is plotted as a function of τ_{long} . The grey shaded areas indicate the domains where τ_{short} and τ_{long} are experimentally indistinguishable or correspondingly A_{long} is extremely small.

dark-bright transition rates γ_\downarrow and/or larger defect related nonradiative decay rate, due to e.g. different efficiencies of the micelle wrapping, Γ_{NR} . Secondly, the initial population of the dark and bright states P_B could be different. However, a discussion of this parameter would be purely speculative, as no information exists on this topic.

Keeping all other parameters the same as for the (6,5) SWCNTs, modifying Γ_{nr}^{ex} would in fact, reduce A_{long} but would also lead to fast effective decay times τ_{short} . In order to reproduce the experimentally observed decay times this would require larger Γ_B in the range of 80–100 ps to reproduce the experimental data.

Smaller coupling rates between the bright and dark state, γ_\downarrow and γ_\uparrow , are expected for increasing bright-dark splitting energies ΔE_{bd} . Calculated and experimentally measured splitting energies ΔE_{DB} for the same SWCNT chirality can cover a broad range of 5–30 meV [91, 92, 251, 252]. While ΔE_{DB} could be experimentally determined in case of the (6,5) SWCNT and SWCNTs with larger diameters between 1–1.3 nm [252], at present no experimental data is available for the (6,4) SWCNT, while theory reports values of 40 meV [253]. However, theory predicts that ΔE_{DB} scales inversely with the square of the diameter [92]. Despite the uncertainty of the exact ΔE_{DB} values, the influence of a changing ΔE_{DB} can be investigated qualitatively.

Based on the predicted diameter dependence of the splitting energy, smaller dark-bright coupling rates and thus in general smaller A_{long} values for the (6,4) compared to the (6,5) SWCNT would be expected, considering the different SWCNT diameters of $d_{(6,4)}=0.683\text{ nm}$ vs.

$d_{(6,5)}=0.747$ nm. From the modeled dependence of A_{long} as a function of ΔE_{DB} in Fig. 5.7 it becomes obvious that already a slight increase of ΔE_{DB} by a few meV leads to a considerable reduction of A_{long} by a factor of two. For the modeling, all parameters, except for ΔE_{DB} , were kept the same as for the modeling of PL decays of the (6,5) SWCNT in the previous sections.

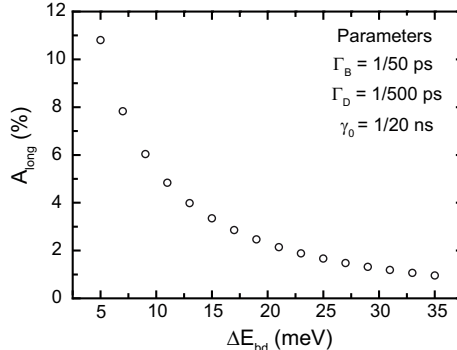


Fig. 5.7. Dependency of A_{long} on the dark-bright splitting energy ΔE_{DB} . Here the same decay rates are assumed as described in the main text. ΔE_{DB} decays exponentially and therefore A_{long} responds more sensitive to smaller changes. In the case of the (6,4) tubes, which are supposed to exhibit a slightly larger ΔE_{DB} due to the inverse diameter scaling of E_{DB} . This might explain the low yield of biexponential decays compared to the (6,5) SWCNTs.

Differences in ΔE_{DB} indeed might explain the low yield of biexponential decays for the (6,4) SWCNT. Furthermore, fluctuations of the local dielectric environment can also lead to changes in ΔE_{DB} [252] and by this contribute to the variations of A_{long} values. However, for a better understanding of the diameter (chirality) dependence of the biexponential decays, the PL decay dynamics of more SWCNT chiralities has to be analyzed.

5.5. Conclusion

In summary the influence of the environment on the PL decay dynamics of SWCNTs was studied by TCSPC and PL spectroscopy of individual SWCNTs. Two different chiralities were studied, the (6,5) and (6,4) SWCNT, produced by different synthesis methods, the HiPco and CoMoCAT CVD process. The SWCNTs were either deposited on glass or embedded in aqueous agarose gels.

One aim of this study was to clarify the PL decay dynamics of (6,5) CoMoCAT SWCNTs. In contrast to the reported decay behavior in reference [243], it was found here that the PL decay behavior of this SWCNT material is strictly monoexponential irrespective of the specific SWCNT environment. However, consistent with the observations reported in ref. [243], the

majority of (6,5) HiPco SWCNTs in aqueous agarose gels and on glass surfaces exhibit a biexponential decay behavior.

The environment of the SWCNT and even more importantly the specific synthesis method considerably affects the PL decay dynamics and PL decay times. In general, the average PL decay time of HiPco SWCNTs is significantly larger compared to the one of CoMoCAT material with the same chirality and exposed to identical environmental conditions. The fraction of biexponential decays of (6,5) HiPco SWCNTs in gel is considerably larger than for HiPco SWCNTs on glass substrates, stressing the importance of the different environment. The short time components of the HiPco SWCNTs exhibit a broad distribution between 15–80 ps, while the long decay component is in the range of 0.2–2 ns with small fractional amplitudes between 3–15 %. In most of the cases, biexponential decays are observed for HiPco SWCNTs with a short decay time component larger than approximately 35 ps. No biexponential decays were observed for the (6,4) chirality irrespective of SWCNT material and the environmental conditions.

The analysis of the PL spectra and corresponding decay times suggest that fast defect related nonradiative decay channels are responsible for the systematic differences of the PL decay dynamics of HiPco and CoMoCAT SWCNTs. The reason for this might be that the different synthesis conditions of the HiPco and CoMoCAT processes result in different average defect densities, whereas the defect density of CoMoCAT SWCNTs is in general higher compared to the one of HiPco SWCNTs. A kinetic three level model which considers the phonon-mediated coupling between the bright excitonic state and a lower energy dark state [124] was successfully employed to reproduce the transitional behavior between mono- and biexponential PL decays. Based on the model and consistent with the experimental observations, defects related to the different environments or synthesis methods give rise to an additional fast nonradiative decay channels affecting the population decay of both, the bright and dark state. The rate of the nonradiative decay is correlated with the specific defect density of a SWCNT and is expected to be large for SWCNTs which are highly defective. This additional defect related nonradiative decay channel reduces the amplitude of the long decay time component and also reduces the long decay time. If the nonradiative rate (defect concentration) exceeds a certain threshold level mono- and biexponential decays become experimentally indistinguishable.

6. Defect Induced PL of Dark Excitonic States in Individual SWCNTs

This chapter is based on the papers "*Defect induced photoluminescence of dark excitonic states in individual SWCNTs*" and "*Photoluminescence from disorder induced states in individual single-walled carbon nanotubes*" which have been published in *Nano. Lett.* **9**, 2010 (2009) and *phys. stat. sol. (b)*, **246**, 2579 (2009), respectively.

6.1. Introduction

SWCNTs exhibit a complex sequence of singlet and triplet excitonic bands below the free-carrier bandgap [80, 94, 106]. The majority of these excitons in SWCNTs are dark excitons, optically forbidden due to optical dipole transitions rules, such as parity and spin selection rules. Dark excitonic states below the optically bright state such as the odd parity and the sequence of triplet states are expected to participate in the optical relaxation processes [81, 221]. Detailed studies of the properties of the experimentally difficult to assess dark excitonic manifold are therefore essential for both full understanding of the excited state dynamics and for engineering of the optical properties of SWCNTs. Symmetry breaking effects, like disorder, such as defects or impurities, or externally applied electric or magnetic fields, are expected to relax the optical selection rules and lead to brightening of nominally dark states [94].

The direct "brightening" of a dark states was reported the first time by Srivastava et al. [252]. In their pioneering work, a strong magnetic field was applied aligned parallel to the axis of the tubes, which resulted in the emergence of a new low lying emission peak energetically separated from the main emission peak by only 1–4 meV and was assigned to the odd parity $\text{}_0\text{A}_1^+$ exciton. Low-energy forbidden states were also used to explain the dynamics observed in pump-probe experiments [102, 217] and the temperature dependence of PL intensities [95]. Furthermore, low-energy PL satellite bands were observed in ensemble [221] and single nanotube PL measurements [98]. These bands were attributed to emission from various low lying ("deep") dark excitonic states while the mechanisms enabling optically forbidden transitions and the interplay between bright and dark excited states remain to be clarified. Only recently, the origin of another group of low-energy PL satellite bands was clarified. Here, a PL band consistently appearing at 140 meV below the main emission band of (6,5) SWCNTs were attributed to a phonon-replica of the finite momentum K excitons [99, 100].

The complex sequence of dark excitonic states and possible nonradiative relaxation channels associated with them are expected to have an important impact on the low PL quantum yield of SWCNTs and fast exciton decay rates [124, 209, 223], consistent with the experimental finding of the previous chapter. Here, the origin of the observed biexponential PL decays was attributed to a slow phonon-mediated coupling between the bright and a dark excitonic state, presumably the odd parity ${}_0A_0^+$ exciton. A small phonon-mediated dark-bright coupling rate needs to be assumed to explain the experimental results, indicating that both states are not in thermal equilibrium. Furthermore, the transition from the dark state to the ground state was purely nonradiative and/or could not be spectrally resolved at room-temperature due to the small energy separation between both states. However, whether the coupling between the bright and dark state is an intrinsic property of the SWCNT mediated by intrinsic acoustic phonon modes or whether the coupling is induced by external perturbations, such as defect related low-energy phonon modes, still needs to investigated. In this context, it is demonstrated in this chapter that disorder introduced to individual SWCNTs can enhance the coupling between intrinsic optically allowed and dark excitonic states. Moreover it and finally results in "brightening" of the dark state, leading to additional low-energy PL satellites.

6.2. Optical Characterization of Photoinduced Low-energy Emission Bands

Confocal PL spectroscopy in combination with TCSPC measurements is used to acquire PL spectra and PL transients. Laser excitation was provided by a Ti:sapphire oscillator, which was operated at a photon energy of 1.63 eV (760 nm). The repetition rate was 76 MHz and the pulse duration was estimated to be 150 fs. Details about the measurement procedures for the acquisition of PL spectra and PL transients are given in the experimental section Chap. 3. The sample material used for this study are micelle encapsulated CoMoCAT SWCNTs using SC as a surfactant. Samples with spatially isolated SWCNTs were prepared according to the description in Sec. 3.2.2.

In the following, the creation of low-energy satellite peaks in the PL spectra of two individual SWCNTs with different chiralities is illustrated.

Fig. 6.1 shows the initial PL spectra (black curves), which were acquired at low power pulsed excitation intensities of approximately $I_0 = 3 \cdot 10^{13}$ photons pulse $^{-1}$ cm $^{-2}$. Both initial spectra exhibit a single emission band corresponding to the bright excitonic state $|B\rangle$ each centered at (a) 1.41 eV and (b) 1.46 eV, respectively. Based on the PL energies, the chiralities of the SWCNTs can be assigned to a (6,4) in the case of Fig. 6.1(a) and to (5,4) SWCNT in Fig. 6.1(b) [50]. Persistent irradiation of the nanotubes for 10–100 seconds with an order of magnitude higher pulse intensity $17 \cdot I_0$ results in several cases in significantly modified PL spectra (red curves) with additional red-shifted shoulders on the main PL peak, or as shown here with low-energy PL satellite bands energetically well separated from the main PL band, transfer-

ring substantial spectral weight to these new emission features. Importantly, no such spectral changes were induced at the corresponding averaged power levels using CW excitation suggesting that high pulse intensities initiating multi-photon processes are crucial to induce these modifications. High power CW excitation, on the other hand, mainly leads to photobleaching and blinking of the nanotube PL [126].

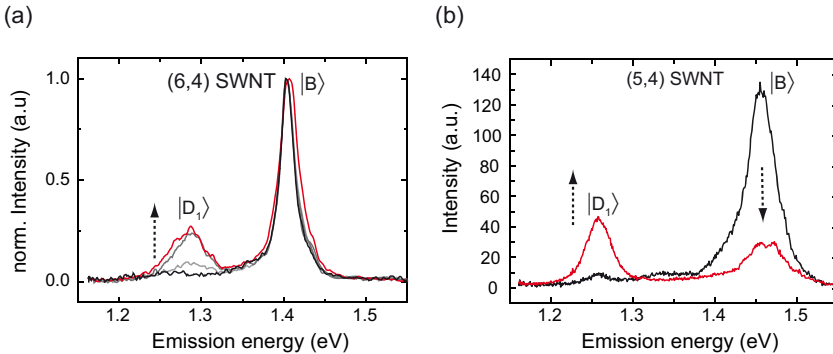


Fig. 6.1. Creation of low-energy satellite peaks in the PL spectrum of a (a) (6,4) SWCNT and (b) a (5,4) SWCNT. Initial spectra (black) acquired at low excitation intensity $I_0 = 3 \cdot 10^{13}$ photons $\text{pulse}^{-1} \text{cm}^{-2}$ and considerably modified spectra (red) of the same nanotubes acquired after exposure to high excitation intensity $17I_0$. Low-energy satellite contributions shifted by 30–60 meV ($|D_2\rangle$) and 110–190 meV ($|D_1\rangle$) with respect to the bright exciton emission are assigned to PL from optically dark states. The spectra in (a) were acquired sequentially between initial and final spectrum at an intermediate intensity of $7I_0$ illustrating the step-like creation of the additional bands.

No direct correlation between the excitation intensity and the intensity of the newly induced emission band can be observed. The grey lines in Fig. 6.1(a) are spectra acquired sequentially between initial and final spectrum at an intermediate intensity of $7I_0$. The appearance of the new emission band is rather step-like and random.

The satellite peaks for different (6,4) and (5,4) nanotubes consistently appear at similar energies. They can be roughly divided into two groups with energy separations to the PL of the $|B\rangle$ state of $\sim 110\text{--}190$ meV and $30\text{--}60$ meV. According to [98], will be denoted as $|D_1\rangle$ and $|D_2\rangle$, respectively. The determined energy separations are in good agreement with the PL energies of the satellite peaks in reference [98]. Comparable splitting energies of 130 and 40 meV were predicted for the triplet and even parity singlet excitons in (6,4) nanotubes, respectively [253]. The polarization analysis of the PL emission of the $|B\rangle$ band and the newly created emission satellite $|D_1\rangle$ is depicted in Fig. 6.2. Both show the same $\cos^2\theta$ angular dependence, proving that both emission bands belong to the same nanotube and indicate that the red-shifted emission in fact originates from an intrinsic state of the SWCNT.

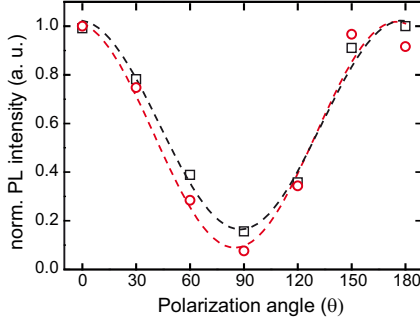


Fig. 6.2. Polarization dependence of the PL emission for the bright exciton $|B\rangle$ (red circles) and the dark exciton $|D_1\rangle$ (black squares) determined from a series of spectra recorded for the same (6,4) nanotubes. The dashed lines are $\cos^2 \theta$ fits to the data.

6.3. PL Decay Dynamics of the Dark and Bright States

In order to determine the population dynamics of both the main and satellite PL emission bands and to study the effect of the disorder created due to the intense laser irradiation, time-resolved PL measurements of the different emission bands were performed before and after creation of emission satellites. Fig. 6.3 (a) and (b) depict representative PL transients of two individual nanotubes belonging to the (6,4) and (5,4) chirality, respectively. For the acquisition of the transients, PL emission was detected only from the narrow spectral range which indicated by the grey shaded boxes in the insets.

Two important conclusions can be drawn from this data. First, upon creation of the satellite peaks the bright exciton lifetime is decreased (grey curve) compared to the initial decay (black curve), and second, the $|D_1\rangle$ emission has a much longer decay time. Monoexponential fits (dashed lines) to these transients give the lifetimes of the main emission peaks before and after creation of the red-shifted band of 20 ps and 6 ps for the (6,4) nanotube Fig. 6.3 (a) and 13 ps and 2 ps for the (5,4) tube (Fig. 6.3 (b)), respectively. The emission bands with smaller energy shifts in the range of several 10 meV ($|D_2\rangle$) exhibit exactly the same decay behavior as the main peak (data not shown).

The decay of the dark exciton $|D_1\rangle$ is dominated by much longer time constants, 65 ps and 177 ps for the (6,4) and the (5,4) nanotube in the present example. Thus, other origins of the low-energy bands such as bi-excitons and phonon replica of the bright exciton can be ruled out based on this slow decay dynamics. Additionally, a fast decay component was observed (8 ps and 2 ps) with far smaller photon flux (about factor 1/20). This component is either due to transitions from $|D_1\rangle$ to $|B\rangle$ or to other dark excitonic states within the $|D_1\rangle$ manifold. In general, the decay dynamics of $|D_1\rangle$ is expected to be complex and difficult to assess since the defects responsible for the brightening will be localized, presumably affecting only finite length nanotube sections on the order of the diffusional range of about 110 nm [113,126].

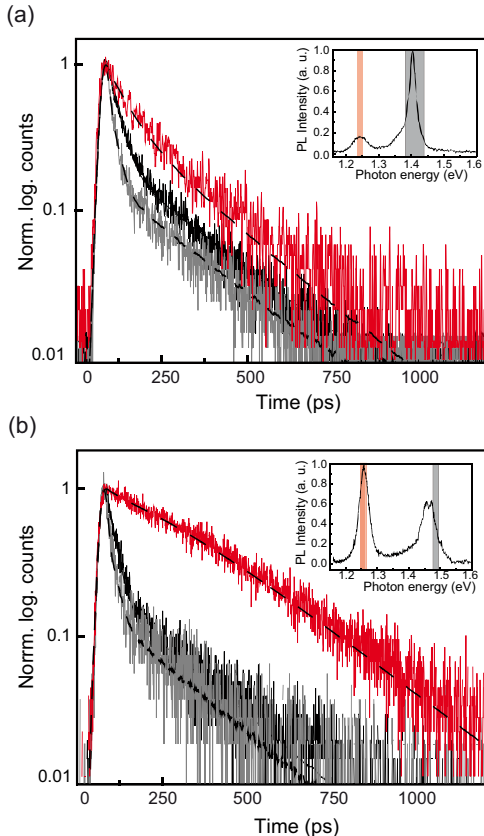


Fig. 6.3 Semi-logarithmic plot of the PL transients visualizing the decay dynamics of different emission peaks in the spectra of individual SWCNT (insets) for two different chirality nanotubes: (6,4) (a) and (5,4) (b). Black curves show the decay of the $|B\rangle$ state detected in the grey shaded spectral range in the insets before creation of the low-energy satellites. After creation of the dark state emission the decay rate of the bright exciton is increased significantly (grey lines). The PL decay of the dark excitonic state $|D_1\rangle$, which is red shifted by 110–190 meV with respect to the emission of the $|B\rangle$ state, is substantially slower (red curves). PL decay traces detected for smaller shifts of 30–60 meV resulting from $|D_2\rangle$ are identical to those of the bright exciton (data not shown). Dashed lines are exponential fits to the data (see text).

Because of the large separation of the emission peaks and the detected spectral windows (shaded areas in insets in Fig. 6.3 (a) and (b)), overlapping emission contributions from the $|B\rangle$ state are not sufficient to explain this decay component. Measurements on several other (6,4) and (5,4) SWCNTs consistently show the same effects with $|D_1\rangle$ lifetimes ranging up to 177 ps. Decay times derived from time-resolved PL and pump-probe data in the range of 50–300 ps with small relative amplitudes have been reported previously [215, 224] from ensemble samples as part of multiexponential decay. Presumably these decay times could originate from the newly created states observed here.

6.4. Investigation of the Dark State "Brightening" Process

Two findings of the previous sections indicate that defects are created in the SWCNTs upon "brightening" of the dark state using high power laser pulses. First, there is the reduced PL intensity of the main emission band after "brightening" of the dark state. Second, the PL decay times of the $|B\rangle$ are considerably smaller after the "brightening". On the one hand, the reduced PL intensity might indicate a substantial transfer of oscillator strength from the bright to the dark state. On the other hand also photoinduced PL bleaching might account for this behavior, which would be also supported by the reduction of PL decay times. In Chap. 4 it was shown that inherently present defects in SWCNTs lead to broad PL decay time distributions and are the dominant factor for facilitating the fast nonradiative decay for the studied CoMoCAT material. A small PL decay time can be attributed to an increased number of PL quenching defects along the SWCNT.

6.4.1. Raman Spectroscopy of Photoinduced Defects

Symmetry breaking processes are known to facilitate the mixing of excitonic states with different parity and/or spin [94, 106]. Thus, photoinduced defects created in consequence of the high power pulsed irradiation might account for the "brightening" of the dark state. In the following, the role of externally introduced defects in the "brightening" process is studied in more detail, starting with Raman spectroscopy of SWCNTs, which allows to evaluate the degree of disorder introduced in sp^2 hybridized carbon materials by monitoring the I_D/I_G -ratio of the first order D and G Raman bands (see also Sec. 1.6).

In the following the effect of the pulsed laser irradiation on the Raman spectra of individual SWCNTs is studied. The sample material for these experiments are DNA-wrapped CoMoCAT SWCNTs. For those it was found that they exhibit a stronger Raman signals at the available laser wavelength of 594 nm compared to the SC encapsulated SWCNTs. The excitation wavelength is nearly matching the energy of the E_{22} transitions of the (6,4) and (6,5) chiralities at 578 nm and 566 nm, respectively. The stronger Raman signals of DNA-wrapped SWCNTs can be attributed to improved resonant excitation conditions as the result of a more red-shifted E_{22} transition energy in the case of the DNA-wrapped material. Such systematical shifts in transition energies are well known and are the consequence of differences in the local dielectric environment of the nanotube

In order to conduct "brightening" and Raman experiments on the same SWCNT, the foci of the 760 nm Ti:Sapphire oscillator and of a 594 nm HeNe CW laser were overlapped on the sample. The relative positions of both foci were controlled and optimized by repeatedly acquiring PL images until with each laser until the PL features appeared at identical positions in both scan images. Raman spectra were acquired before and after irradiation with high power laser pulses with integration times of 20 s and excitation powers of $81 \mu\text{W}$. In test experiments it was verified that CW excitation with these acquisition settings does not result in significant

changes of the Raman bands. The intensity of the "brightening" pulsed excitation light was $6 \cdot 10^{13}$ photons pulse $^{-1}$ cm 2 .

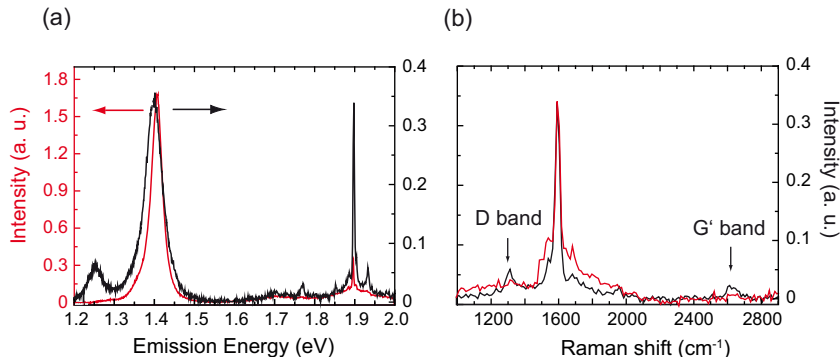


Fig. 6.4. (a) PL and (b) Raman spectra of a single DNA-wrapped (6,4) SWCNT before (red curve) and after (black curves) exposure to high power pulsed laser irradiation at 760 nm ($6 \cdot 10^{13}$ photons pulse $^{-1}$ cm $^{-2}$) for 20 s. The spectra were recorded using CW 594 nm laser excitation and excitation powers of $81 \mu\text{W}$. The intensity axis in (a) left side: before, right side: after exposure to pulsed laser light.

Fig. 6.4 illustrates the changes introduced to the (a) PL and (b) Raman spectrum of an individual SWCNTs upon exposure to high power pulsed laser light. Spectra acquired before and after the high power exposure are red and black, correspondingly. In the PL spectra of Fig. 6.4 (a) the high power irradiation leads to the emergence of a $|D_1\rangle$ PL satellite band. Consistent with the observation in Fig. 6.1(b) also here the PL peak intensity is reduced to approximately 1/5 of its initial value. Furthermore, also the corresponding Raman spectrum in Fig. 6.4 (b) is modified by the pulsed irradiation. While in the initial spectrum (red curve) the intensity of the defect related D band at 1300 cm^{-1} is very small, it is slightly increased in the modified spectrum (black). This in turn results in an increase of the I_D/I_G intensity ratio, typically attributed to the introduction of additional defects [132]. Furthermore, the relative decrease of the PL compared to the Raman G-band intensity indicates a reduction of PL quantum yield.

Another example for the changes in the Raman and PL spectra as the result of the "brightening" process is shown in Fig. 6.5. Here, an individual (6,4) SWCNT was exposed in consecutive intervals of 30 s to the pulsed excitation. Between each illumination step the Raman spectra was measured. For the sake of clarity only three spectra are plotted. The PL spectra are plotted in Fig. 6.5 (a) and show the evolution of the $|B\rangle$ and a $|D_2\rangle$ satellite band. In the beginning, pulsed laser irradiation leads only to PL bleaching. After six illumination cycles the new PL band appears abruptly. Further illumination only results in changes of the $|B\rangle/|D_2\rangle$ PL intensity ratio. The intensity of the first order Raman G-band (Fig. 6.5 (c)) and the second order D- and G'-bands in Fig. 6.5 (c) and(d) change after each illumination period

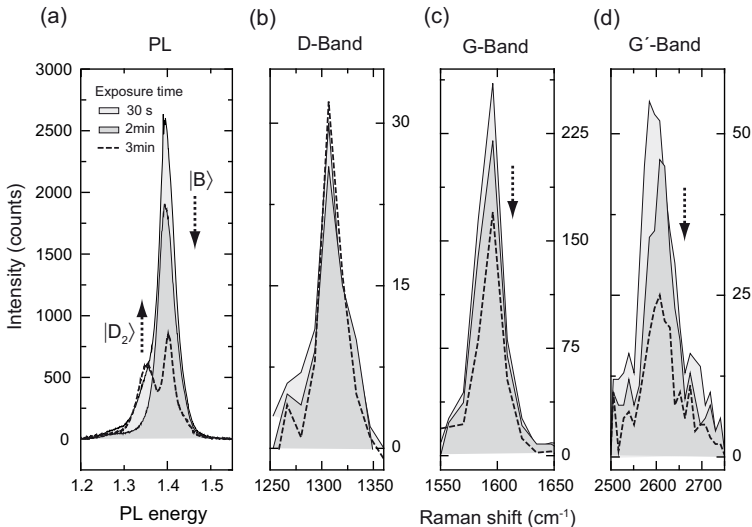


Fig. 6.5. Temporal evolution of PL (a) and Raman spectra (b-d) measured for a single DNA-wrapped (6,4) SWCNT after consecutive illumination with high power laser pulses ($6 \cdot 10^{13}$ photons $\text{pulse}^{-1} \text{cm}^{-2}$) at 760 nm. The exposure time was 20 s per cycle. The initial (white), final (dotted) and intermediate (grey) spectra are shown. (Please note: For the sake of clarity intermediate spectra are omitted). The brightening of the $|D_2\rangle$ which is approximately $\Delta E_{DB}=50$ meV below the bright state is accompanied by a reduction of the PL and Raman G-band intensity, whereas the Raman D-Band intensity slightly increases.

with the pulsed laser. A small increase in the D-band intensity and a more pronounced decrease of the G-band intensity results in an overall increase of the I_D/I_G intensity ratio, indicating that also here additional defect sites are created.

It is to note that PL bleaching accompanied by an increase of the I_D/I_G -ratio can be also observed for CW excitation and is not an exclusive phenomena associated with the high power pulsed excitation. The PL bleaching of a DNA-wrapped (6,5) SWCNT is shown in Fig. 6.6. Here, spectra are acquired in a kinetic series with 30 s integration time, while constantly illuminating the SWCNT with CW excitation at 594 nm and excitation powers of 50 μW . While the PL intensity is significantly reduced (Fig. 6.6 (a)), the Raman D-Band intensity increases which overall results in an increase of the I_D/I_G -ratio.

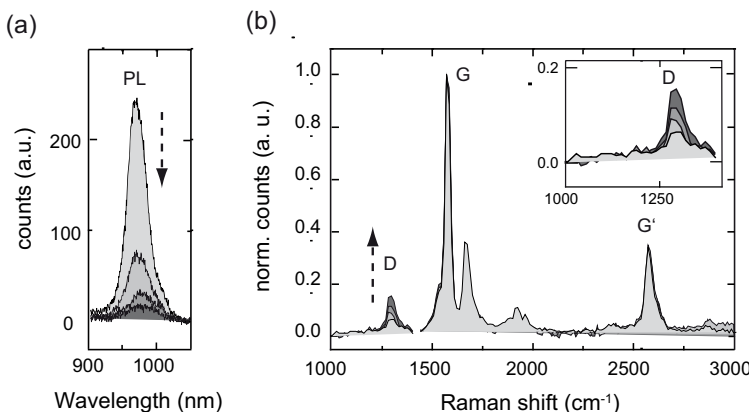


Fig. 6.6. Evolution of PL and Raman spectra of a (6,5) DNA-wrapped CoMoCAT SWCNT upon continuous CW excitation. (a) Decrease of the PL intensity. (b) Corresponding Raman spectra normalized to the G-band intensity. The reduction of PL intensity is accompanied by an increase of the Raman D-Band. The excitation wavelength was 594 nm and the excitation powers were 50 μW with an acquisition time per spectrum of 30 s.

The experiments so far indicate that the high power pulsed laser irradiation used for the brightening of the dark states leads to an increase of disorder by creation of defects, consistent with the observation of an increase in the I_D/I_G -ratio and of strong PL bleaching. However, the same photo modifications of the PL and Raman spectra can be observed also for CW excitation, where the low-energy satellite bands do not appear. This indicates that the defects causing PL bleaching and the defects activating the "brightening" process are different. As the defects responsible for PL bleaching also lead to the increase of the I_D/I_G -ratio, no direct correlation between the brightening process and the D-band intensity is possible. Furthermore, it could be shown that the "brightening" of the SWCNTs is independent of the nature of the surfactant. The same new emission can be created also in the PL spectra of DNA-wrapped

SWCNTs, which indicates that the "brightening" is not due to a photo-induced chemical reaction exclusively specific for a certain surfactant.

6.4.2. The Role of Oxygen in the Photoinduced "Brightening" Process

The process proposed for PL bleaching of SWCNTs deposited on glass substrates and exposed to ambient atmosphere is a photoinduced sidewall oxidation. This process occurs already at low to medium CW excitation powers ($5\text{--}100\text{ kW cm}^{-2}$) and leads to the creation of a hole at the oxidation site, which in consequence facilitates the nonradiative decay of the bright exciton due to an efficient Auger recombination process [126, 129]. The availability of physisorbed oxygen appears to be controlled not only by the oxygen concentration in the atmosphere but also by the surface morphology and coverage [126] and it was indicated that PL bleaching can be significantly reduced, when working in an inert gas atmosphere or covering the SWCNTs by immersion oil. While no additional PL sidebands were reported in similar CW PL bleaching studies, it might be speculated that the higher photon densities due to the pulsed excitation might open additional oxidation pathways, including multi-photon processes. This might lead to oxygen assisted removal of carbon atoms under formation of carbon dioxide or carbon monoxide and thus the introduction of vacancy sites.

In order to study the influence of the availability of oxygen on the brightening process, the PL spectra of micelle encapsulated CoMoCAT SWCNTs and DNA wrapped CoMoCAT SWCNTs covered either by immersion oil or by a polymer film of poly(methyl methacrylate)(PMMA) were acquired before and after irradiation with high power laser pulses of $\sim 50 \cdot I_0$. For both oxygen reducing media, the satellite peaks could be created, however the percentage of "brightening" events compared to the ambient conditions was significant smaller. Exemplarily, the PL spectra of an individual DNA wrapped (6,4) SWCNT embedded in matrix of PMMA before and after the "brightening" are depicted in Fig. 6.7.

The initial spectrum (black) shows the emission from the $|B\rangle$ state, with the broad PL linewidth characteristic for DNA-wrapped SWCNTs compared to micelle encapsulated SWCNTs [198]. The emission energy of the satellite band 1.25 eV and can be assigned to the $|D_1\rangle$ group.

The smaller number of observed dark state "brightening" events for SWCNTs embedded in oxygen reducing environments suggests that the availability of oxygen plays a crucial role for the brightening process. On the other hand, If the defects induced by the laser pulse are sidewall modifications of the robust sp^2 hybridized structure of the nanotube then the modification barrier, larger than the excitation photon energy, will probably be very sensitive to the thermal conductivity of the system.

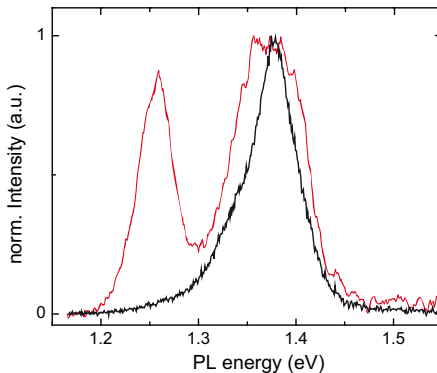


Fig. 6.7. PL spectra of an individual DNA-wrapped (6,4) SWCNT covered by a thin layer of PMMA. The initial spectrum (black) shows broad emission from the $|B\rangle$ state, characteristic for DNA-wrapped nanotubes [198]. Also in the case of an oxygen reducing environment the PL satellite bands can be created with high power pulsed irradiation (red). However, the process here is far less efficient than in ambient atmosphere with a significant reduced yield of "brightening" events.

6.4.3. Brightening by Treatment With a Colloidal Gold Solution

An alternative approach for the "brightening" of dark excitonic states is guided by the idea that transition metal adatoms adsorbed at the SWCNT sidewalls might lead to the formation of localized states with high spin densities and magnetic moments [254, 255]. These perturbations of the electronic structure then might also facilitate the mixing of excitonic states with different spin/purities and eventually lead to the "brightening" of those. In order to test this possibility, suspensions of CoMoCAT SWCNTs with SC as surfactant were mixed with a pH-neutralized aqueous solution of gold. The solution was prepared by reduction of HAuCl_4 using acetone and was pH neutralized by addition of sodiumhydroxide [256]. The resulting solution was centrifuged to remove most parts of colloidal gold nanoparticles. The violet supernatant solution was then further diluted with distilled water until it became almost transparent.

Strikingly, covering the sample with this gold solution results in similar changes in the single nanotube PL spectrum without requiring high-power pulsed excitation. This is demonstrated in Fig. 6.8, which shows the PL spectra of the same tube before (black) and after addition of the gold solution. The second spectrum was recorded after evaporation of the aqueous solvent and using low power CW excitation at 760 nm.

A higher yield of SWCNTs exhibiting PL satellite peaks was obtained when the aqueous SWCNTs solution was premixed with the gold solution prior to deposition on the glass substrates, thus facilitating the surface adsorption of the metal. In such samples, the (6,4) SWCNTs exhibited red-shifted emission satellites at comparable energies, indicating that the same emissive $|D_1\rangle$ state is brightened. This was further confirmed by time-resolved measurements which

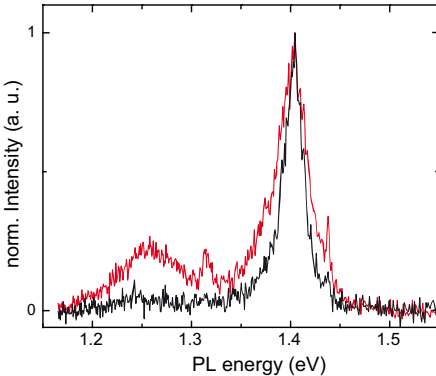


Fig. 6.8. Creation of low-energy PL bands in the spectra of SWCNTs after treatment with a colloidal gold solution. The initial spectrum shows the PL band of a (6,4) SWCNT (black). After covering the sample with a pH neutralized colloidal gold solution, an additional low-energy PL band is inherently present (black line) and does not require any further high power laser irradiation. The spectra were acquired with moderate CW power levels at 760 nm. The narrow emission features centered at 1.437 eV and 1.314 eV are the G and G' Raman bands of the SWCNT, respectively.

revealed a broad distribution of lifetimes in the range of 7–150 ps with a considerably longer average decay time than the $\langle \tau \rangle = 14$ ps determined for the $|B\rangle$ state.

However, there is a noteworthy difference between the two dark state "brightening" methods. As shown in Fig. 6.9, after the gold treatment, the emission of the dark state is far less stable, even under low-power CW excitation. Pronounced spectral diffusion and blinking can be observed, which is presumably due to the mobility of the adsorbed Au atoms on the nanotube surface causing an unstable interaction with the nanotube and thus leading to the varying spectral characteristics [257]. Importantly, no additional PL bands were observed in control experiments on single nanotubes that have been deposited on gold films as well as in near-field optical experiments using sharp gold tips [198], indicating that the new PL bands are not created by metal-surface-induced electromagnetic field enhancement.

6.5. Discussion

In the following the results of the PL decay time measurement of the bright and dark states are discussed in more detail regarding their population dynamics and the possible coupling between the states. Finally, an assignment of the new PL satellite bands to corresponding nanotube intrinsic excitonic states is suggested, based on the spectroscopic data and the processes leading to "brightening" of the dark state.

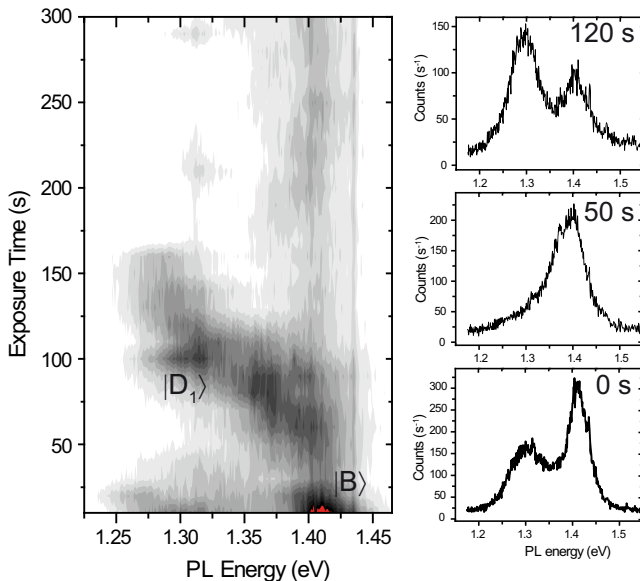


Fig. 6.9. Series of PL spectra from a (6,4) SWCNT after treatment with a colloidal gold solution, showing the temporal evolution of the PL emission. The spectral dynamics of the bright and dark state PL of SWCNTs treated by the gold solution is distinct different compared to the PL of SWCNTs, where the laser "brightening" method was used. It is characterized by pronounced spectral diffusion as well as PL blinking even at low power CW excitation. The characteristic emission of the low-energy $|D_1\rangle$ PL satellite band at 1.28 eV is fluctuating with time and can be observed in the time intervals 0–40 s and 100–160 s. The integration time per spectrum was one second.

6.5.1. Population Dynamics of the Bright and Dark States

The observation of the more rapid decay of the bright exciton in the presence of the red-shifted satellite peaks (Fig. 6.3) and the reduced PL intensity of the $|B\rangle$ peak suggests that disorder-inducing defects are responsible for additional nonradiative recombination channels depopulating the bright excitonic state. Two possible competing channels can be distinguished. First, population transfer to the dark state $|D_1\rangle$, mediated by the introduced defects and second, decays to the ground state, facilitated by enhanced exciton-phonon coupling, because of defect-associated local phonon-modes [125, 236]. Both relaxation channels require propagation of the bright exciton along the nanotube to enable interaction with localized defects. Therefore, faster decay also serves as an evidence for the mobility of excitons in nanotubes [112, 126, 258].

Based on the PL decay dynamics of the bright state, population of the dark state via direct population transfer from the bright exciton is not the dominant population pathway. Direct population transfer is expected to result in a delayed rise in the transients of the $|D_1\rangle$ emission with a rise time that is equal to the decay time of the bright state. Such a delayed rise, which would be detectable in the TCSPC measurements, especially for nanotubes with longer decay times of the $|B\rangle$ state up to 25 ps, was not observed, suggesting that a substantial fraction of the dark state population is built up directly upon photoexcitation. Importantly, the fact that the bright exciton maintains a different and finite lifetime in the presence of the dark state $|D_1\rangle$ clearly shows that these two states are not in thermal equilibrium.

In the previous section it was found that the weak phonon-mediated coupling between the bright and a dark state $|D\rangle$ only few meV below the bright state, leads to biexponential PL decays in SWCNTs. The energy level diagram of the coupling scheme is depicted in Fig. 6.10, while an extensive discussion of the model is given in Sec. 5.3. Small coupling rates on the order of 0.05 ns^{-1} were required to reproduce the biexponential decays, indicating that both states are not in thermal equilibrium.

Assuming that the $|D_2\rangle$ observed here is identical to $|D\rangle$, its similar decay dynamics with the $|B\rangle$ state indicates that, because of the defect-induced mixing of the excitonic states, the efficiency of the coupling is significantly increased, leading to faster transition rates and thermal equilibration between the two states.

Similarly, the population dynamics of the $|D_1\rangle$ can be investigated by assuming the same three level scheme for the coupling between the states, but now replacing $|D\rangle$ by $|D_1\rangle$ in Fig. 6.10. The reduced but finite lifetime of $|B\rangle$ in the presence the dark state $|D_1\rangle$ implies that coupling between both states must be slow. Based on the phonon-mediated coupling between both states, where the up-down coupling rates, γ_\uparrow and γ_\downarrow , depend on the phonon-population and the energy separation of both states as defined in Eqn. 5.1, slow decay rates are expected for the average observed splitting energies. Furthermore, if such a coupling exist, the decay times should critically depend on the energy separation between the dark and bright state.

Assuming a fast zero temperature bright to dark transition rate $\gamma_0 = 1\text{ ps}^{-1}$, the dependence of the $|D_1\rangle$ decay time on the dark-bright splitting energy can be reproduced. A plot of the

$|D_1\rangle$ decay times of (6,4) and (5,4) SWCNTs against splitting energies is depicted in Fig. 6.10. The black dotted line is a model curve, assuming ground state recombination rates $\Gamma_B = 2 \text{ ps}^{-1}$ and $\Gamma_D = 200 \text{ ps}^{-1}$ and an equal initial population of the bright and dark state.

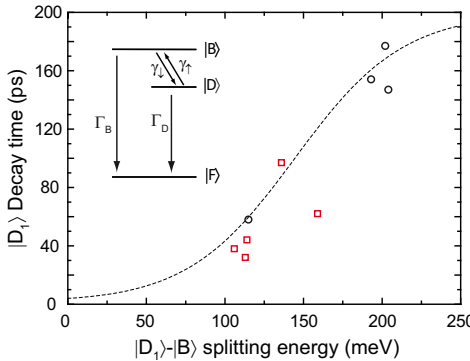


Fig. 6.10. Plot of $|D_1\rangle$ decay time against the dark-bright splitting energy. The PL decay time of the $|D_1\rangle$ state depends on the energy splitting between the dark and $|B\rangle$ state indicating thermally activated depopulation of the dark state. The dotted black line is a reproduction of this dependence employing the kinetic three level model depicted in the upper right (for details on the model refer to Sec. 5.3). Red squares indicate (6,4) SWCNTs and black circles (5,4) SWCNTs.

Although it would be a simplification to treat the nanotubes excited states as a simple three-level system, neglecting the exciton mobility, the general behavior can be reproduced by employing thermally activated coupling of $|D_1\rangle$ to the higher lying $|B\rangle$ state via phonon-induced exciton scattering and assuming a Bose-Einstein distribution of phonons at 400 K.

6.5.2. Assignment of the PL Satellite Bands

The strongly polarized emission of the $|D_1\rangle$ state depicted in Fig. 6.2 and its regular appearance at similar emission energies for different nanotubes makes the possibility of simply having luminescent defects unlikely. Recent experimental studies on ensemble samples enriched with (6,5) chirality nanotubes have attributed low-energy emission bands to 160 meV phonon sidebands of K-momentum excitons that are higher in energy than the $|B\rangle$ state [99]. However, the large energy separation of the $|D_1\rangle$ state of 190 meV observed in the present work also excludes this scenario. On the other hand, the manifold of triplet states predicted to lie below the optically bright exciton [91, 94, 103, 106, 253], represents an additional set of intrinsic accessible states. The energy separation for the bright exciton and the $|D\rangle$ state determined in the experimenters is in good agreement with the energy separation of the triplet state calculated for the (6,4) chirality in ref. [253]. Based on the

significant longer PL decay times of the $|D_1\rangle$ emission compared to the PL decay times characteristic for the studied SWCNT material ($\langle\tau\rangle=14$ ps) and the good agreement between the experimentally determined emission energy with the theoretical predictions for small diameter nanotubes [253], the emission of the $|D_1\rangle$ state can be assigned to the radiative recombination of a triplet exciton.

A triplet lifetime of 100–190 ps as observed here is considerably faster than one would expect for such a system. Possibly, also this state couples efficiently to nonradiative decay channels, comparable to the situation of the bright exciton. Considering that for the "brightening" process disorder and defects need to be generated in the SWCNT, which obviously affect the nonradiative decay rates of the bright state and thus lead to a decrease of its PL decay times accompanied by a reduction of PL intensity, this seems also plausible for the decay dynamics of the dark state.

The assignment of the $|D_1\rangle$ state to an intrinsic triplet-state of the SWCNT is further supported when considering the two different "brightening" methods presented here and the different kinds of defects related to them: The high power laser irradiation and on the other hand the treatment of the SWCNTs with the gold solution. In order to observe PL from triplet states, inter-system crossing rates need to be significantly enhanced. The presence of localized states with high magnetic moments and/or spin densities are known to enhance the spin-orbit coupling and thus facilitate inter-system crossing between single and triplet states. In materials, such as SWCNTs and graphene, midgap high-spin density states are predicted for carbon vacancy sites created in the SWCNT sidewalls but also for ad-atoms of elements with high atomic numbers such as e.g. gold or cobalt [259].

Multi-photon processes initiated by the high-power pulsed laser irradiation might result in the creation of carbon vacancy sites. The energy of 5 eV which is needed to create a vacancy [254] can be provided through multiphoton excitation processes, which explains the high pulse energies required for the creation of $|D_1\rangle$. The slow PL decay times for the triplet exciton can be explained by the spin-dependent nature of the nonradiative relaxation mechanism.

On the other hand for the treatment of the SWCNTs with the gold solutions, it is expected that gold atoms attached to the sidewall of the SWCNTs give rise to high spin density states which can promote efficiently inter-system crossing. Similarly, trace amounts of magnetic impurities such as iron or molybdenum catalyst particles attached to the SWCNT sidewalls [185] might explain the observation of inherent dark state emission observed for different nanotube materials [98, 146, 221]. Different mobilities of the vacancy sites and the gold atoms at room temperature along the nanotube might account for the different temporal characteristics of the dark state PL, which was observed in case of the different "brightening" mechanisms. Carbon vacancies are less mobile and represent a more localized type of defect at room-temperature. For gold ad-atoms on graphene very high mobilities were found. The PL of the $|D_2\rangle$ state exhibit the similar PL decay times and the same dynamics as the

main bright emission band and indicates that these states Based on the dark-bright energy separation 30–60 meV ($|D_2\rangle$) one might speculate that this is also a state of the triplet manifold.

Since the publication of the results of this study, several other reports on the creation of low-energy PL satellite peaks were published, which discussed specifically experimental evidence for triplet emission in SWCNTs. As these to put the results of this work in a more general context, some reports are summarized in the following:

The laser pulsed "brightening" method presented here was successfully applied at cryogenic temperatures to create low-energy satellite peaks in individual SWCNTs [101]. Similar bright-dark splitting in the range 30–100 meV for SWCNTs in the diameter range of 0.82–1.16 nm were found. Based on the predicted $1/d^2$ dependence of the splitting energies on the diameter [260], the PL was attributed to the emission of a triplet exciton. As the experiments were carried out in vacuum, defects related to photoinduced oxygen states can be ruled to activate the "brightening" process consistent with the observation in this work that low energy emission bands can be created in PMMA or embedded in oil. In a very recent publication from Nagatsu et al. it could be shown that a similar ad-atom related "brightening" mechanism as it was used in this study, leads to the brightening of triplet states. After exposure of air-suspended individual SWCNTs to molecular hydrogen, additional low-energy PL bands with dark-bright splitting energies between 40–80 meV, were observed. Also, in this study the assignment of the satellite peak as a triplet-exciton is based on the diameter dependence of the splitting energy only, while time-resolved data would be highly interesting. It was suggested that the brightening of the triplet-states is due to the enhancement of spin-orbit interactions as consequence of distortions to the sp^2 lattice, which are induced by the presence of the ad-atoms [261]. Signatures of triplet excitons were also observed in a combination of magnetic-brightening and photocurrent measurements. By applying a weak magnetic field to SWCNTs embedded in an europium-sulfide matrix additional low-energy peaks arose in the photocurrent spectra, with relatively small dark-bright splitting energies of 20 meV [262]. The small singlet-triplet splitting energies observed in their experiments owe to the fact that SWCNTs with large diameters between 1.44–1.82 nm were studied. Based on the dependence of the splitting energy on the magnetic field orientation the photocurrent features were assigned to triplet exciton states.

6.6. Conclusion

In summary, it could be shown for the first time that nominally dark excitonic states in individual SWCNTs can be "brightened" by the introduction of defects. As a consequence low-energy satellite bands emerge in the PL spectra separated by 10–190 meV from the main emission band. The PL decay dynamics of this satellite bands is characterized by PL decay times up to two orders of magnitude larger than the one of the main PL band. Furthermore,

in the course of the "brightening" process the PL intensity of the main PL band is reduced and its PL decay dynamics becomes faster, which indicates the opening of additional defect related nonradiative decay channels.

Two different "brightening" mechanisms were investigated: (1) The irradiation with high power laser pulses and (2) the treatment of the SWCNTs with a diluted gold colloid solution. While for both brightening mechanisms the same groups of low-energy PL satellite bands can be observed, they exhibit distinctly different spectral dynamics. The states "brightened" with method (1) are persistent even at low power CW excitation, while for (2) the new emission bands exhibit pronounced spectral jumps and blinking on the second time scale. These observations imply that two different types of defects facilitate the "brightening" which possibly exhibit different mobilities along the SWCNT axis. Based on the large energy splitting and slow PL decay dynamics of the lowest dark state emission and its occurrence upon exposure of SWCNTs to gold, that is predicted to create local states with high spin densities [259], we suggest that low energy emission results from triplet exciton recombination facilitated by magnetic defects and impurities.

It was shown that the PL properties of a single SWCNT can be intentionally modified by the introducing disorder to the system. This enables a single SWCNT to simultaneously emit at two well separated wavelength whose PL decay dynamics differs by two orders of magnitude. While the microscopic nature of the different defects needs to be investigated in more detail to further understand and control the "brightening" processes, the findings of this study indicate novel routes for the engineering of SWCNT PL properties.

Part III.

Elastic White Light Scattering Spectroscopy of Individual SWCNTs

7. Elastic White Light Scattering Microscopy of Individual SWCNTs

In this chapter the results of elastic white light scattering spectroscopy of individual SWCNTs on substrates are presented. The method is based on a common path interference scattering approach (iSCAT), where the detected signal originates from the superposition of the scattered field of the particle and the reflected field from the substrate interface. By combining confocal microscopy with a supercontinuum white light source it can be shown that the iSCAT signal of individual SWCNTs is sufficiently strong for imaging and spectroscopy. The most prominent signal contribution in the scattering spectra can be assigned to the second E₂₂ excitonic transition and can be used to distinguish different SWCNT chiralities. Further, it is found that the presence of a single SWCNT in the laser excitation focus reduces the amount of back reflected laser light off the glass substrate by approximately 4–8%, which is comparable to the extinction signals of 20 nm gold nanoparticles. By comparing the scattering amplitudes of gold particles with well known optical constants and the one of SWCNTs, the resonant absorption/extinction cross section of the E₂₂ excitonic transition of (6,5) SWCNTs can be estimated. An outlook on future experiments is given, where PL and elastic white light scattering measurements are combined to study the E₁₁ and E₂₂ optical transitions of the same SWCNT.

7.1. Introduction

PL and Raman based optical imaging and spectroscopy methods for studying the optical and electronic properties of SWCNTs on the single nanotube level can be realized by combining confocal or widefield microscopy with high sensitivity detection. An alternative, however less widespread, spectroscopy method which is also well suited for single SWCNT studies is the elastic scattering microscopy/spectroscopy, which is also commonly referred to as "Rayleigh" scattering spectroscopy.

The elastic interaction between light and matter is governed by the optical susceptibility χ or equivalently the dielectric function ϵ of the material. These properties are in turn directly related to the inherent electronic structure such as the bandstructure or density of states. The elastic scattering response becomes particularly strong if the excitation energy matches the energy of an electronic or vibronic transition. Especially in combination with a broadband white light excitation source this offers the possibility to probe several optical transition simultaneously and makes this method a valuable tool for the chirality assignment of SWCNTs.

Elastic scattering methods offer certain advantages regarding their applicability as spectroscopy tool for SWCNTs compared to the well established PL and Raman spectroscopy. First, the elastic scattering signals are expected to be significantly larger than Raman or PL signals, as the elastic scattering cross section of small particles exceeds corresponding Raman cross sections by orders of magnitudes. and the PL of SWCNTs suffers from its low QYs. Efficiently, this reduces excitation powers and/or acquisition times. Furthermore, the elastic scattering process does not suffer from the peculiarities inherent to the PL process, like blinking or bleaching due to intrinsic and extrinsic nonradiative decay processes. PL spectroscopic data of SWCNTs gives only information about the radiative E_{11} optical transitions. To obtain information about higher excitonic energies elusive photoluminescence excitation measurements would need to be performed which is a non trivial task on the single nanotube level. Combining here elastic scattering spectroscopy with a broadband excitation source such as white light allows to probe several optical transitions simultaneously. The elastic scattering process is not restricted to semiconducting SWCNTs only as it is the case for the PL. Metallic SWCNTs and even the composition of nanotube bundles can be studied and semiconducting and metallic SWCNTs can be well distinguished based on the lineshape of the scattering signal. Raman spectroscopy can be also used to probe electronic transitions in SWCNTs based on the resonance profile of the first order RBM mode. However, the method is experimentally elaborate, as it requires the use of several different laser lines to probe a single electronic resonance, resulting in low acquisition rates.

One of the drawbacks of elastic scattering spectroscopy is the strong non-resonant background signal originating from scattering from all matter within the excitation volume. Due to the small scattering cross section of nanoparticles the background signal exceeds the scattering signal of the object and leads to a weak image contrast. As there is no frequency shift between the elastically scattered light of the object and the background light, spectral filtering is not a viable way to reduce the contribution of the background light. However, various approaches exist, to minimize the contribution of the excitation beam and to reduce the amount of the background scattered light. For instance, excitation and detection schemes are employed, such as in dark-field microscopy, where the light of the excitation beam and the scattered light from the object propagate in spatially different parts of the detection beam and can be separated by using specially shaped beam stops [263]. Another possibility is to use non-propagating evanescent light fields for excitation which is realized in total internal reflection or frustrated total internal reflection excitation schemes [264].

Alternatively, however experimentally more elaborate, the contribution from the background can be minimized by reducing the excitation volume to nearly match the physical dimensions of the nanoparticle. This scattering approach can be realized e.g. by aperture-type near-field scanning optical microscopy (NSOM) [265]. Another near-field based scattering approach relays on the strong local enhancement of the scattering response of the particles in the presence of gold tip by employing an apertureless scattering type NSOM scheme [266]. An elegant way to nearly completely avoid the contribution of the background light is to simply

not use a substrate and to detect the scattering signal with an second objective in transmission geometry which is aligned in an oblique angle with respect to the illumination objective. This method is suitable for spatially extended objects such as e.g. SWCNTs or graphene [267–269]. These can be freely suspended by first growing or depositing the material on a substrate and then etching slits into it. If the length of these slit is considerably larger than the diameter of the excitation focus the scattering measurements are nearly background free.

Elastic scattering experiments on individual and bundled SWCNTs so far have been performed by utilizing scattering or dark-field configurations. The SWCNTs in these studies were freely suspended in air by crossing slits with a length of several tens of μm [65, 267, 268, 270]. The scattered light emanating from such samples was collected either in a transmission geometry where a second objective is arranged in an oblique angle [267] or in reflection geometry, where the backscattered light is collected by the same objective [271]. Only recently, Joh et al. reported on the successful implementation of a dark-field excitation scheme for Rayleigh scattering imaging of SWCNTs deposited on substrates. In this study a sandwich-like sample configuration was used, consisting of a stack of refractive index matching media. Spatially well separated SWCNTs were deposited on a quartz substrate and embedded in a thin layer of glycerol while a glass cover slide was placed on top. For excitation only the outer part of a high NA oil immersion objective was filled with a broadband white light beam, so that the focused light can only incline in a large angle on the sample. The beam enters and passes through the sandwich configuration until it undergoes total internal reflection at the upper glass-air interface. Only the elastically scattered light of SWCNTs excited by this back reflected beam is then collected by a second objective positioned above the sample [272].

An alternative approach for studying the elastic scattering response of nanoparticles on (transparent) substrates are interference scattering schemes. The detected scattering signal here is due to the interference between the scattered light of the SWCNT and a reference beam. In its simplest realization the reference beam is the reflected beam from the substrate or the transmitted excitation beam, depending on the direction of detection (compare also Sec. 2.2). In fact the characteristics of the back-reflected or transmitted excitation light is exploited to enhance the scattering signal. The method has been successfully applied to study the elastic scattering properties of gold-nanoparticles [158, 273], semiconductor quantum dots [174] or even single molecules [163, 171]. It was also used for fast imaging the movement of HIV-viruses on lipid bilayers [168]. Moreover, real-time interferometric detection with single particle sensitivity can be achieved and was demonstrated for counting polystyrene beads or viruses in fluids based on their scattering signals [161, 169, 170, 274].

In this chapter the iSCAT-method is combined with a broadband white light excitation source. The aim of this chapter is to explore the capability of this approach for elastic scattering imaging and spectroscopy of individual SWCNTs on substrates. In the first two sections the performance of the iSCAT setup is tested by measuring the scattering response of materials with well known optical properties, such as gold nanoparticles with different diameters and

of single layer graphene on a quartz substrate. The results of the iSCAT imaging and spectroscopy of individual SWCNTs are then presented in the next section, the physical description of the extinction cross section of the E_{22} is estimated. Combined PL and scattering on the same SWCNTs are then used to determine the energies of the first and second transition energies E_{11} and E_{22} . The effect of dielectric shielding on the excitonic binding energies is discussed.

7.2. Reference Measurements on Gold Nanoparticles

The experimental setup for the iSCAT measurements consists of the standard inverted lasers scanning confocal microscope, described in Sec. 3.1, which is combined with a PCF as a white light excitation source (compare Sec. 3.5). In the following, the performance of the iSCAT setup is tested by acquiring confocal elastic scattering images and spectra of spherical GNPs with diameters of 20 and 60 nm. As a reference serves here the study of Lindfors et al. where an identical experimental approach was employed to measure the scattering (plasmon) spectra of spherical GNPs [158].

The optical properties of spherical GNPs are determined by particle plasmons [68], which in turn depend on the shape, size and the dielectric constant of the particle and the one of its surrounding medium. Spherical GNP with small diameters of 5–40 nm are of interest as non-toxic and non-bleaching markers for labeling of biological samples [275]. The properties of single GNPs are well studied, experimentally and theoretically. Therefore they are ideally suited as a reference sample. The scattering and extinction cross sections as well as the scattered fields can be calculated by using the results of Mie scattering theory. For the scattering problem of conducting, spherical particles significantly smaller than the excitation wavelength ($a \ll \lambda$) the problem can be solved exactly and analytical solutions are available [182, 276].

Samples with individual GNPs deposited on a glass cover slide and embedded in immersion oil were prepared according to the description in Sec. 3.2.4. The acquisition of elastic scattering scan images and spectra is described in detail in Sec. 3.5.2. Two confocal white light scattering images of spherical GNPs with nominal diameters of $d = 60$ nm and $d = 20$ nm are shown in Fig. 7.1(a) and (b), respectively. The experiment illustrates nicely the transition from a positive to a negative optical scattering contrast which is expected for decreasing particle diameters. The particles appear as diffraction limited spots with nearly uniform signal intensities.

Representative scattering spectra for the excitation range of 500–800 nm of the GNPs marked in the scan images are plotted in Fig. 7.1(b) and (d). In the case of the 60 nm gold sphere the scattering spectrum resembles the particles' plasmon resonance with a maximum at ~565 nm and a signal amplitude of ~35. Compared to the spectra of the 60 nm GNP in ref. [158] the plasmon resonance here is slightly red-shifted by 7 nm and has an asymmetric

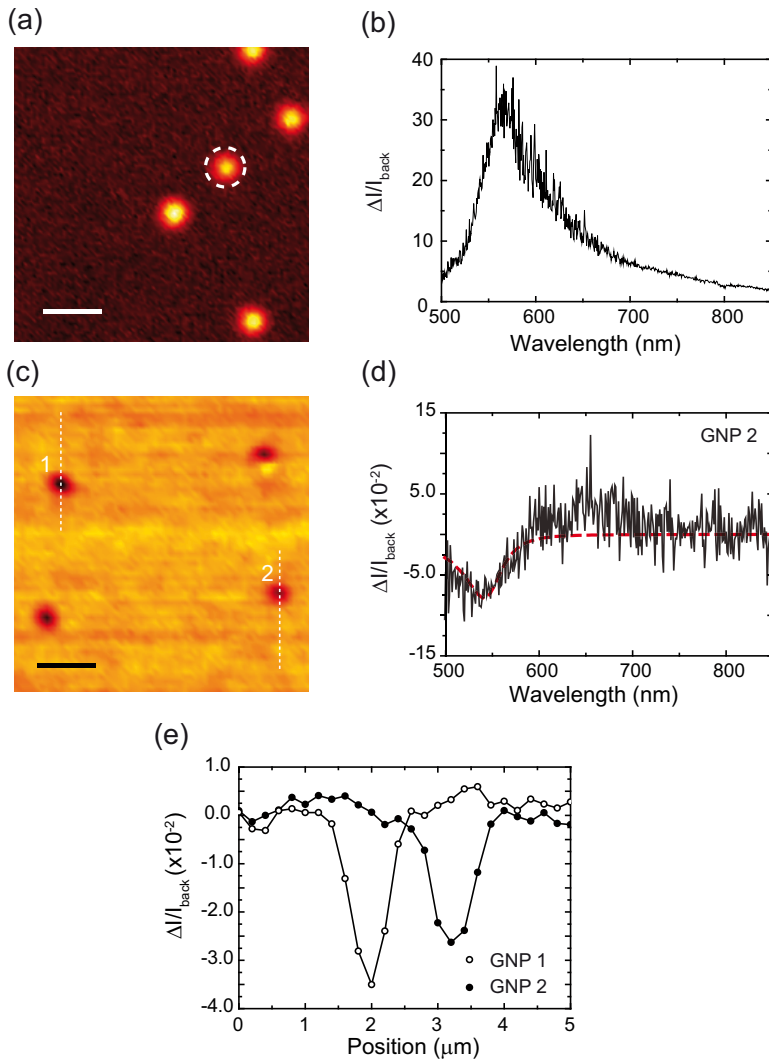


Fig. 7.1. White light scattering confocal scan images of gold spheres deposited on a glass substrate and covered by immersion oil. The diameters of the spheres are (a) 60 nm and (c) 20 nm, respectively. The scale bars are: (a) 2 μm and (c) 2.4 μm . (b) and (d) are scattering spectra of the particles marked in the corresponding scan images. The red dotted curve in (d) is a fit based on the model described in the text. The positive scattering contrast of $d=60$ nm spheres is dominated by pure scattering which scales with $|s|^2$, while the negative signal of the $d=20$ nm sphere with the minimum amplitude of the signal at $\lambda = 540$ nm originates from the interference term $-2r|s|\cos\phi$ (compare Eqn. 2.15). (e) Integrated white light scattering contrast of two 20 nm GNPs along the cross-sections in (c).

slope towards larger wavelength. This might be attributed to either an aggregation of several particles or deviations from the ideal spherical shape. Considering the rather uniform signal intensities in the scan image, aggregation related to varying particle numbers is less likely. The minimum contrast of the 20 nm particle is found at ~ 540 nm with an absolute value of $|\delta| \approx 0.08$. However, a comparison of several scattering contrast spectra of 20 nm particles reveals large particle to particle variations for the maximum amplitude of the contrast between 0.04 and 0.35 owing to the diameter distribution of the particles.

The findings here are in general agreement with the results of ref. [158]. The small deviations in the signal amplitudes and the spectral position of the contrast minimum/maximum values are most likely due to the different immersion oils used in both experiments and consequently lead to different dielectric environments of the GNPs. Moreover, a different glass/immersion oil combination would further lead to changes of the reflectivity r and, as will be demonstrated in Sec. 7.6, thereby also affect the signal amplitudes. Fluctuations of the background signal due to the surface roughness of the microscope cover slides, as were reported in ref. [273] are not observed and did not affect the background correction.

Discussion

In the following the contrast formation of the iSCAT method is elucidated for the example of the 20 nm gold particle. As a basis serves the simple model for the iSCAT contrast which was introduced in Sec. 2.2. Various factors influencing the amplitude of the scattering signal, such as a displacement of the particle along the optical axis (defocusing) and changes in the substrate reflectivity are discussed.

Briefly repeating the final expression for the normalized interferometric contrast δ :

$$\delta = \frac{\Delta I}{I_{\text{back}}} = \eta \frac{|s|^2}{r^2} + 2\eta \frac{|s|}{r} \cos \left(\frac{\pi}{2} + \arctan \frac{z}{z_r} + \arctan \frac{\text{Im}(\alpha)}{\text{Re}(\alpha)} \right) \quad (7.1)$$

Here r is the reflection amplitude coefficient related to the reflection of the excitation light at the glass oil interface and s is the complex scattering amplitude factor, which relates the scattered light field to the incident excitation light field.

The first term is the pure scattering term and the second term is the interference term. The cosine expression of the interference term contains the total phase difference between the reflected excitation field and the scattered field of the particle. Assuming that no additional phase terms arise due to propagation of the light fields in different spatial modes, the relative phase difference between reference and scattered fields is determined by the Gouy phase term and the wavelength dependent oscillator phase of the GNP [158, 181].

The change in contrast for the different sized GNPs of 60 nm and 20 nm can be explained by the interplay of the pure scattering term and the interference term. In the Rayleigh approximation which holds for particle diameters significant smaller than the excitation

wavelength, s is connected via the polarizability to the volume of the particle d^3 . For the 60 nm GNP the pure scattering term, which is proportional to d^6 , dominates the contrast and leads to the positive scattering signal. On the other hand, the d^3 scaling of the interference term becomes increasingly important for decreasing particle sizes and in this case destructive interference leads to the negative contrast of the $d=20$ nm GNP.

Assuming that the 20 nm particle can be treated within the Rayleigh approximation for small particles [182] the scattering properties can be described in terms of radiation of a dipole with the polarizability α . For the modeling of the contrast the scattering amplitude coefficient s and the reflectivity r need to be calculated. For the simplest scenario where the directions of the incident excitation light on the sphere and detected scattered light in backscattering direction are identical the expression for s of Eqn. 2.13 can be used, where $s \propto -k^3 \alpha$. Values for ϵ_{gold} are calculated by an analytical formula for the dielectric constant of bulk gold [277] which reproduces well the experimentally determined data of Johnson and Christy [278]. ϵ_{med} is related via the Maxwell formula $\epsilon_{med} = n_{med}^2$ to the refractive index of the surrounding medium. Assuming that the refractive index matching condition of the glass substrate and immersion oil provide a isotropic, homogenous environment $n_{med}=1.518$ is assumed. Further, the wavelength dependent reflectivity of the glass-oil interface r is calculated using Fresnel-equation [148]. The required refractive indices for the immersion oil and the cover slides are obtained from manufacturer's data. In order to account for the detection and collection efficiency of the setup a freely adjustable wavelength dependent parameter η is introduced which also accounts for the finite interaction cross section of the particle with respect to the focal area of the excitation beam.

A plot of the modeled scattering contrast as a function of the focus displacement and the excitation wavelength is shown in Fig. 7.2 (a). Here the parameter η in Eqn. 2.13 was varied until good agreement with the experimental contrast was achieved (compare red curve in Fig. 7.1). For the present case it was assumed that the GNP is located directly in the focus ($z=0$).

Due to the Gouy phase term the contrast is sensitive to the axial position of the GNP with respect to the excitation focus. This is illustrated for a cross section along a line $\lambda=540$ nm in Fig. 7.2 (b). The asymmetric dependence upon defocusing is caused by the non-resonant oscillator phase contribution of the GNP at this wavelength. A symmetric behavior would be expected for $\lambda \approx 503$ nm where the oscillator phase ϕ_p contribution becomes equal to $\pi/2$. The Gouy phase dependence of the optical contrast (SNR) was investigated theoretically by Hwang et al. for particles with varying contributions of the imaginary or real part of the dielectric function [181] and has been investigated experimentally for single quantum dots using monochromatic excitation [174].

For the experimental configuration used in this work, it was not possible to quantify the broadening of the line shape of the scattering signal upon defocusing. It was found that defocusing leads to a general decrease in the contrast upon defocusing without any notable change in lineshape. As the change in contrast is expected to occur for an axial displacement on the order of the Rayleigh range of the focused beam, it would require a more precise

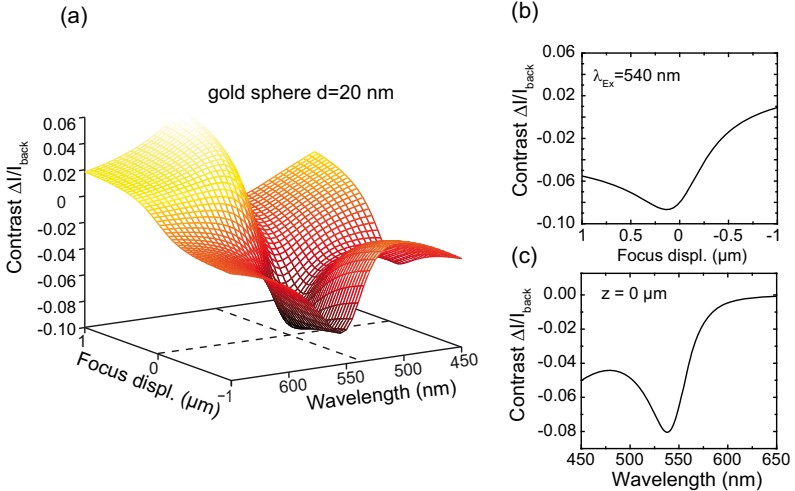


Fig. 7.2. (a) Modeled scattering contrast of a $d=20$ nm gold sphere as function of axial displacement of the particle (defocusing) and excitation wavelength based on Eqn. 7.1. (b) Plot of scattering contrast against focusing for fixed wavelength of $\lambda_{\text{Ex}}=540$ nm. (c) Plot of contrast against wavelength for a GNP located in the excitation focus ($z=0$).

control of the z position of the particle with respect to the focus than it can be realized with the coarse approach wheel of the objective. In principle, it is possible to estimate the axial displacement based upon the size and shape of a reflected image of a tightly focused laser beam at a glass-air interface [68], but because of the reduced reflectivity of the glass-oil interface in the experiments and the contribution of the different wavelength components of the white light, the observation of such reflected intensity pattern is difficult.

The dependency of the amplitude and also the line shape of the wavelength dependent contrast on defocusing is an important result and should be considered when working with this iSCAT method. Both parameters depend on the complex interplay between the dielectric constant of the scatterer and the various phases introduced by defocusing and might complicate the quantitative analysis of scattering spectra especially when working with white light excitation. Furthermore, the reflectivity r acts basically as a scaling factor which affects the different contributions of the pure scattering and interference part and thus also determines the sign of the contrast. In consequence, depending on r the diameter of a particle for which the transition from a positive to a negative scattering contrast occurs might vary. As it will be shown Sec. 7.6, controlling r might be used to invert and even increase the elastic scattering contrast.

In summary a confocal white light scattering scheme based on a common-path iSCAT approach was established, which is capable of measuring the plasmon spectra of individual GNPs with diameters as small as 20 nm. The observed scattering spectra of the GNPs are in good agreement with the reported results in reference [158].

7.3. Reference Measurements on Single Layer Graphene

In order to test the performance of the white light scattering setup throughout a broad spectral range, the elastic scattering contrast of single layer graphene on a transparent quartz substrate was measured. Freely suspended single layer graphene has a constant absorbance of 2.3% throughout the visible spectral range [269, 279], which makes it an ideal material for testing the contrast formation and the stability of the white light throughout a broad spectral range. With regard to the scattering experiments of SWCNTs especially the performance of the setup for the spectral range associated with the E_{11} optical transitions between ~880–980 nm is here of interest.

Single layer graphene flakes on a quartz substrate were provided by Dr. A. C. Ferrari (Cambridge, UK). Single layer flakes were first identified by their characteristic Raman spectrum. Confocal white light scattering images and spectra were acquired as described in the previous section Sec. 7.2.

A confocal elastic white light scattering image of a large flakes is shown in Fig. 7.3 (a). The flake exhibits a negative scattering contrast which is spatially uniform across the whole flake. The optical contrast, acquired at the position marked by the circle in Fig. 7.3 (a), is nearly constant at ~ -0.11 throughout the whole experimentally accessible spectral range between 500–1000 nm (red line as guide to the eye).

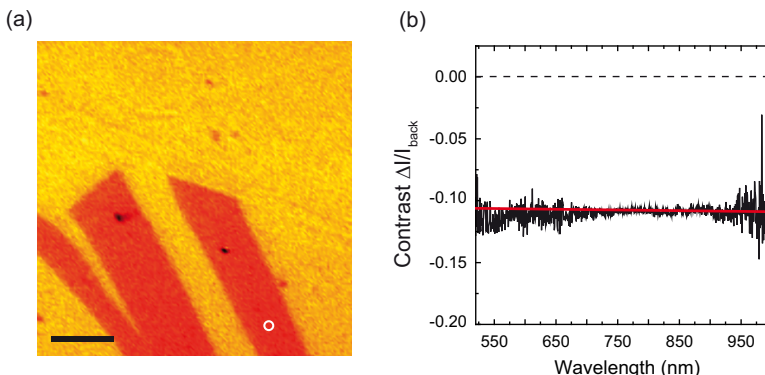


Fig. 7.3. (a) Confocal white light scattering image of single layer graphene on a quartz substrate. (b) Scattering contrast as function of wavelength, recorded at the white circle in (a). Single layer graphene deposited on quartz exhibits a constant optical contrast of ~0.11 in the spectral range of 500–1000 nm. The scalebar is 8 μm

Being able to observe the spectrally uniform scattering contrast of graphene indicate a sufficiently high temporal and spatial stability of the white light source. Furthermore, the normalization by a background spectrum indeed cancels out all modulations to the signal related to the spectral composition of the excitation white light as well as the wavelength dependent transmission/reflection/sensitivity characteristics of the optical components of the microscope. Notable is the increased noise level of the contrast the spectral regions between 500–650 and 950–1000 nm. The bad SNR for this regions is a consequence of the small detection/reflection efficiencies of the CCD camera and grating combination for this spectral regions (compare Fig. 3.11) and thus can not be significantly reduced by averaging over several spectra. Assuming shot noise-limited detection it should be possible to increase the SNR by increasing the number of detected photons. However, the detected white light spectra are spectrally not uniform with the strongest wavelength contributions in the spectral range between ~700–850 nm. For a typical measurement the acquisition times and excitation powers are adjusted so that the detected photon counts for the strongest wavelength contribution is close to the saturation limit per pixel of the CCD ($\approx 10^6$ photons). Increasing the excitation power or acquisition times to improve the SNR for signals arising in the spectral ranges with low CCD detection efficiencies might lead to the saturation of the CCD camera. Improvements in the SNR might be achieved by using a detector with higher detection sensitivity in this spectral regions.

7.4. Elastic White Light Scattering Spectroscopy of Individual SWCNTs

In the following the results of iSCAT based elastic white light scattering imaging and spectroscopy of individual SWCNTs are presented. The SWCNTs under study are small diameter semiconducting SWCNTs which exhibit near-infrared PL within the detectable range of the CCD camera. To ensure that the white light signals indeed originate from *individual* SWCNTs corresponding PL spectrum is acquired.

For sample preparation, 30 μl of an aqueous solution of micelle encapsulated CoMoCAT SWCNTs in SC (Hersam, Northwestern) were spin cast on a clean glass coverslide. The CoMoCAT material was enriched for small diameter tubes and the average length of the SWCNTs determined by AFM measurements is ~550 nm. The samples were then covered by immersion oil to reduce the contribution of the back reflected excitation light from the glass substrate.

Confocal white light scattering images of the samples were acquired by spectroscopic imaging. For this imaging method at each scan pixel a single scattering spectrum is recorded with typical integration times of 200 ms. Scattering intensity images of the sample for different spectral windows are then generated with the help of a Matlab script. The average white light excitation powers are on the order of 10–100 μW . After the acquisition of scattering scan images and identification of scattering features, PL and corresponding white light scattering spectra were acquired at these locations. In order to avoid contributions from second order

grating effects in the scattering spectra, especially for the spectral region associated with the E_{11} optical transitions of the SWCNTs between 830 nm and 1000 nm, a longpass filter 520 nm was placed in the excitation beam path. An adequate SNR up to 30 in the scattering spectra was achieved by averaging over 20–30 individual scattering spectra (compare also Sec. 3.5.1).

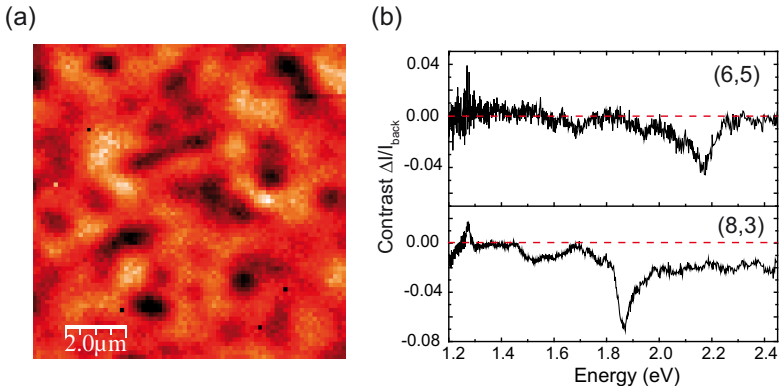


Fig. 7.4. (a) Confocal white light scattering scan image of individual CoMoCAT SWCNTs with SC as surfactant. Spot like and elongated features with negative scattering contrast can be observed. Representative elastic scattering spectra of individual (6,5) and (8,3) SWCNTs are shown in (b). The spectra are dominated by a single broad band (\sim 50–150 meV) with a signal amplitude of -0.02 to -0.1. Based on the spectral position these bands can be assigned to the E_{22} excitonic transitions. A clear scattering signal associated with the E_{11} transition in the spectral range (1.2–1.4 eV) is missing.

Fig. 7.4 (a) shows a representative confocal white light scattering image of surfactant encapsulated SWCNTs deposited on a glass cover slide. Diffraction limited point-like as well as extended scattering features with a negative contrast can be observed. Scattering spectra acquired at these positions confirm that in most of the cases these features can be attributed to individual SWCNTs. Two representative scattering spectra of individual (6,5) and (8,3) SWCNTs are shown in Fig. 7.4 (b). In general, the scattering spectra are dominated by a single band which can be assigned to the excitonic E_{22} transitions, which occur for the specific chiralities in the spectral range of 1.8–2.3 eV [49]. Complementary PL spectra acquired at the same sample positions confirm the chirality assignment (see also next section). The amplitude of the E_{22} signal is on the order of -0.02 to -0.1, thus of comparable magnitude as the contrast of the $d=20$ nm gold particles. Variations in the scattering contrast might be attributed to varying orientations of the SWCNTs with respect to the polarization of the excitation light and different SWCNT lengths.

In most of the cases, the scattering signals can be fitted sufficiently well with a single Lorentzian function. The linewidth of the E_{22} bands shows large variations between 50–150 meV, thus being considerably broader than the typical PL bands ($\text{FWHM(PL)} \approx 20\text{--}25$ meV) associated with the E_{11} transitions (compare Fig. 3.4). The broader E_{22} linewidth which is observed here is

also reported for the E_{22} linewidth determined in PLE bulk measurements [120]. The ultrafast intrasubband relaxation times from the E_{22} to the E_{11} excitonic states determined by pump probe experiments [249] indicate that the linewidth of the E_{22} is mainly lifetime broadened [57].

On some occasions also additional broader scattering features arise in the spectral range between 1.4 and 1.6 eV, as can be observed for the (8,3) SWCNT in Fig. 7.4 (b). Similar features 200 meV above the main excitonic E_{ii} transitions have been observed in photothermal absorption spectra [147] and elastic scattering measurements [270] of individual SWCNTs and were attributed to exciton-phonon bound states corresponding to: $E_{ii}+G\text{-mode}$ [82].

It is to note that the bright contrast areas in the scan images Fig. 7.4 (a) and also some of the scattering features with negative contrast exhibit broad unstructured scattering spectra. Such scattering signals can be attributed to scattering from contaminants of the substrate surface, such as e.g. residual surfactant. From shear-force raster scanning and AFM measurements of micelle wrapped SWCNTs on glass substrates it is known that surfactant crystallize or forms inhomogeneous films [199, 223]. Cleaning of the sample, e.g. by repeatedly rinsing with distilled water, did not completely remove the surfactant. However, the contaminants and the SWCNTs, exhibit different scattering spectra which allows for a clear distinction between both materials.

Finally, the most intriguing observation is the absence of a scattering signal associated with the excitonic E_{11} transitions. For the (6,5) and (8,3) SWCNTs in Fig. 7.4 (b) these would be expected in the spectral range between 1.2 and 1.4 eV. The oscillator strength of the E_{11} optical transition is predicted to be of comparable magnitude as the E_{22} transition or even larger [84, 280, 281] which becomes evident e.g. in the ensemble absorption measurements [197]. The present CoMoCAT sample material is well characterized by ensemble absorption measurements and also by PL measurements on the single SWCNT level. PL signals, corresponding to the E_{11} transition, of all five small diameter semiconducting SWCNT chiralities which exhibit PL emission wavelength within the detectable wavelength range are typically observed (compare Sec. 3.3).

7.4.1. Discussion

In the following various factors which might lead to the absence or inhibit the detection of the E_{11} scattering signal are discussed. Here one can distinguish instrumentation related experimental factors or (photo)physical properties of the SWCNT.

The scattering cross section of SWCNTs is determined by their optical susceptibility according to $\propto |\chi|^2$ [282]. The optical susceptibility is a function of the density of states and the transition matrix element (oscillator strength). One possibility for the absence of the signal corresponding to the E_{11} optical transition might be that the oscillator strength of the transition is intrinsically very small or is reduced by external processes. However, from absorption measurements it is well known that the strength of the first optical transition is usually larger or at least of comparable magnitude as the E_{22} optical transition. Exemplarily, the calculated optical susceptibility χ of a (6,5) SWCNT which considers the excitonic nature of the

excited state is depicted in Fig. 7.5 (a) (data provided by Dr. Ermin Malic, TU Berlin). The corresponding scattering cross section σ_{scat} , which was calculated using the formula for the scattering cross section of an infinite cylinder in Eqn. A.8) is shown in Fig. 7.5 (b).

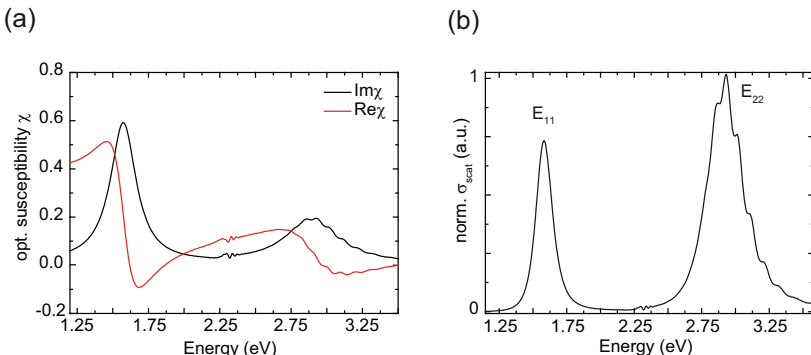


Fig. 7.5. Computed optical susceptibility χ and scattering cross section σ_{scat} of a (6,5) SWCNT. (a) Real and imaginary part of χ . (b) Normalized σ_{scat} : Both E_{11} and E_{22} cross sections are of comparable magnitude. Please note: For the calculations $\epsilon=1$ was assumed, which leads to different absolute excitonic energies compared to the experiment. The calculations were performed by Dr. E. Malic (TU, Berlin) [283].

Doping leads to considerable shifts of the Fermi energy and in consequence the oscillator strength of the first optical transition can be reduced due to state filling. Hole- or electron doping shifts the Fermi energy level into the valence or conduction band which might lead to the complete suppression of the absorption of the first optical transition [284]. This effect is more pronounced for SWCNTs with large diameters which exhibit smaller bandgaps. Hole-doping due to adsorption of oxygen is known as an important factor influencing the excited states in micelle encapsulated SWCNTs deposited on surfaces. For the small diameter SWCNTs high doping levels would be required to bleach the transition. However, the still detectable PL does not indicate this. Another process which might lead to the reduction of oscillator strength is state-filling caused by multiple excitations.

Presumably the most important factor which inhibits the detection of the E_{11} signal, is the low detection efficiency of the detector. The overall detection efficiency of the experiment is mainly determined by the quantum efficiency of the CCD-camera and the reflectivity of the grating of the spectrograph. Based on manufacturers data this is for the E_{11} spectral region between 880–1000 nm only ~23–3%. The magnitude of the signal contrast for the E_{22} optical transition is on the order of 0.08–0.1 corresponding to an attenuation of the back reflected white light intensity by 8–10%. Assuming an initially similar reduction of the back-scattered light for the E_{11} transition and considering the overall low count rates in this spectral region, the resulting relative change in the white light intensity could be obscured by the noise.

iSCAT Scattering Contrast of SWCNTs

The experimental scattering contrast of SWCNTs was found to be negative, indicating the interferometric nature of the detected signal. For a qualitative description of the contrast Eqn. 7.1 is used. Typically, in terms of the dimension and shape of the scattering objects, SWCNTs are typically modeled as infinite long right circular cylinders. This is certainly valid for the case of SWCNTs with lengths significantly exceeding the diameter of the excitation focus as it is the case for the scattering experiments in refs. [57, 267, 281]. However, for the present CoMoCAT material the average length of the SWCNTs is about 550 nm, thus being of comparable size as the wavelength of the excitation light. In this case a model description of SWCNTs as an infinite cylinder is not suitable anymore, but they also can not be treated as a dipolar emitter anymore within the electrostatic approximation. As a consequence for the iSCAT experiments this might give rise to even more complex phase contributions for different wavelength regions which might lead to also to dispersive signal contributions and thus further complicate the interpretation of the detected signal.

As mentioned before, the length of a SWCNT is expected to determine its scattering behavior which give rise to different phase contributions. In terms of electrodynamical Mie scattering theory long SWCNTs can be modeled as infinite right circular cylinders. Similar to homogeneous spheres, analytical expressions for the scattered fields and also the scattering amplitude factors can be derived [182, 183]. Simple expression for s are obtained to a first approximation, when only excitation with light incident normal to the SWCNT axis and with the electric field polarized parallel to the tube axis is considered. Furthermore, only the scattered fields in backward direction are detected (see also Chap. A). In the small particle limit, $k \cdot n_{med} \cdot r_t \ll 1$, the scattering amplitude factor is approximately given as:

$$s \approx -i \cdot \pi \cdot k_m^2 \cdot r_t^2 (m^2 - 1) \quad (7.2)$$

Here r_t is the diameter of the SWCNT and m is the relative refractive index: $m = n_t/n_{med}$ between the SWCNT and the embedding medium. The refractive index of the SWCNT n_t was calculated using the optical susceptibility of the (6,5) SWCNT, which is shown in Fig. 7.5. Compared to the dipolar case, s depends here only quadratically on the radius of the particle and importantly the solution for the scattered light field are now cylindrical waves instead of spherical waves. This give rise to an additional complex phase shift term of $\pm \exp i\pi/4$ compared to the dipolar case.

7.5. Determining the Resonant E_{22} Extinction Cross Section

In the following an estimation for the resonant extinction cross section σ_{ext} for the excitonic E_{22} transition of a (6,5) SWCNT is derived.

The interferometric signal of small particles originates from extinction (absorption) of the

incident excitation light. The amplitude of the interferometric signal does depend on various (wavelength dependent) parameters which are difficult to assess quantitatively, such as for example the exact mode overlap between the reflected and scattered field [174], the reflectivity of the substrate/oil interface and the Gouy phase shift due to defocusing. Therefore it is not directly possible to assign the detected signal to an extinction cross section σ_{ext} .

Kukura et al. suggested an indirect approach for determining the extinction cross section based on the comparison of the iSCAT signal amplitude of the object under study with those of a GNP of known size measured for identical experimental conditions [174]. Accordingly, the extinction cross section σ_{ext} per unit length of a SWCNT can be determined. Ideally, the maximum signal amplitudes of the SWCNT E_{22} optical transition and the plasmon resonance of the 20 nm GNPs, denoted as S_{SWCNT} and S_{GNP} respectively, are of comparable magnitude and appear at similar wavelength which allows a comparison of both signals.

For the (6,5) SWCNTs, the average value for the amplitude of the maximum E_{22} signal is approximately 0.043 ± 0.017 and appears at an average wavelength of 570 nm. Only such signals were considered which exhibit a zero baseline as depicted for the (6,5) SWCNT in Fig. 7.4 (b). Accordingly, for the GNP the amplitude $S_{GNP} \approx -0.025$ at 570 nm is determined.

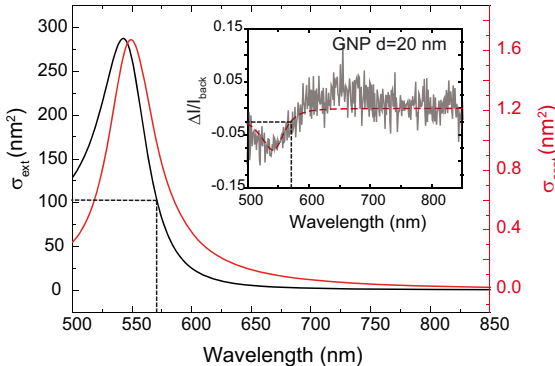


Fig. 7.6. Calculated extinction (black curve) and scattering cross section (red curve) of a 20 nm GNP. The modeling of the cross sections is based on Mie scattering theory [182]. For the refractive index of the embedding medium $n_{med} = 1.518$ was assumed. The refractive index of gold was calculated according to an analytical expression given in ref. [277]. Inset: Representative detected wavelength dependent contrast of a 20 nm GNP. At a wavelength of $\lambda=570$ nm, corresponding to the wavelength of the maximum amplitude of the SWCNT E_{22} contrast, $S_{GNP}(570\text{ nm}) \sim -0.025$ and a extinction cross section $\sigma_{ext}^{GNP}(570\text{ nm}) 100\text{ nm}^2$.

In a next step σ_{ext}^{GNP} is assigned to the amplitude of the GNP signal at 570 nm. In the recent literature, no σ_{ext} values are reported for the specific experimental conditions of this work:

20 nm GNPs embedded in oil and excited at 570 nm.

A first crude estimation can be made based on the σ_{ext} values of GNPs reported by Arbouet et al. They studied the extinction (absorption) properties of individual GNPs deposited on a glass substrate and embedded in water. For a $d=20$ nm GNP at an excitation wavelength of 532 nm they determined an σ_{ext}^{GNP} of 195 nm^2 [165]. With a signal amplitude of $S_{SWCNT} \sim -0.08$ and considering the average length of the CoMoCAT SWCNT material of 550 nm, this translates to $\sigma_{ext}^{E_{22}} \sim 610 \text{ nm}^2/\mu\text{m}$. This value is about seven times larger than the E_{22} extinction cross section of (6,5) SWCNTs $\sigma_{ext}^{E_{22}} \sim 90 \text{ nm}^2/\mu\text{m}$ determined by photothermal measurements for similar SWCNT material [124]. Certainly, this estimation suffers from the unfavorable σ_{ext} of the GNP that does not consider the actual experimental parameters.

In order to determine σ_{ext} of a 20 nm GNP at matching experimental conditions, the wavelength dependent σ_{ext} is modeled based on Mie scattering theory [182]. The modeled wavelength dependent extinction (black curve) and scattering cross sections (red curves) are depicted in Fig. 7.6. For the modeling an average refractive index of the embedding medium $n_{med} = 1.518$ was assumed and the refractive index of gold was calculated according to an analytical fit function to the dielectric constants of bulk gold [277]. At a wavelength of $\lambda=570$ nm the extinction cross section of the GNP is $\sigma_{ext}^{GNP} \sim 100 \text{ nm}^2$, which translates to an E_{22} extinction cross section of the (6,5) SWCNT of $\sigma_{ext}^{E_{22}} \sim 310 \text{ nm}^2/\mu\text{m}$. While there is an improvement of the $\sigma_{ext}^{E_{22}}$ value by a factor of three using the theoretical values for the extinction of the GNPs, there is still the uncertainty of the real size of the GNP as well as for length of the SWCNT. In order to improve the estimation for $\sigma_{ext}^{E_{22}}$ one would need to collect larger data sets of scattering spectra of both GNPs and SWCNTs and repeat the analysis for the corresponding averaged scattering amplitudes.

7.6. Manipulation of the iSCAT signal

It was already indicated in the discussion of the scattering contrast of the GNPs in Sec. 7.2 that the reflection coefficient r affects both the sign and amplitude of the observed scattering signal. Assuming that for very small structures only the interference term does significantly contribute to the measured signal, the contrast is expected to increase inversely with r (compare Eqn. 2.25). This dependency of the signal on the reflectivity does complicate a quantitative analysis of scattering related properties and puts high demands on the smoothness and homogeneity of the optical interface.

On the other hand the dependency of the signal on r can be exploited to enhance and/or inverse the scattering contrast [180]. The reflection coefficient r associated with the interface between two media is a function of the respective wavelength dependent refractive indices of the materials and of the polarization and angle of incidence of the incident light beam.

Motivated by the absence of the E_{11} scattering signal in the NIR spectral region, which might be caused by an increased reflectivity in this spectral region, the refractive index of the glass

cover slide and of the immersion oil were investigated over the whole range of white light excitation wavelength. Furthermore, the effect of a sample/immersion oil combination on the iSCAT signal of individual SWCNTs was studied, which is expected to exhibit a more favorable wavelength dependent reflectivity curve.

For optimum index matching conditions the refractive indices of the substrate and immersion oil should be nearly identical and should exhibit the same wavelength dispersion throughout the whole spectral range of interest. Fig. 7.7 (a) shows the refractive index curves of three different materials: "Schott M263" glass cover slide (red) and BK-7 glass (black) and the standard immersion oil "Nikon Type A" (blue). The wavelength dependent refractive indices in (a) were calculated based on the Abb numbers provided by the manufacturer. In the previous experiments the standard combination for the sample substrate and immersion oil were the "Schott M263" glass and "Nikon Type A" oil, respectively. Their refractive indices are offset by about 0.05 units but both exhibit a similar dispersion. Improved index matching conditions are expected for the same immersion oil and BK-7 glass (black curve), which is typically used as a standard material for optical elements. Compared to the other material combination the difference between both curves is smaller, especially for in NIR spectral region and the refractive index curves cross at 560 nm.

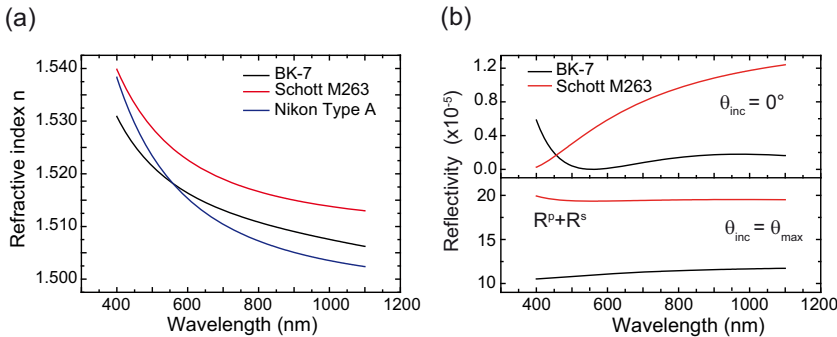


Fig. 7.7. (a) Wavelength dependence of refractive indices for two types of glass substrates (BK-7 and Schott M263) and the immersion oil (Nikon Type A). The curves are calculated based on the Abb numbers specified by the manufacturer by using Sellmeyer's formula or the Cauchy equation respectively. (b) Wavelength dependent reflectivity R calculated for the two glass-immersion oil interfaces (BK-7/Nikon Type A) and (M263/Nikon Type A). Upper panel: Normal incidence $\theta_{inc} = 0^\circ$; Lower panel: averaged reflectivity for s-and-p polarized light at the maximum angle of incidence $\theta_{inc} = \theta_{max}$ as defined by the $NA=1.4$.

The corresponding reflectivity curves R for two different incident angles θ_{inc} are shown in Fig. 7.7 (b). The reflectivity R is related to the reflection coefficient r in Eqn. 7.1 via: $R = r^2$. The curves represent the average reflectivity over the contributions of parallel R^p and perpendicular R^s incident light. For normal incident light, $\theta_{inc} = 0$, the reflectivity of the BK-7/Nikon Type A interface (black curve) in the NIR region is approximately a factor

4 smaller than the reflectivity of the MK263/Nikon Type A interface. Moreover, due to the crossing of the refractive index curves, the reflectivity is extremely small in the spectral region between 500–650 nm, which is favorable for the iSCAT signal amplitude of the E_{22} contrast of the (6,5) SWCNT. The reflectivity increases with increasing incident angle and becomes maximal for incident angles corresponding to the maximum focusing angle of a $NA=1.4$ objective $\theta_{inc}=\theta_{max} \approx 67^\circ$. At this incident angle the reflectivity is nearly one order of magnitude larger compared to the case of normal incident light.

In order to test the effect of the different BK-7 glass/Nikon Type A oil combination on the scattering contrast, CoMoCAT SWCNTs were deposited on the planar surface of an uncoated plano-convex lens made of N-BK7 glass (Thorlabs, LA1207). The lens was then placed on the sample holder of the microscope with the side covered by SWCNTs facing towards the microscope objective. Upon focusing the lens comes into contact with the immersion oil.

As can be seen in Fig. 7.8 the different reflectivity r of the substrate/immersion oil combination indeed leads to a change of the sign of the scattering contrast. In a few cases also an enhanced scattering contrast of (6,5) SWCNTs could be observed with signal amplitudes considerably larger than 0.15, which has been not observed for the standard material configuration consisting of the M263 glass/Nikon-Type A (compare Fig. 7.8 (a)). The narrow Lorentzian shaped PL spectra acquired at the same sample positions indicate that the scattering signal indeed originates from individual SWCNTs in the excitation volume and not from bundles or agglomerates.

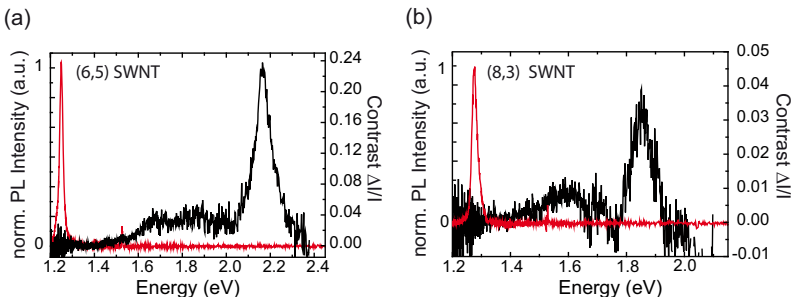


Fig. 7.8. Scattering (black) and PL spectra (red) of individual (6,5) (a) and (8,3) (b) SWCNTs deposited glass. The optical interface consists of BK-7 glass and Nikon Type A immersion oil. A change in the glass/immersion medium combination and in consequence a change of r of the interface leads for the particular case in an inversion of the scattering contrast. The amplitude of the E_{22} iSCAT signal of (6,5) SWCNTs which fall into a wavelength region where a small reflectivity r is expected are slightly enhanced.

The inversion of the contrast might be explained with the help of the refractive index curve in Fig. 7.7. For small wavelength up to the wavelength of the crossing point of the

BK-7/Nikon-Type refractive index curves at 560 nm the reflection is an internal reflection where $n_{oil} > n_{glass}$. For larger wavelength beyond the crossing point the characteristics of the reflection change to an external reflection as $n_{oil} < n_{glass}$ (Note: n_{oil} is here the refractive index of the incident and n_{glass} the one of the transmitted medium). The change from internal to external reflection results in a change of the sign of r (for small incident angles) [148]. For the M263 glass/Nikon Type A oil on the other hand only internal reflection is expected.

In summary, it could be shown that the scattering contrast, its amplitude as well as its sign, can be modified by changing the reflection coefficient r of the substrate/immersion medium interface. This might be exploited for elastic scattering imaging of the sample, while on the other hand the dependency of the iSCAT signal on r complicates the quantitative interpretation of the scattering spectra.

7.7. Combined PL and Elastic Scattering Measurements

It was demonstrated in the previous sections that elastic white light scattering of individual SWCNTs based on the iSCAT approach can be readily used for imaging and spectroscopy. For a quantitative analysis of the signals a detailed understanding of the parameters influencing the amplitude and line shape of the scattering signals is required. Since most of the parameters, such as e.g. the reflection coefficient r , are expected to be continuously and slowly varying functions of the wavelength and the E_{22} signals exhibit rather narrow linewidths, the spectral position of the signal maxima is expected to remain largely unaffected and therefore might be used for data analysis.

The iSCAT method can be easily combined with PL measurements of the same SWCNTs. This was used implicitly in the previous sections as a control measurement to identifying single SWCNTs. In the following, in the sense of an outlook, some interesting SWCNT specific problems are outlined, which can be addressed by the combination of both spectroscopy techniques.

Combined PL and white light scattering measurements of the same SWCNT can be effortlessly realized without any further modifications of the experimental white light excitation beam path (compare Sec. 3.1). The excitation for the PL experiments is delivered by the Ti:Sapph oscillator operating in CW mode at 800 nm and then guided through the PCF to the microscope. In this case, no white light is generated in the PCF and it acts just as a normal fibre. Laserline filters in front of the microscope and suitable longpass and bandpass filters in the detection path are added. Because of the identical beam path, there is virtually no displacement between the PL and the white light focus on the sample. In a first step, confocal PL images and spectra are acquired from a sample area. After this the Ti:Sapphire laser is switched to mode-locked operation and white light scattering spectra are recorded at the positions of the SWCNTs which the PL images.

From the previous PL measurements on the same sample material the abundance of luminescent semiconducting SWCNT chiralities for the 800 nm excitation wavelength is well known (compare also: Sec. 3.3). Five SWCNTs chiralities can be observed in PL measurements: (6,5), (8,3), (9,1) and (6,4) and (5,4), whereas the abundance of the latter is very small. In the correlated PL and white light scattering measurements, E_{22} scattering signals were mainly observed for the (6,5) and (8,3) and in rare occasions also from the (9,1) SWCNT. The (6,4) SWCNT shows strong PL but does not exhibit a detectable scattering signal.

At the current state of the experimental work, only the E_{22} energies of small diameter SWCNTs are accessible with the iSCAT experiments, while the corresponding E_{11} energies require complementary PL measurements. The knowledge about the two lowest optical transition energies is valuable in particular for the (n,m) assignment of the aforementioned tube chiralities. In the following this is illustrated for the example of the (8,3) and (6,5) SWCNTs.

From PL and absorption measurements on ensembles and on the single SWCNT level it is known that variations of the local dielectric constant ϵ lead to tube-to-tube shifts of the PL energy [225, 285–287] and in consequence to broad distributions of the E_{11} energies. For the present SC encapsulated CoMoCAT (8,3) and (6,5) SWCNTs these distributions are centered at 975 nm and 990 nm, respectively. Importantly, both distributions partially overlap which complicates the unambiguous chirality assignment of individual SWCNTs with E_{11} energies falling into this overlap region when solely relying on PL information. PL spectra of individual (8,3) and (6,5) with PL energies within this overlap region are displayed in Fig. 7.9 (a).

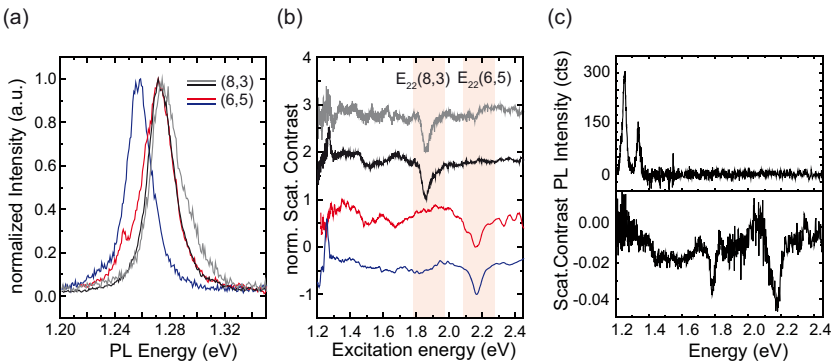


Fig. 7.9. Chirality assignment based on the E_{22} and E_{11} excitonic transition energies of the same SWCNT (a) Normalized scattering contrast of (8,3) (grey and black curves) and (6,5) SWCNTs (red and blue curves). The spectral range associated with excitonic E_{22} transitions of the (8,3) and (6,5) SWCNTs is marked by the red shaded areas. Spectra are offset for clarity. (b) Corresponding PL spectra (c) PL and scattering spectra of a small aggregate of SWCNTs consisting of a (8,3) and (6,5) SWCNT.

As can be seen in Fig. 7.9 (b), the E_{22} energies of both chiralities are well separated by approximately 300 meV, which allows for an unambiguous chirality assignment. Especially, for the exceptionally blue shifted PL spectrum of the (6,5) SWCNT in Fig. 7.9 (a) the additional E_{22} information is required. Chirality determination based on the PL emission energy solely, leads to the conclusion that this is in fact a (8,3) SWCNT. The same analysis can also be extended to spectra with multiple emission bands, typically observed if several SWCNTs are in the focus are excited simultaneously or for small bundles as indicated in Fig. 7.9 (c).

From the comparison of the (6,5) center energies of the PL and scattering bands in Fig. 7.9 (a) and (b) it becomes obvious that while the PL bands are shifted in energy by 10 meV the corresponding E_{22} energies of both SWCNTs are nearly identical. As it was mentioned before the transition energies of SWCNTs change with varying local dielectric environment and it is well known that the corresponding exciton energies E_{11} and E_{22} of a specific SWCNT chirality are affected differently [288–290]. On the single SWCNT level, this is exemplarily illustrated for the (6,5) and (8,3) in Fig. 7.10.

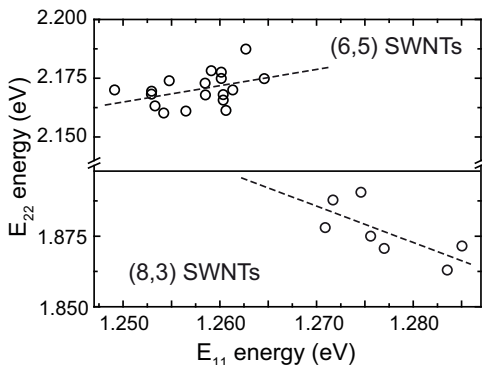


Fig. 7.10. (a) Correlation of E_{22} vs. E_{11} energies of individual (6,5) and (8,3) SWCNTs.

Here the E_{22} energies are plotted against the corresponding E_{11} transition energies. While in the case of the (6,5) SWCNT the data indicates that red-shifted E_{11} energies are correlated with red-shifted E_{22} energies (positive slope), the contrary situation is observed for the (8,3) SWCNTs where red-shifted E_{11} energies are correlated with blue-shifted E_{22} energies.

Finally, it is worthy of note that indeed E_{11} white light scattering signals of SWCNTs is observable, unfortunately not for individual SWCNTs but for larger aggregates. Fig. 7.11 shows the white light scattering spectra (a) and corresponding PL spectra (b) acquired for such an aggregate. The normalized scattering spectra shows a variety of different bands, which can be assigned to the optical transitions of different SWCNT chiralities as follows [200]: 2.167 eV → E_{22} (6,5); 2.101 eV → E_{22} (6,4); 1,877 eV → E_{22} (8,3) and finally a broad intense band

at 1.256 eV which is comprised of the E_{11} signal contributions of the (9,1), (8,3) and (6,5) chiralities.

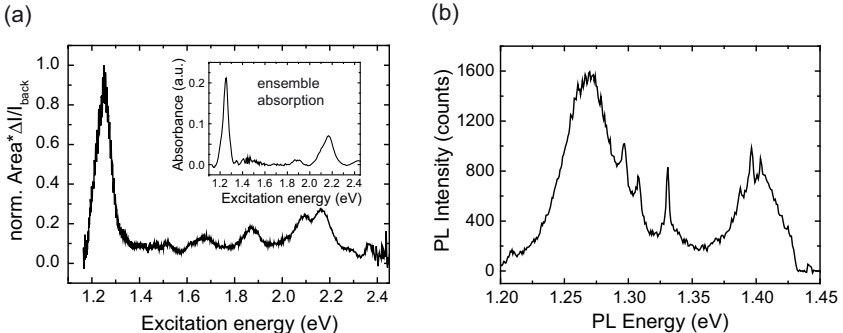


Fig. 7.11. (a) White light scattering spectra of a large aggregate of SWCNTs. The scattering spectra exhibits scattering signals in the spectral region between 1.7–2.3 eV, which can be assigned to the E_{22} optical transitions of small diameter SWCNTs (see main text for a detailed assignment). The strong and broad scattering signal centered at 1.256 eV can be assigned to the combined E_{11} contributions of the (6,5), (8,3) and (9,1) SWCNTs. The scattering spectra resembles fairly well an ensemble absorption spectrum of the same SWCNT material (inset) (b) Corresponding PL spectrum. Although the E_{11} scattering and ensemble absorption signal of (6,4) and (5,4) SWCNT is not detectable, a broad PL band which can be assigned to those chiralities is observed in the spectral region between ~1.38 and 1.43 eV.

A direct assignment of the band at 1.661 eV is not possible. The band appears in a spectral region associated with the semiconducting E_{22} and metallic E_{11} optical transitions, but also a phonon-sideband $E_{11}+G$ -band of the (6,4) SWCNT is expected in this spectral region. The scattering signals here are positive as the BK7-glass/Nikon Type A substrate/immersion oil combination was used. Remarkably, the normalized scattering spectrum resembles fairly well the ensemble absorption spectrum (inset). In agreement, with the single nanotube studies of the previous sections also here the E_{11} scattering signal of the (6,4) SWCNT in the scattering spectra as well as in the ensemble spectra is absent. Then again the PL spectrum in Fig. 7.11 (b) shows clear signatures for the (6,4) SWCNT. The heterogeneously broadened PL band between 1.25–1.32 eV is comprised of the PL contributions of the (6,5), (8,3) and (9,1) chiralities. The second broadened band in the range of 1.39–1.43 eV is due to the PL of (6,4) SWCNTs and possibly also (5,4) SWCNTs. The narrow bands on top of the PL signal are the characteristic Raman bands of SWCNTs.

7.8. Conclusion

In conclusion, the first results of elastic white light scattering spectroscopy of individual SWCNTs on a transparent substrate were presented. It could be shown that the simple common-

path interference scattering approach utilizing an inverted confocal microscope in reflection mode in combination and employing a photonic crystal fibre as broadband white light excitation source is capable of elastic scattering imaging and spectroscopy of individual SWCNTs. The technique further allows the simultaneous acquisition of PL and elastic scattering study on the same tube without major adjustments of the setup.

The method is suited for a quick analysis of the SWCNT chirality, however quantitative information about e.g. the scattering/extinction cross section or an analysis of the lineshape of the scattering signals are hampered because of the interferometric nature of the iSCAT signal. The assignment of the magnitude of the iSCAT signal to material specific electronic or optical parameters can be realized only indirectly and does require supplementary measurements of particles with well known optical properties. In this context it was possible to tentatively determine the scattering cross section of the E_{22} excitonic transition of (6,5) SWCNTs.

In its current state the microscope setup requires further optimization of its instrumentation. Especially the low detection efficiency of the CCD camera in the NIR spectral region inhibits the observation of the first optical E_{11} transitions of small diameter SWCNTs. Furthermore, the setup would also profit from a power stabilization and a more spectrally uniform white light output which might result in an improvement of the SNR. Due to the scattering geometry, the detected iSCAT signal is governed by the extinction (absorption) of SWCNTs giving rise to a negative contrast in the elastic scattering scan images swell as in corresponding elastic scattering spectra. In order to study the real scattering properties of SWCNTs a dark field illumination/detection apertures need to be included as e.g. used to study the scattering of small diameter GNPs in ref. [291].

Part IV.

Optical Characterization of Plasma Treated Graphene

8. Optical Characterization of Oxygen Plasma Treated Graphene

It is shown for the first time that photoluminescence (PL) can be induced in single layer graphene (SLG) upon brief exposure to a "mild" oxygen plasma. In this chapter the first optical characterization of this novel material is presented utilizing spectroscopic methods, such as (time-resolved) PL-, Raman-, and elastic white light scattering spectroscopy. The PL of the oxygen plasma treated graphene, in the following denoted as photoluminescent graphene (PLG), is stable and spatially uniform across the whole flakes. A single broad emission band extends from the blue visible into the NIR spectral region. The evolution of the defect induced Raman D-band with increasing plasma exposure times suggests the loss of sp^2 connectivity within the graphene flakes and the formation of nanocrystallite sp^2 islands with an average diameter of $L_a \approx 1\text{ nm}$. Deviations from graphenes' intrinsic structural and electronic properties become also apparent in the corresponding elastic white light scattering spectra. The modeling of the elastic scattering contrast yields a refractive index similar to the one of graphene oxide. Remarkably, the PL is only observed for SLG, while PL from multilayer graphene (MLG) is strongly suppressed by subjacent layers. The possible origin of the PL is discussed.

The studies for this chapter were carried out in close collaboration with the research group of Dr. Andrea Ferrari (Engineering Department, University of Cambridge). The sample preparation and parts of the Raman spectroscopy were performed by the group in Cambridge. This chapter is based on the results which were published as "*Making Graphene Luminescent by Oxygen Plasma Treatment*" in *ACS Nano*, **3**, 3963 (2009).

8.1. Introduction

To date graphene is at the center of intense research efforts. The outstanding properties of graphene such as near-ballistic transport at room temperature [11] and high charge carrier mobilities up to $20^4\text{ cm}^2/\text{Vs}$ [15, 17, 292] make it a promising material for nanoelectronic devices. Furthermore, its transparency [269, 279] and mechanical properties are ideally suited for micro and nanomechanical systems, transparent and conductive composites and electrodes [293, 294] and photonics [295]. Despite these promising perspectives the applicability of graphene as material for transistors or in optoelectronic devices such as light emitting diodes, photodiodes or as solar cells is hampered, as it does not exhibit an intrinsic bandgap. In ideal graphene the valence and conduction bands touch at distinct points at the Fermi level which makes graphene a zero-band gap semiconductor with an linearly decreasing DOS ap-

proaching the K points [1–3].

Manipulating the electronic band structure of graphene is of great technological interest. To date, there are two main avenues to modify the electronic structure of graphene. Both are aiming to exploit the quantum confinement effect (see Sec. 1.2) for opening a bandgap near the Fermi level. The effect occurs when the physical size of an object is on the order of the wavelength of the electrons [58, 296]. Experimentally this can be achieved by lithographically cutting a graphene sheet and producing narrow stripes of graphene, so called graphene nanoribbons, or graphene quantum dots [297–303]. Furthermore, it could be demonstrated that also the longitudinal unzipping of carbon nanotubes [304, 305] and bottom-up organic chemistry synthesis methods are viable routes for the preparation of narrow graphene nanoribbons [39, 40, 306]. The second approach relies on the chemical or physical treatment of graphene with different gases, bombardment with ions or irradiation with soft x-rays aiming at the reduction of the π -bond connectivity of graphene [144, 307–309]. Hydrogen plasma was used to controllably and reversibly modulate the electronic properties of individual graphene flakes, turning them into insulators [307] and aggressive oxygen treatment was applied to create graphene islands [310]. Thus far, no PL indicating a band gap opening has been observed from individual graphene layers, either cut into ribbons or dots.

In the following it is shown that it is possible to turn single-layer graphene luminescent upon exposure to a mild oxygen plasma. The electronic and vibrational properties of this photoluminescent graphene (PLG) are characterized by employing various optical spectroscopy techniques. The findings in this work also provide new insights in the microscopic origin of the PL in graphene oxide, which to date is still under debate.

8.2. Preparation of PLG

Graphene samples were prepared by micromechanical exfoliation of pyrolytic graphite, following the general procedure described in ref. [11] and the supporting online material therein. The graphene samples were transferred to a silicon substrate with a 100 nm cover layer of SiO_2 . Prior to plasma exposure, single-layer graphene flakes were identified based on their elastic scattering contrast and their characteristic Raman spectrum. [134, 311].

Luminescent graphene was then prepared by exposing the samples to a mild oxygen/argon (1:2) RF plasma (0.04 bar, 10 W). In order to study the influence of different plasma exposure times, six batches of plasma treated graphene samples were fabricated using plasma exposure times ranging from one to six seconds.

8.3. PL Spectroscopy and Time-resolved PL Measurements of PLG

Confocal PL images were obtained by raster scanning the sample through the focus of a high NA air objective ($NA=0.95$) (compare Fig. 3.1) and detecting the optical response either by an APD or by a combination of a spectrograph and CCD camera for spectroscopic imaging. CW excitation at 473 nm for PL imaging and spectra acquisition was provided by a solid state

diode laser (Cobolt Blues 473 nm). Small excitation powers of $20\text{ }\mu\text{W}$ and pixel acquisition times of 10–20 ms were used for PL imaging in order to avoid sample heating effects and photobleaching. PL spectra were acquired at slightly higher excitation powers at $\sim 50\text{ }\mu\text{W}$ and acquisition times of 10 s utilizing a grating with 150 lines/mm blazed at 800 nm. All PL spectra presented in the following are corrected for the wavelength dependent variations originating from the transmission characteristics of the optical components, such as beam splitter, optical filters as well for the wavelength dependent reflectivity/detection efficiency of the grating/CCD-camera.

PL transients were recorded with the TCSPC setup described in Sec. 3.4. Pulsed laser excitation at a wavelength of 530 nm (2.34 eV) was provided by a PCF (see Sec. 3.5.1 for details). Two $530\pm 10\text{ nm}$ bandpass filters (Thorlabs, FB530–10) were used to select the designated wavelength from the white light output of the PCF and to ensure complete suppression of all other wavelength components. A $647\pm 10\text{ nm}$ bandpass filter (Chroma, Z647/10x) was placed in front of the APD for detection of PL close to the wavelength of the maximum of the PL band. The IRF which was used for transient fitting was recorded with the TCSPC setup by detecting laser light at 647 nm reflected from a bare glass cover slide.

Fig. 8.1 shows two confocal PL scan images of graphene exposed to the oxygen plasma treatment times for (a) 3 s and (b) 5 s. For exposure times smaller than four seconds only spot like PL is observed. Consequently, longer treatment times >4 s result in the complete transformation of graphene into PLG. The PL intensity of such flakes is spatially uniform across but slightly decreasing towards the edges. Irradiation with high power laser pulses exceeding $200\text{ }\mu\text{W}$ leads to irreversible photo bleaching, as it can be observed for the position 3 in Fig. 8.1(b). Interestingly, the plasma etching starts at the flake center and not, as expected, at the graphene edges, which are supposed to be reaction centers with increased chemical activity. Presumably, the transformation starts at pre-existing defect sites across the lattice, like protrusions introduced by the substrate topology, or vacancies, since these sites exhibit an increased chemical activity, as for example dangling carbon bonds in the case of vacancy sites which are readily available for chemical attacks.

Representative for all batches prepared at different plasma etching times, the PL spectra of PLG prepared with an exposure time of 5 s are shown in Fig. 8.1(c). A single spectrally broad band, extending from 490 to 900 nm (FWHM $\sim 0.5\text{ eV}$), and centered at 700 nm (1.77 eV) is dominating the spectra. Each of the spectra was acquired at a different position across the flake and is marked by the numbers in Fig. 8.1(b). Small variations in the maximum peak position and shape may occur. It was further found that the different plasma exposure times do not affect the shape or center position of the PL band significantly. Importantly, PL spectra acquired with pulsed and CW excitation at the same average power levels are virtually identical, which excludes the possibility that the observed emission bands are just the long wavelength tail of blackbody radiation whose origin might be laser induced heating of the material.

The PL decay dynamics of PLG is complex and can be well described by a triple-exponential function, yielding average decay constants (relative amplitudes) of 40 ps (64 %), 200 ps (29 %)

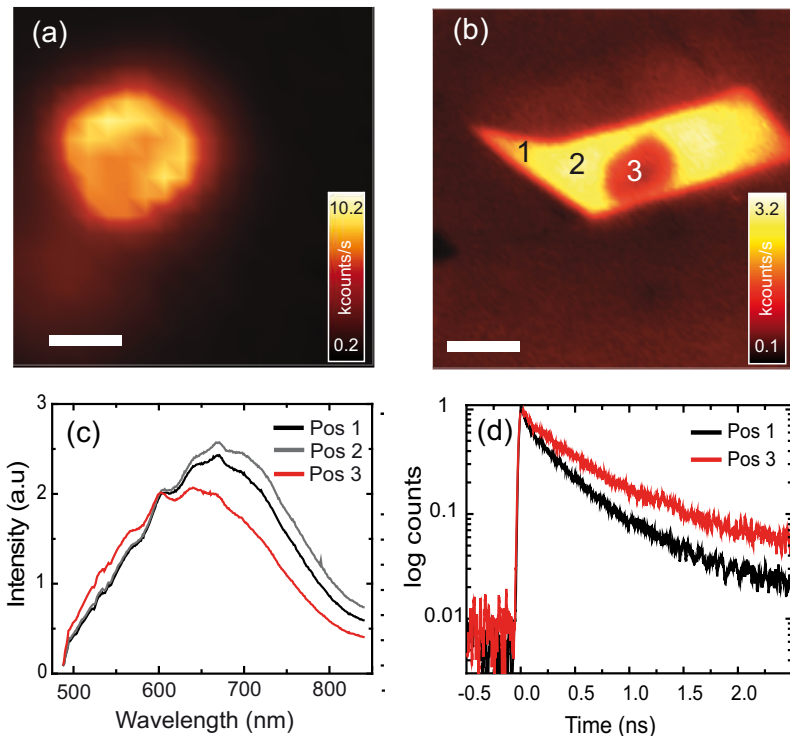


Fig. 8.1. (a) Confocal PL images of graphene samples exposed to the oxygen plasma for 3 s and (b) for 5 s. Excitation wavelength was 473 nm (2.62 eV). Scale bars are 4 μm and 10 μm , respectively. Point like areas are observed for small oxidation times while for longer treatment times the PL is uniform across the flakes. (c) PL spectra taken at sample positions designated in (b) and corrected for the detector response. The PL arises as a single broad band centered at \sim 700 nm (1.77 eV) with a FWHM of \approx 0.5 eV. (d) PL transients recorded at positions indicated in (b). The decay dynamics is complex and can be well described by a triple-exponential fit function with decay times (relative amplitudes) of 40 ps (64 %), 200 ps (29 %) and 1000 ps (6 %).

and 1000 ps (6%). The PL transients in Fig. 8.1(c) were measured at two different positions showing bright and weak PL on the flake in Fig. 8.1(b). The decay times observed here are much larger than reported for e.g. semiconducting SWCNTs or amorphous carbon [124, 312, 313].

8.4. Raman Spectroscopy of PLG

So far the PL spectroscopic data could not provide specific information on the transformation steps from pristine graphene to PLG. Complementary Raman spectroscopic data can yield further insights on the structural changes caused by the oxygen plasma etching. Raman spectra were recorded with a Renishaw micro-Raman spectrograph using the 514 nm line of an Ar⁺-ion laser. Excitation powers were in the range of 1–2 mW. The spatial resolution is estimated to be ~800 nm.

Fig. 8.2 plots the Raman spectra and main fitting parameters as function of plasma treatment time. Basically instantaneously, after one second of plasma exposure the Raman spectrum is markedly different from the spectrum of pristine graphene. Additional Raman bands arise and for treatment times longer than two seconds, the broad PL can be observed as a slowly rising background in the spectra. Most notable is the appearance of the strong defect related D-(1350 cm⁻¹) and D'-bands and their combination modes D+D' at 2950 cm⁻¹, which indicate the introduction of a significant amount of structural disorder (compare Sec. 1.6). In fact, the most dominant Raman band for small plasma exposure times is the defect activated D-band at 1350 cm⁻¹. Further evidence for the introduction of disorder is the broadening of the G-Band at 1600 cm⁻¹ whose FWHM at longer treatment times is about 10 times larger than for pristine graphene. This broadening can be attributed to the merging of the G-band with the D' band, which typically occurs at ~1620 cm⁻¹. The partial overlap of the two bands results in a single broadened band. But also the second order Raman D- and D'- bands are significantly broadened which can be attributed to the relaxation of the back-scattering condition in the double resonance process.

The evolution of the I_D/I_G -ratio with exposure time, plotted in Fig. 8.2 (b), gives further information about the changes of the microscopic structure within the flakes. The intensities of the D and G bands are given here as the integrated areas beneath the respective Raman bands. Nearly instantaneously upon plasma exposure the I_D/I_G -ratio raises to its maximum value of 1.8 and then gradually decreases to a constant level around 0.76.

Based on the empirical relation established by Tuinstra and Koenig between the I_D/I_G -ratio and the size of nanocrystallite domains L_a in sp² carbon materials (compare Eqn. 1.53) it is possible to obtain an estimation for the average cluster size where the original sp² connectivity of the graphene layer is preserved. Two different regimes for the dependency of the I_D/I_G -ratio on the cluster size are reported. Regime (1), where the I_D/I_G -ratio is proportional to $1/L_a$; and regime (2) for $L_a < 2$ nm where the I_D/I_G -ratio decreases rapidly for decreasing L_a and is characterized by a L_a^{-2} dependency. This regime is described

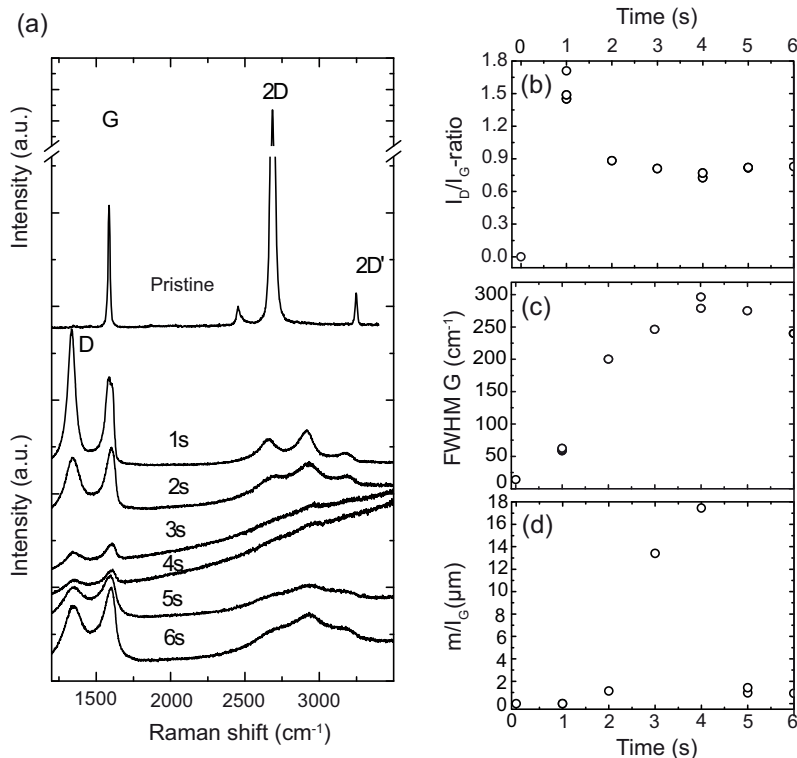


Fig. 8.2. Evolution of Raman spectra and deduced quantities as function of plasma exposure time. (a) Raman spectra of pristine graphene (topmost spectra) and PLG. (b) Intensity ratio of the Raman D and G band: I_D/I_G . (c) Linewidth of the Raman G band measured as FWHM. (d) Ratio of the PL background slope (m) to G peak intensity I_G .

by a modified Tuinstra-Koenig relation: $I_D/I_G = C'(\lambda)L_a^2$ with the proportionality factor $C'(514\text{ nm})=0.55\text{ nm}^{-2}$ [145]. Assuming that the observed decrease of the I_D/I_G -ratio with plasma exposure time is related to an increase of structural disorder and therefore a reduction of the cluster size. Employing this relation to the data, one finds that the average cluster size L_a is continuously decreasing to a minimum value of $\sim 1\text{ nm}$ for the longest plasma treatment times, indicating that the carbon network starts loosing six folded rings already for treatment times larger than 1 s.

This is validated further by the evolution of the FWHM of the Raman G-band, $\text{FWHM}(G)$, with exposure time in Fig. 8.2(c). In defect-free graphene, a variation in the $\text{FWHM}(G)$ might originate from doping, changes in temperature or stress [314–317]. However, in the case of defective carbon materials, peak broadening is a result of the activation of $\mathbf{q} \neq 0$ phonons. The relation between $\text{FWHM}(G)$ and L_a for different disordered and amorphous carbon materials was studied in ref. [318]. Comparing $\text{FWHM}(G)$ in Fig. 8.2(c) with the empirically determined trend reported in that publication (Fig. 14 in [318]), again an average cluster size $L_a \approx 1\text{ nm}$ is found for the longest treatment times. Moreover, the large FWHM of the G-band implies a distribution L_a around an average value.

A measure for the strength of the PL of a carbonaceous material, $m(\text{PL})/I_G$, can be defined as the ratio of the slope of the PL background m to the intensity of the first order Raman G-band I_G . This definition was introduced in reference [319] to compare the strength of the PL of amorphous carbons with different compositions. A plot of the PL strength against treatment time is shown in Fig. 8.2(d). The PL strength reaches a maximum at around four seconds and then decreases rapidly for the longest treatment times. The weak PL for long plasma treatment times is consistent with the absence of PL from graphene samples which were oxidized in an O_2/Ar gas flow at elevated temperatures [310].

In summary, the Raman spectroscopic data of PLG reveals the introduction and continuous increase of structural disorder upon the oxygen plasma treatment. This can be attributed to a reduction of sp^2 connectivity and correspondingly to an increasing fraction of sp^3 -bonds and/or carbon vacancies within the PLG. The data suggests that small clusters are formed for which the conjugated sp^2 lattice of graphene is preserved. The average cluster size is as small as $\sim 1\text{ nm}$ for the longest treatment times. Depending on the reaction conditions, the size distribution of the clusters changes. The formation of small clusters for the plasma treatment is in agreement with the findings of Raman experiments on intentionally damaged graphene, where carbon atoms were removed by an argon-ion-bombardment [144] or by irradiation with soft x-ray radiation [309].

8.5. Elastic White Light Scattering of PLG

Elastic white light scattering spectroscopy is a complementary optical technique to Raman spectroscopy which also allows to determine precisely the layer number of few layer

graphenes. Single-layer graphene can be quickly identified by its elastic scattering contrast when deposited on a layered Si/SiO₂ substrate with a well defined thickness of the SiO₂ top layer [13, 311]. The optical contrast in confocal white light scattering images can be defined as the difference between the reflected light intensity detected at a sample position with graphene flake I_{det} and a background position I_{back} . A normalization by I_{back} cancels out the various wavelength dependent modulations introduced to the signal which originate from the transmission/reflection/sensitivity characteristics of the optical elements and detectors used in the experiment:

$$\delta = \frac{I_{det} - I_{back}}{I_{back}} \quad (8.1)$$

The detected signal I_{det} arises mainly from the superposition of the reflected light field from the air/graphene and from the SiO₂/Si interface. Accordingly, the background signal I_{back} is the superposition of the reflected field from the air/SiO₂ and SiO₂/Si interfaces. The visibility of graphene deposited on such a layered substrate configuration can be enhanced by exploiting the interferometric nature of the detected signals. The background intensity I_{back} becomes minimal and in consequence the contrast (visibility) of graphene reaches its maximum value for a phase differences between the two interfering light fields equal to multiples of $\pi/2$. Experimentally such an enhancement condition can be realized by adjusting the thickness of the SiO₂ spacer layer, e.g. for illumination with green light at an wavelength of 580 nm the optimum SiO₂ layer thickness for a maximum graphene contrast can be either 100 or 300 nm [311, 320, 321]. As the elastic scattering contrast of few layer graphene scales linearly with the layer number up to a maximum number of ten, the method can be also used for determining the number of layers in multilayer graphene (MLG) [311]. Further information on the elastic white light scattering of graphene and MLG and the modeling of the elastic scattering contrast of graphene on layered substrates can be found in Appendix B.

The elastic white light scattering experiments were performed by using the confocal microscope combined with a PCF as a supercontinuum white light source as described in Sec. 3.1 and Sec. 3.5.1. The detectable part of the white light output covered a spectral range between ~500–980 nm (compare Sec. 3.5.1). Elastic white light scattering images were recorded using either direct detection of the scattering response by an APD or by spectroscopic imaging with an combination of spectrograph and CCD camera. For the latter an elastic scattering spectrum is acquired at each scan pixel. In a subsequent post-processing step scattering intensity maps of the sample for different spectral windows can be generated. Typical excitation powers on the sample were about 60 μ W and pixel integration times of 50 ms were used.

The wavelength dependent scattering contrast δ of the PLG flake prepared with 5 s plasma exposure time (compare Fig. 8.1(a)) (red) is plotted in Fig. 8.3 (a). For comparison a modeled curve of the elastic scattering contrast of SLG is shown (black). For the modeling, the identical Si/SiO₂ substrate configuration as in the case of the PLG sample was considered. Furthermore,

the refractive index of bulk graphite, determined by electron energy loss spectroscopy [322], was used in a first approximation for the refractive index of graphene. The white light scattering response of the PLG is distinctly different to the one of SLG. The latter exhibits a negative contrast throughout the whole range of excitation wavelength with a maximum absolute value of $|\delta_{\max}| \approx 0.11$ at 610 nm, while the contrast of the PLG is in general smaller with maximum value of $|\delta_{\max}| \approx 0.05$ at 640 nm. Remarkably, the PLG contrast becomes positive for wavelengths smaller than 580 nm. This is also visualized in Fig. 8.3 (b) and (c), which shows the elastic scattering scan images of the graphene flake for the spectral windows of 500–550 nm and 625–650 nm, respectively.

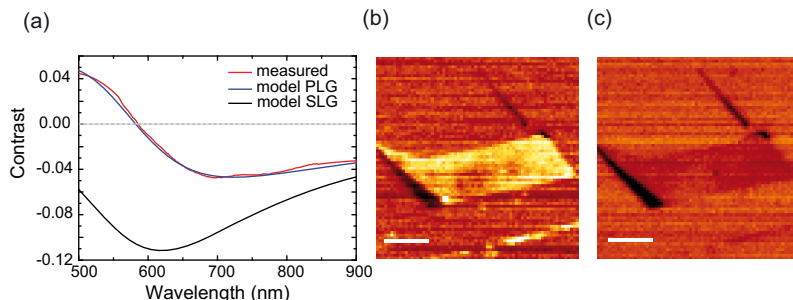


Fig. 8.3. (a) Elastic white light scattering spectra of luminescent graphene (red) exposed to the oxygen plasma for 5 sec (red curve). The blue curve is the modeled scattering contrast for PLG assuming a complex refractive index similar to the one observed for graphene oxide [323]. The modeled contrast of pristine graphene (black curve) is shown for comparison. The images in (b) and (c) are the white light elastic scattering maps representing the intensity of PLG integrated over the spectral range of 500–550 nm (b) and 625–650 nm (c). Scalebars are $10 \mu\text{m}$.

The blue curve in Fig. 8.3 (a) is the modeled contrast of the PLG based on an analytical model for the reflectance/transmittance of multi-layer systems (compare Chap. B). Input parameters for the model are only the refractive indices of the different materials which form the multi-layer system. While for the refractive indices of Si and SiO_2 the tabulated data in literature was used, the refractive index of the PLG was set as a free parameter. For the fitting the refractive index can be represented by the general Cauchy Formula: $n' = A_n + B_n/\lambda^2 + i(A_k + B_k/\lambda^2)$. Good agreement between experiment and model is obtained for the Cauchy parameters $A_n = 2.76$, $A_k = 0.06$, $B_n = 3000$ and $B_k = 1500$, which are comparable to the ones reported for graphene oxide [323].

So far the optical studies were focusing on plasma treated single layer graphene. The PL and elastic scattering properties of plasma treated multilayer graphene (MLG) are distinctly different. This is illustrated in Fig. 8.4, where (a) the PL of plasma treated graphene flakes with varying layer numbers is compared with the corresponding elastic white light scattering signal (b). The number of layers of the different flakes is denoted in the elastic white light scattering

image (b) and was determined separately by Raman spectroscopy prior to the plasma treatment. The elastic scattering contrast of plasma treated MLG does not scale linearly with the layer number as compared to the case of untreated MLG. Furthermore, the elastic scattering spectrum of untreated MLG on the specific substrate configuration features only negative contrast, while the positive contribution below 580 nm observed for PLG is absent. The scattering spectra of treated MLG can be represented by a superposition of PLG and untreated SLG/MLG. PL intensity and scattering contrast are directly correlated, as seen in Fig. 8.4 (c) for flakes with different layer numbers. Strong PL is observed only for single layered PLG, while PL is nearly absent for plasma treated MLG with layer numbers of two to three layers.

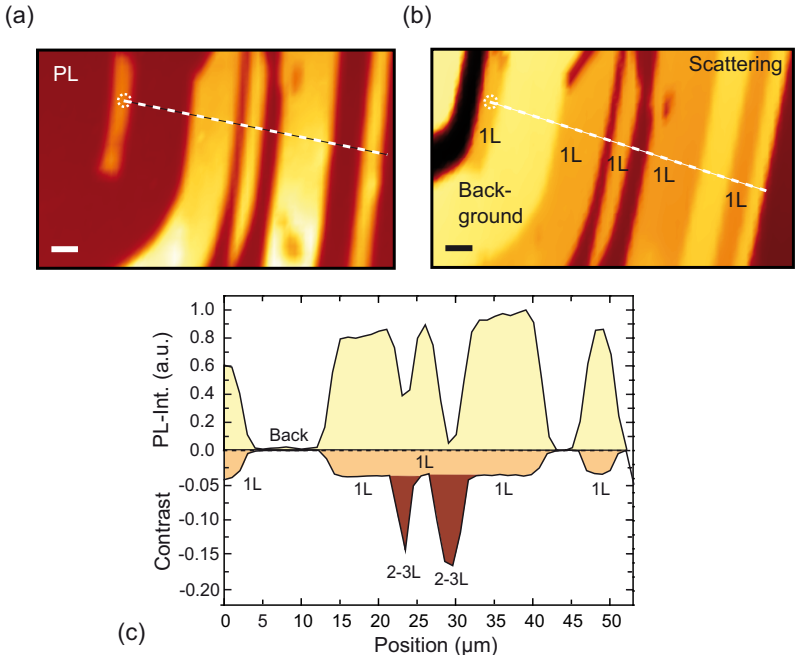


Fig. 8.4. Correlation between PL intensity and graphene layer number. (a) Confocal PL image; (b) elastic white light scattering image of the same sample area. (c) Corresponding cross sections taken along the dashed lines in (a) and (b). The circles mark the starting point of the cross sections. Strong PL (upper panel) is only observed from plasma treated single layer graphene, marked 1L. PL in multilayer graphene with 2–3 layers, is efficiently quenched. The scalebars are 10 μm .

Oxygen plasma etching of graphite proceeds layer by-layer [324] and thus only the topmost layer of MLG is expected to be affected by the treatment. The strong suppression of the PL from plasma treated multilayer graphene might be explained in terms of PL quenching by subjacent untreated layers. A similar observation has been made for the fluorescence of a dye

film deposited on single layer graphene. The fluorescence intensity of the dye was reduced by about three orders of magnitude compared to a reference sample without graphene as substrate. Energy and/or electron transfer from the dye to the graphene layer was suggested as possible process leading to the efficient PL quenching [325].

8.6. Discussion

Due to the missing bandgap luminescence from pristine graphene is not expected in the first place. For linear excitation power regime the photoexcited electrons and holes thermalize fast by carrier-carrier and carrier-phonon scattering [326]. However, broad nonlinear PL was observed for excitation with picosecond and femtosecond pulses whose origin is still under discussion [327–329]. Moreover, luminescence in the NIR and visible spectral region in terms of black-body radiation was observed for electrically heated graphene and graphene films [330, 331]. Due to the persistence of the PL also at low power CW excitation, where sample heating effects are not expected, both processes can be excluded as possible origin of the PL from PLG.

The observation of a broad PL of graphene after plasma treatment naturally implies that the PLG possess a distinct different structural and/or chemical composition. Strong evidence for the introduction of structural disorder induced in the graphene lattice was found in the Raman and elastic scattering spectra. Especially the emergence of the defect activated 2nd order D- and D' bands as well as the characteristic broadening of the G-band even for the shortest plasma treatment times support this. A more quantitative picture on the degree of disorder introduced by the etching process could be obtained from the analysis of the gradual decrease of the Raman intensity I_D/I_G -ratio for increasing plasma treatment times (compare Sec. 8.4). A decrease of the I_D/I_G ratio indicates that the sp^2 lattice is continually loosing the connectivity. More precisely the number of intact six-folded carbon rings which are required for the activation for the D-band scattering is steadily decreasing for increasing treatment times [144, 145] and based on the empirical Tuinstra-Koenig relation an average cluster size of $L_a=1\text{ nm}$ could be deduced for the longest plasma treatment times.

The exact mechanism how the "mild" oxygen plasma, its composition and the specific reaction conditions, affects the graphene structure cannot be answered with the optical spectroscopy techniques used in this work. Complementary high resolution AFM or STM might give further insights about the changes in the morphology, while ^{13}C solid-state NMR could give information on the changes in the chemical composition and more specifically on oxidized carbon groups formed during the plasma treatment.

In a recent study where the effect of physically and chemically driven oxygen plasma etching processes on the surface morphology of graphite was investigated by STM measurements revealed that both processes result in different types and size of surface defects. The physical driven etching process, where the carbon lattice is damaged by the ballistic impact of

accelerated high-energy ions, results in a stochastical distribution of defect sites across the exposed graphite surface without any notable site selectivity [332]. In the chemically driven process, oxygen radicals and/or O_2^+ ions initiate oxidation reactions at reactive lattice sites followed by desorption of carbon monoxide (CO) or carbon dioxide (CO_2). This oxidative etching is more site selective and occurs preferentially at preexisting defect sites and continues at newly created vacancy sites. This leads to the growth of nanometer sized pits [332]. A similar mechanism might explain the transformation of point like PL spots across the flake observed at small plasma exposure times to complete luminescent flakes at increasing oxygen treatment times.

The formation of large pits was also reported for the oxidative etching of single and multi-layer graphene using an oxygen/argon gas mixture at high temperatures [310]. In addition to the removal of carbon from the graphene lattice, it was found that this kind of chemical etching leads to persistent oxidized carbon sites. Depending on the specific reaction conditions it is expected that the endoperoxides or hydroperoxides are formed [310]. For neither of the previously mentioned etching processes conducted on graphene, physically or chemically driven, the observation of PL has been reported so far.

Graphene oxide (GO) is a chemical modified graphene derivative, which, when dispersed in solvents or dried as a film, is luminescent. Depending on the preparation method narrow PL bands in the UV or a broad PL extending from the visible to the NIR spectral region are observed [333–337]. GO is typically synthesized by oxidative cleaving of graphite using strong oxidation agents (e.g. potassium permanganate) and mineral acids in a wet chemistry approach [338]. Hydrophilic functional groups such as hydroxy- or carboxyl groups facilitate the water-soluble and also prevent the congregation of the flakes and allows to prepare single layer flakes. It is assumed that different preparation methods for PLG and GO lead to different chemical compositions of C-O functional groups as well as the degree of oxidation might be different for PLG and GO. The origin of the PL in GO is still under debate. One model which is supported by several groups assigns the PL to bandgap emission from electron confined sp^2 islands surrounded by sp^3 hybridized lattice sites, which were created in the course of the oxidation process [333–335].

Similarly, such a model might be adapted to explain the PL of the PLG. Based on the average cluster size of $L_a \approx 1\text{ nm}$ deduced from the Raman experiments, quantum confinement would be indeed a plausible explanation for the observed PL. To elucidate this in more detail, a proposal for the structure of PLG based is depicted in Fig. 8.5 (a). The oxygen plasma treatment damages the regular graphene structure and leads to the formation of a multitude of smaller graphene fragments where the sp^2 carbon lattice remains unaltered. These fragments or clusters are embedded in a mixed matrix of sp^3 hybridized carbon or vacancy sites. The clusters are represented in Fig. 8.5 by the intact hexagonal graphene honeycomb lattice in the figure, while the damaged graphene lattice is not explicitly pictured (white).

The electrons in graphene behave as massless fermions [1, 339] with a linear energy dispersion: $E = \hbar v_f |k|$, where v_f is the Fermi velocity. For an electron in a box, here represented by

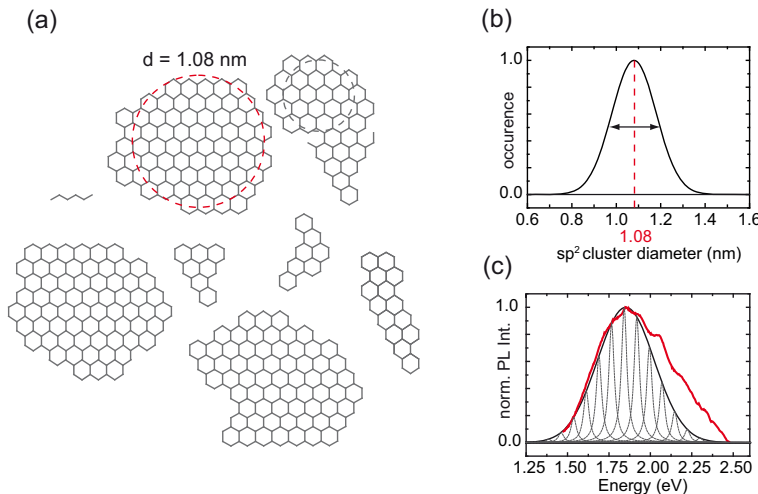


Fig. 8.5. (a) Presumed structural model of PLG which could explain the PL as a consequence of quantum confinement. The oxygen plasma treatment damages the graphene sp² network and leads to the creation of vacancy sites and/or oxidized carbon sites. Clusters with intact sp² lattice (black hexagons) are surrounded and separated by a matrix of sp³ hybridized carbon bonds or vacancies (white background). The observed broad PL spectrum of PLG can be explained by (b) assuming, that the size of the clusters is distributed around an average value of approximately 1 nm as determined in Raman experiments (e.g. indicated as the diameter of the circular area). Due to the small cluster size quantum confinement might occur which in consequence would lead to a band gap opening of $\Delta E \approx v_f h / 2d \approx 2 \text{ eV} \cdot \text{nm} / d$. v_f is here the Fermi velocity of the electrons and d is the diameter of the "box" (see text for details). Assuming further that the distribution of cluster size is a Gaussian distribution centered at 1.08 nm and a FWHM=0.35 nm this would translate to the PL energy distribution in (c), which nearly resembles the measured PL spectrum of PLG. The average cluster size $L_a=1.08 \text{ nm}$ corresponds to a bandgap of 1.85 eV, equal to the center energy of the maximum of the observed PL. For such a scenario, the observed broad PL spectrum would be due to heterogeneous broadening, in the sense of a superposition of a multitude of narrow PL emission bands (here: indicated as narrow Lorentzian emission bands) centered at size-controlled emission energies.

a cluster, with the length d the boundary condition would lead to a quantization of the allowed k vectors according to $k=n \cdot \pi/d$. In consequence, quantum confinement would result in a bandgap opening on the order of $\Delta E \approx v_f h / 2d \approx 2 \text{ eV} \cdot \text{nm}/d$. Using this simple particle-in-the box model for reproducing the PL center emission wavelength of the PLG at approximately 1.85 eV, one needs to assume that the average diameter of the clusters is about $\sim 1.08 \text{ nm}$ (indicated as the red dotted circle in Fig. 8.5). This value is also close to the average cluster diameter of $L_a=1 \text{ nm}$ determined in the Raman experiments. Accordingly, the broad width (FWHM) of the PL band of the PLG might be explained. Quantum confinement relates a distribution of different sized sp^2 clusters (Fig. 8.5 (b), for instance assuming here a Gaussian distribution centered at $\approx 1.1 \text{ nm}$ and a FWHM of $\approx 0.35 \text{ nm}$, to the broad energy spectrum in Fig. 8.5 (c) (black curve).

For the scenario discussed here, the origin of the large width of the PL band of 0.5 eV would be the result of heterogeneous broadening, where the PL band is just the superposition of a multitude of overlapping bands with narrow linewidth centered at different size-controlled (i.e. quantum confined) energies. This is indicated by the narrow Lorentzian PL bands in (Fig. 8.5 (c)). In this case, the optical properties of the PLG would resemble those of π -conjugated polymer films, where a distribution of conjugation lengths translates into a heterogeneously broadened density of states [340]. For such conjugated films spectral diffusion due to energy migration is reported, a process where fast energy transport occurs to sites across the film which exhibit lower site energies. Possible transport mechanisms might be Förster energy transfer between suitable fluorophores or thermal activated hopping of the excited state and radiative recombination at such low energy sites. In both cases PL would preferentially be observed from lower energy states. Depending on the time scale of this process, this can be followed by ultrafast time-resolved spectroscopy or by measuring the spectral dependence of the PL decays of such films with e.g. TCSPC. Energy migration would lead to a faster decay for emission of the blue part of the PL spectrum while at the same time the transients of the red part of the spectrum should exhibit an delayed rise of the signal with a time constant on the order of the blue decay.

To test this hypothesis, spectrally dependent PL transients across the broad PL band of PLG for four narrow emission windows centered at 646 ± 10 , 690 ± 10 , 834 ± 7 and $880 \pm 20 \text{ nm}$ were acquired. In order to prevent effects on the PL transients caused by photo degradation of the PLG, the transients were acquired at different closely neighbored spots on the flake. The excitation wavelength was 530 nm and low excitation powers of $\sim 10 \mu\text{W}$ were used. As can be observed in Fig. 8.6 (a), there is no direct correlation between emission wavelength and decay dynamics. All four transients can be well fitted by a three exponential function with similar decay times and amplitudes. The small variations in the transients are most likely due to inhomogeneities across the flake as similar site dependent differences in the shape of the transients were observed before. The results so far indicate that there is no energy migration to states with lower site energies.

Alternatively, for a heterogenous ensemble of emitters one would expect that at room temperature, laser excitation in the red flank of the broad PL would lead to selective

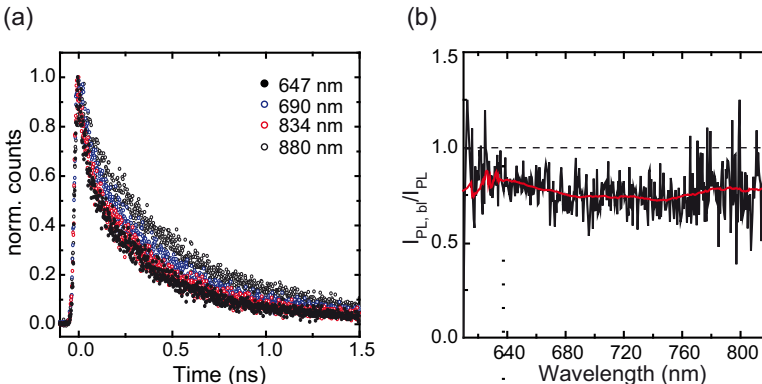


Fig. 8.6. (a) Wavelength dependent PL decay in PLG. The transient were recorded using low power pulsed excitation at 530 nm and detecting the PL emission at four different wavelength as designated in the figure. No obvious correlation between emission wavelength and decay times is observed. This indicates that spectral diffusion due to energy migration, as would be expected for a heterogeneously broadened system, is absent. (b) Plot of the PL intensity ratio $I_{PL,bleached}/I_{PL}$. I_{PL} and $I_{PL,bleached}$ are the PL intensities before and after irradiation with high power laser pulses at 647 nm, respectively. After bleaching the PL intensity decreases spectrally uniform without showing signatures of spectral holes.

excitation of a subset of quantum confined states. Then, spectral hole burning in the sense of the selective photobleaching of a particular subset of homogeneously broadened lines should be possible. This bleaching could be a photochemical modification or even a complete removal of the absorbing subset. As a result a spectral hole, a dip in the broad PL band, should occur. Fig. 8.6 (b) plots the ratio of PL intensities measured before (I_{PL}) and after ($I_{PL,bleached}$). For PL bleaching high power ($>600 \mu\text{W}$) pulsed laser light at 647 nm was used and for subsequent PL excitation at 530 nm and low power levels ($\approx 10 \mu\text{W}$). No spectral hole is generated in the observable spectral range, as it would be expected for a heterogeneous ensemble of narrow bandwidth emitters. Instead, only an irreversible and uniform reduction of PL intensity occurs. For other bleaching energies in the red spectral range (760, 800 nm), the same uniform decrease is observed, while in the blue (473, 514 nm) the PL slightly shifts to shorter wavelength (compare Fig. 8.1 c).

Thus, it is found that the observed large spectral width of 0.5 eV reflects mainly homogeneous broadening of a single emissive species which is distributed uniform across the PLG sheet. This is also supported by the absence of spectral diffusion in the time-resolved data, which is expected for heterogeneous films. If the PL would indeed result from quantum confined states as suggested e.g. in ref. [333] as the origin of the PL in graphene oxide, size-related heterogeneous broadening would need to be far smaller, probably below 0.1 eV. This in turn would require a very narrow size distribution with a FWHM of about 0.08 nm, instead of the 0.35 nm which was used to explain the broad width of the PL emission band. Since oxidation

is expected to occur at different lattice sites and configurations, such high degree of ordering seems unreasonable. Moreover, while for increasing oxidation times a successive shift of the average cluster size to smaller sizes and in consequence a continuous blue-shift of the PL energy would be expected, the spectral characteristics of the PL emission remains nearly constant for all plasma treatment times.

Thus, although the identification of L_a as the quantum confinement length of massless electrons would be tempting, the spectroscopic data so far does not support this model. More likely, the observed PL originates from CO-related localized electronic states at the oxidation sites.

8.7. Conclusion

The optical properties of oxygen plasma treated graphene have been characterized with different optical spectroscopy methods. It was shown that spatially uniform PL can be induced in single-layer graphene by selective plasma oxidation. The PL of this novel material is characterized by a single broad emission band extending from the blue visible to the NIR spectral region. The PL decay exhibits a complex dynamics indicating the heterogenous composition of the material. Raman and elastic white light scattering spectroscopy revealed severe structural and/or changes in the chemical composition following the oxygen plasma treatment. The analysis of the evolution of the Raman I_D/I_G -ratio with plasma exposure time indicated the formation of nanometer sized sp^2 islands across the flakes whose diameter gradually decrease down to 1 nm for the longest treatment time. However, PL from quantum confined states as it is also discussed as origin for the PL in graphene oxide [333–335] can be excluded based on the results of a spectrally resolved decay time analysis and spectral hole burning experiments. This is further supported by the persistence of the spectral position of the PL band for increasing plasma etching time, whereas in the case of quantum confinement a blue-shift of the main PL band as consequence of a decreasing cluster size would be expected. Thereby, it is proposed that the origin of the PL is due to emission from localized CO-related electronic states at oxidation sites. Remarkably, bi- and multilayer flakes remain non-luminescent, while their elastic scattering spectra indicate the formation of sandwich-like structures comprised of both etched and unetched layers. The optical measurements presented in this study represent only the first step in the characterization of this material. Of further interest is also how the electric conductivity of the PLG flakes has changed with respect to pristine graphene. The perspective to prepare thin luminescent and highly conductive films by a combination of lithography and oxygen plasma treatment is certainly motivating to perform additional conductivity measurements on the PLG.

Part V.

Summary

9. Summary

The optical and electronic properties of single-walled carbon nanotubes (SWCNTs) have been studied intensely within the last few years. Time resolved photoluminescence (PL) studies on the single nanotube level are still rare but promise new insights about the intrinsic and extrinsic factors governing the excited state dynamics of SWCNTs. In the course of this work the optical properties of SWCNTs and of a luminescent graphene derivative were investigated by confocal microscopy and spectroscopy techniques.

The excited state dynamics of semiconducting SWCNTs are dominated by efficient nonradiative relaxation processes which in turn result in low PL quantum yields and fast decay times on the picosecond timescale. In the **first part** (chapters 4–6) of this work time correlated single photon counting (TCSPC) measurements combined with PL spectroscopy were employed to identify nonradiative decay channels and to evaluate their contribution to the whole PL process. The PL decay times of individual SWCNTs deposited on glass cover slides were found to be in the low picosecond regime with tube-to-tube variations between 1–40 ps. Based on a correlation between PL linewidth and PL decay times, PL quenching and excited state dephasing facilitated by defect related localized phonon modes were identified as nonradiative decay channels. Thereby, the origin of the observed PL decay distributions can be attributed to varying defect densities of different SWCNTs. The nanotube ends represent an intrinsic defect present in any carbon nanotube. In the currently accepted picture of PL quenching of highly mobile excitons at the nanotube ends, a length dependence of the PL decay times is expected. PL decay time measurements on length sorted samples with average lengths between 200–600 nm support this picture by revealing that SWCNT samples with a large average length exhibit longer average PL decay times. Only small differences in the average PL decay times (<3 ps) were found, which allowed for the conclusion that for the present sample material PL quenching at the nanotube ends is not the dominant nonradiative decay channel. The observation of varying PL decay times differing by up to 30 % along the length of individual SWCNTs further stress the relevance of the local environment and defects for the excited state dynamics. This study presented the first time-resolved PL measurements of individual SWCNTs at room-temperature, where it was possible to collect a statistically relevant number of PL decay times for different chiralities. The findings obtained here complement the recent single nanotube low-temperature study in ref. [223] and strengthen the proposed picture of defect related nonradiative decay mechanisms. The second finding of this part was, that synthesis-dependent differences in the defect densities and varying environmental conditions lead to different excited state dynamics in SWCNTs. This was studied for two of the most widespread commercially available SWCNT materials, synthesized either by a chemical vapor deposition process using cobalt

molybdenum catalyst particles (CoMoCAT) or by the high pressure decomposition of carbon monoxide process (HiPco). Both materials were either embedded in an aqueous gel or deposited on a glass substrate. It could be shown, that the PL decay dynamics of CoMoCAT SWCNTs is strictly monoexponential irrespective of the respective environment. The radiative decay of HiPco SWCNTs on the other hand follows a biexponential decay law, whereby the fraction of biexponential decays in gel is considerably larger. The origin of the transition from biexponential to a monoexponential decay behavior for the different materials can be explained by different synthesis-dependent defect densities which facilitate fast nonradiative relaxation of the excited state. By extending a kinetic three-level model, which was previously introduced to describe the biexponential decays in SWCNTs, by the additional defect related nonradiative rates, the experimental observation could be well reproduced. This work emphasized the importance of SWCNTs processing and observation conditions for obtaining high quality luminescent nanotubes and provided new insights into the excited states processes which lead to the controversial reports of the PL decay dynamics reported for single nanotube experiments.

Defects and disorder do not only affect the PL decay dynamics and lead to fast excited state recombination, but they can alter the PL properties of a single SWCNT completely. It could be shown for the first time that intrinsic dark excitonic states are "brightened" by intentionally introducing defects. Two different "brightening" methods were presented, irradiation with high power laser pulses and the adsorption of gold atoms to the SWCNT sidewalls, which in both cases resulted in the emergence of different groups of low energy satellite PL bands separated by 30–190 meV from the main band. Upon "brightening" of the dark state the PL decay times of the main emission is considerably reduced. Within the context of the previous findings, this can be attributed to the creation of structural defects, which is further confirmed by an increase of the defect induced Raman D-band observed in accompanying Raman experiments. Thereby, the "brightening" process can be interpreted as the defect induced symmetry breaking of the exciton wavefunctions which facilitates the mixing of excitonic states with different parity and spin [94, 106]. Moreover, for the defect related states high spin densities are expected which promote inter-system crossing. Based on the large energy splitting and the nature of the brightening processes the energy lowest satellite band is attributed to the radiative recombination of a triplet state. The assignment is further confirmed by PL decay time measurements of this band which yield lifetimes up to two orders of magnitude larger than the decay of the main PL band. The results of this work showed promising new ways to modify the PL properties of SWCNTs.

The **second part** (chapter 7) presented preliminary results of elastic white light scattering experiments of individual SWCNTs deposited on glass substrates. Here a common-path interference scattering (iSCAT) approach was employed [158, 168], where the detected signal originates from the superposition of the scattered light field and the reflected light field off the substrate surface. Experimentally, this scattering concept was realized in a simple manner by utilizing an standard inverted confocal microscope in combination with a photonic

crystal fibre as a supercontinuum white light source. It was successfully demonstrated that elastic scattering imaging and spectroscopy of single SWCNTs is possible. The iSCAT signal originates from the extinction (absorption) of the SWCNTs giving rise to an image contrast of 4–8%. Due to the limited detection sensitivity of the silicon based detector in the NIR spectral region the full potential of the white-light scattering spectroscopy could not be exploited. Only the second excitonic transition (E_{22}) of small diameter semiconducting SWCNT could be probed. Based on the characteristic E_{22} energies a chirality assignment was possible, which was further supported by complementary PL spectroscopy. Due to the interferometric nature of the signal and the general scattering geometry the magnitude and shape of the iSCAT signal depends critically on a multitude of different parameters, such as the reflectivity of the substrate interface and the mode overlap between the scattered and reflected light which prevents direct quantification of an extinction cross section. By comparing the iSCAT signals of the SWCNTs with the signal of gold nanoparticles with known optical properties, a resonant extinction cross section per unit length of $\sigma_{ext}(E_{22}) \approx 310 \text{ nm}^2/\mu\text{m}$ for (6,5) SWCNTs could be estimated, which is in general agreement with the values determined by photothermal absorption measurements [124]. Furthermore, a prospect for future experiments combining elastic white light scattering and PL experiments was given.

In the **third part** (chapter 8) of this thesis it was shown for the first time that single layer graphene becomes luminescent ("luminescent graphene") upon a mild oxygen plasma treatment. Strong and spatially uniform PL is observed which is characterized by a single broad band centered at 700 nm and extending from the blue visible to the NIR spectral region. Importantly, with relevance for possible future applications, PL is only observed for single layer graphene, while PL of multi layer graphene is suppressed by subjacent layers. The elastic white light scattering contrast of the PLG is distinctly different to the one of graphene. Complementary modeling of the scattering contrast allowed to deduce optical constants which are similar to the ones of graphene oxide. The rise of the defect related D- and D' Raman bands indicated that even for the smallest plasma exposure time of one second, nanocrystalline islands for which the sp^2 conjugation of the graphene lattice is still preserved are formed. Based on the analysis of the Raman I_D/I_G intensity ratio it was possible to assess the average size of these islands to $L_a \sim 1 \text{ nm}$ for longest plasma treatment times. While the formation of nanometer sized sp^2 clusters suggests that the observed broad PL spectra originate from the superposition of a multitude of narrow linewidth emission bands centered at different size controlled (quantum confined) energies, this picture is not supported by the results of complementary spectral hole burning experiments and wavelength resolved PL decay time measurements. Tentatively the PL is assigned to emission from carbon-oxygen related localized electronic states at oxidation sites.

Part VI.

Appendix

A. Scattered Field of a Carbon Nanotube

The detected signal in the iSCAT method depends critically on the relative phase difference between the reference field and the scattered field. Some of the contributions to these phases were introduced in Sec. 2.2. However, for this treatment it was assumed that the scatterer is small compared to the wavelength, so that its scattered fields can be approximated within the Rayleigh scattering theory as dipole fields. For the case of a long SWCNT significantly larger than the diameter of the excitation focus this approximation does not hold anymore. The exact solutions for such a scattering problem can be derived analytically in terms of the Mie scattering theory. In this case, the SWCNT is treated as an infinite right circular cylinder [182]. Importantly, with consequences for the iSCAT scattering method, the solutions for the scattered fields are no plane waves anymore but cylinder waves, whose propagation factor exhibit a different phase relation compared to the plane wave case. The different mode overlap between the reference field and scattered field compared to the dipole case would lead to different iSCAT signal amplitudes. The solutions of the scattering problem are sketched in the following and an expression for the scattering cross section of extended SWCNTs is derived.

The general scattering geometry of an obliquely illuminated cylinder is depicted in Fig. A.1. For modeling of the scattering contrast in Chap. 7, it is assumed that the SWCNT is illuminated normal ($\zeta=90^\circ$) to its axis (z-axis), and that the incident field is polarized parallel to the tube axis. Accordingly, only light which is scattered under the angles $\zeta=90^\circ$ and $\varphi=0^\circ$ back into the direction of incidence is detected.

For this special scattering conditions it can be shown that the relation between the scattered and incident field is given by [182]:

$$\begin{bmatrix} E_s^{\parallel} \\ E_s^{\perp} \end{bmatrix} = e^{i3\pi/4} \sqrt{\frac{2}{\pi kr}} e^{ikr} \begin{bmatrix} T_1 & 0 \\ 0 & T_2 \end{bmatrix} \begin{bmatrix} E_i^{\parallel} \\ E_i^{\perp} \end{bmatrix}. \quad (\text{A.1})$$

The components of the scattered field perpendicular and parallel to the plane of incidence are E_s^{\parallel} and E_s^{\perp} , respectively. These are related to their corresponding incident electrical field components by an amplitude scattering matrix. The solutions of the scattered fields of a cylinder are cylindrical waves, whose propagation is described by the term in front of the amplitude matrix. The propagation factor differs by an additional factor of $\exp i3\pi/4$ from the one a spherical or plane wave. In the small particle limit, which is justified if the size factor $x=k \cdot r_{cyl} \ll 1$, where k is the wave vector of light and r_{cyl} is the radius of the cylinder, simple approximations for the scattering amplitude factors T_1 and T_2 can be obtained. For the SWCNTs in the studies, the r_{cyl} is < 0.5 nm and the small particle approximation is valid for visible

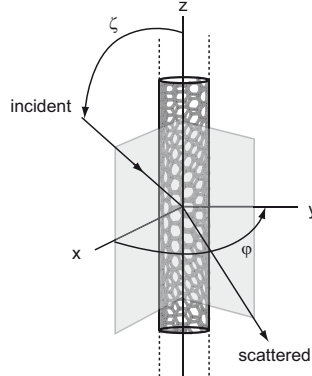


Fig. A.1. Scattering geometry for an infinite circular cylinder (SWCNT). The cylinder is obliquely illuminated by a plane wave. The plane of incidence and the scattering plane (grey) are indicated. φ is defined as the angle between the plane of incidence and the plane of scattering. ζ is the angle between the direction of incidence of the excitation light and the nanotube axis.

light.

For the special case here, where the scattering direction is identical to the direction of the normal incident light ($\varphi = 0^\circ$, $\zeta = 90^\circ$), the expressions T_1 and T_2 become: $T_1 = b_0$ and $T_2 = 0$, where b_0 is the scattering amplitude coefficient. The general expression for these coefficients are the solutions of the Mie scattering problem and for the special case has the form:

$$b_{nI}(\zeta = 90^\circ) = b_n = \frac{J_n(mx)J_n(x) - mJ'_n(mx)J_n(x)}{J'_n(mx)H_n^{(1)}(x) - mJ_n(mx)H_n^{(1)}(x)}. \quad (\text{A.2})$$

J_n are first kind Bessel functions of order n and $H^{(1)}$ are so called Hankel functions of the first kind, which are a sum of a first kind Bessel function J_n and second kind Bessel function Y_n : $H^{(1)} = J_n + iY_n$. m is here the relative refractive index of the cylinder compared to its embedding medium: $m = n_{cyl}/n_{med}$ and $x = k r_{cyl}$ is the size factor. The Bessel functions and their derivatives can be approximated by the first terms of their series expansions:

$$\begin{aligned} J_0(x) &\approx 1 - \frac{x^2}{4}, & J'_0(x) &\approx -\frac{x}{2} + \frac{x^3}{16}, \\ H_0(x) &\approx \frac{2}{\pi} \log\left(\frac{x}{2}\right), & H'_0(x) &\approx \left(\frac{2}{\pi x}\right). \end{aligned} \quad (\text{A.3})$$

Substituting these expressions for the Bessel functions in Eqn. A.2 and retaining only the terms with smallest orders in x , the scattering amplitude factor b_0 is approximately:

$$b_0 \approx -i \cdot \pi \cdot k_m^2 \cdot r_t^2 (m^2 - 1) . \quad (\text{A.4})$$

Finally, by substituting the expression for b_0 into Eqn. A.1 one obtains for the scattered fields with polarizations perpendicular and parallel to the scattering plane:

$$E_s^{\parallel}(\varphi = 0^\circ) = E_s^{\perp}(\varphi = 0^\circ) = e^{i\pi/4} \sqrt{\frac{2}{\pi kr}} e^{ikr} (-\pi \cdot k_m^2 \cdot r_t^2 (m^2 - 1)) E_i^{\parallel} . \quad (\text{A.5})$$

For the special scattering conditions assumed here, a simple expression for the scattering cross section for cylinders can be derived, which is commonly found in literature to discuss the scattering properties of SWCNTs [57, 282, 283]. The scattering cross section per unit length is defined as the ratio of the rate at which energy W_s passes a concentric cylindrical surface A to the rate of incident irradiance I_s :

$$\sigma = \frac{W_s}{I_s} , \quad (\text{A.6})$$

where the rate of the scattered energy W_s is given as:

$$W_s = rL \int_0^{2\pi} (\mathbf{S}_s)_r d\phi . \quad (\text{A.7})$$

Here r and L are the radius and the length of the imaginary cylindrical surface A , while $(\mathbf{S}_s)_r = 1/2\text{Re}\{\mathbf{E}_s \times \mathbf{H}_s^*\}$ is the radial component of the scattering poynting vector. Performing the integration in Eqn. A.7 with the scattered field given in Eqn. A.5 and inserting the result in the general definition of the scattering cross section Eqn. A.6, the scattering cross section per unit length of a cylinder reads [57, 104]:

$$\sigma_s(\omega) = \frac{\pi^2}{4c^3} r^4 \omega^3 |\chi(\omega)|^2 = \frac{k^3 r^4}{4\pi} |\chi(\omega)|^2 , \quad (\text{A.8})$$

Here it was assumed that the embedding medium is air with $n_{med} = 1$ and correspondingly $m = n_{cyl}$ which allows to use the relation between the refractive index and the optical susceptibility: $\chi(\omega) = n_{cyl}(\omega)^2 - 1$.

B. Elastic White Light Scattering of Single and Multi-layer Graphene

In this section elastic white light scattering spectroscopy is applied to study single and multi-layer graphene deposited on a Si/SiO₂ substrate. It can be demonstrated that a single layer of atoms can be visualized based on its contrast in optical microscopy by exploiting the interferometric nature of the detected signal. The method provides a fast and precise way to identify single layer graphene and to determine the layer numbers in multi-layer graphene. It is found that the optical contrast scales linearly with the layer number up to a maximum number of ten. An analytical model based on the multiple reflections from multi-layered dielectric films is employed to reproduce the experimental elastic scattering contrast. The modeled data shows excellent agreement with the experimental results and suggests alternative substrate combinations for the elastic scattering measurements of graphene. The experimental results presented here were achieved in collaboration with Dr. C. Casiraghi (FU Berlin), while the model was introduced by Dr. E. Lidorikis (University of Ioannina, Greece). This chapter is based on the paper "Rayleigh Imaging of Graphene and Graphene Layers", which has been published in *Nano Lett.*, 7, 2711 (2007).

B.1. Introduction

Single layer graphene can be observed with standard microscopes based on its elastic white light scattering contrast when deposited on an oxidized silicon substrate with a well defined SiO₂ layer thickness of 100 or 300 nm [11]. Nowadays, elastic scattering microscopy and spectroscopy is established as a fast and non-destructive optical method for characterizing single layer and multi-layer graphene [311, 320, 321, 341] and ideally complements the information provided by Raman or AFM measurements. The multi-layered substrate is crucial for enhancing the magnitude of the scattering contrast. The additional optical path length provided by the spacer layer leads to an enhanced interferometric scattering contrast. This signal is sensitive to small changes in the optical constants of the material under study which can be exploited to determine the layer numbers of multi-layer graphene or to monitor changes in the dielectric constant of these materials as it has been demonstrated in Fig. 8.3.

In the following, an analytical model for the optical contrast of graphene for a multi-layer substrate based on the theory for multiple reflections within assemblies of thin films is presented. First, the basic concept for the formation of the interferometrical scattering

contrast of a single layer of graphene is described. Then an analytical model relying only on the optical material constants is presented in detail. The simple model yields quantitative results for the scattering contrast, which is demonstrated in the last part of this section, where experimental and modeled elastic white light scattering spectra are compared. Due to the excellent agreement between theoretical description and experiment, the same model was used for modeling the elastic scattering spectra of the oxygen plasma treated graphene in Chap. 8 and to determine its optical constants. The following presentation of the topic⁷ is based on the theory presented in refs. [311] and [68].

B.2. Model for the Scattering Contrast of Graphene

Starting with the general sample geometry and illumination scheme, an illustration of the multi-layer system graphene/SiO₂/Si is depicted in Fig. B.1(a).

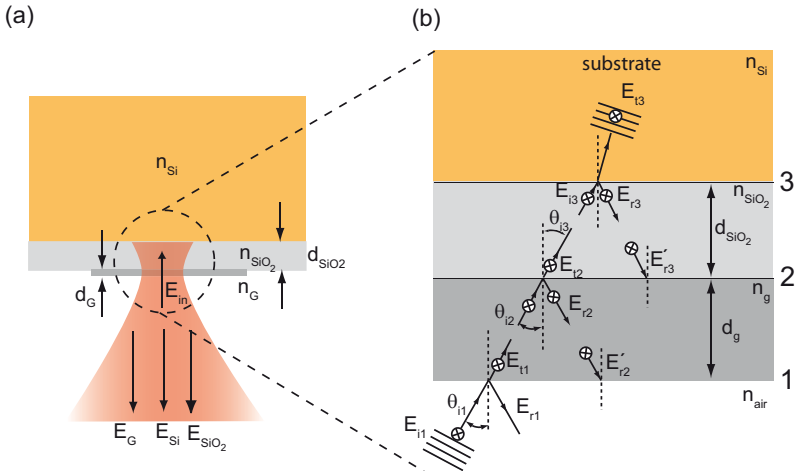


Fig. B.1. (a) Cross-sectional view of the multi-layer system graphene/SiO₂/Si. The incident light field is denoted as E_{in} . Reflections occur at each boundary between two materials giving rise to the fields: E_G , E_{Si} and E_{SiO_2} . The detected signal in back-scattering direction results from the superposition of these fields. (b) Detailed view of the multiple reflections occurring at the different optical boundaries (1-3) of the multi-layer system.

The sample is irradiated by the incident laser light field (E_{in}) with the graphene layer facing the direction of the incident beam. The incident light is transmitted and reflected at each boundary occurring between materials with different optical properties. For the present sample configuration, three boundaries need to be considered: An (1) air-graphene (E_G), a (2)

⁷Equivalent model descriptions and experimental results may be found also in refs. [320, 321, 341, 342].

graphene-SiO₂ (\mathbf{E}_{SiO_2}) and a (3) SiO₂-Si interface (\mathbf{E}_{Si}). The notation of the reflected fields at each boundary \mathbf{E}_i is given in parentheses. The reflected fields \mathbf{E}_i are related to the incident light field \mathbf{E}_{in} by a complex (amplitude) reflection coefficient r_i which considers the multiple reflection at each boundary and propagation through layers with different optical path length: $\mathbf{E}_i = r_i \mathbf{E}_{in}$. The aim of the following paragraphs is to derive a model description for the reflection coefficient r for the whole multi-layer sample configuration and in the end to calculate the optical contrast. Before addressing this, a more general view on the contrast formation process is presented, which elucidates the interferometric nature of the detected signal and the different contributions of the various reflected fields to the signal.

The detected signal I_{det} results from the superposition of all three reflected fields at each boundary, \mathbf{E}_G , \mathbf{E}_{SiO_2} and \mathbf{E}_{Si} . Based on the high reflectance expected for the air-graphene and especially the SiO₂-Si interface, the dominant contributions to the signal are \mathbf{E}_G and \mathbf{E}_{Si} and the detected signal I_{det} writes:

$$I_{det} \approx |E_G + E_{Si}|^2 = |E_G|^2 + |E_{Si}|^2 + 2|E_G||E_{Si}|\cos\phi. \quad (\text{B.1})$$

While the first and second terms correspond to the intensities of the light reflected from the respective interfaces, the cosine expression is the interference term, whose magnitude depends on the relative phase difference ϕ between the two reflected fields E_G and E_{Si} :

$$\phi = \vartheta_G - (\vartheta_{Si} + 2\pi n_{SiO_2} 2d_{SiO_2}/\lambda_0) \quad (\text{B.2})$$

The reflection at each boundary leads to a phase change of ϑ_G and ϑ_{Si} compared to the phase of the incident field. An additional phase shift corresponding to an increased optical path length arises for the E_{Si} field as the SiO₂ layer is passed twice, first by the light incident on the Si substrate and a second time by the reflected light. The additional optical path length is defined in terms of the SiO₂ layer thickness d_{SiO_2} , its refractive index n_{SiO_2} and by the wavelength of the incident light λ_0 (the dependence on the angle of incidence is omitted for this simplified treatment).

Analogous to Eqn. B.1 an expression for the reflected signal from a background position I_{back} can be defined, which results here from the superposition of the fields reflected from the air-SiO₂ interface and of the SiO₂-Si interface:

$$I_{back} \approx |E_{Si} + E_{SiO_2}|^2 = |E_{Si}|^2 + |E_{SiO_2}|^2 + 2|E_{Si}||E_{SiO_2}|\cos\phi. \quad (\text{B.3})$$

As mentioned before, the reflection coefficient r of the Si-SiO₂ interface is considerably larger than the one of the air-SiO₂ interface and in consequence $|E_{Si}|^2 > |E_{SiO_2}|^2$. Moreover, compared to $|E_{Si}|^2$ the interference term in Eqn. B.3 represents only a small correction to the detected signal, so that I_{back} is mainly governed by the reflection from the silicon:

$$I_{back} \approx |E_{Si}|^2 . \quad (\text{B.4})$$

The optical contrast (visibility) δ of graphene is defined as the normalized difference of the intensities I_{det} and I_{back} :

$$\delta = \frac{I_{det} - I_{back}}{I_{back}} \simeq \frac{|E_G|^2}{|E_{Si}|^2} + 2 \frac{|E_G|}{|E_{Si}|} \cos \phi . \quad (\text{B.5})$$

Assuming further that the field reflected from graphene is negligible small compared to the one of silicon, corresponding to $|E_G|^2/|E_{Si}|^2 \ll 1$, the optical contrast δ results mainly from interference with the strong field reflected by the silicon.

$$\delta \simeq 2 \frac{r_g}{r_{Si}} \cos \phi . \quad (\text{B.6})$$

The sign of the contrast depends on the cosine term in Eqn. B.6. The reflectance R is the ratio between the reflected power and the incident power and is related to the Fresnel reflection coefficient by $R = r \cdot r^*$. Assuming that the reflection coefficient r_{Si} is nearly one, Eqn. B.6 reduces to:

$$\delta = 2\sqrt{R_g} \cos \phi . \quad (\text{B.7})$$

From Eqn. B.7 it becomes obvious that the optical contrast is determined (1) by the reflectance R_g of graphene, which is further modulated by (2) the phase variations caused by the reflection from the SiO_2 -Si interface. Experimentally, the phase can be controlled by varying the SiO_2 layer thickness, which can be exploited to maximize the optical contrast.

At this point a more precise model, which considers the multiple reflections and interference of fields of all three boundaries is presented. The general approach is based on the idea that the whole sample arrangement can be regarded as a set of stacking thin films, similar to the dielectric multi-layer films which are used as antireflection coatings. The reflectance and transmittance of such systems can be calculated based on a recurrent matrix method [68,343], where the electric and magnetic fields at each side of an interface are related by an characteristic matrix.

A schematic cross section of the multi-layer system along with the notation for the different parameters is depicted in Fig. B.1(b). The sample arrangement can be regarded as two thin films deposited on a substrate, which gives rise to three optical boundaries, denoted as 1-3: The (1) air-graphene, (2) the graphene- SiO_2 and (3) the SiO_2 -Si boundary. The total electric and magnetic fields at each boundary are calculated for the various layers by applying the

boundary conditions of electromagnetic waves. These demand that the tangential electric and magnetic field components must be continuous across the boundaries. For boundary (1) and (2) these conditions are fulfilled for:

$$\begin{aligned} E_1 &= E_{i1} + E_{r1} = E_{t1} + E'_{r2}, & H_1 &= \sqrt{\frac{\epsilon_0}{\mu_0}}(E_{i1} - E_{r1})n_g \cos \theta_{i1}, \\ E_2 &= E_{i2} + E_{r2} = E_{t2}, & H_2 &= \sqrt{\frac{\epsilon_0}{\mu_0}}(E_{i2} - E_{r2})n_{SiO_2} \cos \theta_{i2}. \end{aligned} \quad (\text{B.8})$$

Here n_g and n_{SiO_2} are the refractive indices of graphene and SiO₂, respectively. Further, the electric and magnetic fields across the first (1) and the second boundary (2) are related via:

$$\begin{aligned} E_2 &= E_{t1} e^{-\phi_g} + E'_{r2} e^{+\phi_g}, \\ H_2 &= (E_{t1} e^{-\phi_g} - E'_{r2} e^{+\phi_g}) \sqrt{\frac{\epsilon_0}{\mu_0}} n_{SiO_2} \cos \theta_{i2}. \end{aligned} \quad (\text{B.9})$$

By propagating through graphene a wave accumulates a phase shift of $\phi_g = k_0 h_g$. Here k_0 is the vacuum wavevector and $h_g = n_g 2 d_g \cos \theta_{i2}$ is the additional optical path length due to propagation through the graphene layer. Further, n_g is the complex refractive index of graphene and d_g the graphene layer thickness.

Solving the equations in Eqn. B.9 for E_{t1} and E'_{r2} and plugging the resulting equations into Eqn. B.8 one obtains:

$$\begin{aligned} E_1 &= E_2 \cos \phi_g + H_2 (i \sin \phi_g) / Y_1, \\ H_1 &= E_2 Y_1 i \sin \phi_g + H_2 \cos \phi_g, \end{aligned} \quad (\text{B.10})$$

with $Y_1 = \sqrt{\frac{\epsilon_0}{\mu_0}} n_g \cos \theta_{i2}$.

In matrix notation Eqn. B.10 reads:

$$\begin{bmatrix} E_1 \\ H_1 \end{bmatrix} = \begin{bmatrix} \cos \phi_g & (i \sin \phi_g) / Y_1 \\ Y_1 i \sin \phi_g & \cos \phi_g \end{bmatrix} \begin{bmatrix} E_2 \\ H_2 \end{bmatrix}. \quad (\text{B.11})$$

Repeating the derivation for the fields E_2 and E_3 at the graphene/SiO₂ boundary (3), one obtains an analogous matrix equation:

$$\begin{bmatrix} E_2 \\ H_2 \end{bmatrix} = \begin{bmatrix} \cos \phi_{SiO_2} & (i \sin \phi_{SiO_2}) / Y_2 \\ Y_2 i \sin \phi_{SiO_2} & \cos \phi_{SiO_2} \end{bmatrix} \begin{bmatrix} E_3 \\ H_3 \end{bmatrix}, \quad (\text{B.12})$$

with $Y_2 = \sqrt{\frac{\epsilon_0}{\mu_0}} n_{SiO_2} \cos \theta_{i3}$. Here ϕ_{SiO_2} is the phase shift due to propagating through the SiO₂ layer and is defined as: $k_0 h_{SiO_2}$ with $h_{SiO_2} = n_{SiO_2} 2 d_{SiO_2} \cos \theta_{i3}$.

An expression which relates the fields E_1 and E_3 can be obtained by substituting E_2 in Eqn. B.12 by the corresponding expression of Eqn. B.11:

$$\begin{bmatrix} E_1 \\ H_1 \end{bmatrix} = \mathbf{M}_1 \mathbf{M}_2 \begin{bmatrix} E_3 \\ H_3 \end{bmatrix}. \quad (\text{B.13})$$

Here \mathbf{M}_1 and \mathbf{M}_2 are the characteristic matrices for each boundary. The characteristic matrix of the whole system is then just: $\mathbf{M} = \mathbf{M}_1 \cdot \mathbf{M}_2$, which is a 2×2 matrix:

$$\mathbf{M} = \begin{bmatrix} m_{11} & m_{12} \\ m_{21} & m_{22} \end{bmatrix}. \quad (\text{B.14})$$

Substituting now E_1 and H_1 in Eqn. B.13 by their corresponding expressions given in Eqn. B.8, one obtains:

$$\begin{bmatrix} (E_{i1} + E_{r1}) \\ (E_{i1} - E_{r1}) Y_0 \end{bmatrix} = \mathbf{M} \begin{bmatrix} E_{t3} \\ E_{t3} Y_3 \end{bmatrix}. \quad (\text{B.15})$$

The reflection and transmission coefficients of the whole multi-layer system are defined as: $r = E_{r1}/E_{i1}$ and $t = E_{t3}/E_{i1}$, respectively. Factoring out E_{i1} and using the expressions for the definitions for r and t , Eqn. B.15 becomes:

$$\begin{aligned} 1 + r &= m_{11}t + m_{12}Y_3t, \\ (1 - r)Y_0 &= m_{21}t + m_{22}Y_3t, \end{aligned} \quad (\text{B.16})$$

with:

$$Y_0 = \sqrt{\frac{\epsilon_0}{\mu_0}} n_{air} \cos \theta_{i1}, \quad (\text{B.17})$$

$$Y_3 = \sqrt{\frac{\epsilon_0}{\mu_0}} n_{Si} \cos \theta_{t3}. \quad (\text{B.18})$$

Solving Eqn. B.18 for the reflection coefficient r , one obtains the general expression:

$$r = \frac{Y_0 m_{11} + Y_0 Y_3 m_{12} - m_{21} - Y_3 m_{22}}{Y_0 m_{11} + Y_0 Y_3 m_{12} + m_{21} + Y_3 m_{22}}. \quad (\text{B.19})$$

Replacing the matrix elements m_{ii} by their corresponding expressions and choosing the simplest case of normal incidence light, where the angles of incidence and refraction, θ_{i1} , θ_{2i} and θ_{3t} , are all zero, the numerator and denominator of r read:

$$r_{num} = \left[\cos \phi_g^0 \cos \phi_{SiO_2}^0 \left(\frac{n_{air}}{n_{Si}} - 1 \right) + \sin \phi_g^0 \sin \phi_{SiO_2}^0 \left(\frac{n_g}{n_{SiO_2}} - \frac{n_{SiO_2} n_{air}}{n_g n_{Si}} \right) \right] \\ + i \left[\cos \phi_g^0 \sin \phi_{SiO_2}^0 \left(\frac{n_{air}}{n_{SiO_2}} - \frac{n_{SiO_2}}{n_{Si}} \right) + \sin \phi_g^0 \cos \phi_{SiO_2}^0 \left(\frac{n_{air}}{n_g} - \frac{n_g}{n_{Si}} \right) \right], \quad (B.20)$$

$$r_{denom} = \left[\cos \phi_g^0 \cos \phi_{SiO_2}^0 \left(\frac{n_{air}}{n_{Si}} + 1 \right) - \sin \phi_g^0 \sin \phi_{SiO_2}^0 \left(\frac{n_g}{n_{SiO_2}} + \frac{n_{SiO_2} n_{air}}{n_g n_{Si}} \right) \right] \\ + i \left[\cos \phi_g^0 \sin \phi_{SiO_2}^0 \left(\frac{n_{air}}{n_{SiO_2}} + \frac{n_{SiO_2}}{n_{Si}} \right) + \sin \phi_g^0 \cos \phi_{SiO_2}^0 \left(\frac{n_{air}}{n_g} + \frac{n_g}{n_{Si}} \right) \right]. \quad (B.21)$$

With the reflection coefficients known for the multi-layer system the reflectance R_G can be calculated. The reflectance for the background configuration R_{back} can be calculated accordingly, however in this case, only reflections at the air-SiO₂ and SiO₂-Si need to be considered. Finally, the contrast δ can be expressed in terms of the reflectances, R_G and R_{back} , of the two layered systems:

$$\delta = \frac{R_G - R_{back}}{R_{back}}. \quad (B.22)$$

For the modeling it is further to note that for normal incident light $\theta_{1i} = 0^\circ$, the phase terms ϕ_g for the different layers ($i=\text{air}\dots\text{silicon}$) are given as: $\phi_i^0 = k_0 n_i d_i$. For all other angles of incidence θ_{1i} , with s-polarization of the incident field (transverse electric field), the same formula applies, however with the substitution $n_i \rightarrow \cos \theta_i$. For p-polarized incident light, every refractive index ratio changes according to: $n_i/n_j \rightarrow n_i \cos \theta_j/n_j \cos \theta_i$. The angles of incidence and refraction θ_i for each layer are calculated by Snell's law: $\theta_i = \arcsin(n_0/n_i \sin \theta_0)$. For absorbing layers, such as graphene and the silicon substrate an effective refractive index $n'_i = f(n_i, \theta_i)$ needs to be used, which is a function of the incident angle from vacuum [344]. The corresponding refractive angle from such an absorbing layer is then calculated according to $\theta_i = \arcsin[\sin \theta_0 / Re(n'_i)]$. Further, one needs to consider the anisotropic optical response of graphene for incident fields polarized either in s- or p-direction. In case of s-polarized light, corresponding to the orientation of the field vector parallel to the graphene sheet, the refractive index is simply $n_g = n_\perp$. For p-polarized light, both in-plane and out-of-plane field components exist, leading to an angle-dependent refractive index $n_p^{-2} = n_{G\perp}^{-2} \cos \theta_{1i}^{-2} + n_{G\parallel}^{-2} \sin \theta_{1i}^{-2}$. In the experiment a high NA air objective is used, which provides a large range of incident angles θ_{1i} between zero and a maximum angle defined as: $\theta_{1i,max} = \arcsin(NA/n_{air})$. Considering a gaussian beam profile for the incident focused laser light, the modeled response needs to be integrated with a weight distribution $f(\theta_{1i}) = e^{-2 \sin^2 \theta_{1i} / \sin^2 \theta_{max}} 2\pi \sin \theta_{1i}$ in order to account for the influence of all possible polar-

izations and incident angles. Thus, the general expression for calculating the reflectance of R_G or R_{back} is:

$$R(\theta_{il}) = \frac{1}{2} \sum_{a=s,p} \int_0^{\theta_{il,max}} r_a(\theta_{il}) r_a^*(\theta_{il}) f(\theta_{il}) d\theta_{il}, \quad (B.23)$$

where the summation indicates the averaging over s- and p-polarized incident light.

The model basically requires only the refractive indices of the different materials as input parameters and the layer thicknesses of graphene and SiO₂. The wavelength dependent refractive indices of Si and SiO₂ are well known and tabulated in literature [345], while the layer thicknesses can be determined with high precession with ellipsometry or e.g. AFM measurements in the case of graphene (0.6 nm [311]). The refractive index of graphene, however, is unknown and instead the refractive index of graphite is used, determined by electron energy loss experiments [322].

The modeling here also offers the possibility to determine the refractive index of the material deposited on the substrate within certain limits by fitting the measured contrast with the refractive index as free parameter. As a model function for the refractive index a Couchy formula: $n^2 = A_n + B_n/\lambda^2 + i(A_k + B_k/\lambda^2)$ can be used. Based on this approach, the range of values for the refractive index of the oxygen plasma treated graphene in Sec. 8.5 was evaluated.

B.3. Elastic White Light Scattering Measurements of Graphene

A detailed description of the microscope setup, which was used for the white light scattering experiments of graphene is presented in Sec. 3.5. Briefly, the sample (see also Fig. B.1) was mounted up-side down on the sample holder of an inverted confocal microscope. Pulsed supercontinuum white light is provided by a photonic crystal fibre. An air objective (Nikon CFI Plan Fluor 100x NA=0.9) was used for focusing the collimated white light on the sample. The back aperture of the objective was not filled completely by the laser beam, resulting in an effective NA of 0.7. The sample was raster scanned through the focus and the scattered intensity was detected either by an APD or alternatively by spectroscopic imaging utilizing a combination of a spectrograph (grating: 150 l/mm; Blaze: 800 nm) and CCD camera. For the latter imaging technique, a spectrum is acquired at each image pixel, which allows to generate in a postprocessing-step scattering intensity maps of the sample for certain well defined spectral windows.

The graphene sample was prepared by micromechanical exfoliation of bulk graphite and was then transferred to a silicon substrate covered with a 300 nm SiO₂ layer (IDB Technologies Ltd, UK). Prior to the white light scattering measurements, the layer number of different flakes was determined by combined Raman and AFM measurements.

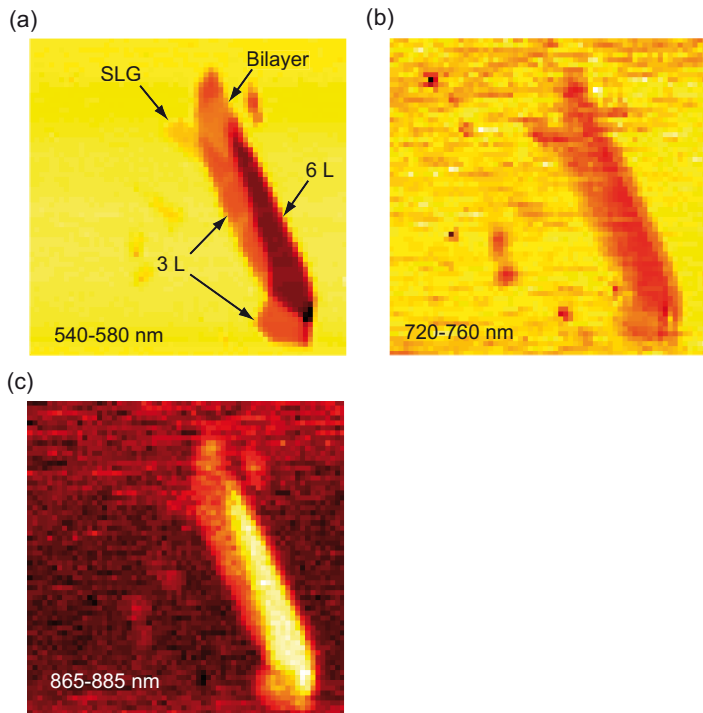


Fig. B.2. Confocal white light scattering images of single and multi-layer graphene showing the integrated optical contrast in the spectral regions: (a) 540–580 nm (b) 720–760 nm and (c) 865–885 nm. The contrast of single layer graphene changes with increasing wavelength from negative to positive. It is nearly not visible anymore in the wavelength interval (c). The number of layers is indicated in (a).

Fig. B.2 shows representative white light scattering images of a large graphene flake, which consists of areas with 1–6 single graphene layers. Each image represents the integrated scattering intensity in the spectral range of (a) 520–540 nm, (b) 720–760 nm and (c) 865–885 nm. The number of layers are indicated in Fig. B.2 (a). The scattering contrast scales with the number of layers and changes for different excitation wavelength. The contrast of single layer graphene is negative for small wavelength, becomes nearly zero in the wavelength range of 720–760 nm and is positive for larger wavelength.

The wavelength dependent optical contrast of the different layers (filled dots) together with the corresponding modeled curves (solid lines) is plotted in Fig. B.3 (a).

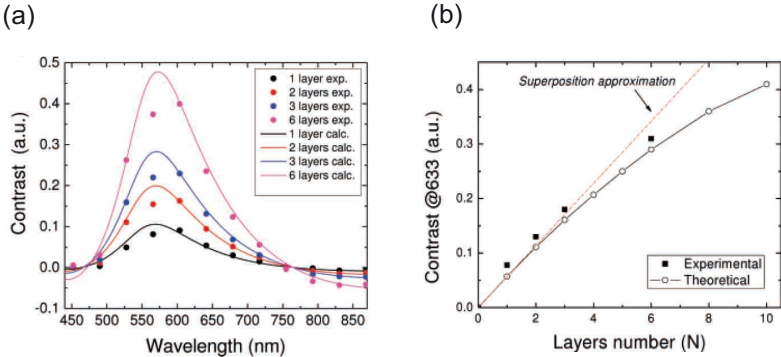


Fig. B.3. (a) Experimental (dots) and modeled scattering contrast (solid lines) as a function of wavelength. Note: The sign of the contrast is reversed. (b) Maximum contrast at 633 nm as a function of layer number. The red line indicates the simple linear scaling relation using the refractive index of graphite, adapted from [311].

Each data point plotted I_{det} for a respective layer number represents the averaged intensity over 16 image pixels. In order to avoid artifacts originating from fluctuations in the white light, the data for the background correction I_{back} was taken at the same scan-line as the corresponding pixel. The contrast increases for increasing number of layers while for this range of layers no phase change is observed. The theoretical curves were calculated with the analytical model presented in the previous section (E. Lidorikis, University of Ioannina). Remarkably, one finds an excellent agreement between the experimental and modeled contrast. The contrast of SLG becomes maximal $\delta \sim -0.09$ at 570 nm and is zero at 750 nm. The phaseshift introduced by the graphene layer ϑ_G can be estimated using equations Eqn. B.2 and Eqn. B.7 and assuming $\vartheta_{Si} = -\pi$. For this, $\vartheta_G \simeq -\pi$ is found as would be expected for an ultrathin film [343]. The dependency of the scattering contrast on the layer numbers is shown in Fig. B.3 (b). For layer numbers $N_L < 6$ the optical contrast can be well approximated by a superposition of individual non-interacting graphene layers. Within this approximation the maximum contrast at $\lambda=570$ nm can be easily calculated by: $\delta(N_L) = 0.9 \cdot N_L$. The modeling further suggests

that within the estimated error of 5% for the contrast measurements the dielectric constants of graphene and graphite are very similar. For the optical properties of graphite this implies that these are basically independent of the thickness of the material and are governed mostly by the optical response of the electrons within each layer with little perturbations from adjacent layers. However, the linear approximation fails for larger layer numbers $N_L \gtrsim 6$ resulting to a slower increase of the contrast and eventually to saturation. This deviation from linearity is also well reproduced by the model. Presumably, absorption losses and more importantly the additional optical path length in graphene start to affect the contrast. The latter becomes even more relevant, when studying multi-layer graphene with $N_L \gtrsim 10$ layers as it is shown in Fig. B.4.

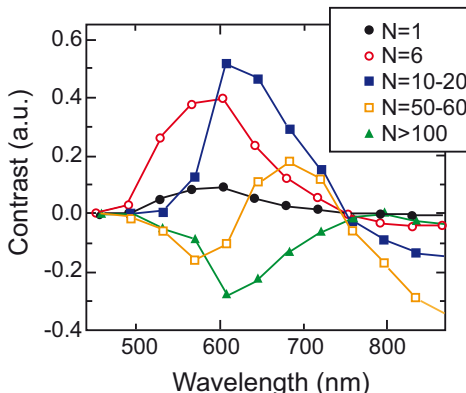


Fig. B.4. Measured optical contrast for samples with increasing layer number. Note: Contrast is reversed, adapted from [311].

With increasing layer numbers N_L the optical contrast, e.g. at 600 nm, first saturates, then starts to red-shift and for even larger number to increase until it becomes positive (Note: Contrast in Fig. B.4 is reversed). Further it is to note that for small N_L , the variation along the vertical (wavelength) axis is largely between zero and negative (i.e. reflectivity reduction only), while for a large number of layers, the variation is from positive to negative (i.e. both reflectivity reduction *and* enhancement). This can be attributed to two different effects. First, for small N_L , graphene basically just reduces the reflectivity of the *air-SiO₂* interface, without affecting the optical path length. (2) For large N_L the reflectivity of the *air-graphene* interface saturates while the effect of the increasing optical path within the now thick graphite layer becomes significant. This change is not a monotonic function of N_L . While these two effects are different, they both contribute to a shift of the reflectivity resonance condition, and thus explain the increasing visibility of thicker graphene layers, when measured for a fixed excitation energy.

The resonance condition can be also shifted by varying the SiO₂ layer thickness. Fig. B.5 maps

the modeled optical contrast of a single layer graphene as function of the SiO₂ layer thickness and excitation wavelength. The maximum contrast occurs at the minima of the background reflectivity. This is expected because this is the most sensitive point in terms of phase matching, and small changes become most visible.

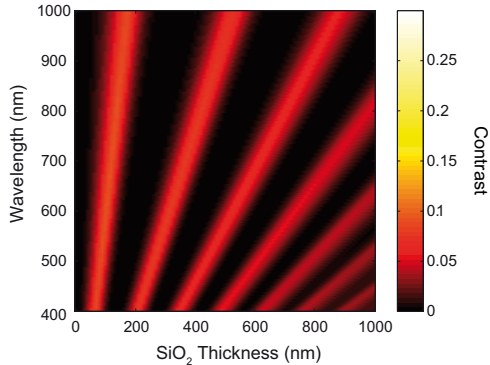


Fig. B.5. Calculated contrast of single layer graphene as a function of the SiO₂ layer thickness and excitation wavelength. The maximum scattering contrast occurs when the reflectance of the background becomes minimal. For a given wavelength that is fulfilled if the optical path length through the spacerlayer becomes a multiple of $\lambda/4$.

This implies that the maximum contrast of graphene is achieved, when the optical path length provided by the SiO₂ is equal to a quarter wavelength, according to: $2n_{SiO_2} d_{SiO_2}/\lambda = (m + 1/2)$. This explains why the substrate with a 300 nm SiO₂ layer yields a good contrast in the visible range around 600 nm. However, another strong maximum is found for 100 nm, which could provide an alternative viable substrate for this kind of experiments.

In summary, it was shown that elastic white light scattering microscopy could be used to visualize a single layer of graphene. The contrast can be enhanced interferometrical when deposited on a layered substrate, whose properties matches resonance conditions. The optical contrast of graphene increase linearly with the number of layers up to a maximum of $N_L \sim 10$ and indicates that such samples optically behave as superposition of single non-interacting sheets. The measured optical contrast can be well reproduced by an analytical model based on the theory of multiple reflections in multi-layered thin films.

Bibliography

- [1] P. Wallace, *The Band Theory of Graphite*, Phys. Rev. **71**, 622–634 (1947).
- [2] J. W. McClure, *Diamagnetism of graphite*, Phys. Rev. **104**, 666–671 (1956).
- [3] J. C. Slonczewski and P. R. Weiss, *Band Structure of Graphite*, Phys. Rev. **109**, 272–279 (1958).
- [4] L. Radushkevich and V. Luk'yanovich, Zh. Fiz. Khim. (1953).
- [5] A. Oberlin, M. Endo, and T. Koyama, *High resolution electron microscope observations of graphitized carbon fibers*, Carbon **14**, 133–135 (1976).
- [6] A. Oberlin, M. Endo, and T. Koyama, *Filamentous growth of carbon through benzene decomposition*, Journal of Crystal Growth **32**, 335–349 (1976).
- [7] H. P. Boehm, A. Clauss, G. Fischer, and U. Hofmann, *Thin Carbon Leaves*, Z. Naturforsch. **17b**, 150–153 (1962).
- [8] S. Iijima, *Helical microtubules of graphitic carbon*, Nature **354**, 56–58 (1991).
- [9] S. Iijima and T. Ichihashi, *Single-shell carbon nanotubes of 1-nm diameter*, Nature **363**, 603–605 (1993).
- [10] D. Bethune, C. Klang, M. de Vries, G. Gorman, R. Savoy, J. Vazquez, and R. Beyers, *Cobalt-catalysed growth of carbon nanotubes with single-atomic-layer walls*, Nature **363**, 605–607 (1993).
- [11] K. S. Novoselov, A. K. Geim, S. V. Morozov, D. Jiang, Y. Zhang, S. V. Dubonos, I. V. Grigorieva, and A. A. Firsov, *Electric field effect in atomically thin carbon films*, Science **306**, 666–669 (2004).
- [12] C. Berger, Z. Song, T. Li, X. Li, A. Y. Ogbazghi, R. Feng, Z. Dai, A. N. Marchenkov, E. H. Conrad, P. N. First, and W. A. de Heer, *Ultrathin Epitaxial Graphite: 2D Electron Gas Properties and a Route toward Graphene-based Nanoelectronics*, J. Phys. Chem. B **108**, 19 912 (2004).
- [13] K. S. Novoselov, D. Jiang, F. Schedin, T. J. Booth, V. V. Khotkevich, S. V. Morozov, and A. K. Geim, *Two-dimensional atomic crystals*, PNAS **102**, 10 451–10 453 (2005).

- [14] K. S. Novoselov, Z. Jiang, Y. Zhang, S. V. Morozov, H. L. Stormer, U. Zeitler, J. C. Maan, G. S. Boebinger, P. Kim, and A. K. Geim, *Room-Temperature Quantum Hall Effect in Graphene*, Science **315**, 1379 (2007).
- [15] Y. Zhang, Y.-W. Tan, H. L. Stormer, and P. Kim, *Experimental observation of the quantum Hall effect and Berry's phase in graphene*, Nature **438**, 201–204 (2005).
- [16] T. Dürkop, S. A. Getty, E. Cobas, and M. S. Fuhrer, *Extraordinary Mobility in Semiconducting Carbon Nanotubes*, Nano Lett. **4**, 35–39 (2004).
- [17] S. Morozov, K. S. Novoselov, M. I. Katsnelson, F. Schedin, D. C. Elias, J. A. Jaszczak, and A. K. Geim, *Giant Intrinsic Carrier Mobilities in Graphene and Its Bilayer*, Phys. Rev. Lett. **100**, 016 602 (2008).
- [18] P. Kim, L. Shi, A. Majumdar, and P. L. McEuen, *Thermal Transport Measurements of Individual Multiwalled Nanotubes*, Phys. Rev. Lett. **87**, 215 502 (2001).
- [19] A. A. Balandin, S. Ghosh, W. Bao, I. Calizo, D. Teweldebrhan, F. Miao, and C. N. Lau, *Superior Thermal Conductivity of Single-Layer Graphene*, Nano Lett. **8**, 902–907 (2008).
- [20] M. M. J. Treacy, T. W. Ebbesen, and J. M. Gibson, *Exceptionally High Young's modulus observed for individual carbon nanotubes*, Nature **381**, 678–680 (1996).
- [21] C. Lee, X. Wei, J. W. Kysar, and J. Hone, *Measurement of the Elastic properties and Intrinsic Strength of Monolayer Graphene*, Science **321**, 385–388 (2008).
- [22] R. Martel, T. Schmidt, H. R. Shea, T. Hertel, and P. Avouris, *Single- and multi-wall carbon nanotube field-effect transistors*, Appl. Phys. Lett. **73**, 2447–2449 (1998).
- [23] S. J. Tans, A. R. M. Verschueren, and C. Dekker, *Room-temperature transistor based on a single carbon nanotube*, Nature **393**, 49–52 (1998).
- [24] W. B. Choi, D. S. Chung, J. H. Kang, H. Y. Kim, Y. W. Jin, I. T. Han, Y. H. Lee, J. E. Jung, N. S. Lee, G. S. Park, and J. M. Kim, *Fully sealed, high-brightness carbon-nanotube field-emission display*, Appl. Phys. Lett. **75**, 3129–3131 (1999).
- [25] T. Mueller, M. Kinoshita, M. Steiner, V. Perebeinos, A. A. Bol, D. B. Farmer, and P. Avouris, *Efficient narrow-band light emission from a single carbon nanotube p-n diode*, Nature Nanotechnology **5**, 27–31 (2010).
- [26] F. Xia, T. Mueller, Y. Lin, A. Valdes-Garcia, and P. Avouris, *Ultrafast graphene photodetector*, Nature Nanotechnology **4**, 839–843 (2009).
- [27] T. Mueller, F. Xia, and P. Avouris, *Graphene photodetectors for high-speed optical communications*, Nature Photonics **4**, 297–301 (2010).

- [28] S. Nie, D. T. Chiu, and R. N. Zare, *Probing Individual Molecules with Confocal Fluorescence Microscopy*, Science **266**, 1018–1021 (1994).
- [29] X. S. Xie and J. K. Trautman, *Optical Studies of Single Molecules at Room Temperature*, Annu. Rev. Phys. Chem. **49**, 441–480 (1989).
- [30] W. Ambrose, P. Goodwin, J. Jett, A. van Orden, J. Werner, and R. Keller, *Single Molecule Fluorescence Spectroscopy at Ambient Temperature*, Chem. Rev. **99**, 2929–2956 (1999).
- [31] A. Hartschuh, H. N. Pedrosa, L. Novotny, and T. D. Krauss, *Simultaneous fluorescence and Raman scattering from single carbon nanotubes*, Science **301**, 1354–1356 (2003).
- [32] S. Park and R. S. Ruoff, *Chemical methods for the production of graphenes*, Nature Nanotechnology **4**, 217–224 (2009).
- [33] M. Lotya, P. J. King, U. Khan, S. De, and J. N. Coleman, *High-Concentration, Surfactant-Stabilized Graphene Dispersions*, ACS Nano **4**, 3155–3162 (2010).
- [34] T. Hasan, F. Torrisi, Z. Sun, D. Popa, V. Nicolosi, G. Privitera, F. Bonaccorso, and A. C. Ferrari, *Solution-phase exfoliation of graphite for ultrafast photonics*, phys. stat. sol. (b) **247**, 2953–2957 (2010).
- [35] K. V. Emtsev, A. Bostwick, K. Horn, J. Jobst, G. L. Kellogg, L. Ley, J. L. McChesney, T. Ohta, S. A. Reshanov, J. Röhr, E. Rotenberg, A. K. Schmid, D. Waldmann, H. B. Weber, and T. Seyller, *Towards wafer-size graphene layers by atmospheric pressure graphitization of silicon carbide*, Nature Materials **8**, 203–207 (2009).
- [36] X. Li, W. Cai, J. An, S. Kim, J. Nah, D. Yang, R. Piner, A. Velamakanni, I. Jung, E. Tutuc, S. K. Banerjee, L. Colombo, and R. S. Ruoff, *Large-Area Synthesis of High-Quality and Uniform Graphene Films on Copper Foils*, Science **324**, 1312–1314 (2009).
- [37] L. Gao, J. R. Guest, and N. P. Guisinger, *Epitaxial Graphene on Cu(111)*, Nano Lett. **10**, 3512–3515 (2010).
- [38] S. Bae, H. Kim, Y. Lee, X. Xu, J.-S. Park, Y. Zheng, J. Balakrishnan, T. Lei, H. R. Kim, Y. I. Song, Y.-J. Kim, K. S. Kim, B. Özyilmaz, J.-H. Ahn, B. H. Hong, and S. Iijima, *Roll-to-roll production of 30-inch graphene films for transparent electrodes*, Nature Tech. **5**, 574–578 (2010).
- [39] V. Palermo, S. Morelli, C. Simpson, K. Müllen, and P. Samor, *Self-organized nanofibers from a giant nanographene: Effect of solvent and deposition method*, J. Mater. Chem. **16**, 266–271 (2006).
- [40] X. Yang, X. Dou, A. Rouhanipour, L. Zhi, H. J. Räder, and K. Müllen, *Two-Dimensional Graphene Nanoribbons*, J. Am. Chem. Soc. **130**, 4216–4217 (2008).

- [41] A. Thess, R. Lee, P. Nikolaev, H. Dai, P. Petit, J. Robert, C. Xu, Y. Lee, S. Kim, A. Rinzler, D. Colbert, G. Scuseria, D. Tomanek, J. Fischer, and R. Smalley, *Crystalline Ropes of Metallic Carbon Nanotubes*, Science **297**, 483–487 (1996).
- [42] V. Geringer, M. Liebmann, T. Echtermeyer, S. Runte, M. Schmidt, R. Rückamp, M. C. Lemme, and M. Morgenstern, *Intrinsic and extrinsic corrugation of monolayer graphene deposited on SiO₂*, Phys. Rev. Lett. **102**, 076 102 (2009).
- [43] C. H. Lui, L. Liu, K. F. Mak, G. W. Flynn, and T. F. Heinz, *Ultraflat graphene*, Nature **462**, 339–341 (2009).
- [44] J. C. Meyer, A. K. Geim, M. I. Katsnelson, K. S. Novoselov, T. J. Booth, and S. Roth, *The structure of suspended graphene sheets*, Nature **446**, 60–63 (2007).
- [45] L. X. Zheng, M. J. O’Connell, S. K. Doorn, X. Z. Liao, Y. H. Zhao, E. A. Akhadov, M. A. Hoffbauer, B. J. Roop, Q. X. Jia, R. C. Dye, D. E. Peterson, S. M. Huang, J. Liu, and Y. T. Zhu, *Ultralong single-wall carbon nanotubes*, Nature Materials **3**, 673–676 (2004).
- [46] S. Reich, C. Thomsen, and J. Maultzsch, *Carbon Nanotubes: Basic Concepts and Physical Properties* (Wiley-VCH Verlag, Weinheim, 2004).
- [47] S. Maruyama, *Nanotube coordinate generator with a viewer for windows*, <http://www.photon.t.u-tokyo.ac.jp/~maruyama/wrapping3/wrapping.html>.
- [48] M. Damnjanović, I. Milošević, T. Vuković, and R. Sredanovic, *Full symmetry, optical activity and potentials of single-wall and multiwall nanotubes*, Phys. Rev. B **60**, 2728–2739 (1999).
- [49] M. J. O’Connell, S. M. Bachilo, C. Huffman, V. Moore, M. Strano, E. Haroz, K. Rialon, P. Boul, W. Noon, C. Kittrell, J. Ma, R. H. Hauge, R. B. Weisman, and R. Smalley, *Band Gap Fluorescence from Individual Single-Walled Carbon Nanotubes*, Science **297**, 593–596 (2002).
- [50] S. M. Bachilo, M. S. Strano, C. Kittrell, R. H. Hauge, R. Smalley, and R. B. Weisman, *Structure-Assigned Optical Spectra of Single-Walled Carbon Nanotubes*, Science **298**, 2361–2366 (2002).
- [51] A. Jorio, C. Fantini, M. A. Pimenta, R. B. Capaz, G. G. Samsonidze, G. Dresselhaus, M. S. Dresselhaus, J. Jiang, N. Kobayashi, A. Grneis, and R. Saito, *Resonance Raman spectroscopy (n,m)-dependent effects in small-diameter single-wall carbon nanotubes*, Phys. Rev. B **71**, 075 401 (2005).
- [52] R. Saito, G. Dresselhaus, and M. S. Dresselhaus, *Physical Properties of Carbon Nanotubes* (Imperial College Press, London, 1998).

- [53] N. Hamada, S.-I. Sawada, and A. Oshiyama, *New one-dimensional conductors: Graphitic microtubules*, Phys. Rev. Lett. **68**, 1579–1581 (1992).
- [54] R. Saito, M. Fujita, G. Dresselhaus, and M. Dresselhaus, *Electronic structure of graphene tubules based on C₆₀*, Phys. Rev. B **46**, 1804–1811 (1992).
- [55] S. Reich, J. Maultzsch, C. Thomsen, and P. Ordejón, *Tight-binding description of graphene*, Phys. Rev. B **66**, 035 412 (2002).
- [56] M. Machón, S. Reich, C. Thomsen, D. Sánchez-Portal, and P. Ordejón, *Ab initio calculations of the optical properties of 4-Å-diameter single-walled nanotubes*, Phys. Rev. B **66**, 155 410 (2002).
- [57] A. Jorio, M. S. Dresselhaus, and G. Dresselhaus, *Carbon Nanotubes*, Vol. 111 of Topics in Applied Physics (Springer-Verlag, Berlin/Heidelberg, 2008).
- [58] Y.-W. Son, M. L. Cohen, and S. G. Louie, *Energy Gaps in Graphene Nanoribbons*, Phys. Rev. Lett. **97**, 216 803 (2006).
- [59] J. W. Mintmire and C. T. White, *Universal Density of States for Carbon Nanotubes*, Phys. Rev. Lett. **81**, 2056 – 2059 (1998).
- [60] P. Kim, T. Odom, J. Huang, and C. M. Lieber, *Electronic Density of States of Atomically Resolved Single-Walled Carbon Nanotubes: Van Hove Singularities and End States*, Phys. Rev. Lett. **82**, 1225–1228 (1999).
- [61] A. Jorio, A. G. S. Filho, G. Dresselhaus, M. S. Dresselhaus, R. Saito, J. H. Hafner, C. M. Lieber, F. M. Matinaga, M. S. S. Dantas, and M. A. Pimenta, *Joint density of electronic states for one isolated single-wall carbon nanotube studied by resonant Raman scattering*, Phys. Rev. B **63**, 245 416 (2001).
- [62] R. Saito, G. Dresselhaus, and M. S. Dresselhaus, *Trigonal warping effect of carbon nanotubes*, Phys. Rev. B. **61**, 2981–2990 (2000).
- [63] G. G. Samsonidze, R. Saito, A. Jorio, M. A. Pimenta, A. G. Souza, A. Grüneis, G. Dresselhaus, and M. S. Dresselhaus, *The Concept of Cutting Lines in Carbon Nanotube Science*, Journal of Nanoscience and Nanotechnology **3**, 431–458 (2003).
- [64] S. Reich and C. Thomsen, *Chirality dependence of the density-of-states singularities in carbon nanotubes*, Phys. Rev. B **62**, 4273–4276 (2000).
- [65] M. Y. Sfeir, T. Beetz, F. Wang, L. Huang, X. H. Huang, M. Huang, J. Hone, S. O'Brien, J. Misewich, T. F. Heinz, L. Wu, Y. Zhu, and L. E. Brus, *Optical Spectroscopy of Individual Single-Walled Carbon Nanotubes of Defined Chiral Structure*, Science **312**, 554–556 (2006).

- [66] H. Kataura, Y. Kumazawa, Y. Maniwa, I. Umezu, S. S. Y. Ohotsuka, and Y. Achiba, *Optical Properties of Single-Wall Carbon Nanotubes*, Synth. Met. **103**, 2555 (1999).
- [67] P. T. Araujo, S. K. Doorn, S. Kilina, D. Tretiak, S. Tretiak, E. Einarsson, S. Maruyama, H. Chacham, M. Pimenta, and A. Jorio, *Third and fourth optical transitions in semiconducting carbon nanotubes*, Phys. Rev. Lett. **98**, 067401 (2007).
- [68] L. Novotny and B. Hecht, *Principles of Nano-Optics* (Cambridge University Press, Cambridge, 2006).
- [69] E. B. Barrosa, A. Jorio, G. G. Samsonidze, R. B. Capaz, A. G. S. Filho, J. M. Filho, G. Dresselhaus, and M. S. Dresselhaus, *Review on the symmetry-related properties of carbon nanotubes*, Phys. Rep. **431**, 261–302 (2006).
- [70] E. B. Barros, R. B. Capaz, A. Jorio, G. G. Samsonidze, A. G. S. Filho, S. Ismail-Beigi, C. D. Spataru, S. G. Louie, G. Dresselhaus, and M. S. Dresselhaus, *Selection rules for one- and two-photon absorption by excitons in carbon nanotubes*, Phys. Rev. B **73**, 241406(R) (2006).
- [71] M. S. Dresselhaus, G. Dresselhaus, and A. Jorio, *Group Theory* (Springer-Verlag, Berlin, Heidelberg, 2010).
- [72] M. Kasha, *Characterization of electronic transitions in complex molecules*, Discuss. Faraday Soc. **9**, 14–19 (1950).
- [73] H. Ajiki and T. Ando, *Carbon nanotubes: Optical absorption in Aharonov-Bohm flux*, Jpn. J. Appl. Phys. Suppl. **34-1**, 107 (1994).
- [74] L. X. Benedict, S. G. Louie, and M. L. Cohen, *Static polarizabilities of single-wall carbon nanotubes*, Phys. Rev. B **52**, 8541–8549 (1995).
- [75] S. Tasaki, K. Maekawa, and T. Yamabe, *π -band contribution to the optical properties of carbon nanotubes: Effects of chirality*, Phys. Rev. B **57**, 9301–9318 (1998).
- [76] Y. Miyauchi, M. Oba, and S. Maruyama, *Cross-polarized optical absorption of single-walled nanotubes by polarized photoluminescence excitation spectroscopy*, Phys. Rev. B **74**, 205440 (2006).
- [77] J. Lefebvre and P. Finnie, *Polarized Photoluminescence Excitation Spectroscopy of Single-Walled Carbon Nanotubes*, Phys. Rev. Lett. **98**, 167406 (2007).
- [78] M. Ichida, S. Mizuno, Y. Saito, H. Kataura, Y. Achiba, and A. Nakamura, *Coulomb effects on the fundamental optical transition in semiconducting single-walled carbon nanotubes: Divergent behavior in the small-diameter limit*, Phys. Rev. B **65**, 241407(R) (2002).

- [79] C. Kane and E. J. Mele, *Ratio Problem in Single Carbon Nanotube Fluorescence Spectroscopy*, Phys. Rev. Lett. **90**, 207 401 (2003).
- [80] J. Ando, *Excitons in Carbon Nanotubes*, J. Phys. Soc. Jpn. **66**, 1066–1073 (1997).
- [81] H. Zhao and S. Mazumdar, *Electron-electron interaction effects on the optical excitations of semiconducting single-walled carbon nanotubes*, Phys. Rev. Lett. **93**, 157 402 (2004).
- [82] V. Perebeinos, J. Tersoff, and P. Avouris, *Effect of Exciton-Phonon Coupling in the Calculated Optical Absorption of Carbon Nanotubes*, Phys. Rev. Lett. **92**, 257 402 (2004).
- [83] C. D. Spataru, S. Ismail-Beigi, L. Benedict, and S. G. Louie, *Excitonic Effects and Optical Spectra of Single-Walled Carbon Nanotubes*, Phys. Rev. Lett. **92**, 077 402 (2004).
- [84] J. Maultzsch, R. Pomraenke, S. Reich, E. Chang, D. Prezzi, A. Ruini, E. Molinari, M. S. Strano, C. Thomsen, and C. Lienau, *Exciton binding energies in carbon nanotubes from two-photon photoluminescence*, Phys. Rev. B **72**, 241 402(R) (2005).
- [85] F. Wang, G. Dukovic, L. E. Brus, and T. F. Heinz, *The Optical Resonances in Carbon Nanotubes Arise from Excitons*, Science **308**, 838–841 (2005).
- [86] G. Dukovic, F. Wang, D. Song, M. Sfeir, T. F. Heinz, and L. Brus, *Structural Dependence of Excitonic Optical Transitions and Band-Gap Energies in Carbon Nanotubes*, Nano Lett **5**, 2314–2318 (2005).
- [87] P. Y. Yu and M. Cardona, *Fundamentals of Semiconductors: Physics and Materials properties* (Springer, Berlin, Heidelberg, New York, 2006), third edition edn.
- [88] F. Wang, D. J. Cho, B. Kessler, J. Deslippe, P. J. Schuck, S. G. Louie, A. Zettland, T. F. Heinz, and Y. R. Shen, *Observation of Excitons in One-Dimensional Metallic Single-Walled Carbon Nanotubes*, Phys. Rev. Lett. **99**, 227 401 (2007).
- [89] M. Rohlfing and S. G. Louie, *Electron-hole excitations and optical spectra from first principles*, Phys. Rev. B **62**, 4927–4944 (2000).
- [90] V. Perebeinos, J. Tersoff, and P. Avouris, *Scaling of Excitons in Carbon Nanotubes*, Phys. Rev. Lett. **92**, 257 402 (2004).
- [91] J. Jiang, R. Saito, G. G. Samsonidze, A. Jorio, S. G. Chou, G. Dresselhaus, and M. S. Dresselhaus, *Chirality dependence of exciton effects in single-wall carbon nanotubes: Tight-binding model*, Phys. Rev. B **75**, 035 407 (2007).
- [92] R. B. Capaz, C. D. Spataru, S. Ismail-Beigi, and S. G. Louie, *Diameter and chirality dependence of exciton properties in carbon nanotubes*, Phys. Rev. B **74**, 121 401 (2006).
- [93] M. S. Dresselhaus, G. Dresselhaus, R. Saito, and A. Jorio, *Exciton Photophysics of Carbon Nanotubes*, Annu. Rev. Phys. Chem. **58**, 719–747 (2007).

- [94] V. Perebeinos, J. Tersoff, and P. Avouris, *Radiative Lifetime of Excitons in Carbon Nanotubes*, Nano Lett. **5**, 2495–2499 (2005).
- [95] I. B. Mortimer and R. J. Nicholas, *Role of Bright and Dark Excitons in the Temperature-Dependent Photoluminescence of Carbon Nanotubes*, Phys. Rev. Lett. **98**, 027 404 (2007).
- [96] J. Shaver, J. Kono, O. Portugall, V. Krstic, G. L. J. A. Rikken, Y. Miyauchi, S. Maruyama, and V. Perebeinos, *Magnetic brightening of carbon nanotube photoluminescence through symmetry breaking*, Nano Lett. **7**, 1851–1855 (2007).
- [97] R. Matsunaga, K. Matsuda, and Y. Kanemitsu, *Direct observation of dark excitonic states in single carbon nanotubes*, Journal of Luminescence **129**, 1702–1705 (2009).
- [98] O. Kiowski, K. Arnold, S. Lebedkin, F. Hennrich, and M. M. Kappes, *Direct Observation of Deep Excitonic States in the Photoluminescence Spectra of Single-Walled Carbon Nanotubes*, Phys. Rev. Lett. **99**, 237 402 (2007).
- [99] O. Torrens, M. Zheng, and J. Kikkawa, *Energy of K-Momentum Dark Excitons in Carbon Nanotubes by Optical Spectroscopy*, Phys. Rev. Lett. **101**, 157 401 (2008).
- [100] Y. Murakami, B. Lu, S. Kazaoui, N. Minami, T. Okubo, and S. Maruyama, *Photoluminescence sidebands of carbon nanotubes below the bright singlet excitonic levels*, Phys. Rev. B **79**, 195 407 (2009).
- [101] R. Matsunaga, K. Matsuda, and Y. Kanemitsu, *Origin of low-energy photoluminescence peaks in single carbon nanotubes: K-momentum dark excitons and triplet dark excitons*, Phys. Rev. B **81**, 033 401 (2010).
- [102] H. Y. Seferyan, M. B. Nasr, V. Senekerimyan, R. Zadoyan, P. Collins, and V. A. Apkarian, *Transient Grating Measurements of Excitonic Dynamics in Single-Walled Carbon Nanotubes: The Dark Excitonic Bottleneck*, Nano Lett. **6**, 1757–1760 (2006).
- [103] S. Tretiak, *Triplet absorption in carbon nanotubes: A TD-DFT study*, Nano Lett. **7**, 2201–2206 (2007).
- [104] E. Malic, *Many-particle theory of optical properties in low-dimensional nanostructures*, Dissertation, Technische Universität Berlin (2008).
- [105] A. G. Walsh, A. N. Vamivakas, Y. Yin, S. B. Croninc, M. S. Ünlü, B. B. Goldberg, and A. K. Swan, *Scaling of exciton binding energy with external dielectric function in carbon nanotubes*, Physica E **40**, 2375–2379 (2008).
- [106] C. D. Spataru, S. Ismail-Beigi, R. B. Capaz, and S. G. Louie, *Theory and ab-initio calculation of radiative lifetime of excitons in semiconducting carbon nanotubes*, Phys. Rev. Lett. **95**, 247 402 (2005).

- [107] E. Chang, G. Bussi, A. Ruini, and E. Molinari, *Excitons in Carbon Nanotubes: An Ab-Initio Symmetry-Based Approach*, Phys. Rev. Lett. **92**, 077 402 (2004).
- [108] J. Maultzsch, R. Pomraenke, S. Reich, E. Chang, D. Prezzi, A. Ruini, E. Molinari, M. S. Strano, C. Thomsen, and C. Lienau, *Excitons in carbon nanotubes*, phys. stat. sol. (b) **243**, 3204–3208 (2006).
- [109] Y.-Z. Ma, L. Valkunas, S. M. Bachilo, and G. R. Fleming, *Exciton Binding Energy in Semiconducting Single-Walled Carbon Nanotubes*, J. Phys. Chem. B **109**, 15 671 (2005).
- [110] Y. Miyauchi, H. Hirori, K. Matsuda, and Y. Kanemitsu, *Radiative lifetimes and coherence lengths of one-dimensional excitons in single-walled carbon nanotubes*, Phys. Rev. B. **80**, 081 410(R) (2009).
- [111] M. W. Graham, Y.-Z. Ma, A. A. Green, M. C. Hersam, and G. R. Fleming, *Pure optical dephasing dynamics in semiconducting single-walled carbon nanotubes*, J. Chem. Phys. **134**, 034 504 (2011).
- [112] L. Lüer, S. Hoseinkhani, D. Polli, J. Crochet, T. Hertel, and G. Lanzani, *Size and mobility of excitons in (6,5) carbon nanotubes*, Nature Physics **5**, 54–58 (2009).
- [113] L. Cognet, D. T. Tysbouski, J.-D. R. Rocha, C. Doyle, J. M. Tour, and R. Weisman, *Step-wise quenching of exciton fluorescence in carbon nanotubes by single-molecule reactions*, Science **316**, 1465–1468 (2007).
- [114] S. Moritsubo, T. Murai, T. Shimada, Y. Murakami, S. Chiashi, S. Maruyama, and Y. K. Kato, *Exciton Diffusion in Air-Suspended Single-Walled Carbon Nanotubes*, Phys. Rev. Lett. **104**, 247 402 (2010).
- [115] C. Georgi, M. Böhmler, H. Qian, L. Novotny, and A. Hartschuh, *Probing exciton propagation and quenching in carbon nanotubes with near-field optical microscopy*, phys. stat. sol. (b) **246**, 2683–2688 (2009).
- [116] O. N. Torrens, D. E. Milkie, M. Zheng, and J. M. Kikkawa, *Photoluminescence from intertube carrier migration in single-walled carbon nanotube bundles*, Nano Lett. **6**, 2864–2867 (2006).
- [117] P. H. Tan, A. G. Rozhin, T. Hasan, P. Hu, V. Scardaci, W. I. Milne, and A. C. Ferrari, *Photoluminescence Spectroscopy of Carbon Nanotube Bundles: Evidence for Exciton Energy Transfer*, Phys. Rev. Lett. **99**, 137 402 (2007).
- [118] H. Qian, C. Georgi, N. Anderson, A. A. Green, M. C. Hersam, L. Novotny, and A. Hartschuh, *Exciton energy transfer in pairs of single-walled carbon nanotubes*, Nano Lett. **8**, 1363–1367 (2008).

- [119] M. Jones, C. Engrakul, W. K. Metzger, R. J. Ellingson, A. J. Nozik, M. J. Heben, and G. Rumbles, *Analysis of photoluminescence from solubilized single-walled carbon nanotubes*, Phys. Rev. B **71**, 115 426 (2005).
- [120] T. Hertel, V. Perebeinos, J. Crochet, K. Arnold, M. Kappes, and P. Avouris, *Intersubband Decay of 1-D Exciton Resonances in Carbon Nanotubes*, Nano Lett. **8**, 87–91 (2008).
- [121] J. Lefebvre and P. Finnie, *Excited Excitonic States in Single-Walled Carbon Nanotubes*, Nano Lett. **8**, 1890–1895 (2008).
- [122] S.-Y. Ju, W. P. Kopcha, and F. Papadimitrakopoulos, *Brightly Fluorescent Single-Walled Carbon Nanotubes via an Oxygen-Excluding Surfactant Organization*, Science **323**, 1319–1323 (2009).
- [123] J. Lefebvre, D. G. Austing, J. Bond, and P. Finnie, *Photoluminescence Imaging of Suspended Single-Walled Carbon Nanotubes*, Nano Lett. **6**, 1603–1608 (2006).
- [124] S. Berciaud, L. Cognet, and B. Lounis, *Luminescence decay and the absorption cross section of individual single-walled carbon nanotubes*, Phys. Rev. Lett. **101**, 077 402 (2008).
- [125] V. Perebeinos and P. Avouris, *Phonon and Electronic Nonradiative Decay Mechanisms of Excitons in Carbon Nanotubes*, Phys. Rev. Lett. **101**, 057 401 (2008).
- [126] C. Georgi, N. Hartmann, T. Gokus, A. A. Green, M. C. Hersam, and A. Hartschuh, *Photoinduced Luminescence Blinking and Bleaching in Individual Single-Walled Carbon Nanotubes*, ChemPhysChem **9**, 1460–1464 (2008).
- [127] M. Strano, C. Huffman, V. Moore, M. O. Connell, E. Haroz, J. Hubbard, M. Miller, K. Kittrel, S. Ramesh, R. Hauge, and R. Smalley, *Reversible, Band-Gap-Selective Protonation of Single-Walled Carbon Nanotubes in Solution*, J. Phys. Chem. B **107**, 6979–6985 (2003).
- [128] L. Cognet, D. A. Tsypoulski, J.-D. Rocha, C. Doyle, J. M. Tour, and R. B. Weisman, *Stepwise quenching of exciton fluorescence in carbon nanotubes by single-molecule reactions*, Science **316**, 1465–1468 (2007).
- [129] G. Dukovic, B. E. White, Z. Zhou, F. Wang, S. Jockusch, M. L. Steigerwald, T. F. Heinz, R. A. Friesner, N. J. Turro, and L. E. Brus, *Reversible Surface Oxidation and Efficient Luminescence Quenching in Semiconductor Single-Wall Carbon Nanotubes*, J. Am. Chem. Soc. **126**, 15 269–15 276 (2004).
- [130] A. Hartschuh, H. Qian, A. Meixner, N. Anderson, and L. Novotny, *Nanoscale Optical Imaging of Excitons in Single-Walled Carbon Nanotubes*, Nano Lett. **5**, 2310–2313 (2005).
- [131] J. Crochet, M. Clemens, and T. Hertel, *Optical properties of structurally sorted single-wall carbon nanotube ensembles*, phys. stat. sol. (b) **11**, 3964–3968 (2007).

- [132] M. Dresselhaus, G. Dresselhaus, R. Saito, and A. Jorio, *Raman spectroscopy of carbon nanotubes*, Physics Reports **409**, 47–99 (2005).
- [133] S. Piscanec, M. Lazzeri, F. Mauri, A. Ferrari, and J. Robertson, *Kohn Anomalies and Electron-Phonon Interactions in Graphite*, Phys. Rev. Lett. **93**, 185 503 (2004).
- [134] A. C. Ferrari, J. C. Meyer, V. Scardaci, C. Casiraghi, M. Lazzeri, F. Mauri, S. Piscanec, D. Jiang, K. S. Novoselov, S. Roth, and A. K. Geim, *Raman Spectrum of Graphene and Graphene Layers*, Phys. Rev. Lett. **97**, 187 401 (2006).
- [135] A. Jorio, A. G. S. Filho, G. Dresselhaus, M. S. Dresselhaus, A. K. Swan, M. S. Ünlü, B. B. Goldberg, M. A. Pimenta, J. H. Hafner, C. M. Lieber, and R. Saito, *G-band resonant Raman study of 62 isolated single-wall carbon nanotubes*, Phys. Rev. B **65**, 155 412 (2002).
- [136] A. Jorio, R. Saito, J. H. Hafner, C. M. Lieber, M. Hunter, T. McClure, G. Dresselhaus, and M. Dresselhaus, *Structural (n,m) determination of isolated single-wall carbon nanotubes by Resonant Raman Scattering*, Phys. Rev. Lett. **86**, 1118–1121 (2001).
- [137] C. Casiraghi, A. Hartschuh, H. Qian, S. Piscanec, C. Georgi, A. Fasoli, K. S. Novoselov, D. M. Basko, and A. C. Ferrari, *Raman Spectroscopy of Graphene Edges*, Nano Lett. **9**, 1433–1441 (2009).
- [138] C. Thomsen and S. Reich, *Double Resonant Raman Scattering in Graphite*, Phys. Rev. Lett. **85**, 5214–5217 (2000).
- [139] C. Thomsen, *Second-order Raman spectra of single and multiwalled carbon nanotubes*, Phys. Rev. B **61**, 4542–4544 (2000).
- [140] J. Maultzsch, S. Reich, S. Webster, R. Czerw, D. L. Carroll, S. M. C. Vieira, P. R. Birkett, C. A. Rego, and C. Thomsen, *Raman characterization of boron-doped multiwalled carbon nanotubes*, Appl. Phys. Lett. **81**, 2647–2649 (2002).
- [141] F. Tuinstra and J. L. Koenig, *Raman Spectrum of Graphite*, J. Chem. Phys. **53**, 1126–1130 (1970).
- [142] R. P. Vidano, D. B. Fischbach, L. J. Willis, and T. M. Loehr, *Observation of Raman band shifting with excitation wavelength for carbons and graphites*, Solid State Commun. **39**, 341–344 (1981).
- [143] D. Knight and W. White, *Characterization of diamond films by Raman spectroscopy*, J. Mater. Res. **4**, 385–393 (1989).
- [144] M. Lucchese, F. Stavale, E. M. Ferreira, C. Vilani, M. V. O. Moutinho, R. B. Capaz, C. A. Achete, and A. Jorio, *Quantifying ion-induced defects and Raman relaxation length in graphene*, Carbon **48**, 1592–1597 (2010).

- [145] A. C. Ferrari and J. Robertson, *Interpretation of Raman spectra of disordered and amorphous carbon*, Phys. Rev. B **61**, 14 095 (2000).
- [146] J. Lefebvre, J. Fraser, P. Finnie, and Y. Homma, *Photoluminescence from an individual single-walled carbon nanotube*, Phys. Rev. B **69**, 075 403 (2004).
- [147] S. Berciaud, L. Cognet, P. Poulin, R. B. Weisman, and B. Lounis, *Absorption Spectroscopy of Individual Single-Walled Carbon Nanotubes*, Nano Lett. **7**, 1203–1207 (2007).
- [148] E. Hecht and A. Zajac, *Optics* (Addison-Wesley Longman, Amsterdam, 2003), 4th international edn.
- [149] R. Webb, *Confocal Optical Microscopy*, Rep. Prog. Phys. **59**, 427–471 (1996).
- [150] M. Minsky, *Memoir on inventing the confocal scanning microscope*, Scanning **10**, 128–138 (1988).
- [151] J. B. Pawley, *Handbook of Biological Confocal Microscopy* (Springer-Verlag, New York, 2006), 3rd edn.
- [152] S. W. Hell and J. Wichmann, *Breaking the diffraction resolution limit by stimulated emission: stimulated-emission-depletion fluorescence microscopy*, Optics Letters **19**, 780–782 (1994).
- [153] B. Huang, W. Wang, M. Bates, and X. Zhuang, *Three-Dimensional Super-Resolution Imaging by Stochastic Optical Reconstruction Microscopy*, Science **319**, 810–813 (2008).
- [154] A. E. Siegman, *Lasers* (University Science Books, Sausalito, USA, 1986).
- [155] L. G. Gouy, *Sur une propriété nouvelle des ondes lumineuses*, Comptes rendus hebdomadiers des sances de l'Académie des Sciences **110**, 1251–1253 (1890).
- [156] R. W. Boyd, *Intuitive explanation of the phase anomaly of focused light beams*, J. Opt. Soc. Am. **70**, 877–880 (1980).
- [157] R. J. Gordon and V. J. Barge, *Effect of the Gouy phase on the coherent phase control of chemical reactions*, J. Chem. Phys. **127**, 204 302 (2007).
- [158] K. Lindfors, T. Kalkbrenner, P. Stoller, and V. Sandoghdar, *Detection and Spectroscopy of Gold Nanoparticles Using Supercontinuum White Light Confocal Microscopy*, Phys. Rev. Lett. **93**, 037 401 (2004).
- [159] V. Jacobsen, P. Stoller, C. Brunner, V. Vogel, and V. Sandoghdar, *Interferometric optical detection and tracking of very small gold nanoparticles at a water-glass interface*, Opt. Express **14**, 405–414 (2006).

- [160] M. A. van Dijk, A. L. Tchebotareva, M. Orrit, M. Lippitz, S. Berciaud, D. Lasne, L. Cognet, and B. Lounis, *Absorption and scattering microscopy of single metal nanoparticles*, Phys. Chem. Chem. Phys. **8**, 3486–3495 (2006).
- [161] F. V. Ignatovich and L. Novotny, *Real-Time and Background-Free Detection of Nanoscale Particles*, Phys. Rev. Lett. **96**, 013 901 (2006).
- [162] J. S. Batchelder and M. Taubenblatt, *Interferometric detection of forward scattered light from small particles*, Appl. Phys. Lett. **55**, 215–217 (1989).
- [163] T. Plakhotnik and V. Palm, *Interferometric Signatures of Single Molecules*, Phys. Rev. Lett. **87**, 183 602 (2001).
- [164] M. A. van Dijk, M. Lippitz, and M. Orrit, *Detection of Acoustic Oscillations of Single Gold Nanospheres by Time-Resolved Interferometry*, Phys. Rev. Lett. **95**, 267 406 (2005).
- [165] A. Arbouet, D. Christofilos, N. D. Fatti, F. Valle, J. Huntzinger, L. Arnaud, P. Billaud, and M. Broyer, *Direct Measurement of the Single-Metal-Cluster Optical Absorption*, Phys. Rev. Lett. **93**, 12 401 (2004).
- [166] S. Berciaud, D. Lasne, G. A. Blab, L. Cognet, and B. Lounis, *Photothermal heterodyne imaging of individual metallic nanoparticles: Theory versus experiment*, Phys. Rev. B **73**, 045 424 (2006).
- [167] S. Berciaud, L. Cognet, G. A. Blab, and B. Lounis, *Photothermal Heterodyne Imaging of Individual Nonfluorescent Nanoclusters and Nanocrystals*, Phys. Rev. Lett. **93**, 257 402 (2004).
- [168] P. Kukura, H. Ewers, C. Mller, A. Renn, A. Helenius, and V. Sandoghdar, *High-speed nanoscopic tracking of the position and orientation of a single virus*, Nature Methods **6**, 923–927 (2009).
- [169] F. V. Ignatovich, A. Hartschuh, and L. Novotny, *Detection of nanoparticles using optical gradient forces*, Journal of Modern Optics **50**, 1509–1520 (2003).
- [170] A. Mitra, B. Deutsch, F. Ignatovich, C. Dykes, and L. Novotny, *Nano-optofluidic Detection of Single Viruses and Nanoparticles*, ACS Nano **4**, 1305–1312 (2010).
- [171] J. Y. P. Butter, B. Hecht, B. R. Crenshaw, and C. Weder, *Absorption and fluorescence of single molecules*, J. Chem. Phys. **125**, 154 710 (2006).
- [172] M. Celebrano, P. Kukura, A. Renn, and V. Sandoghdar, *Single-molecule imaging by optical absorption*, Nature Photonics **5**, 95–98 (2011).
- [173] M. Zhao, X. Wang, and D. D. Nolte, *Molecular interferometric imaging*, Optics Express **16**, 7102–7118 (2008).

- [174] P. Kukura, M. Celebrano, A. Renn, and V. Sandoghdar, *Imaging a Single Quantum Dot When It Is Dark*, Nano Lett. **9**, 926–929 (2009).
- [175] O. Muskens, N. D. Fatti, F. Valle, J. Huntzinger, P. Billaud, and M. Broyer, *Single metal nanoparticle absorption spectroscopy and optical characterization*, Appl. Phys. Lett. **88**, 063109 (2006).
- [176] M. D. Brabander, R. Nuydens, G. Geuens, M. Moeremans, and J. D. Mey, *The Use of Submicroscopic Gold Particles Combined With Video Contrast Enhancement as a Simple Molecular Probe for the Living Cell*, Cell Motil. Cytoskeleton **6**, 105–113 (1986).
- [177] V. Jacobsen, P. Stoller, C. Brunner, V. Vogel, and V. Sandoghdar, *Interferometric optical detection and tracking of very small gold nanoparticles at a water-glass interface*, Optics Express **14**, 405–414 (2006).
- [178] D. Boyer, P. Tamarat, A. Maali, B. Lounis, and M. Orrit, *Photothermal imaging of nanometer-sized metal particles among scatterers*, Science **297**, 1160–1163 (2002).
- [179] A. Gaiduk, M. Yorulmaz, P. V. Ruijgrok, and M. Orrit, *Room-Temperature Detection of a Single Molecule's Absorption by Photothermal Contrast*, Science **330**, 353–356 (2010).
- [180] T. Züchner, A. V. Failla, M. Steiner, and A. J. Meixner, *Probing dielectric interfaces on the nanoscale with elastic scattering patterns of single gold nanorods*, Optics Express **16**, 14 635–14 644 (2008).
- [181] J. Hwang and W. Moerner, *Interferometry of a single nanoparticle using the Gouy phase of a focused laser beam*, Optics Communications **280**, 487–491 (2007).
- [182] C. F. Bohren and D. R. Huffman, *Absorption and scattering of light by small particles* (John Wiley & Sons, Inc., New York, 1998).
- [183] H. van de Hulst, *Light Scattering by Small Particles* (Dover Publications, Inc New York, 1981).
- [184] B. Kitayanan, W. E. Alvarez, J. H. Harwell, and D. E. Resasco, *Controlled production of single-wall carbon nanotubes by catalytic decomposition of CO on bimetallic Co-Mo catalysts*, Chem. Phys. Lett. **317**, 497–503 (2000).
- [185] P. Nikolaev, M. J. Bronikowski, R. K. Bradley, F. Rohmund, D. T. Colbert, K. A. Smith, and R. E. Smalley, *Gas-phase catalytic growth of single-walled carbon nanotubes from carbon monoxide*, Chem. Phys. Lett. **313**, 91–97 (1999).
- [186] A. Kukovecz, C. Kramberger, V. Geogakilas, M. Prato, and H. Kuzmany, *A detailed Raman study on thin single-wall carbon nanotubes prepared by the HiPCO process*, Eur. Phys. J. B **38**, 223–230 (2002).

- [187] S. Bachilo, L. Balzano, J. Herrera, F. Pompeo, D. Resasco, and R. Weisman, *Narrow (n,m)-Distribution of Single-Walled Carbon Nanotubes Grown Using a Solid Supported Catalyst*, *J. Am. Chem. Soc.* **125**, 11186–11187 (2003).
- [188] V. Moore, M. Strano, E. Haroz, R. Hauge, and R. Smalley, *Individually suspended Single-Walled Carbon Nanotubes in various surfactants*, *Nano Lett.* **3**, 1379–1382 (2003).
- [189] M. F. Islam, E. Rojas, D. M. Bergey, A. T. Johnson, and A. G. Yodh, *High Weight Fraction Surfactant Solubilization of Single-Wall Carbon Nanotubes in Water*, *Nano Lett.* **3**, 269–273 (2003).
- [190] F. Chen, B. Wang, Y. Chen, and L.-J. Li, *Toward the Extraction of Single Species of Single-Walled Carbon Nanotubes Using Fluorene-Based Polymers*, *Nano Lett.* **7**, 3013–3017 (2007).
- [191] V. Zorbas, *Preparation and Characerization of Individual Peptide-Wrapped Single-Walled Carbon Nanotubes*, *J. Am. Chem. Soc.* **126**, 7222–7227 (2004).
- [192] M. Zheng, A. Jagota, E. Semke, B. Diner, R. Mclean, S. Lustig, R. Richardson, and N. Tassi, *DNA-assisted dispersion and separation of carbon nanotubes*, *Nature Materials* **2**, 338–342 (2003).
- [193] X. Tu, S. Manohar, A. Jagota, and M. Zheng, *DNA sequence motifs for structure-specific recognition and separation of carbon nanotubes*, *Nature* **460**, 250–253 (2009).
- [194] M. S. Arnold, A. A. Green, J. F. Hulvat, S. I. Stupp, and M. C. Hersam, *Sorting carbon nanotubes by electronic structure using density differentiation*, *Nature Nanotechnology* **1**, 60 (2006).
- [195] F. Hennrich, R. Krupke, K. Arnold, J. A. R. Stütz, S. Lebedkin, T. Koch, T. Schimmel, and M. M. Kappes, *The mechanism of cavitation-induced scission of single-walled carbon nanotubes*, *J. Phys. Chem. B* **111**, 1932–1937 (2007).
- [196] T. K. Leeuw, R. M. Reith, R. A. Simonette, M. E. Harden, P. Cherukuri, D. A. Tsybouski, K. M. Beckingham, and R. B. Weisman, *Single-Walled Carbon Nanotubes in the Intact Organism: Near-IR Imaging and Biocompatibility Studies in Drosophila*, *Nano Lett.* **7**, 2650–2654 (2007).
- [197] M. Arnold, S. Stupp, and M. Hersam, *Enrichment of Single-Walled Carbon Nanotubes by diameter in density gradients*, *Nano Lett.* **5**, 713–718 (2005).
- [198] H. Qian, P. T. Araujo, C. Georgi, T. Gokus, N. Hartmann, A. A. Green, A. Jorio, L. N. M. C. Hersam, and A. Hartschuh, *Visualizing the local optical response of semiconducting carbon nanotubes to DNA-wrapping*, *Nano Lett.* **8**, 2706–2711 (2008).

- [199] C. Georgi, A. A. Green, M. C. Hersam, and A. Hartschuh, *Probing Exciton Localization in Single-Walled Carbon Nanotubes Using High-Resolution Near-Field Microscopy*, ACS Nano **4**, 5914–5920 (2010).
- [200] R. B. Weisman and S. M. Bachilo, *Dependence of Optical Transition Energies on Structure for Single-Walled Carbon Nanotubes in Aqueous Suspension: An Empirical Kataura Plot*, Nano Lett. **3**, 1235–1238 (2003).
- [201] W. Becker, *The bh TCSPC Handbook* (Becker & Hickl GmbH, Berlin, 2006).
- [202] W. Becker, *Advanced Time-Correlated Single Photon Counting Techniques, Series in Chemical Physics*, Vol. 81 (Springer-Verlag,, 2005).
- [203] PicoQuant GmbH, *Fluofit User's Manual and Technical Data* (PicoQuant GmbH, Berlin, Version 4.4, 2009).
- [204] D. V. O'Connor and D. Phillips, *Time Correlated Single Photon Counting* (Academic Press, London, 1984).
- [205] R. Alfano and S. L. Shapiro, *Observation of Self-Phase Modulation and Small-Scale Filaments in Crystals and Glasses*, Phys. Rev. Lett. **24**, 592–594 (1970).
- [206] C. Lin and R. H. Stolen, *New nanosecond continuum for excited-state spectroscopy*, Appl. Phys. Lett. **28**, 216–218 (1976).
- [207] J. K. Ranka, R. S. Windeler, and A. J. Stentz, *Visible continuum generation in air-silica microstructure optical fibers with anomalous dispersion at 800 nm*, Optics Letters **25**, 25–27 (2000).
- [208] Newport Corporation, *Application Note 28: Supercontinuum Generation in SCG-800 Photonic Crystal Fiber* (Newport Corporation, 2006).
- [209] F. Wang, G. Dukovic, L. E. Brus, and T. F. Heinz, *Time-resolved fluorescence of Carbon Nanotubes and its implication for radiative lifetime*, Phys. Rev. Lett. **92**, 177 401–177 404 (2004).
- [210] A. Hagen, G. Moos, V. Talalaev, and T. Hertel, *Electronic structure and dynamics of optically excited single-wall carbon nanotubes*, Appl. Phys. A **78**, 1137–1145 (2004).
- [211] L. J. Carlson, S. E. Maccagnano, J. S. M. Zheng, and T. D. Krauss, *Fluorescence Efficiency of Individual Carbon Nanotubes*, Nano Lett. **12**, 3698–3058 (2007).
- [212] J. Crochet, M. Clemens, and T. Hertel, *Quantum yield heterogeneities of aqueous single-wall carbon nanotube suspensions*, J. Am. Chem. Soc. **129**, 8058–8059 (2007).

- [213] Y.-Z. Ma, J. Stenger, J. Zimmermann, S. M. Bachilo, R. E. Smalley, R. B. Weisman, and G. R. Fleming, *Ultrafast carrier dynamics in single-walled carbon nanotubes probed by femtosecond spectroscopy*, *J. Chem. Phys.* **120**, 3368–3373 (2004).
- [214] G. N. Ostojic, S. Zaric, J. Kono, M. S. Strano, V. C. Moore, R. H. Hauge, and R. E. Smalley, *Interband Recombination Dynamics in Resonantly Excited Single-Walled Carbon Nanotubes*, *Phys. Rev. Lett.* **92**, 117 402 (2004).
- [215] L. Huang, H. N. Pedrosa, and T. D. Krauss, *Ultrafast Ground-State Recovery of Single-Walled Carbon Nanotubes*, *Phys. Rev. Lett.* **93**, 017 403 (2004).
- [216] S. Reich, M. Dworzak, A. Hoffmann, C. Thomsen, and M. Strano, *Excited-state carrier lifetime in single-walled carbon nanotubes*, *Phys. Rev. B* **71**, 033 402 (2005).
- [217] Z. Zhu, J. Crochet, M. S. Arnold, M. C. Hersam, H. Ulbricht, D. Resasco, and T. Hertel, *Pump-Probe Spectroscopy of Exciton Dynamics in (6,5) Carbon Nanotubes*, *J.Phys.Chem C* **111**, 3831–3835 (2006).
- [218] M. Jones, W. K. Metzger, T. J. McDonald, C. Engrakul, R. J. Ellingson, G. Rumbles, and M. J. Heben, *Extrinsic and Intrinsic Effects on the Excited-State Kinetics of Single-Walled Carbon Nanotubes*, *Nano Lett.* **7**, 300–306 (2007).
- [219] H. Hirori, K. Matsuda, Y. Miyauchi, S. Maruyama, and Y. Kanemitsu, *Exciton Localization of Single-Walled Carbon Nanotubes Revealed by Femtosecond Excitation Correlation Spectroscopy*, *Phys. Rev. Lett.* **97**, 257 401 (2006).
- [220] R. Matsunaga, Y. Miyauchi, K. Matsuda, and Y. Kanemitsu, *Symmetry-induced nonequilibrium distributions of bright and dark exciton states in single carbon Nanotubes*, *Phys. Rev. B* **80**, 115 436 (2009).
- [221] G. D. Scholes, S. Tretiak, T. J. McDonald, W. K. Metzger, C. Engrakul, G. Grumbles, and M. J. Heben, *Low-Lying Exciton States Determine the Photophysics of Semiconducting Single Wall Carbon Nanotubes*, *J. Phys. Chem. C* **111**, 11139 (2007).
- [222] L. Lüer, J. Crochet, T. Hertel, G. Cerullo, and G. Lanzani, *Ultrafast Excitation Energy Transfer in Small Semiconducting Carbon Nanotube Aggregates*, *ACS Nano* **4**, 4265–4273 (2010).
- [223] A. Hagen, M. Steiner, M. B. Raschke, C. Lienau, T. Hertel, H. Qian, A. J. Meixner, and A. Hartschuh, *Exponential Decay Lifetimes of Excitons in Individual Single-Walled Carbon Nanotubes*, *Phys. Rev. Lett.* **95**, 197 401 (2005).
- [224] S. Berger, C. Voisin, G. Cassabois, C. Delalande, P. Roussignol, and X. Marie, *Temperature Dependence of Exciton Recombination in Semiconducting Single-Wall Carbon Nanotubes*, *Nano Lett.* **7**, 398–402 (2007).

- [225] T. Hertel, A. Hagen, V. Talalaev, K. Arnold, F. Hennrich, M. Kappes, S. Rosenthal, J. McBride, H. Ulbricht, and E. Flahaut, *Spectroscopy of Single- and Double-Wall Carbon Nanotubes in Different Environments*, Nano Lett. **5**, 511–514 (2005).
- [226] T. Pedersen and K. Pedersen, *Stability and Signatures of Biexcitons in Carbon Nanotubes*, Nano Lett. **5**, 291–294 (2005).
- [227] F. Wang, G. Dukovic, E. Knoesel, L. E. Brus, and T. F. Heinz, *Observation of rapid Auger recombination in optically excited semiconducting carbon nanotubes*, Phys. Rev. B **70**, 241 403 (2004).
- [228] L. Valkunas, Y.-Z. Ma, and G. R. Fleming, *Exciton-exciton annihilation in single-walled carbon nanotubes*, Phys. Rev. B **73**, 115 432 (2006).
- [229] Y. Z. Ma, L. Valkunas, S. L. Dexheimer, S. M. Bachilo, and G. R. Fleming, *Femto-second spectroscopy of optical excitations in single-walled carbon nanotubes: Evidence for exciton-exciton annihilation*, Phys. Rev. Lett. **94**, 157 402 (2005).
- [230] H. Htoon, M. H. O. Connel, P. Cox, S. Doorn, and V. Klimov, *Low temperature emission spectra of individual single-walled carbon nanotubes: Multiplicity of subspecies within single-species nanotube ensembles*, Phys. Rev. Lett. **93**, 027 401 (2004).
- [231] M. Steiner, M. Freitag, J. C. Tsang, V. Perebeinos, A. A. Bol, A. V. Failla, and P. Avouris, *How does the substrate affect the Raman and excited state spectra of a carbon nanotube ?*, Appl. Phys. A **96**, 271–282 (2009).
- [232] S. Berger, F. Iglesias, P. Bonnet, C. Voisin, G. Cassabois, J.-S. Lauret, C. Delalande, and P. Roussignol, *Optical properties of carbon nanotubes in a composite material: The role of dielectric screening and thermal expansion*, J. Appl. Phys. **105**, 094 323 (2009).
- [233] Y.-Z. Ma, M. W. Graham, G. R. Fleming, A. A. Green, and M. C. Hersam, *Ultrafast Exciton Dephasing in Semiconducting Single-Walled Carbon Nanotubes*, Phys. Rev. Lett. **101**, 217 402 (2008).
- [234] T. Inoue, K. Matsuda, Y. Murakami, S. Maruyama, and Y. Kanemitsu, *Diameter dependence of exciton-phonon interaction in individual single-walled carbon nanotubes studied by microphotoluminescence spectroscopy*, Phys. Rev. B **73**, 233 401 (2006).
- [235] K. Yoshikawa, R. Matsunaga, K. Matsuda, and Y. Kanemitsu, *Mechanism of exciton dephasing in a single carbon nanotube studied by photoluminescence spectroscopy*, Appl. Phys. Lett. **94**, 093 109 (2009).
- [236] B. F. Habenicht, H. Kamisaka, K. Yamashita, and O. V. Prezhdo, *Ab Initio Study of Vibrational Dephasing of Electronic Excitations in Semiconducting Carbon Nanotubes*, Nano Lett. **7**, 3260–3265 (2007).

- [237] A. D. Vita, J. C. Charlier, X. Blase, and R. Car, *Electronic structure at carbon nanotube tips*, Appl. Phys. A **68**, 283–286 (1999).
- [238] D. L. Carroll, P. Redlich, P. M. Ajayan, J. C. Charlier, X. Blase, A. D. Vita, and R. Car, *Electronic Structure and Localized States at Carbon Nanotube Tips*, Phys. Rev. Lett. **78**, 2811–2814 (1997).
- [239] L. C. Venema, J. Janssen, M. R. Buitelaar, J. Wildöer, S. G. Lemay, L. P. Kouwenhoven, and C. Dekker, *Spatially resolved scanning tunneling spectroscopy on single-walled carbon nanotubes*, Phys. Rev. B **62**, 5238–5244 (2000).
- [240] A. Rajan, M. S. Strano, D. A. Heller, T. Hertel, and K. Schulten, *Length-Dependent Optical Effects in Single Walled Carbon Nanotubes*, J. Phys. Chem. B **112**, 6211–6213 (2008).
- [241] H. Qian, C. Georgi, N. Anderson, A. A. Green, M. C. Hersam, L. Novotny, and A. Hartschuh, *Exciton transfer and propagation in carbon nanotubes studied by near-field optical microscopy*, phys. stat. sol. (b) **245**, 2243–2246 (2008).
- [242] D. A. Heller, R. M. Mayrhofer, S. Baik, Y. V. Grinkova, M. L. Usrey, and M. S. Strano, *Concomitant Length and Diameter Separation of Single-Walled Carbon Nanotubes*, J. Am. Chem. Soc. **126**, 14 567–14 573 (2004).
- [243] J. G. Duque, M. Pasquali, L. Cognet, and B. Lounis, *Environmental and Synthesis-Dependent Luminescence Properties of Individual Single-Walled Carbon Nanotubes*, ACS Nano **3**, 2135–2156 (2009).
- [244] Y. Miyauchi, K. Matsuda, Y. Yamamoto, N. Nakashima, and Y. Kanemitsu, *Length-Dependent Photoluminescence Lifetimes in Single-Walled Carbon Nanotubes*, J. Phys. Chem. C **114**, 12 905 (2010).
- [245] C. Georgi, *Exciton Mobility and Localized Defects in Single Carbon Nanotubes Studied with Tip-Enhanced Near-Field Optical Microscopy*, Ph.D. thesis, LMU München (2010).
- [246] T. Hertel, S. Himmelein, T. Ackermann, D. Stich, and J. Crochet, *Diffusion Limited Photoluminescence Quantum Yields in 1-D Semiconductors: Single-Wall Carbon Nanotubes*, ACS Nano **4**, 7161–7168 (2010).
- [247] A. Hgele, C. Galland, M. Winger, and A. Imamoglu, *Photon Antibunching in the Photoluminescence Spectra of a Single Carbon Nanotube*, Phys. Rev. Lett. **101**, 217 401 (2008).
- [248] T. Gokus, L. Cognet, J. Duque, M. Pasquali, A. Hartschuh, and B. Lounis, *Mono- and Bi-exponential Luminescence Decays of Individual Single-Walled Carbon Nanotubes*, J. Phys. Chem. C **114**, 14 025–14 028 (2010).

- [249] C. Manzoni, A. Gambetta, E. Menna, M. Meneghetti, G. Lanzani, and G. Cerullo, *Intersubband Exciton Relaxation Dynamics in Single-Walled Carbon Nanotubes*, Phys. Rev. Lett. **94**, 207 401 (2005).
- [250] D. A. Tsyboulski, J. D. R. Rocha, S. M. Bachilo, L. Cognet, and R. B. Weisman, *Structure-dependent fluorescence efficiencies of individual single-walled carbon nanotubes*, Nano Lett. **7**, 3080–3085 (2007).
- [251] S. Kilina, E. Badaeva, A. Piryatinski, S. Tretiak, A. Saxena, and A. R. Bishop, *Bright and dark excitons in semiconductor carbon nanotubes: Insights from electronic structure calculations*, Phys. Chem. Chem. Phys. **11**, 4097–4420 (2009).
- [252] A. Srivastava, H. Htoon, V. Klimov, and J. Kono, *Direct Observation of Dark Excitons in Individual Carbon Nanotubes: Inhomogeneity in the Exchange Splitting*, Phys. Rev. Lett. **101**, 087 402 (2008).
- [253] E. Chang, D. Prezzi, A. Ruini, and E. Molinari, *Dark Excitons in Carbon Nanotubes*, arXiv:cond-mat/0603085v1 (2006).
- [254] P. Lehtinen, A. V. Krasheninnikov, A. Foster, and R. Nieminen, *Carbon Based Magnetism* (Elsevier, Amsterdam, 2006).
- [255] P. Lehtinen, A. S. Foster, A. Ayuela, A. Krasheninnikov, K. Nordlund, and R. Nieminen, *Magnetic Properties and Diffusion of Adatoms on a Graphene Sheet*, Phys. Rev. Lett. **91**, 017 202 (2003).
- [256] J. Davies, *The Kinetics of the Coagulation of Gold Sols. An Investigation of the Thermo-Senescence Effect exhibited at Elevated Temperatures*, J. Phys. Chem. **33**, 276 (1929).
- [257] L. S. Yanjie Gan and F. Banhart, *One- and Two-Dimensional Diffusion of Metal Atoms in Graphene*, Small **4**, 587–591 (2008).
- [258] A. J. Siitonens, D. A. Tsyboulski, S. M. Bachilo, and R. B. Weisman, *Surfactant-Dependent Exciton Mobility in Single-Walled Carbon Nanotubes Studied by Single-Molecule Reactions*, Nano Lett. **10**, 1595–1599 (2010).
- [259] A. Krasheninnikov, A. S. Foster, and R. M. Nieminen, *Defect-mediated engeneering of the electron structure of carbon nanosystems*, NT08 Conference Book, Book of Abstracts (2008).
- [260] R. B. Capaz, C. D. Spataru, S. Ismail-Beigi, and S. G. Louie, *Excitons in carbon nanotubes: Diameter and chirality trends*, phys. stat. sol. (b) **244**, 4016–4020 (2007).
- [261] A. H. C. Neto and F. Guinea, *Impurity-Induced Spin-Orbit Coupling in Graphene*, Phys. Rev. Lett. **103**, 026 804 (2009).

- [262] A. D. Mohite, T. S. Santos, J. S. Moodera, and B. W. Alphenaar, *Observation of the triplet exciton in EuS-coated single-walled nanotubes*, Nature Nanotechnology **4**, 425–429 (2009).
- [263] S. Schultz, D. R. Smith, J. J. Mock, and D. A. Schultz, *Single-target molecule detection with nonbleaching multicolor optical immunolabels*, PNAS **97**, 996–1001 (2000).
- [264] C. Sönnichsen, S. Geier, N. E. Hecker, G. von Plessen, J. Feldmann, H. Ditlbacher, B. Lamprecht, J. R. Krenn, F. R. Aussenegg, V. Z.-H. Chan, J. P. Spatz, and M. Mller, *Spectroscopy of single metallic nanoparticles using total internal reflection microscopy*, Appl. Phys. Lett. **77**, 2949–2951 (2000).
- [265] T. Klar, M. Perner, S. Grosse, G. von Plessen, W. Spirk, and J. Feldmann, *Surface-Plasmon Resonances in Single Metallic Nanoparticles*, Phys. Rev. Lett. **80**, 4249–4252 (1998).
- [266] H. F. Hamann, A. Gallagher, and D. J. Nesbitt, *Enhanced sensitivity near-field scanning optical microscopy at high spatial resolution*, Appl. Phys. Lett. **73**, 1469–1471 (1998).
- [267] M. Sfeir, F. Wang, L. Huang, C.-C. Chuang, J. Hone, S. P. O'Brien, T. F. Heinz, and L. E. Brus, *Probing Electronic Transitions in Individual Carbon Nanotubes by Rayleigh Scattering*, Science **306**, 1540–1543 (2004).
- [268] F. Wang, M. Sfeir, L. Huang, X. H. Huang, Y. Wu, J. Kim, J. Hone, S. O'Brien, L. E. Brus, and T. F. Heinz, *Interactions between Individual Carbon Nanotubes Studied by Rayleigh Scattering Spectroscopy*, Phys. Rev. Lett. **96**, 167 401 (2006).
- [269] R. R. Nair, P. Blake, A. N. Grigorenko, K. S. Novoselov, T. J. Booth, T. Stauber, N. M. R. Peres, and A. K. Geim, *Fine structure constant defines visual transparency of graphene*, Science **320**, 1308 (2008).
- [270] S. Berciaud, C. Voisin, H. Yan, B. Chandra, R. Caldwell, Y. Shan, L. E. Brus, J. Hone, and T. F. Heinz, *Excitons and high-order optical transitions in individual carbon nanotubes: A Rayleigh scattering spectroscopy study*, Phys. Rev. B **81**, 041414(R) (2010).
- [271] H. Zeng, L. Jiao, X. Xian, X. Qin, Z. Liu, and X. Cui, *Reflectance spectra of individual single-walled carbon nanotubes*, Nanotechnology **19**, 045 708 (2008).
- [272] D. Y. Joh, L. H. Herman, S.-Y. Ju, J. Kinder, M. A. Segal, J. N. Johnson, G. K. L. Chan, and J. Park, *On-Chip Rayleigh Imaging and Spectroscopy of Carbon Nanotubes*, Nano Lett. **11**, 1–7 (2011).
- [273] V. Jacobsen, P. Stoller, C. Brunner, V. Vogel, and V. Sandoghdar, *Interferometric optical detection and tracking of very small gold nanoparticles at a water-glass interface*, Opt. Express **14**, 405–414 (2006).

- [274] B. Deutsch, R. Beams, and L. Novotny, *Nanoparticle detection using dual-phase interferometry*, Appl. Optics **49**, 4922–4925 (2010).
- [275] P. K. Jain, K. S. Lee, I. H. El-Sayed, and M. A. El-Sayed, *Calculated Absorption and Scattering Properties of Gold Nanoparticles of Different Size, Shape, and Composition: Applications in Biological Imaging and Biomedicine*, J. Phys. Chem. B **110**, 7238–7248 (2006).
- [276] G. Mie, *Beiträge zur Optik trüber Medien speziell kolloidaler Metallösungen*, Ann. Phys. **25**, 377–445 (1908).
- [277] P. G. Etchegoin, E. C. L. Ru, and M. Meyer, *An analytic model for the optical properties of gold*, J. Chem. Phys. **125**, 164 705 (2006).
- [278] P. B. Johnson and R. W. Christy, *Optical constants of the noble metals*, Phys. Rev. B **6**, 4370–4379 (1972).
- [279] K. F. Mak, M. Y. Sfeir, Y. Wu, C. H. Lui, J. A. Misewich, and T. F. Heinz, *Measurement of the Optical Conductivity of Graphene*, Phys. Rev. Lett. **101**, 196 405 (2008).
- [280] E. Malic, M. Hirtschulz, F. Milde, A. Knorr, and S. Reich, *Analytical approach to optical absorption in carbon nanotubes*, Phys. Rev. B **74**, 195 431 (2006).
- [281] E. Malic, J. Maultzsch, S. Reich, and A. Knorr, *Excitonic absorption spectra of metallic single-walled carbon nanotubes*, Phys. Ref. B **82**, 035 433 (2010).
- [282] E. Malic, M. Hirtschulz, F. Milde, Y. Wu, J. Maultzsch, T. Heinz, A. Knorr, and S. Reich, *Theory of Rayleigh scattering from metallic carbon nanotubes*, Phys. Rev. B **77**, 045 432 (2008).
- [283] E. Malic, J. Maultzsch, S. Reich, and A. Knorr, *Excitonic Rayleigh scattering spectra of metallic single-walled carbon nanotubes*, Phys. Rev. B **82**, 115 439 (2010).
- [284] M. J. O’Connell, E. E. Eibergen, and S. K. Doorn, *Chiral selectivity in the charge-transfer bleaching of single-walled carbon-nanotube spectra*, Nature Materials **4**, 413–418 (2005).
- [285] D. A. Tsypbalski, S. M. Bachilo, and R. B. Weisman, *Versatile Visualization of Individual Single-Walled Carbon Nanotubes with Near-Infrared Fluorescence Microscopy*, Nano Lett. **5**, 975–979 (2005).
- [286] C. Fantini, A.Jorio, M.Souza, M.S.Strano, M.S.Dresselhaus, and M.A.Pimenta, *Optical Transition Energies for Carbon Nanotubes from Resonant Raman Spectroscopy: Environment and Temperature Effects*, Phys. Rev. Lett. **93**, 147 406 (2004).
- [287] A. G. Walsh, A. N. Vamivakas, Y. Yin, S. B. Cronin, M. S. Ünlü, B. B. Goldberg, and A. K. Swan, *Screening of Excitons in Single, Suspended Carbon Nanotubes*, Nano Lett. **7**, 1485–1488 (2007).

- [288] T. Okazaki, T. Saito, K. Matsuura, S. Ohshima, M. Yumura, and S. Iijima, *Photoluminescence Mapping of "As-Grown" Single-Walled Carbon Nanotubes: A Comparison with Micelle-Encapsulated Nanotube Solutions*, Nano Lett. **5**, 2618–2623 (2005).
- [289] Y. Ohno, S. Iwasaki, Y. Murakami, S. Kishimoto, S. Maruyama, and T. Mizutani, *Chirality-dependent environmental effects in photoluminescence of single-walled carbon nanotubes*, Phys. Rev. B. **73**, 235427 (2006).
- [290] J. H. Choi and M. S. Strano, *Solvatochromism in single-walled carbon nanotubes*, Appl. Phys. Lett. **90**, 223114 (2007).
- [291] C. Sönnichsen, *Plasmons in metal nanostructures*, Ph.D. thesis, LMU München (2001).
- [292] K. S. Novoselov, A. K. Geim, S. V. Morozov, D. Jiang, M. I. Katsnelson, I. V. Grigorieva, S. V. Dubonos, and A. A. Firsov, *Two-dimensional gas of massless Dirac fermions in graphene*, Nature **438**, 197–200 (2005).
- [293] X. Wang, L. Zhi, and K. Müllen, *Transparent, Conductive Graphene Electrodes for Dye-Sensitized Solar Cells*, Nano Lett. **8**, 323–327 (2008).
- [294] T. Hasan, Z. Sun, F. Wang, F. Bonaccorso, P. H. Tan, A. G. Rozhin, and A. C. Ferrari, *Nanotube-Polymer Composites for Ultrafast Photonics*, Advanced Materials **21**, 3874–3899 (2009).
- [295] Z. Sun, T. Hasan, F. Torrisi, D. Popa, G. Privitera, F. Wang, F. Bonaccorso, D. M. Basko, and A. C. Ferrari, *Graphene Mode-Locked Ultrafast Laser*, ACS Nano **4**, 803–810 (2010).
- [296] K. Nakada, M. Fujita, G. Dresselhaus, and M. Dresselhaus, *Edge state in graphene ribbons: Nanometer size effect and edge shape dependence*, Phys. Rev. B **54**, 17954–17961 (1996).
- [297] X. Li, X. Wang, L. Zhang, S. Lee, and H. Dai, *Chemically Derived Ultrasmooth Graphene Nanoribbon Semiconductors*, Science **319**, 1229–1232 (2008).
- [298] M. Y. Han, B. Özyilmaz, Y. Zhang, and P. Kim, *Energy Band-Gap Engineering of Graphene Nanoribbons*, Phys. Rev. Lett. **98**, 206805 (2007).
- [299] Z. Chen, Y. Lin, M. Rooks, and P. Avouris, *Graphene nano-ribbon electronics*, Physica E **40**, 228–232 (2007).
- [300] C. Stampfer, J. Göttinger, F. Molitor, D. Graf, T. Ihn, and K. Ensslin, *Tunable Coulomb blockade in nanostructured graphene*, Appl. Phys. Lett. **92**, 012102–3 (2008).
- [301] L. A. Ponomarenko, F. Schedin, M. I. Katsnelson, R. Yang, E. W. Hill, K. S. Novoselov, and A. K. Geim, *Chaotic Dirac Billiard in Graphene Quantum Dots*, Science **320**, 356–358 (2008).

- [302] L. Ci, Z. Xu, L. Wang, W. Gao, F. Ding, K. F. Kelly, B. I. Yakobson, and P. M. Ajayan, *Controlled Nanocutting of Graphene*, Nano Res. **1**, 116–122 (2008).
- [303] X. Wang and H. Dai, *Etching and narrowing of graphene from the edges*, Nature Chemistry **2**, 661–665 (2010).
- [304] D. V. Kosynkin, A. L. Higginbotham, A. Sinitskii, J. R. Lomeda, A. Dimiev, B. K. Price, and J. M. Tour, *Longitudinal unzipping of carbon nanotubes to form graphene nanoribbons*, Nature **458**, 872–877 (2009).
- [305] L. Jiao, L. Zhang, X. Wang, G. Diankov, and H. Dai, *Narrow graphene nanoribbons from carbon nanotubes*, Nature **458**, 877–880 (2009).
- [306] J. Cai, P. Ruffieux, R. Jaafar, M. Bieri, T. Braun, S. Blankenburg, M. Muoth, A. P. Seitsonen, M. Saleh, X. Feng, K. Müllen, and R. Fasel, *Atomically precise bottom-up fabrication of graphene nanoribbons*, Nature **466**, 470–473 (2010).
- [307] D. C. Elias, R. R. Nair, T. M. G. Mohiuddin, S. V. Morozov, P. Blake, M. P. Halsall, A. C. Ferrari, D. W. Boukhvalov, M. I. Katsnelson, A. K. Geim, and K. S. Novoselov, *Control of graphene's properties by reversible hydrogenation: Evidence for graphane*, Science **323**, 610–613 (2009).
- [308] S. Park and R. Rouff, *Chemical methods for the production of graphenes*, Nature Nanotechnology **4**, 217–224 (2009).
- [309] S. Y. Zhou, Ç. Ö. Girit, A. Scholl, C. J. Jozwiak, D. A. Siegel, P. Yu, J. T. Robinson, F. Wang, A. Zettl, and A. Lanzara, *Instability of two-dimensional graphene: Breaking sp^2 bonds with soft x rays*, Phys. Rev. B **80**, 121 409(R) (2009).
- [310] L. Liu, S. Ryu, M. R. Tomaszik, E. Stolyarova, N. Jung, M. S. Hybertsen, M. L. Steigerwald, L. E. Brus, and G. W. Flynn, *Graphene oxidation: Thickness-dependent etching and strong chemical doping*, Nano Lett. **8**, 1965–1970 (2008).
- [311] C. Casiraghi, A. Hartschuh, E. Lidorikis, H. Qian, H. Harutyunyan, T. Gokus, K. S. Novoselov, and A. C. Ferrari, *Rayleigh Imaging of Graphene and Graphene Layers*, Nano Lett. **7**, 2711–2712 (2007).
- [312] T. Gokus, A. Hartschuh, H. Harutyunyan, M. Allegrini, F. Hennrich, M. Kappes, A. A. Green, M. C. Hersam, P. T. Arajo, and A. Jorio, *Exciton decay dynamics in individual carbon nanotubes at room temperature*, Appl. Phys. Lett. **92**, 153 116–153 113 (2008).
- [313] M. H. W. Lormes and L. Ley, *Time resolved photoluminescence of amorphous hydrogenated carbon*, J. Non-Cryst. Solids **570**, 227–230 (1998).
- [314] C. Casiraghi, S. Pisana, K. Novoselov, A. Geim, and A. Ferrari, *Fingerprint of charged impurities in graphene*, Appl. Phys. Lett. **91**, 233 108 (2007).

- [315] A. Das, S. Pisana, B. Chakraborty, S. Piscanec, S. Saha, U. Waghmare, K. Novoselov, H. Krishnamurthy, A. Geim, A. Ferrari, and A. Sood, *Monitoring dopants by Raman scattering in an electrochemically top-gated graphene transistor*, Nature Nanotechnology **3**, 210–215 (2008).
- [316] S. Pisana, M. Lazzeri, C. Casiraghi, K. Novoelov, A. K. Geim, A. Ferrari, and F. Mauri, *Breakdown of the Adiabatic Born-Oppenheimer Approximation in Graphene*, Nature Materials **6**, 198–201 (2007).
- [317] T. M. G. Mohiuddin, A. Lombardo, R. R. Nair, A. Bonetti, G. Savini, R. Jalil, N. Bonini, D. M. Basko, C. Gallois, N. Marzari, K. S. Novoselov, A. K. Geim, and A. C. Ferrari, *Uniaxial strain in graphene by Raman spectroscopy: G peak splitting, Grneisen parameters, and sample orientation*, Phys. Rev. B **79**, 205 433 (2009).
- [318] A. Ferrari, S. E. Rodil, and J. Robertson, *Interpretation of infrared and Raman spectra of amorphous carbon nitrides*, Phys. Rev. B. **67**, 155 306 (2003).
- [319] C. Casiraghi, A. Ferrari, and J. Robertson, *Raman spectroscopy of hydrogenated amorphous carbons*, Phys. Rev. B **72**, 085 401 (2005).
- [320] S. Roddaro, P. Pingue, V. Piazza, V. Pellegrini, and F. Beltram, *The Optical Visibility of Graphene: Interference Colors of Ultrathin Graphite on SiO₂*, Nano Lett. pp. 2707–2710 (2007).
- [321] P. Blake, E. W. Hill, A. H. C. Neto, K. S. Novoselov, D. Jiang, R. Yang, T. J. Booth, and A. K. Geim, *Making graphene visible*, Appl. Phys. Lett. **91**, 063 124 (2007).
- [322] A. B. Djurišić and E. H. Li, *Optical properties of graphite*, J. Appl. Phys. **85**, 7404–7410 (1999).
- [323] I. Jung, M. Vaupel, M. Pelton, R. Piner, D. A. Dikin, S. Stankovich, J. An, and R. S. Ruoff, *Characterization of Thermally Reduced Graphene Oxide by Imaging Ellipsometry*, J. Phys. Chem. C **112**, 8499–8506 (2008).
- [324] H.-X. You, N. Brown, and K. F. Al-Assadi, *Radio-Frequency (RF) Plasma Etching of Graphite with Oxygen: A Scanning Tunnelling Microscope Study*, Surf. Sci. **284**, 263–272 (1993).
- [325] L. Xie, X. Ling, Y. Fang, J. Zhang, and Z. Liu, *Graphene as a Substrate To Suppress Fluorescence in Resonance Raman Spectroscopy*, J. Am. Chem. Soc. **131**, 9890–9891 (2009).
- [326] J. M. Dawlaty, S. Shivaraman, M. Chandrashekhar, F. Rana, and M. G. Spencer, *Measurement of ultrafast carrier dynamics in epitaxial graphene*, Appl. Phys. Lett. **92**, 042 116 (2008).

- [327] C. Lui, K. Mak, J. Shan, and T. Heinz, *Ultrafast Photoluminescence from Graphene*, Phys. Rev. Lett. **105**, 127 404 (2010).
- [328] R. J. Stöhr, R. Kolesov, J. Pflaum, and J. Wrachtrup, *Fluorescence of laser created electron-hole plasma in graphene*, Phys. Rev. B **82**, 121 408(R) (2010).
- [329] W.-T. Liu, S. W. Wu, P. J. Schuck, M. Salmeron, Y. R. Shen, and F. Wang, *Nonlinear broadband photoluminescence of graphene induced by femtosecond laser irradiation*, Phys. Rev. B **82**, 081 408(R) (2010).
- [330] M. Freitag, H.-Y. Chiu, M. Steiner, V. Perebeinos, and P. Avouris, *Thermal infrared emission from biased graphene*, Nature Nanotechnology **5**, 497–501 (2010).
- [331] D. Yu and L. Dai, *Voltage-induced incandescent light emission from large-area graphene films*, Appl. Phys. Lett. **96**, 143 107 (2010).
- [332] P. Sols-Fernandez, J. Paredes, A. Coso, A. Martnez-Alonso, and J. Tascn, *A comparison between physically and chemically driven etching in the oxidation of graphite surfaces*, Journal of Colloid and Interface Science **344**, 451–459 (2010).
- [333] Z. Luo, P. M. Vora, E. J. Mele, A. T. C. Johnson, and J. M. Kikkawa, *Photoluminescence and band gap modulation in graphene oxide*, Appl. Phys. Lett. **94**, 111 903 (2009).
- [334] X. Sun, Z. Liu, K. Welsher, J. T. Robinson, A. Goodwin, S. Zaric, and H. Dai, *Nano-graphene oxide for cellular imaging and drug delivery*, Nano. Res. **1**, 203–212 (2008).
- [335] G. Eda, Y.-Y. Lin, C. Mattevi, H. Yamaguchi, H.-A. Chen, I.-S. Chen, C.-W. Chen, and M. Chhowalla, *Blue photoluminescence from chemically derived graphene oxide*, Advanced Materials **22**, 505–509 (2009).
- [336] J. Lu, J. Yang, J. Wang, A. Lim, S. Wang, and K. P. Loh, *One-Pot Synthesis of Fluorescent Carbon Nanoribbons, Nanoparticles, and Graphene by the Exfoliation of Graphite in Ionic Liquids*, ACS Nano **8**, 2367–2375 (2009).
- [337] T. V. Cuong, V. H. Pham, Q. T. Tran, S. H. Hahn, J. S. Chung, E. W. Shin, and E. J. Kim, *Photoluminescence and Raman studies of graphene thin films prepared by reduction of graphene oxide*, Materials Letters **64**, 399–401 (2010).
- [338] W. S. Hummers and R. E. Offeman, *Preparation of Graphitic Oxide*, J. Am. Chem. Soc. **80**, 1339 (1958).
- [339] A. K. Geim and K. S. Novoselov, *The rise of graphene*, Nature Materials **6**, 183–191 (2007).
- [340] S. C. J. Meskers, J. Hübner, M. Oestreich, and H. Bässler, *Dispersive Relaxation Dynamics of Photoexcitations in a Polyfluorene Film Involving Energy Transfer: Experiment and Monte Carlo Simulations*, J. Phys. Chem. B **105**, 9139–9149 (2001).

- [341] D. S. L. Abergel, A. Russell, and V. I. Fal'ko, *Visibility of graphene flakes on a dielectric substrate*, Appl. Phys. Lett. **91**, 063125 (2007).
- [342] Z. H. Ni, H. M. Wang, J. Kasim, H. M. Fan, T. Yu, Y. H. Wu, Y. P. Feng, and Z. X. Shen, *Graphene Thickness Determination Using Reflection and Contrast Spectroscopy*, Nano Lett. **7**, 2758–2763 (2007).
- [343] M. Born and E. Wolf, *Principles of Optics 7th (expanded) edition* (Cambridge University Press, Cambridge, 1999).
- [344] P. E. Ciddor, *Refraction into an absorbing medium*, Am. J. Phys. **44**, 786–787 (1976).
- [345] E. D. Palik, *Handbook of Optical Constants of Solids* (Academic Press, New York, 1991).

List of Abbreviations

0D	...	zero-dimensional
1D	...	one-dimensional
2D	...	two-dimensional
3D	...	three-dimensional
DOS	...	density of states
AFM	...	atomic force microscopy
APD	...	avalanche photodiode
BPF	...	band pass filter
BZ	...	Brillouin zone
CCD	...	charged coupled device
CFD	...	constant fraction discriminator
CLSM	...	confocal laser scanning microscopy
CVD	...	chemical vapor deposition
CW	...	continuous wave
DIC	...	differential interference contrast microscopy
DOC	...	sodium deoxycholate
EMA	...	effective mass approximation
FRET	...	Förster resonance energy transfer
GNP	...	gold nanoparticle
HiPco	...	high-pressure catalytic decomposition of carbon monoxide
HOPG	...	highly oriented pyrolytic graphite
IRF	...	instrument response function
iSCAT	...	interference scattering microscopy/spectroscopy
JDOS	...	joint density of states
LA	...	longitudinal acoustic
LED	...	light emitting diode
LO	...	longitudinal optical
LPF	...	long pass filter
MLG	...	multi-layer graphene
MPD	...	multi-phonon decay
MWCNT	...	multi-walled carbon nanotubes
NA	...	numerical aperture
NIM	...	nuclear instrument module
NIR	...	near infrared
NSOM	...	near-field scanning optical microscopy
PAIEI	...	phonon-assisted indirect exciton ionization

PLE	...	photoluminescence excitation spectroscopy
PLG	...	photoluminescent graphene
PMMA	...	poly(methyl methacrylate)
PSF	...	point-spread function
RBM	...	radial breathing mode
RF	...	radio frequency microwave
RRS	...	resonant Raman scattering
SC	...	sodium cholate
SDS	...	sodiumdodecylsulfate
SLG	...	single-layer graphene
SNR	...	signal to noise ratio
STED	...	stimulated emission depletion
STM	...	scanning tunneling microscopy
SWCNT	...	single-walled carbon nanotubes
TA	...	transverse acoustic
TAC	...	time to amplitude converter
TCSPC	...	time correlated single photon counting
TK	...	Tuinstra-Koenig relation
TO	...	transverse optical
vHs	...	van Hove singularities
XRD	...	x-ray diffraction

List of Figures

1.1.	Unit cell and first Brillouin zone of graphene	6
1.2.	Construction of a SWCNT unit cell from graphene	7
1.3.	Overview about metallic and semiconducting SWCNTs	9
1.4.	Electronic energy dispersion relation of graphene	14
1.5.	Brillouin zone of metallic and semiconducting SWCNTs.	17
1.6.	Zone folding approach: Energy dispersion relation of SWCNTs	18
1.7.	One dimensional dispersion relation and DOS of SWCNTs.	19
1.8.	Zone folding approach: The cutting line concept	21
1.9.	Dependency of E_{ii} on the SWCNT diameter: Kataura plot	23
1.10.	Symmetry elements of SWCNTs	25
1.11.	Optical transitions in SWCNTs: Band edge transitions	28
1.12.	Excitonic states in chiral SWCNTs: Mixing of electron and hole states	32
1.13.	Classification of excitons based on their center-of-mass momentum	33
1.14.	Excitonic energy dispersion relation of a (6,5) SWCNT	34
1.15.	Influence of the Coulomb interaction on the one-particle energies	37
1.16.	Phonon-assisted non-radiative decay process	40
1.17.	Feynman diagram of a first-order Raman process	41
1.18.	Energy level diagrams of Raman scattering processes	42
1.19.	Phonon dispersion relation of graphene	44
1.20.	Classification of Raman processes in SWCNTs and graphene	45
1.21.	Raman phonon modes of SWCNTs and graphene	46
1.22.	Dependency of the Raman I_D/I_G ratio on the crystallite size L_a	49
2.1.	Schematic illustration of the confocal principle	53
2.2.	Definition of the numerical aperture of a focusing lens	54
2.3.	Excitation point-spread function of a confocal microscope	56
2.4.	Illustration of the optical resolution limit	57
2.5.	Gaussian laser beam and Gouy phase shift	59
2.6.	Schematic of the common-path iSCAT geometry	62
2.7.	iSCAT phase contribution: The Gouy phase ϕ_{total}	66
2.8.	iSCAT phase contributions: The oscillator phase ϕ_{total}	67
3.1.	Schematic diagram of the confocal microscope	73
3.2.	Quantum efficiency of the APD	75
3.3.	AFM image of micelle encapsulated SWCNTs on glass	77

3.4.	Confocal scan image and PL spectra of individual SWCNTs	81
3.5.	Schematic representation of the TCSPC method	83
3.6.	Time resolution of the TCSPC experiments	87
3.7.	PL transient and fit of an individual SWCNT	88
3.8.	Biexponential fits of SWCNT PL transients	89
3.9.	Influence of the IRF on the Fit results of PL transients	90
3.10.	White light excitation beam path	92
3.11.	Detectable spectral output of the PCF	93
3.12.	Wavelength dependent detection efficiency and transmission profiles	94
4.1.	PL decay time distribution of individual CoMoCAT SWCNTs	102
4.2.	Influence of high excitation powers on PL intensities and decay times	104
4.3.	Influence of low excitation powers on PL decay times	105
4.4.	Plot of PL decay times vs. spectral parameters	106
4.5.	Length dependence of PL decay times: Decay time distributions	110
4.6.	Length dependence of PL decay times for different length samples	111
4.7.	Variation of the PL decay times along an individual SWCNT	112
4.8.	Modeled PL decay times as function of SWCNT length	114
5.1.	PL decay time histograms of (6,5) HiPco and CoMoCAT SWCNTs	120
5.2.	PL decay time histograms of (6,4) HiPco SWCNTs on glass and in gel	121
5.3.	Correlation of τ and PL linewidth of different SWCNT materials	122
5.4.	Kinetic three level model for biexponential PL decays	123
5.5.	Parameter space of P_B and γ_0 for the kinetic model	125
5.6.	Model for the transition from bi- to monoexponential PL decays	129
5.7.	Dependency of A_{long} on the dark-bright splitting energy ΔE_{DB}	130
6.1.	Creation of low-energy PL satellite bands in individual SWCNTs	135
6.2.	Polarization dependence of the low-energy PL satellites	136
6.3.	PL transients of the bright and dark state PL	137
6.4.	Photoinduced defects in a SWCNT probed by Raman spectroscopy	139
6.5.	Evolution of Raman and PL spectra upon pulsed laser irradiation	140
6.6.	Evolution of Raman and PL spectra upon continuous CW laser exposure	141
6.7.	Photoinduced "brightening" of dark states in low-oxygen environments	143
6.8.	Creation of PL satellite bands using colloidal gold solutions	144
6.9.	Spectral dynamics of gold "brightened" dark state PL	145
6.10.	Dependency of the $ D_1\rangle$ PL decay times on the ΔE_{DB}	147
7.1.	Elastic white light scattering of individual gold nanospheres	157
7.2.	Modeled elastic scattering contrast of a 20 nm gold nanoparticle	160
7.3.	Elastic white light scattering of single layer graphene	161
7.4.	Elastic white light scattering images and spectra of individual SWCNTs	163

7.5.	Calculated optical susceptibility χ and σ_{scat} of a (6,5) SWCNT	165
7.6.	Estimation of the E_{22} extinction cross section	167
7.7.	Reflectivities of different glass/oil interfaces	169
7.8.	Inversion of the scattering contrast	170
7.9.	Chirality assignment based on PL and elastic scattering spectra	172
7.10.	Correlation of E_{22} and E_{11} energies of individual SWCNTs	173
7.11.	White light scattering and PL spectra of SWCNT aggregates	174
8.1.	PL spectra and time-resolved PL decays of PLG	182
8.2.	Evolution of Raman signals as function of plasma exposure time	184
8.3.	Elastic white light scattering spectra of PLG	187
8.4.	Correlated confocal PL and elastic scattering scan images of PLG	188
8.5.	Presumed structure of PLG	191
8.6.	PL transients of PLG as function of excitation wavelength	193
A.1.	Scattering geometry of an infinite circular cylinder	204
B.1.	Model: Elastic scattering contrast of graphene on multi-layered substrates . .	208
B.2.	Confocal white light scattering images of SLG and MLG	215
B.3.	Elastic scattering contrast as function of λ_{ex}	216
B.4.	Elastic scattering contrast as function of the graphene layer number	217
B.5.	Elastic scattering contrast as function of SiO_2 layer thickness and λ_{ex}	218

List of Tables

1.1.	Line group notation of electronic states of chiral SWCNTs [69]	26
3.1.	Lasers used for the experiments	72
3.2.	SWCNT sample materials	76
3.3.	Band pass filters for chirality specific detection of SWCNT PL	80

List of Publications

- T. Gokus, L. Cognet, J. Duque, M. Pasquali, A. Hartschuh, and B. Lounis, “Mono- and biexponential luminescence decays in individual single walled carbon nanotubes,” *J. Phys. Chem. C* **114**, 14025 (2010).
- T. Gokus, R. R. Nair, A. Bonetti, M. Böhmler, A. Lombardo, K. S. Novoselov, A. K. Geim, A. C. Ferrari, and A. Hartschuh, “Making Graphene Luminescent by Oxygen Plasma Treatment,” *ACS Nano* **3**, 3963 (2009).
- H. Harutyunyan, T. Gokus, A. Green, M. Hersam, M. Allegrini, and A. Hartschuh, “Photoluminescence from disorder induced states in individual single-walled carbon nanotubes,” *phys. stat. sol. (b)* **246**, 2679 (2009).
- H. Harutyunyan, T. Gokus, A. Green, M. Hersam, M. Allegrini, and A. Hartschuh, “Defect induced photoluminescence from dark excitonic states in individual single walled carbon nanotubes,” *Nano Lett.* **9**, 2010 (2009).
- H. Qian, P. T. Araujo, C. Georgi, T. Gokus, N. Hartmann, A. A. Green, A. Jorio, M. C. Hersam, L. Novotny, and A. Hartschuh, “Visualizing the Local Optical Response of Semiconducting Carbon Nanotubes to DNA-wrapping,” *Nano Lett.* **8**, 2706 (2008).
- C. Georgi, N. Hartmann, T. Gokus, A. A. Green, M. C. Hersam, and A. Hartschuh, “Photo-induced luminescence blinking and bleaching in individual Single-Walled Carbon Nanotubes,” *ChemPhysChem* **9**, 1460 (2008).
- T. Gokus, H. Harutyunyan, F. Hennrich, P. T. Araujo, M. Kappes, A. Jorio, M. Allegrini, A. A. Green, M. C. Hersam, and A. Hartschuh, “Exciton decay dynamics in individual carbon nanotubes at room temperature,” *Appl. Phys. Lett.* **92**, 153116 (2008).
- C. Casiraghi, A. Hartschuh, E. Lidorikis, H. Qian, H. Harutyunyan, T. Gokus, K. S. Novoselov, and A. C. Ferrari, “Rayleigh Imaging of Graphene and Graphene Layers,” *Nano Lett.* **7**, 2711 (2007).
- H. Qian, T. Gokus, N. Anderson, L. Novotny, A. J. Meixner, and A. Hartschuh, “Near-field imaging and spectroscopy of electronic states in single-walled carbon nanotubes,” *physica status solidi (b)* **243**, 3146–3150 (2006).

List of Conferences

6th Nano-Optics Adirondacks Workshop
Inlet(USA), Sept 24.09-27.09.2009

Oral presentation: "White light Scattering Spectroscopy of individual Single-Walled Carbon Nanotubes"

Workshop on Carbon Nanotube Optics (WCNO)
Kleinwalsertal (Austria), July 17.07-19.07.2009

Poster: "Absorption and time-resolved measurements of individual SWCNTs"

DPG Spring Meeting 2009: Condensed Matter Physics
Dresden (Germany), 22.03-27.03.2009

Poster: "Defect Induced Photoluminescence from Dark Excitonic States in Individual Single-Walled Carbon Nanotubes"

DPG Spring Meeting 2008: Condensed Matter Physics
Berlin (Germany), 25.02-29.02.2008

Oral presentation: "Exciton decay dynamics of individual Single-Walled Carbon Nanotubes at Room temperature"

Cens Workshop 2006: Emerging Nanosystems-From Quantum Manipulation to Nanobiomachines
Venice (Italy), 25.09-29.09.2006

Poster: "Nanoscale Optical Imaging of Carbon Nanotubes"

Acknowledgments

During the last four and a half years i had the great pleasure to work and exchange ideas with many supportive and pleasant people. They provided advice, experimental support and friendship and thus significantly contribute to the successful completion of this work. In particular, i want to express my gratitude to the following persons:

First of all, I want to thank my doctoral advisor **Prof. Achim Hartschuh** for giving me the opportunity to work in his group. His encouraging support and and tireless scientific enthusiasm were essential to the progress of this work. He was following all steps of this work with great interest and his advice and suggestions helped to develop new insights and ideas. Further, I want to thank him for organizing my stay in Belo Horizonte and giving me the opportunity to present the results of my work on various workshops and conferences.

I also want to thank **Prof. Alexander Högele** for being the second reviewer of this thesis.

This work wouldn't be possible without the excellent sample materials provided by our collaboration partners, in particular these are: **Prof. Mark Hersam** (CoMoCAT SWNTs), **Dr. Andrea Ferrari** (graphene and "luminescent" graphene), **Prof. Brahim Lounis** (HiPCO SWNTs) and **Dr. Frank Hennrich** (length sorted CoMoCAT SWNTs).

Further, I would like to thank **Dr. Cinzia Casiraghi** for giving me the opportunity to participate in the project on the elastic scattering of graphene, which were the first learning steps to handle the white light setup.

I would like to thank **Dr. Hayk Harutyunyan** for the endless hours spend together in a dark room filled with optical equipment, which, surprisingly, turned out to be quite entertaining and scientifically productive. I also want to thank him for proofreading this rather lengthy thesis.

I'm very much indebted to all present and past group members of the Hartschuh group, in particular to: **Miriam, Nicolai, Carsten, Matthias, Giovanni, Nina, Paulo and Huihong** for their support and all the activities inside and outside the university and not to forget for tons of delicious cakes, meals, beer and other funsies. This made the time more enjoyable.

Further, a big thanks to all bachelor and lab course students: **Martin, Olisea, Jens, Dominik L., Dominik B.** and **Sebastian**, who contributed with their work and ongoing interest to the progress of this work.

I also want to express my gratitude to **Prof. Ado Jorio** for being my host for three month and letting me participate in the ongoing research of his labs and in general for the pleasant stay in Brazil.

Zu guter Letzt, aber dafür umso mehr, möchte ich mich bei meiner **Familie**, meinen Eltern, meinen Brüdern und meinen Freunden für ihre fortwährende Unterstützung, ihr Interesse an meiner Arbeit und die kontinuierlichen Ermutigungen bedanken.